



**HAL**  
open science

# Highly doped semiconductor plasmonic resonators for surface enhanced infrared absorption

Franziska Barho

► **To cite this version:**

Franziska Barho. Highly doped semiconductor plasmonic resonators for surface enhanced infrared absorption. Electronics. Université Montpellier, 2017. English. NNT: 2017MONTTS075. tel-01798349v2

**HAL Id: tel-01798349**

**<https://hal.science/tel-01798349v2>**

Submitted on 7 Dec 2018

**HAL** is a multi-disciplinary open access archive for the deposit and dissemination of scientific research documents, whether they are published or not. The documents may come from teaching and research institutions in France or abroad, or from public or private research centers.

L'archive ouverte pluridisciplinaire **HAL**, est destinée au dépôt et à la diffusion de documents scientifiques de niveau recherche, publiés ou non, émanant des établissements d'enseignement et de recherche français ou étrangers, des laboratoires publics ou privés.

# THÈSE POUR OBTENIR LE GRADE DE DOCTEUR DE L'UNIVERSITÉ DE MONTPELLIER

En Électronique, Optronique et Systèmes

École doctorale Information, Structures et Systèmes

Unité de recherche Institut d'Électronique et des Systèmes – UMR 5214

Ingénierie de résonateurs plasmoniques à base de semi-  
conducteurs fortement dopés pour l'exaltation de  
l'absorption de molécules dans le moyen infrarouge

Présentée par Franziska Barbara BARHO  
Le 29 novembre 2017

Sous la direction de Thierry TALIERCIO

Devant le jury composé de

Pascale GALL-BORRUT, Professeur, IES, Université de Montpellier

Marc LAMY DE LA CHAPELLE, Professeur, IMMM, Le Mans Université

Emmanuel CENTENO, Professeur, Institut Pascal, Université Clermont Auvergne

Bruno MASENELLI, Professeur, INL, INSA Lyon

Thierry TALIERCIO, Professeur, IES, Université de Montpellier

Fernando GONZALEZ-POSADA FLORÈS, Maître de Conférences, IES, Université de Montpellier

Présidente du jury

Rapporteur

Rapporteur

Examineur

Directeur de thèse

Co-encadrant



UNIVERSITÉ  
DE MONTPELLIER





# THÈSE POUR OBTENIR LE GRADE DE DOCTEUR DE L'UNIVERSITÉ DE MONTPELLIER

En Électronique, Optronique et Systèmes

École doctorale Information, Structures et Systèmes

Unité de recherche Institut d'Électronique et des Systèmes – UMR 5214

## Highly doped semiconductor plasmonic resonators for surface enhanced infrared absorption

Présentée par Franziska Barbara BARHO  
Le 29 novembre 2017

Sous la direction de Thierry TALIERCIO

Devant le jury composé de

Pascale GALL-BORRUT, Professeur, IES, Université de Montpellier

Marc LAMY DE LA CHAPELLE, Professeur, IMMM, Le Mans Université

Emmanuel CENTENO, Professeur, Institut Pascal, Université Clermont Auvergne

Bruno MASENELLI, Professeur, INL, INSA Lyon

Thierry TALIERCIO, Professeur, IES, Université de Montpellier

Fernando GONZALEZ-POSADA FLORÈS, Maître de Conférences, IES, Université de Montpellier

Présidente du jury

Rapporteur

Rapporteur

Examineur

Directeur de thèse

Co-encadrant



UNIVERSITÉ  
DE MONTPELLIER



# Contents

<b>Remerciement</b>	<b>ix</b>
<b>Glossary</b>	<b>xi</b>
<b>Introduction</b>	<b>1</b>
<b>Résumé</b>	<b>5</b>
<b>Part I. Theoretical background</b>	<b>11</b>
<b>Mathematical formula and definitions of classical electrodynamics</b>	<b>13</b>
<b>1. Overview of Plasmonics and Plasmons</b>	<b>17</b>
1.1. Overview of different plasmonic excitations, terminology . . . . .	17
1.1.1. The bulk plasmon . . . . .	18
1.1.2. The bulk plasmon-polariton (BPP) . . . . .	20
1.1.3. The propagating surface plasmon-polariton (SPP) and the surface plasmon (SP) as its limiting case . . . . .	20
1.1.4. The localized surface plasmon-polariton (LSP) . . . . .	22
1.1.5. Plasmon resonances . . . . .	23
1.2. Surface plasmon-polaritons in layered systems . . . . .	24
1.2.1. Interface between two semi-infinite media . . . . .	24
1.2.2. SPPs in multilayer systems . . . . .	26
1.2.3. Excitation of SPPs in layered systems . . . . .	29
1.3. Localized surface plasmon-polaritons (LSPs) . . . . .	32
1.3.1. Mie theory . . . . .	32
1.3.2. The quasi-static approximation . . . . .	36
1.4. Surface plasmon-polaritons in nanostructured matter . . . . .	38
1.5. Summary . . . . .	40
<b>2. Generalities of Biosensors and Plasmonic Biosensors</b>	<b>43</b>
2.1. Introduction to biosensors . . . . .	43
2.2. The biorecognition element . . . . .	45

2.3.	Transducing methods . . . . .	47
2.3.1.	Electrochemical transduction . . . . .	48
2.3.2.	Piezoelectric transduction . . . . .	50
2.3.3.	Optical transduction . . . . .	50
2.3.4.	Comparison of the transduction methods . . . . .	50
2.4.	Surface plasmon resonance (SPR) and localised surface plasmon resonance (LSPR) sensors . . . . .	52
2.4.1.	Principle of SPR and LSPR sensors . . . . .	52
2.4.2.	State of the art . . . . .	55
2.5.	Surface enhanced spectroscopy techniques . . . . .	58
2.5.1.	Principles of SEIRA . . . . .	59
2.5.2.	State of the art . . . . .	66
2.6.	Biosensor concept of the project Supreme B (Localized Surface Plasmon Resonance in highly doped Semiconductors for Infrared Biosensing) . . . . .	72
2.7.	Summary . . . . .	73
<b>3.</b>	<b>Alternative Materials for Plasmonics</b>	<b>75</b>
3.1.	The dielectric function . . . . .	75
3.1.1.	The Drude model . . . . .	79
3.2.	Why are alternative materials for plasmonics needed? . . . . .	81
3.3.	State of the art of alternative materials for plasmonics . . . . .	85
3.4.	Plasmonics in the mid-IR spectral range . . . . .	88
3.5.	Comparison of the dielectric functions and the electric field enhancement: InAsSb and gold . . . . .	89
3.6.	Summary . . . . .	94
<b>Part II. Simulations, fabrication and optical characterization of HDSC plasmonic nanostructures</b>		<b>97</b>
<b>4.</b>	<b>Simulation of a 1D Periodic Grating Structure and Parameter Optimization</b>	<b>99</b>
4.1.	Elaboration of a FDTD model for a parameter study . . . . .	99
4.2.	Study on the geometrical parameters . . . . .	102
4.3.	Optimization for sensing around $10\ \mu\text{m}$ . . . . .	108
4.4.	Modeling a refractive index sensing transducer . . . . .	110
4.5.	Modeling absorption enhancement - estimating the SEIRA effect . . . . .	113
4.6.	Summary . . . . .	117
<b>5.</b>	<b>Simulations of 2D Periodic Nanoantenna Arrays</b>	<b>119</b>
5.1.	FDTD models for the rectangular nanoantennas . . . . .	119
5.2.	Comparison of the 2D and the 3D FDTD model . . . . .	119

5.3.	Study on the geometrical parameter of rectangular nanoantennas . . . . .	122
5.4.	Scattering and absorption of rectangular nanoantennas . . . . .	125
5.5.	Summary . . . . .	126
<b>6.</b>	<b>Technological methods for sample fabrication</b>	<b>129</b>
6.1.	Fabrication process based on photolithography and chemical etching . . . . .	129
6.1.1.	Process flow . . . . .	129
6.1.2.	Calibration of the etching rate of InAs(Sb) using citric acid : H <sub>2</sub> O <sub>2</sub> . . . . .	132
6.1.3.	Results . . . . .	134
6.2.	Fabrication process based on laser interference lithography and plasma etching .	137
6.2.1.	Introduction to laser interference lithography . . . . .	137
6.2.2.	The LIL setup . . . . .	138
6.2.3.	Process flow . . . . .	142
6.2.4.	Plasma etching of InAsSb . . . . .	143
6.2.5.	Results . . . . .	147
6.2.6.	Outlook on sample fabrication . . . . .	147
6.3.	Summary . . . . .	149
<b>7.</b>	<b>Optical Characterization of Plasmonic Resonator Structures</b>	<b>151</b>
7.1.	The experimental setup: Fourier transform infrared (FTIR) spectroscopy . . . . .	151
7.1.1.	Principle of FTIR spectroscopy . . . . .	151
7.1.2.	Description of the experimental setup used for the optical characterizations	153
7.2.	Optical characterizations of 1D periodic plasmonic gratings . . . . .	155
7.2.1.	Localized plasmon resonances in 1D periodic plasmonic gratings . . . . .	155
7.2.2.	Tunability of the LSPR by the geometry and the doping level . . . . .	160
7.3.	Optical characterizations of 2D periodic plasmonic nanoantenna arrays . . . . .	161
7.3.1.	Exploring possible geometries . . . . .	161
7.3.2.	Polarization switchable resonances . . . . .	162
7.3.3.	Interaction range in 2D periodic nanoantenna arrays - Influence of the array periodicity . . . . .	165
7.3.4.	Propagating modes on the grating . . . . .	167
7.4.	Summary . . . . .	170
<b>Part III.</b>	<b>Sensing with all-semiconductor plasmonic nanostructures</b>	<b>173</b>
<b>8.</b>	<b>Sensing with HDSC Plasmonic Nanostructures</b>	<b>175</b>
8.1.	SEIRA and SPR sensing using a 1D periodic plasmonic grating . . . . .	175
8.2.	Comparison of the 1D periodic nanoantenna grating to a gold grating . . . . .	178
8.3.	Study on the thickness dependence of LSPR sensing . . . . .	183
8.4.	Sensing of vanillin using a 2D periodic nanoantenna array . . . . .	185

*Contents*

8.5. Comparison of 1D and 2D periodic nanoantenna arrays . . . . .	190
8.6. Summary . . . . .	191
<b>Conclusion</b>	<b>193</b>
<b>A. Derivation of the dispersion relation at a plane interface</b>	<b>199</b>
<b>B. The finite-difference time-domain (FDTD) method</b>	<b>201</b>
<b>C. List of the plasmonic grating structures with a resonance at <math>10\ \mu\text{m}</math></b>	<b>203</b>
<b>D. RCWA calculation of a 2D periodic rectangular nanoantenna array</b>	<b>205</b>
<b>E. Overview of the available beam splitters and detectors for the FTIR spectrometer</b>	<b>207</b>
<b>Bibliography</b>	<b>209</b>
<b>Listes des publications et communications effectuées sur le sujet</b>	<b>231</b>

# Remerciement

Cette thèse n'aurait pas pu s'effectuer sans la contribution de beaucoup de personnes auxquelles ces quelques mots sont dédiés.

Tout d'abord, je tiens à remercier l'ensemble des membres de mon jury de thèse. Je remercie mes deux rapporteurs, M. Marc Lamy de la Chapelle et M. Emmanuel Centeno, ainsi que mon examinateur M. Bruno Masenelli, d'avoir porté de l'intérêt à mon travail, et Mme. Pascale Gall-Borrut d'avoir accepté de présider le jury.

Un grand merci à mon directeur de thèse Thierry Taliercio d'avoir encadré cette thèse, de m'avoir soutenu tout au long de ce travail, et de m'avoir consacré du temps pour discuter de notre recherche et des phénomènes physiques à l'origine des résultats obtenus.

Je remercie Fernando Gonzalez-Posada, d'avoir également encadré cette thèse. Merci pour ta grande disponibilité et aussi pour tes conseils et ton aide quant aux questions autour de l'enseignement.

Ma thèse s'est effectuée au sein de l'équipe Nanomir au laboratoire IES. Je remercie tout l'équipe, avec notre chef d'équipe Eric Tournié de m'y avoir accueilli dans d'excellentes conditions. Ce texte, c'est aussi l'occasion d'adresser un merci à tous les membres de l'équipe : Aurore Vicet, Jean-Baptiste Rodriguez, Laurent Cerutti, Jean-Philippe Perez, Michaël Bahriz, Richard Arinéro, Yves Rouillard, Philippe Christol, Roland Tessier, Alexei Baranov, Ariane Meguekam, Jean-Marc Aniel, Guilhem Boissier et Grégoire Narcy.

J'adresse aussi une pensée à mes professeurs à l'Université de Giessen et à l'Université Montpellier 2 qui m'ont donné le goût d'étudier la physique grâce à leur enseignement intéressant.

Merci aux membres du team plasmonique pour le bon travail ensemble. C'était un plaisir de travailler avec vous, et ça l'est encore. Je suis contente de pouvoir continuer avec vous encore quelque temps. Merci à Laurent qui s'occupe de la croissance des matériaux que nous utilisons. Merci à Mario pour les nombreuses discussions scientifiques et d'avoir apporté ton point de vue parfois critique. Merci aussi à tous nos stagiaires que nous avons pu accueillir durant ces trois années, pour vos contributions à notre recherche.

Le projet de recherche dont ma thèse faisait partie est porté par deux universités, l'UM et l'Université de Technologie de Troyes. Je souhaite remercier Aurélien Bruyant, Gilles Lerondel, Sylvain Blaize, Loïc Le Cunff, Anna Rumyantseva et Yi Huang pour le bon accueil lors de mon séjour à Troyes.

Je remercie également Benoît Charlot et Rudy Desgarceaux d'avoir partagé leurs compétences en matière de fabrication des échantillons par lithographie interférentielle et lithographie Talbot.



## *Remerciement*

Je voudrais adresser mes remerciements au personnel de l'ATEMI pour leur aide précieuse en salle blanche, à Fred Pichot, Jean Lyonnet et Jean-Marie Peiris, et également à Michel Ramonda pour les mesures de microscopie à force atomique.

Enfin, merci à tous les doctorants et postdocs de l'équipe Nanomir, à Quentin et Rémi mes deux camarades de rédaction, à Andrea, Marie, Karine, Julie, Mario, Kaïm, Olivier, Rodolphe, Zayneb, Roman, Daniel, Marta, Hadrien, Timothée, Dilek et Hoang, pour le temps passé ensemble et pour le partage de connaissances.

A mes parents et ma famille :

Danke an meine Eltern, hinter meinen Plänen und Vorhaben zu stehen, und danke dass ihr bei der Soutenance dabei wart. Danke an Marlene und Jonathan für eure Tips zum Manuskript und zum Vortrag. Merci Marcus d'être partant d'aller vivre en France, merci pour l'amour et la compagnie que tu m'apportes.

# Glossary

A-SRR	asymmetric split ring resonator
ATR	attenuated total reflection
AFP	alpha-feto-protein
AZO	aluminum-doped ZnO
BPP	bulk plasmon-polariton
CE	counter electrode
DNA	deoxyribonucleic acid
DOS	density of states
DTGS	deuterated triglycine sulfate
EIA	electromagnetically induced absorption
EIS	electrochemical impedance spectroscopy
EIT	electromagnetically induced transmission
ELISA	enzyme-linked immunosorbent assay
EOT	extraordinary optical transmission
FDTD	finite-difference time-domain
FEM	finite element method
FOM	figure of merit
FPA	focal plane array
FTIR	Fourier-transform infrared
FWHM	full width at half maximum
GIR	grazing incidence reflection
GZO	gallium doped ZnO
h-BN	hexagonal boron nitride
HDSC	highly doped semiconductor
ICP	inductively coupled plasma
IR	infrared
ITO	indium tin oxide
LIL	laser interference lithography
LOD	limit of detection
LSP	localized surface plasmon-polariton
LSPR	localized surface plasmon resonance
MBE	molecular beam epitaxy

## Glossary

MCT	mercury-cadmium-telluride
MIM	metal-insulator-metal
NA	numerical aperture
ODPA	octadecyl phosphonic acid
ODT	octadecanethiol
PA	perfect absorber
PAH	polycyclic aromatic hydrocarbons
PCR	polymerase chain reaction
PDMS	polydimethylsiloxane
PECVD	plasma enhanced chemical vapor deposition
PML	perfectly matched layer
PMMA	polymethylmethacrylate
QCL	quantum cascade laser
RCWA	rigorous coupled wave analysis
RE	reference electrode
RF	radio frequency
RIE	reactive ion etching
RIU	refractive index unit
SA	streptavidin
ssDNA	single-stranded DNA
SEIRA	surface enhanced infrared absorption
SEM	scanning electron microscope
SERS	surface enhanced Raman scattering
SH	second harmonic
SHG	second harmonic generation
SP	surface plasmon
SPP	surface plasmon-polariton
SPR	surface plasmon resonance
SPRi	surface plasmon resonance imaging
SRR	split ring resonator
TCMT	temporal coupled mode theory
TCO	transparent conducting oxide
TE	transverse electric
TFSF	total-field scattered-field
TM	transverse magnetic
TMM	transfer matrix method
WE	working electrode
WGM	whispering gallery mode

# Introduction

The rapid, simple and sensitive detection of biological and chemical substances is required in contexts ranging from the medical domain to environmental control and food safety. Efficient biosensors, devices that enable the detection of molecules with reasonable effort, constitute a step towards objectives such as medical diagnosis at early stages, or the protection and control of the environment through steady sampling. Biosensors based on surface plasmon-polaritons (SPP) have potential to reach high sensitivities and specificity for the detection of molecules using optical read-out techniques.

This doctoral thesis is concerned with the fabrication and the study of plasmonic resonator structures which can be applied as transducers for biosensors. SPPs, collective oscillations of an electron cloud in metallic media coupled to an electromagnetic wave, result from light-matter interaction in materials with free electrons confined to the boundaries of the metallic object. They create a strong electric field confinement and enhancement. Moreover, the surface plasmon frequency depends on the refractive index of the material at the interface of the metallic object. These properties, the electric field enhancement as well as the refractive index sensitivity, can be exploited for the detection of molecules, by enhancing their absorption features or by measuring the variation of the refractive index induced due to the presence of a substance. Refractive index or surface plasmon resonance (SPR) sensing, and the surface enhanced infrared absorption (SEIRA) spectroscopy are complementary methods, both relying on surface plasmon-related effects, which can be combined on one device.

While surface plasmons were mainly discovered using noble metals such as gold and silver, nowadays other material systems are also considered for their complementary or improved properties compared to the standard materials in plasmonics. This is especially required to enlarge the spectral range where plasmonic effects can be observed and exploited. Material science enables to tailor the dielectric function of a material and consequently to control the plasmonic properties. Highly doped III-V semiconductors constitute an alternative to gold and silver for mid-IR plasmonics, due to their dielectric function which resembles the one of the noble metals, but shifted to the mid-IR spectral range. They are even less lossy than gold in the visible. The mid-IR is a spectral range of importance for the detection of chemical and biological substances which display characteristic molecular vibration features that allow their identification due to their so-called «vibrational fingerprint», that is, their characteristic absorption spectrum. Moreover, with the availability of mid-IR light sources, such as quantum cascade lasers, and

mid-IR detectors, the prospect of a lab-on-a-chip using plasmonic structures for sensing becomes conceivable.

This doctoral thesis has been conducted in Nanomir group («Composants à Nanostructures pour Moyen Infrarouge») at the Institut de l'Électronique et des Systèmes (IES) of the University of Montpellier, France. Plasmonic structures based on epitaxially grown, highly doped InAsSb on high index GaSb substrates were investigated, with the aim of molecular detection using SPR sensing and SEIRA spectroscopy. The subject of the thesis is integrated into the French national research agency project «Supreme-B: Localized Surface Plasmon Resonance in highly doped Semiconductors for Infrared Biosensing», with the University of Montpellier, the University of Technology of Troyes and the entreprise Sikémia as project partners. The main objective of the project is the development of a plasmonic biosensor based on highly doped semiconductor (HDSC) material instead of noble metals, with the goals to achieve higher near field enhancement as with gold at mid-IR wavelengths and to integrate the plasmonic semiconductor substrate into a device including surface functionalization and a microfluidic circuit. This thesis deals especially with the development of the HDSC plasmonic nanostructures, in terms of optimization by numerical simulations, fabrication, optical characterization and proof of principle experiments. An initial work on semiconductor plasmonics in Nanomir group was carried out in the thesis of V. NTsame Guilengui [NG13]. My thesis project continued in this line after a relocation of the laboratory and the clean room facilities, so that many technological processes had to be redeveloped.

Effectively, semiconductor plasmonics and metamaterials is a relatively young field of research, starting with highly doped silicon and InSb for the terahertz (THz) spectral range around the year 2003 [GRSHBK03, RKB<sup>+</sup>04, RJBK05]. Further work on mid-IR semiconductor plasmonics followed a few years later [HSB<sup>+</sup>09, Sor10, SHC12]. D. Wasserman's group investigated possible III-V semiconductors, especially InAs, for mid-IR plasmonics [LATW12, LPW13, LYW13, LLW14] and were also the first to demonstrate SEIRA with highly doped III-V semiconductors [LYRW13]. The number of publications on alternative plasmonic materials for diverse spectral ranges has increased in the last years. It is hoped that this thesis helps to broaden the available knowledge on semiconductor plasmonics.

The manuscript is organized in three parts. The first part introduces the theoretical elements, subdivided into three chapter. Chapter 1 gives an overview of the theory of plasmons and notably surface plasmons-polaritons. The dispersion relation of surface plasmon-polaritons is derived. Localized surface plasmon-polaritons are considered in a framework of Mie theory and the quasi-static approximation. Biosensors are the main subject of Chapter 2. After presenting the generalities on biosensors, optical transduction methods relying on surface plasmon-polaritons are investigated in more detail. The fundamentals of surface plasmon resonance sensors are explained, and an overview of state-of-the-art devices is presented. Then, IR spectroscopy techniques and notably surface enhanced IR spectroscopy are detailed, followed by the state of the art of SEIRA substrates. Chapter 3 focuses on materials and their properties. The description of these optical

properties by the dielectric function is summarized and the Drude model, which is widely applied to model the properties of the HDSC, is introduced. The loss issue in plasmonic materials is then discussed. Subsequently, a list of alternative plasmonic materials applied for different applications and in different spectral ranges is presented. The chapter closes with a comparative study of the dielectric functions and the plasmonic properties of InAsSb and gold and shows the advantages of InAsSb with regard to high field enhancement and confinement in the mid-IR spectral range.

The second part of the manuscript presents the experimental and numerical work performed for the characterization of the plasmonic nanostructures. It retraces the three main competences acquired during this thesis, numerical simulation, fabrication and optical characterization of plasmonic nanostructures. It is organized in four chapters. Chapter 4 and 5 deal with numerical finite-difference time-domain (FDTD) simulations of plasmonic gratings and nanoantenna arrays. Chapter 4 focuses on the plasmonic gratings. In a parameter study, it was investigated how the geometrical parameters of the grating impact the optical response. Using electric field profiles, the nature of the plasmonic resonances was clarified. Next, models were established that allow to analyze the performance of the plasmonic structures as sensing platform. Namely, the electric field strength at a targeted wavelength, the SPR shift and the enhancement of vibrational features were investigated. Chapter 5 continues with numerical results on nanoantenna arrays. The fabrication of highly doped semiconductor plasmonic nanostructures is the subject of chapter 6. Two different processes are presented: the first process is based on optical lithography and chemical etching, the second one on laser interference lithography and reactive plasma etching. After a presentation of the experimental setup used for optical characterizations, Chapter 7 details the experimental results of the optical characterization of plasmonic gratings and nanoantenna arrays. Numerical simulations are again used to support the experimental results.

The third part of the manuscript is oriented towards the targeted application of the plasmonic nanostructures as transducing element of a sensor. Chapter 8 presents experimental and numerical results obtained using the plasmonic nanostructures to detect analytes such as polymers and organic molecules. Based on the knowledge acquired from numerical studies and the optical characterization, sensing with HDSC plasmonic nanostructures could successfully be demonstrated.



# Résumé

La détection rapide, simple et à sensibilité élevée des substances biologiques ou chimiques est demandée dans une multitude de disciplines, comme dans le domaine médical, le domaine environnemental ou aussi pour le contrôle de la nourriture. Des biocapteurs efficaces, des dispositifs permettant la détection moléculaire simple, sont une approche possible afin de pouvoir diagnostiquer des maladies en premier stade, ou pour protéger et contrôler l'environnement par le biais d'analyses régulières. Des dispositifs plasmoniques se sont révélés adaptés pour l'usage en tant qu'élément transducteur des biocapteurs, s'appuyant sur des effets de plasmon-polaritons de surface (SPP).

Cette thèse de doctorat a pour but d'étudier des nanostructures plasmoniques tout-semi-conducteur pour les utiliser comme transducteur d'un biocapteur. Elle s'est déroulée au sein du group Nanomir («Composants à Nanostructures pour Moyen Infrarouge») à l'Institut de l'Électronique et des Systèmes (IES) de l'Université de Montpellier. Le sujet de thèse fait partie d'un projet de l'agence national de recherche intitulé «Supreme-B : Localized Surface Plasmon Resonance in highly doped Semiconductors for Infrared Biosensing». Les partenaires dans ce projet sont l'Université de Montpellier, l'Université de Technologie de Troyes ainsi que l'industriel Sikémia. L'objectif de ce projet est le développement d'un biocapteur plasmonique basé sur des semi-conducteurs fortement dopés. Nous devons notamment démontrer que l'exaltation du champ électrique des semi-conducteurs fortement dopés est supérieure à celle de l'or à des longueurs d'ondes dans l'infrarouge (IR). Par ailleurs, l'intégration des nanostructures plasmoniques tout-semi-conducteur dans un dispositif comprenant la fonctionnalisation de la surface et un circuit microfluidique sera un des objectifs. Ce sujet de thèse porte notamment sur le développement des nanostructures plasmoniques. Il prend la suite d'un premier travail sur la plasmonique tout-semi-conducteur qui a été réalisé lors de la thèse de V. NTsame Guilengui [NG13], après un déménagement du laboratoire et de la salle blanche dans la première année de ma thèse.

L'étude s'est centrée autour de trois compétences scientifiques : la modélisation des structures par des méthodes de simulation numérique, la fabrication des structures par des méthodes nanotechnologiques, et enfin la caractérisation optique des structures ainsi que la démonstration de la performance pour la détection des molécules. Le manuscrit est organisé en 8 chapitres regroupés dans trois grandes parties : I. les bases théoriques, II. la modélisation, la réalisation des échantillons et les caractérisations optiques, III. la détection des molécules.

Dans le premier chapitre, nous présentons tout d'abord la théorie des plasmons et plus particulièrement des plasmon-polaritons de surface. Ce sont des oscillations collectives du nuage



électronique des métaux possédant des électrons libres, couplés à une onde électromagnétique, qui leur confère un caractère mixte longitudinal et transverse. Les SPP peuvent se propager le long des interfaces entre métaux et diélectriques ou être localisés, suite à une rupture de symétrie de translation, dans des nanoparticules. Ils engendrent une forte exaltation du champ électrique suite à un confinement sub-longueur d'onde de l'onde électromagnétique incidente. De plus, leur fréquence propre dépend fortement de l'indice de réfraction du milieu avoisinant.

Ces deux effets sont exploités pour la détection de molécules, à laquelle nous nous intéressons au second chapitre de ce manuscrit. Le changement d'indice engendré par la présence de molécules à la surface des structures plasmoniques se traduit par un changement des conditions de résonance et peut être mesuré en interrogeant le spectre, l'angle de couplage dans le cas des SPP propagatifs, ou l'intensité de réflectance à une longueur d'onde fixe pour un angle donné. Cette technique s'appelle la détection par résonance du plasmon de surface ou par résonance du plasmon de surface localisé (surface plasmon resonance (SPR) sensing ou localized surface plasmon resonance (LSPR) sensing en anglais). La forte exaltation et le confinement du champ électrique sont exploités pour l'absorption IR exaltée par la surface (SEIRA en anglais, pour surface enhanced IR absorption). Des molécules qui se situent dans les zones de fort champ électrique interagissent plus efficacement avec le rayonnement IR incident, leur section efficace d'absorption augmente. L'interaction entre le rayonnement et la molécule se fait par l'intermédiaire du plasmon-polariton de surface. Des modèles de couplage, comme celui des oscillateurs couplés, permettent de mieux comprendre ce phénomène : Le mode plasmonique qui se couple plus facilement à la lumière, dit ainsi mode radiatif, transmet l'énergie engendrée par le champ électrique qui agit sur lui au mode vibrationnel de la molécule, dit mode non-radiatif.

Alors qu'à ce jour, la majorité des dispositifs plasmoniques a été réalisée avec des métaux nobles tel que l'or et l'argent, nous proposons dans ce travail de continuer l'exploration de la plasmonique tout-semi-conducteur. Ceci est motivé par le fait que les métaux nobles présentent quelques inconvénients, que nous présentons en détail dans le troisième chapitre. Les pertes ohmiques de ces matériaux sont élevées, leur fréquence plasma (la fréquence en deçà de laquelle le matériau se comporte comme un métal suite à la partie réelle de la fonction diélectrique qui est négative) est fixe et ne peut donc pas être ajustée en fonction de la gamme spectrale dans laquelle on souhaite travailler. Par ailleurs, les métaux nobles ne sont pas compatibles avec les technologies utilisées dans la fabrication des composants électroniques, ce qui limite les perspectives d'intégration d'un composant plasmonique sur des puces électroniques.

Si l'on cherche à élargir la gamme spectrale des dispositifs plasmoniques, on s'aperçoit que les métaux nobles présentent de moins en moins de propriétés plasmoniques en allant vers des grandes longueurs d'onde comme les gammes spectrales de l'IR et du terahertz car la partie réelle de leur fonction diélectrique devient fortement négative. En effet, ils s'approchent d'un comportement de conducteur électrique parfait qui ne permet plus l'existence de plasmon de surface. Si l'on observe des phénomènes plasmoniques dans l'IR, ceci est plutôt lié à un effet d'antenne, avec un champ électrique qui pénètre très peu dans le matériau. En revanche, le confinement du champ

électrique est moins fort et l'exaltation du champ électrique est moindre si l'on n'exploite pas d'effets dits non-résonants comme l'effet de pointe ou encore de «gap-plasmon» qui correspond au confinement du champ électrique dans de faibles volumes entre deux pointes ou deux surfaces métalliques. Néanmoins, la détection de très faibles quantités de molécules, en effet de quelques attomoles, a été démontrée avec cette stratégie et avec des structures supportant des résonances plasmoniques dans l'IR grâce à leur géométrie. Ceci est détaillé au second chapitre dans l'état de l'art de la détection par exaltation de l'absorption des molécules dans l'IR.

Le troisième chapitre met en avant les matériaux qui ont été proposés en tant qu'alternative aux métaux nobles pour la plasmonique. On trouve deux approches pour limiter les pertes ohmiques dans les matériaux. La première consiste à ajouter des porteurs libres dans des semi-conducteurs par le dopage du matériau, le rendant ainsi métallique au-delà de la dégénérescence. Cette stratégie est utilisée pour le silicium et le germanium fortement dopés, les semi-conducteurs III-V, les oxydes transparents conducteurs (TCOs), et les matériaux bidimensionnels comme le graphène. L'autre approche est de réduire la quantité des porteurs libres dans des métaux par alliage ou bien en utilisant des nitrures de métaux de transition comme le TiN.

Après avoir présenté l'utilité de la plasmonique pour le moyen IR, nous avons ensuite mené une étude comparative entre l'InAsSb fortement dopé, le matériau que nous proposons d'étudier dans ce manuscrit, et les métaux nobles, en termes d'exaltation du champ électrique engendrée par ces matériaux. L'InAsSb présente des propriétés plasmoniques au-delà de la longueur d'onde plasma, aux alentours de  $5\ \mu\text{m}$  pour les dopages les plus élevés, ce qui le rend approprié pour la plasmonique dans la gamme spectrale du moyen IR. En utilisant un modèle quasi-statique, on peut constater que l'InAsSb atteint des valeurs d'exaltation du champ aussi élevées que pour l'argent dans le visible et bien plus élevées que pour l'or. D'autre part, en prenant un résonateur en forme de ruban par exemple, l'exaltation du champ électrique pour une longueur d'onde fixe a été évaluée pour l'InAsSb et l'or. La géométrie du ruban a été choisie pour que la résonance se trouve à la longueur d'onde ciblée ce qui aboutit aussi à une plus grande extension spatiale du résonateur dans le cas de l'or. Nous avons pu démontrer qu'à des longueurs d'onde dans le moyen IR, l'InAsSb atteint une exaltation du champ électrique un ordre de grandeur supérieure à celle de l'or avec un meilleur confinement du champ à la surface du matériau (un facteur quatre sur l'extension spatiale). Ceci était l'un des objectifs du projet «Supreme-B».

Dans la seconde partie de ce manuscrit, nous proposons d'étudier des nanostructures en InAsSb fortement dopé accordé en maille sur un substrat en GaSb. Deux types de structure ont été investigués en simulations numériques par la méthode de différences finies dans le domaine temporel (FDTD) puis fabriqués et caractérisés : des simples réseaux unidimensionnels (chapitre 4), puis des structures bidimensionnelles avec notamment des antennes de forme rectangulaire (chapitre 5). Dans le cas de réseau unidimensionnel, l'étude numérique a permis d'évaluer l'impact de la géométrie sur la position spectrale de la résonance. Le spectre de réflectance calculé par la méthode FDTD contient deux résonances dont une principale associée à un LSP localisé à l'interface du réseau avec le substrat et une autre résonance secondaire plus faible, pour

ces structures relativement fines, dont le profil du champ est localisé à l'interface supérieure. Deux effets de la géométrie ont été relevés. D'une part, plus les rubans du réseau sont larges, plus la résonance principale se décale vers le rouge lorsque l'épaisseur et le pas du réseau sont fixes. D'autre part, si l'on réduit l'épaisseur, la résonance principale glisse également vers les grandes longueurs d'onde. Ici c'est l'interaction entre cette dernière et la résonance secondaire qui provoque cet éclatement. La position spectrale de la résonance secondaire reste figée à cause de la proximité de la fréquence plasma. Enfin, l'impact de la périodicité du réseau a été étudié. Pour les rubans les plus proches, il y a une interaction en champ proche qui réduit la fréquence de résonance et décale ainsi la position spectrale vers le rouge. Pour les rubans les plus espacés, la période n'impacte pas la position spectrale car les rubans ne sont pas en interaction. En revanche, l'intensité de la réflectance diminue car il y a moins de matériau métallique par unité de surface lorsque la période augmente. En ajustant sur les paramètres géométriques, il est donc possible de cibler une longueur d'onde précise de résonance, qui, pour le matériau investigué, se situe dans le moyen IR.

Par la suite, les propriétés des réseaux plasmoniques quant à la détection de la modification de l'indice de réfraction ont été analysées par la méthode FDTD. La position spectrale est effectivement considérablement décalée par la présence d'une couche supplémentaire déposée à la surface. Pour des faibles épaisseurs, il y a un régime presque linéaire puis un régime de saturation en allant vers les grandes épaisseurs, en accord avec la littérature. L'utilisation d'un modèle simplifié nous a permis de déterminer la sensibilité des structures à une modification de l'indice de réfraction global dans leur environnement. Des valeurs autour de  $900 \pm 20 \text{ nm/RIU}$  ont été trouvées.

L'exaltation des signaux vibrationnels d'une couche modélisée par un oscillateur de Lorentz a également été étudiée. En faisant varier la largeur des rubans du réseau plasmonique, il a été relevé qu'un bon recouvrement spectral entre la résonance plasmonique et le mode vibrationnel moléculaire aboutit à des meilleurs contrastes du signal, avec une modulation de l'intensité de la résonance plasmonique jusqu'à 9%.

En parallèle à ces études numériques, des procédés technologiques ont été mis au point pour la fabrication des échantillons (chapitre 6). Deux approches applicables à la nanofabrication sur des larges surfaces, simples et peu coûteuses, sont proposées dans ce manuscrit. La photolithographie constitue une première approche pour créer les motifs souhaités, soit des rubans, soit des nanoantennes rectangulaires par une double exposition. En combinaison avec la gravure chimique humide utilisant un mélange d'acide citrique et peroxyde d'hydrogène ( $\text{C}_6\text{H}_8\text{O}_7 : \text{H}_2\text{O}_2$ ) dans un ratio 2 : 1, il est possible de fabriquer des structures en InAsSb sur substrat de GaSb avec une interface bien nette entre les deux matériaux grâce à la forte sélectivité de la gravure.

Afin de réduire la périodicité des réseaux, la lithographie interférentielle a été proposée. Pour la gravure des ouvertures étroites, la gravure chimique humide est difficile à mettre en oeuvre à cause de l'effet de sous gravure. En effet, la pénétration isotrope de l'acide réduit la taille latérale par rapport au motif défini par la lithographie. Il était donc indispensable de privilégier

une gravure par plasma réactif. La recette couramment utilisée pour la gravure de l'InAsSb a été modifiée afin de contrôler la gravure des faibles épaisseurs pour des motifs aussi petits. En perspective, d'autres techniques de lithographie ont été proposées telle que la lithographie Talbot. Cette méthode combine potentiellement la haute résolution de la lithographie interférentielle avec la simplicité de la photolithographie. Elle repose sur le principe de formation des images propres d'une structure périodique à des intervalles réguliers en fonction de la longueur d'onde d'illumination et de la périodicité de la structure.

D'un point de vue expérimental, les structures fabriquées par les méthodes détaillées ci-dessus ont été caractérisées par spectroscopie IR à transformée de Fourier. Les résultats sont présentés en chapitre 7. Les résonances de plasmon-polaritons de surface localisés ont été étudiées. Pour des réseaux unidimensionnels, nous avons vérifié l'accordabilité de la longueur d'onde de résonance en ajustant les paramètres géométriques du réseau ainsi que le niveau de dopage. Les nanoantennes rectangulaires, quant à elles supportent deux résonances plasmoniques à différente longueur d'onde. Elles peuvent être sélectionnées par la polarisation de la lumière incidente. La résonance longitudinale de la nanoantenne est excitée quand le vecteur de polarisation est parallèle à l'axe principal tandis que la résonance transverse l'est pour le vecteur de polarisation perpendiculaire à ce même axe. Ceci est utile car cela permet de détecter de manière résonante des molécules dans deux bandes spectrales en préservant en même temps les résonances étroites qui signifient un facteur de qualité élevé ainsi que de faibles pertes. Enfin, l'étude de l'interaction des nanoantennes a permis de montrer que la distance d'interaction est relativement courte. Ce comportement est lié à la faible diffusion des nanoantennes en InAsSb, ou autrement dit, à une absorption dominante. Des résonances du réseau tels que les anomalies de Rayleigh peuvent se superposer à des résonances plasmoniques pour des périodicités sélectionnées, relativement grandes comme nous avons pu le démontrer en simulations FDTD.

La dernière partie de ce manuscrit concerne la détection par résonances de plasmon de surface localisé (LSPR «sensing») et par la spectroscopie SEIRA. Ces deux techniques expérimentales de biodétection ont été étudiées pour deux types de structures dans le chapitre 8. Différents types d'analytes tels que les polymères polyméthacrylate de méthyle (PMMA) et la photorésine AZMIR 701, ainsi que le benzaldéhyde vanilline présentent des modes vibrationnels à grandes longueurs d'ondes dans le moyen IR. Nous les avons utilisés comme systèmes modèles. Les polymères ont l'avantage de pouvoir être déposé de manière contrôlée par centrifugation.

Dans le cas de la détection par LSPR, la sensibilité des structures plasmoniques vont de  $10^2$  à  $10^3$  nm/RIU. La valeur exacte dépend fortement de la taille et de la géométrie des nanoantennes. La valeur la plus élevée a été trouvée pour une résonance longitudinale des nanoantennes rectangulaires, la résonance excitée avec le vecteur de polarisation orienté le long de l'axe principale de la nanoantenne. Cette résonance correspond à un moment électrique plus fort que pour les résonances transverses.

Dans le cas de la spectroscopie SEIRA, les signaux vibrationnels ont été exaltés d'un facteur allant de 1,2 à 5,7. Cela nous a permis d'en déduire des facteurs d'exaltation autour de  $10^3$  à

$10^4$  pour les réseaux bidimensionnels de nanoantennes plasmoniques. Pour cette évaluation, des profils du champ électriques calculés par la méthode FDTD ont été appliqués afin de déterminer les zones de forte exaltation du champ électrique. Comparé à la littérature récente, ces valeurs se situent dans la gamme typique allant de  $10^3$ -  $10^5$  [NHW<sup>+</sup>17]. Comme nous l'avons mentionné, les meilleurs facteurs d'exaltation sont atteints pour les nanoantennes exploitant aussi des effets non-résonants tels que les effets de pointe ou bien le confinement dans un faible volume entre deux pointes. De plus, la qualité du matériau peut être un facteur critique puisqu'elle impacte les pertes supplémentaires liées aux défauts cristallins. L'utilisation des nanoantennes en or fabriquées à partir de l'or monocristallin a donné lieu à la plus faible quantité de molécules détecté par la spectroscopie SEIRA [NHW<sup>+</sup>17]. Les semi-conducteurs III-V épitaxiés se montrent avantageux quant à la qualité du matériau notamment pour le matériau accordé en maille.

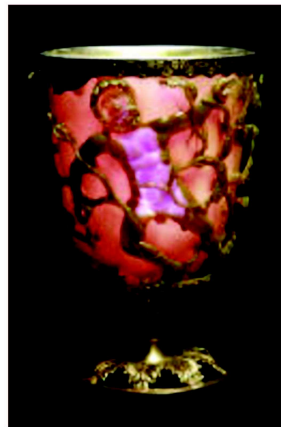
Des études récentes de la spectroscopie SEIRA soulignent en particulier l'importance du ratio entre pertes intrinsèques et extrinsèques, autrement dit, entre l'absorption et la diffusion de la nanostructure, et non seulement l'importance de l'exaltation du champ électrique. Choisir un ratio adapté permet d'optimiser le contraste du signal vibrationnel. Des calculs de sections efficaces de l'absorption et de la diffusion des antennes en InAsSb ont relevé que l'absorption est le mécanisme de pertes dominant dans ces structures pour la gamme des géométries étudiées. En effet, la faible contribution de la diffusion réduit considérablement l'interaction entre des nanoantennes avoisinantes. Tandis que ceci limite les possibilités d'exploiter des effets collectifs de couplage, il permet en revanche de densifier les nanoantennes sans altérer leur réponse optique. Par conséquent, les réseaux de nanoantennes tels que nous les avons proposés seront idéaux pour fabriquer les structures densifiées ayant une forte résonance optique.

En conclusion, les propriétés adaptés du matériau InAsSb fortement dopé pour la plasmonique dans le moyen IR ont été démontrées. Nous nous sommes rapprochés de l'objectif de créer des dispositifs plasmoniques tout-semi-conducteur pour une utilisation comme transducteur de biocapteurs.

## Part I

# Theoretical background

*Surface plasmon related effects in old and new objects*



*The Lykurgus cup in reflection and transmission*

Freestone *et al.* Gold Bulletin 2007 40/4



*Modern plasmonic device confining light at the nanoscale*

Atwater *et al.* Scientific American 2007



# Mathematical formula and definitions of classical electrodynamics

The theory of surface plasmons is based on classical electrodynamics. For this reason, Maxwell's equations are used from time to time in this manuscript. To have them at hand, they are indicated here, together with other important relations of electrodynamics in matter and some standard definitions which will appear in this manuscript. They will be given here without further explication as a collection of formula. Details can be found in electrodynamic textbooks or in introductory chapters in books on optics and plasmonics, for example in [BW02, Mai07].

## Maxwell's equations

The differential forms of Maxwell's equation in SI units are

$$\nabla \times \mathbf{H} = \mathbf{j}_{\text{ext}} + \partial_t \mathbf{D} \quad (0.1)$$

$$\nabla \times \mathbf{E} = -\partial_t \mathbf{B} \quad (0.2)$$

$$\nabla \cdot \mathbf{D} = \rho_{\text{ext}} \quad (0.3)$$

$$\nabla \cdot \mathbf{B} = 0 \quad (0.4)$$

with the four macroscopic fields  $\mathbf{E}$  the electric field,  $\mathbf{H}$  the magnetic field,  $\mathbf{D}$  the dielectric displacement, and  $\mathbf{B}$  the magnetic induction.  $\mathbf{j}_{\text{ext}}$  is the external current density, and  $\rho_{\text{ext}}$  the external charge density.

## Material equations

For nonlinear, isotropic and nonmagnetic media, the material equations or constitutive relations are

$$\mathbf{D} = \epsilon_0 \epsilon \mathbf{E} \quad (0.5)$$

$$\mathbf{B} = \mu_0 \mu \mathbf{H} \quad (0.6)$$

$$\mathbf{j} = \sigma \mathbf{E}. \quad (0.7)$$

$\epsilon_0$  and  $\mu_0$  are the vacuum permittivity and permeability.  $\epsilon$  is the relative permittivity or dielectric function of a medium.  $\mu$  is the relative permeability which equals 1 for nonmagnetic media.  $\sigma$  is the conductivity.



The Drude model, which is a simple model applied to describe the dielectric function of metallic media, will be detailed in chapter 3. It is a frequency dependent function and takes the form

$$\epsilon(\omega) = \epsilon_{\infty} \left( 1 - \frac{\omega_p^2}{\omega^2 + i\gamma\omega} \right) \quad (0.8)$$

with  $\epsilon_{\infty}$  the high frequency dielectric constant,  $\omega_p = \sqrt{\frac{Ne^2}{m^*\epsilon_0\epsilon_{\infty}}}$  the plasma frequency and  $\gamma$  the damping parameter. The formulation of the Drude dielectric function can often be found with  $\epsilon_{\infty}$  taking the value 1, for the response of a free electron gas or a material without background polarizability. In the definition of the plasma frequency,  $N$  is the carrier density,  $e$  the elementary charge and  $m^*$  the reduced electron mass in the material.

### The Helmholtz equation

The wave equation or Helmholtz equation follows from Maxwell's equations. It describes the propagation of electromagnetic waves in the absence of external stimuli  $\rho_{\text{ext}}, j_{\text{ext}} = 0$ , and takes the form

$$\nabla^2 \mathbf{E} + \frac{\omega^2}{c^2} \epsilon \mathbf{E} = 0 \quad (0.9)$$

for electric fields with harmonic time dependence  $\mathbf{E}(\mathbf{r}, t) = \mathbf{E}(\mathbf{r})e^{-i\omega t}$ .  $c = \frac{1}{\sqrt{\mu_0\epsilon_0}}$  is the velocity of light in vacuum.

### Longitudinal and transverse waves

For a wave with wave vector  $\mathbf{k}$ , the oscillating electric field  $\mathbf{E}$  can have different orientations with regard to the propagation direction defined by  $\mathbf{k}$ . If, in an isotropic and homogeneous medium,  $\mathbf{E} \parallel \mathbf{k}$ , the wave is longitudinal. If  $\mathbf{E} \perp \mathbf{k}$ , the wave is said to be transverse. This can also be expressed as

$$\mathbf{k} \times \mathbf{E} = 0 \quad \text{for longitudinal waves and} \quad (0.10)$$

$$\mathbf{k} \cdot \mathbf{E} = 0 \quad \text{for transverse waves.} \quad (0.11)$$

For vector fields, this is generalized to

$$\nabla \times \mathbf{E} = 0 \quad \text{for longitudinal fields and} \quad (0.12)$$

$$\nabla \cdot \mathbf{E} = 0 \quad \text{for transverse fields.} \quad (0.13)$$

### TE and TM polarization

For light waves incident under an angle  $\Theta$ , the polarization direction of the light is given with respect to the incidence plane formed by the wave vector  $\mathbf{k}$  with the surface normal  $\mathbf{n}$ . If the electric field vector is perpendicular to this plane, the light is transverse electric (TE) or *s*-polarized (*s* from german *senkrecht* for perpendicular). If the electric field vector lies in the plane of incidence, and hence, the magnetic vector is perpendicular to the incidence plane,

the light is transverse magnetic (TM) or *p*-polarized (*p* for *parallel*). Figure 0.1 illustrates the geometry for TE and TM polarized light waves.

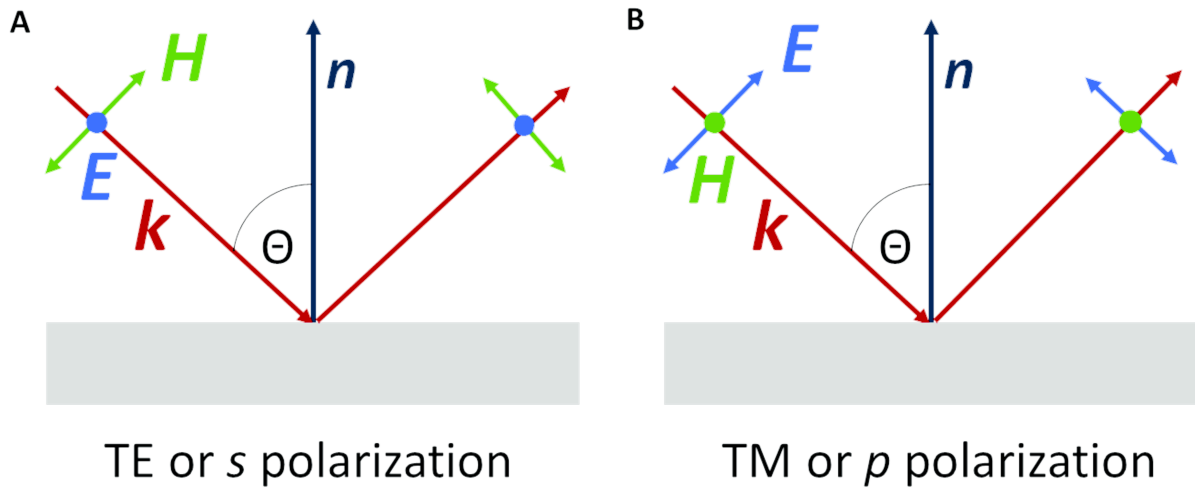


Figure 0.1.: Schematic illustration of A. a TE (*s*) polarized wave and B. a TM (*p*) polarized wave.



# 1. Overview of Plasmonics and Plasmons

Plasmonics is the research field which investigates the interaction of electromagnetic waves with the free electrons in metals and its use for applications. It is associated to the localization of light in subwavelength dimensions, which means that the diffraction limit can be overcome and that light propagation can be controlled on the nanoscale. Furthermore, strong electric field enhancement is obtained in plasmonic structures. The name plasmonics for the research discipline was given in 2000 by H. Atwater's group at the California Institute of Technology [Atw07]. The effects exploited in plasmonics, surface plasmon-polaritons, have been identified in the 1950s [Rit57] and have since then been extensively studied. A new dimension of applications of surface plasmon-polaritons came up with the discovery of the extraordinary optical transmission (EOT) by T. Ebbesen in 1998 [ELG<sup>+</sup>98]. Surface plasmon-polaritons have been observed, unaware of the physical origin, long before the discoveries of Ritchie and other researchers, for example in the color of stained glasses in reflection and transmission. The most famous object is probably the often cited Lycurgus cup.

This first chapter assembles the theoretical background of plasmonics, that is, the physics of surface plasmons and plasmons in general, and introduces the terminology that will be used in this manuscript.

## 1.1. Overview of different plasmonic excitations, terminology

Plasmons belong to the elementary excitations in solid matter. A plasmon is the quantum of charge density waves in a plasma [BH07]. It can be excited in metallic solids whose electronic structure is modeled by a delocalized electron cloud. Concretely, the electron cloud as a collective of the free charges in a metal oscillates under the influence of a driving electric field, illustrated in Figure 1.1. Other quasi-particles quantizing elementary excitations are for example phonons, magnons, and excitons [BH07]. They are quantum quasi-particles because they decay in space or over time [LE09].

Different types of plasmonic excitations can be distinguished, depending on how and in which kind of structure they are excited. They will be presented just below. Though first, another quasiparticle, the polariton, needs to be introduced. A polariton is the elementary excitation of an electromagnetic wave propagating in a medium [LE09]. That is, while the quantum of the electromagnetic wave propagating in vacuum is a photon, it is called polariton when it enters into matter. Polaritons can couple to the elementary excitations of the medium and form mixed excitations like the plasmon-polariton, when the medium disposes of free electrons.

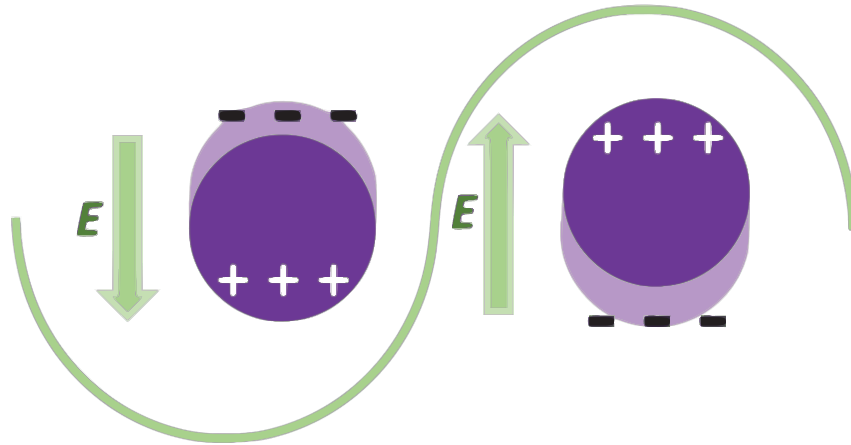


Figure 1.1.: Illustration of a collectively oscillating electron cloud in a metallic particle. The driving force is here the electromagnetic field of the impinging light wave, so that actually the case of a surface plasmon-polariton is illustrated.

The plasmonic excitations used in plasmonics, which is based on light-matter-interaction, are practically all plasmon-polaritons.

All types of plasmon excitations correspond to specific solutions, modes, of a particular system under study. Some types of plasmons exist only when the system features surfaces. The surface allows to create a longitudinal component in the electric field of the charge density wave. Figure 1.2 gives an overview of the different types of plasmons. Notably, one can distinguish plasmons and plasmon-polaritons. The «pure »surface plasmon is only an extrapolation of the propagating surface plasmon-polariton and can be seen as a limiting case when the photon contribution to the mixed mode is small. In contrast, plasmon-polaritons exist in the bulk and at surfaces.

### 1.1.1. The bulk plasmon

The bulk plasmon is an electromagnetic mode which exists in an infinite medium, with translational invariance in all three spatial dimensions. It corresponds to a purely longitudinal electric wave, and has no analogue in vacuum where electromagnetic waves are always transverse. The Maxwell equations state that the electric displacement vector in matter is transverse, that is, it fulfills equation 0.3:

$$\nabla \cdot \mathbf{D} = 0$$

in the absence of external charge  $\rho_{\text{ext}}$ . However, at frequencies where the dielectric function  $\epsilon$  vanishes, the condition is maintained even if  $\mathbf{D}$  is not transverse, because  $\mathbf{D} = \epsilon_0 \epsilon \mathbf{E}$  is still zero. Bulk plasmons exist hence at these frequencies where  $\epsilon = 0$ . If the material is described by a Drude model<sup>1</sup>, this condition is fulfilled at a particular frequency called plasma frequency

1. The Drude model will be further detailed in chapter 3

## 1.1. Overview of different plasmonic excitations, terminology

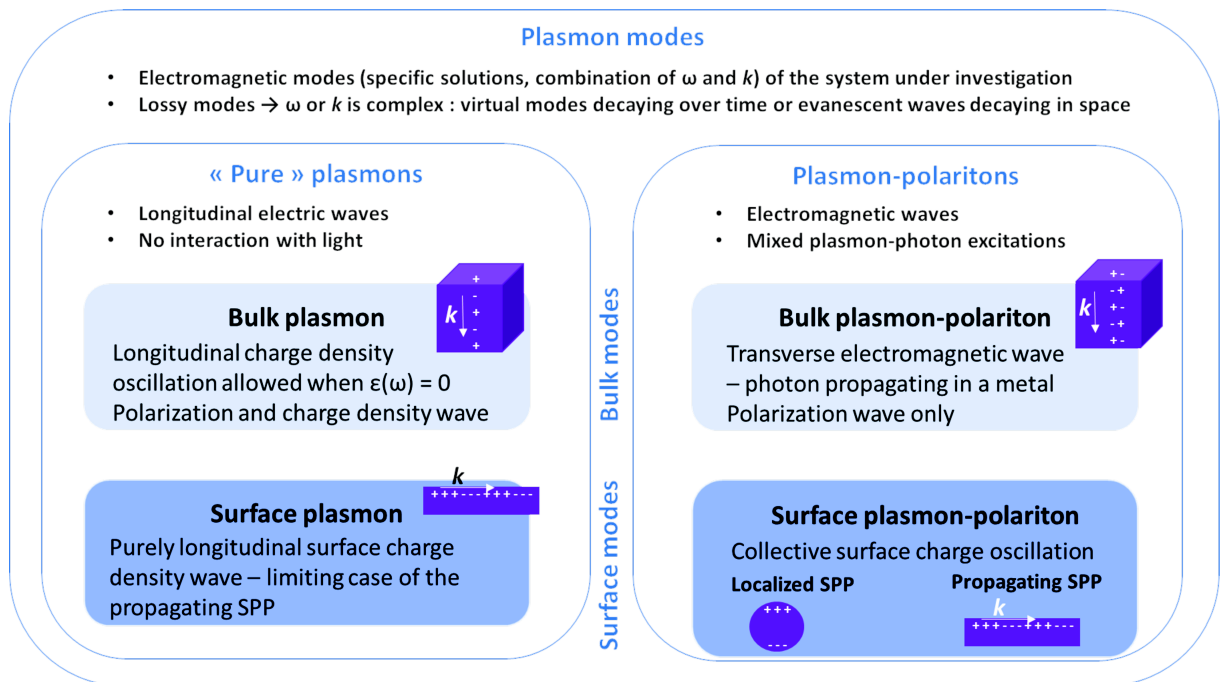


Figure 1.2.: Overview of different types of plasmons. Pure plasmons and plasmon-polaritons are distinguished (left and right part of the figure). Furthermore, surface and bulk modes are discerned. Plasmons relevant to plasmonics applications are the surface plasmon-polaritons in its propagating and localized form. Figure adapted from [LE09].

$\omega_p$ , corresponding to the longitudinal eigenfrequency of the oscillating electron cloud. The bulk plasmon is an electric wave without magnetic field, and it is associated to an internal charge density wave  $\rho_{\text{int}} = -\nabla \cdot \mathbf{P} = \nabla(\epsilon_0 \mathbf{E})$ , see Figure 1.3. Electromagnetic waves which are transverse, like free space incident light, cannot couple to bulk plasmons due to their longitudinal nature. However, electrons travelling through a metal foil can excite bulk plasmons [Pin56, Rae80]. While the bulk plasmon is here described as the electromagnetic wave solution in an infinite medium, it also exists in the volume of a finite object, confined inside the material body by the interfaces.

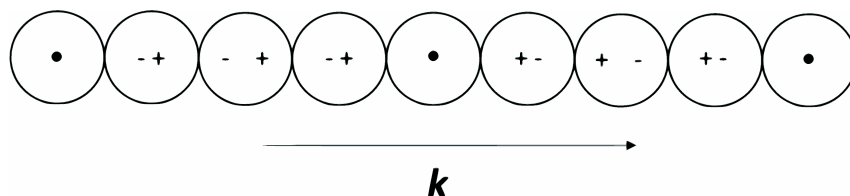


Figure 1.3.: Illustration of a longitudinal polarization wave, associated to a charge density wave. Circles represent atoms and the bold dots positions where the charge density is zero. Figure adapted from [Rae80].

### 1.1.2. The bulk plasmon-polariton (BPP)

The bulk plasmon-polariton is a transverse electromagnetic wave propagating in a metal whose dielectric function is dominated by the free electron plasma. It can be understood as light whose properties are modified by interactions with the electrons of the metal. Like the bulk plasmon, it is found as solution in an infinite medium, but exists in finite objects as well. Due to its transverse nature, the bulk plasmon-polariton does not induce a macroscopic charge density wave, but only an internal polarization wave, contrary to the bulk plasmon (Figure 1.4). The dispersion relation of the bulk plasmon-polariton is given by

$$\omega^2 = \frac{c^2}{\epsilon_\infty} k^2 + \omega_p^2, \quad (1.1)$$

in the case of a Drude dielectric function. It can be conveyed from this expression that the bulk plasmon-polariton occurs at frequencies above the plasma frequency where the dielectric function is positive, and where consequently light propagation inside the medium is allowed.

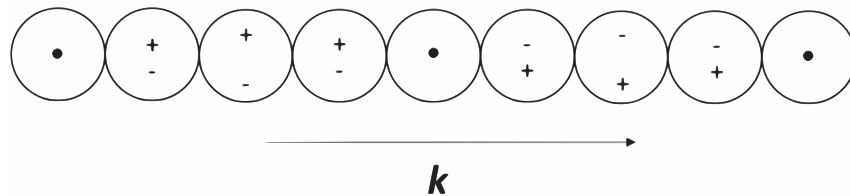


Figure 1.4.: Illustration of a transverse polarization wave. No macroscopic charge density oscillation arises from the transverse polarization wave as the polarization vector is perpendicular to the wave vector  $\mathbf{k}$ . Figure adapted from [Rae80].

### 1.1.3. The propagating surface plasmon-polariton (SPP) and the surface plasmon (SP) as its limiting case

The surface plasmon-polariton (SPP) is a charge density wave confined to an interface between a metal and a dielectric. SPPs exist only in the presence of an interface and their characteristics depend also on the properties of the dielectric forming the interface with the metal. They are hence electromagnetic solutions in systems with translational invariance in two or even less dimensions. At both sides from the interface, the mode must be transverse because of the non-zero dielectric function and the condition of transversality for the electric field in the absence of external stimuli (see equation 0.3). But due to the discontinuity at the interface, a longitudinal component of the electric field is allowed. The SPP is consequently a longitudinal charge density wave associated to a transverse electromagnetic wave. In the initial publication on surface plasmons, it was described as a longitudinal wave, a «pure» surface plasmon, derived from an electrostatic approximation [Rit57]. Effectively, there are retardation effects so that the

## 1.1. Overview of different plasmonic excitations, terminology

electrostatic approximation does not hold. For this reason, only SPPs exist, converging to the SP when the photonic contribution is small. The frequency  $\omega_{\text{SP}}$  of the (hypothetic) SP on a metal film with a dielectric function  $\epsilon_m$  is given by the condition  $\epsilon_m(\omega_{\text{SP}}) = -\epsilon_d$ , where  $\epsilon_d$  is the dielectric constant of the medium forming the interface. Consequently, the properties of the surrounding medium determine the SP frequency. In case of a metal film with a free electron Drude dielectric function in air ( $\epsilon_\infty = 1$  and  $\epsilon_d = 1$ ), the SP frequency is  $\omega_{\text{SP}} = \frac{\omega_p}{\sqrt{2}}$ .

SPP modes propagate if the wave vector component along the considered direction is real. If the wave vector component is imaginary, the wave is evanescent in this direction. If the decay takes place over relatively long distances (several wavelengths), then the mode can be seen as pseudo-propagating. Because of the complex dielectric function of metals wherein the imaginary part accounts for the losses, modes in real metals are always at best pseudo-propagating. If the real part of the metal's dielectric function is smaller than  $-\epsilon_d$ , that is, for frequencies below the SP frequency  $\omega_{\text{SP}}$  given above in the case of the Drude metal, the wave vector components  $k_{z,d}$  and  $k_{z,m}$  in the geometry presented in Figure 1.5 are imaginary, so that the wave is evanescent perpendicular to the surface.  $k_x$  would be real in case of an absorption-less metal and is complex for a realistic metal. When the losses in the metal are sufficiently small, the SPP is accordingly pseudo-propagating [LE09].

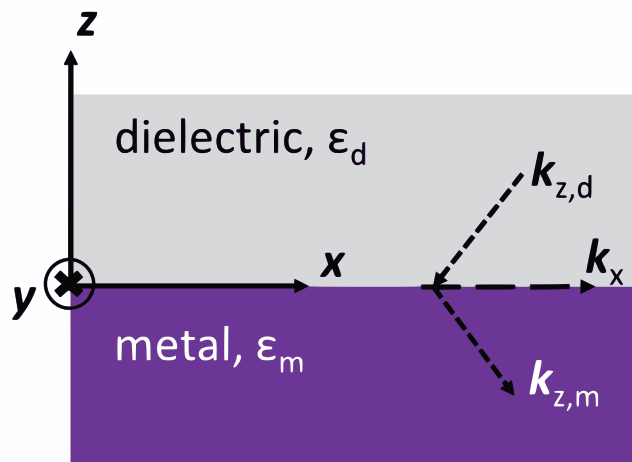


Figure 1.5.: Schematic of the geometry of a planar interface between a metal in the lower halfspace and a dielectric in the upper halfspace. The stratification of the system is in  $z$ -direction, the interface lying in the  $xy$ -plane. Without loss of generality, the in-plane wave vector is  $k_x$ . The  $k$  vector components shown exemplary correspond to the case  $\text{Re}(\epsilon_m) < -\epsilon_d$ , where the SPP is pseudo-propagating (schematized by long dashed lines).

In the frequency interval where the dielectric function of the metal is negative but larger than  $-\epsilon_d$ , the in-plane wave vector is purely imaginary and the components into the metal and the dielectric  $k_{z,d}$  and  $k_{z,m}$  are complex. Modes at these frequencies do not (pseudo-)propagate



along the interface but become localized. The waves away from the interface are also evanescent or they are pseudo-propagating if the absorption in the metal is small. If they propagate so far that they can be measured in the far field, these modes are quasi radiative. Lastly, surface modes exist also when the dielectric function is complex and its real part is positive. These modes are not considered as SPPs which are restricted to the frequency range with  $\epsilon_m < 0$ . The pseudo-propagating surface modes at positive values of the dielectric function are called Brewster modes. Figure 1.6 illustrates the dispersion relation of the different modes, the propagating and localized SPPs and the Brewster mode above  $\omega_p$ .

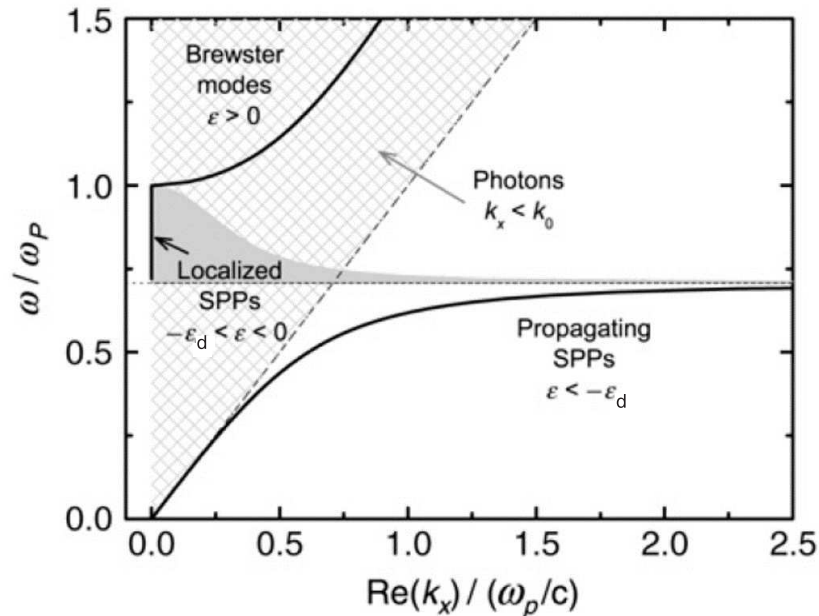


Figure 1.6.: Dispersion relation  $\omega(k_x)$  for the surface modes on an ideal metal-dielectric interface for a Drude metal with a dielectric function labeled  $\epsilon$  without absorption ( $\text{Im}(\epsilon) = 0$ ). Frequencies are normalized to  $\omega_p$ . The hatched area corresponds to the light cone, the dispersion relation of photons with any possible incidence angle from  $0^\circ$  to  $90^\circ$ . The horizontal dashed line corresponds to the surface plasmon frequency  $\omega_{SP}$  where the dispersion of the propagating SPP converges to. The gray shaded area indicates the broadening of the localized SPPs. Figure from [LE09].

#### 1.1.4. The localized surface plasmon-polariton (LSP)

As discussed above, localized surface plasmon-polaritons (LSPs)<sup>2</sup> can exist on flat surfaces in the frequency interval between the SP frequency  $\omega_{SP}$  and the plasma frequency  $\omega_p$ , where the in plane wave vector component is purely imaginary so that the wave cannot propagate in this direction.

2. The abbreviation LSP is chosen conformal with standard literature. The "P" in LSP should be understood to stand for plasmon-polariton.

### 1.1. Overview of different plasmonic excitations, terminology

Surface plasma waves exist also in metallic particles. In this case, they are electromagnetic eigenmodes of a system without translational invariance. A classification by the  $\mathbf{k}$ -vector is then not adapted. LSPs exist at discrete frequencies but with a considerable broadening due to the intrinsic absorption in the metal [LE09]. They are radiative modes which scatter light into the far field.

The frequency of LSPs depends on the material of the particle and its environment but also on the shape and size of the particle. For certain geometries, analytical methods exist to calculate the plasmonic modes, notably the Mie theory which will be addressed in section 1.3.1. The LSP frequency of a sphere which is small compared to the wavelength, can be derived from a quasi-static approximation which gives rather good results when the sphere diameter  $d < \frac{\lambda}{10}$ ,  $\lambda$  denoting the wavelength of the incident electromagnetic wave. The LSP can be excited at the frequency which satisfies  $\epsilon_m(\omega_{\text{LSP}}) = -2\epsilon_d$ , as detailed later on. A Drude metal sphere in vacuum,  $\epsilon_d = 1$ , has accordingly the LSP frequency  $\omega_{\text{LSP}} = \frac{\omega_p}{\sqrt{3}}$ .

#### 1.1.5. Plasmon resonances

The SPPs are examples of bound modes, that is, electromagnetic wave solutions that theoretically exist without an incident wave [LE09], contrary to incident wave modes like reflected or refracted waves. However, as they are lossy they need in practice an incident wave to excite and maintain them. When the incident energy is efficiently transferred to a plasmonic mode, this becomes manifest as a strong effect in the optical response of the structure, for example as large optical absorption, large far-field scattering, or strong local electric field. In Table 1.1, the resonance conditions of the discussed geometries are indicated, in the simplified cases of quasistatic treatments for the planar surface, resulting in the SP frequency, and for the sphere, resulting in the dipolar plasmon frequency. They are found by inserting the dielectric function of the metal described by a Drude model (equation 0.8) in the resonance condition. The last column gives the value for the often considered case when  $\epsilon_d = 1$  and  $\epsilon_\infty = 1$ . The resonance conditions themselves will be derived in more detail in the next few sections.

After this introduction to plasmons and especially the SPPs, a more detailed theoretical treatment is presented for the latter which are the important excitations used in plasmonics. First, the SPP propagating on an interface between two semi-infinite layers will be investigated. This can then be extended to multilayer systems, giving rise to coupling phenomena when the intermediate layer is thin. Then, a short overview of the Mie theory is given, and compared with the quasi-static approximation. Finally, plasmonic resonances in nanostructured matter are discussed. Figure 1.7 illustrates different types of structures that sustain SPPs.

## 1. Overview of Plasmonics and Plasmons

Geometry	Resonance condition	Resonance frequency (Drude metal)	Resonance frequency (Drude metal ( $\epsilon_\infty = 1$ ) in vacuum, $\epsilon_d = 1$ )
Bulk metal	$\epsilon_m(\omega) = 0$	$\omega_p$	$\omega_p$
Planar surface	$\epsilon_m(\omega) = -\epsilon_d$	$\sqrt{\frac{\epsilon_\infty}{\epsilon_\infty + \epsilon_d}} \omega_p$	$\frac{\omega_p}{\sqrt{2}}$
Sphere (dipole mode)	$\epsilon_m(\omega) = -2\epsilon_d$	$\sqrt{\frac{\epsilon_\infty}{\epsilon_\infty + 2\epsilon_d}} \omega_p$	$\frac{\omega_p}{\sqrt{3}}$

Table 1.1.: Overview of the different plasmonic excitations and the associated resonance conditions and frequencies in the case of a material described by a Drude dielectric function. (adapted from [KV95]).

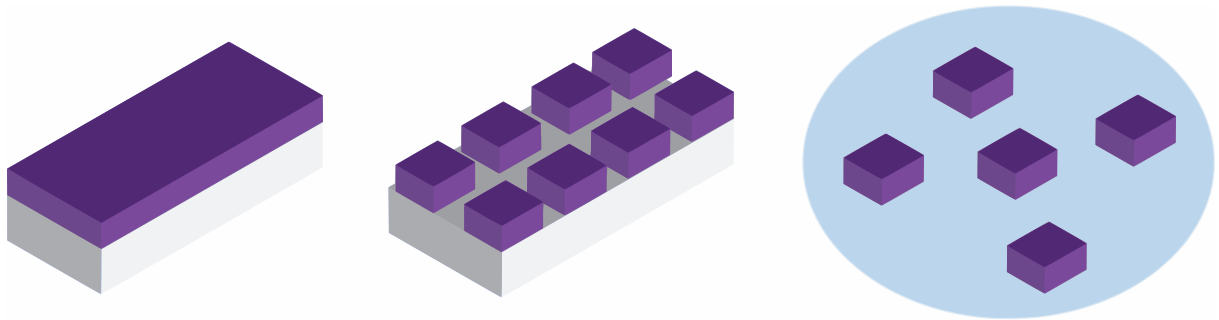


Figure 1.7.: SPPs exist on interfaces, in nanostructured matter and in isolated nanoparticles.

## 1.2. Surface plasmon-polaritons in layered systems

### 1.2.1. Interface between two semi-infinite media

The «textbook» example to derive the dispersion relation of propagating SPPs is the uncorrugated interface between two semi-infinite media, one of them metallic, the other one dielectric, as displayed in Figure 1.5. In order to find the conditions for the existence of SPPs at an interface between the two media and to express their dispersion relation, Maxwell's equations (0.1-0.4) are solved with adequate boundary conditions.

It is convenient to define first the coordinate system within the considered structure. This will considerably simplify the choice of the functional form of the electric and magnetic fields without loss of generality. The coordinate system is also shown in Figure 1.5. The interface lies in the  $xy$ -plane ( $z = 0$ ), and the wave propagates along the  $x$ -direction. The  $y$ -direction is translation invariant.

Maxwell's equations can be solved for TM and TE polarized waves separately. Waves that propagate along the interface must necessarily have a component of the electric field normal to the interface [PSCE07], as illustrated in Figure 0.1. Hence, TE polarized waves do not exist in the considered geometry. The solutions that we search are propagating waves along the  $x$ -direction with the electric field decaying with increasing distance from the interface. The solutions are of

## 1.2. Surface plasmon-polaritons in layered systems

the form:

$$\mathbf{E}_i = (E_{0,i_x}, 0, E_{0,i_z})e^{-\kappa_i|z|}e^{i(\beta_i x - \omega t)} \quad \text{and} \quad (1.2)$$

$$\mathbf{H}_i = (0, H_{0,i_y}, 0)e^{-\kappa_i|z|}e^{i(\beta_i x - \omega t)}, \quad (1.3)$$

where  $i = 1$  at  $z < 0$ , the half space occupied by the metal, and  $i = 2$  at  $z > 0$ .  $\beta_i$  is the magnitude of the in plane wave vector (along the  $x$ -direction).

Inserting this approach into the equation 0.1 in the form  $\nabla \times \mathbf{H}_i = -\frac{i\omega\epsilon_i}{c}\mathbf{E}_i$  yields

$$-\partial_z H_{i_y} = -\frac{i\omega\epsilon_i}{c}E_{i_x}. \quad (1.4)$$

Using  $\partial_z H_{i_y} = -(+)\kappa_i H_{i_y}$  for  $i = 2$  ( $i = 1$  with the sign  $+$  due to the module of  $z$ ), one obtains:

$$i\kappa_1 H_{1_y} = \frac{\omega}{c}\epsilon_1 E_{1_x} \quad (1.5)$$

$$i\kappa_2 H_{2_y} = -\frac{\omega}{c}\epsilon_2 E_{2_x}. \quad (1.6)$$

With the continuity of the tangential electric and magnetic field vector at the boundary,  $E_{1_x} = E_{2_x}$  and  $H_{1_x} = H_{2_x}$ , the following system of equations is derived:

$$\frac{\kappa_1}{\epsilon_1} H_{1_y} + \frac{\kappa_2}{\epsilon_2} H_{2_y} = 0 \quad (1.7)$$

$$H_{1_y} - H_{2_y} = 0. \quad (1.8)$$

The determinant of the system must be zero for solutions to exist. Evaluating the determinant allows to directly obtain the surface plasmon condition

$$\frac{\epsilon_1}{\kappa_1} + \frac{\epsilon_2}{\kappa_2} = 0. \quad (1.9)$$

$\kappa_{1,2}$  being positive, the surface plasmon condition can only be fulfilled at interfaces with opposite sign of the dielectric function. SPPs exist only on interfaces with this property.

An expression linking the wave vector components in  $x$  and  $z$ -directions  $k_{x_i} = \beta_i$  and  $k_{z_i} = \kappa_i$  can be derived from the wave equation (Helmholtz equation) 0.9 for TM waves [Mai07]:

$$\partial_z^2 H_{y_i} + (\epsilon_i \frac{\omega^2}{c^2} - \beta_i^2) H_{y_i} = 0. \quad (1.10)$$

With  $\partial_z^2 H_{y_i} = \kappa_i^2 H_{y_i}$ , it is found that

$$\kappa_i = \sqrt{\beta_i^2 - \epsilon_i \frac{\omega^2}{c^2}}. \quad (1.11)$$

The in plane wave vector is continuous, so that  $\beta_1 = \beta_2 =: \beta$ .

## 1. Overview of Plasmonics and Plasmons

Combining the surface plasmon condition 1.9, the continuity of the in plane wave vector and the expressions for  $\kappa_i$  as shown in the appendix A, the dispersion relation of the SPP is finally obtained:

$$\beta(\omega) = \frac{\omega}{c} \sqrt{\frac{\epsilon_1 \epsilon_2}{\epsilon_1 + \epsilon_2}}. \quad (1.12)$$

With a metal described by a frequency dependent dielectric function in the lower halfspace and a dielectric medium with constant permittivity  $\epsilon_d$  in the upper half space, this results in

$$\beta(\omega) = \frac{\omega}{c} \sqrt{\frac{\epsilon_m(\omega) \epsilon_d}{\epsilon_m(\omega) + \epsilon_d}}. \quad (1.13)$$

The derivation of the dispersion relation holds also for other surface excitations. For example, surface phonon-polaritons have the same general expression for the dispersion relation. Instead of a Drude dielectric function which would be used to specifically describe the metal dispersion, a dielectric function describing the dispersion in polar dielectrics is used [Mir82].

Figure 1.8 shows the dispersion relation for an interface between a semi-infinite highly doped InAsSb and a semiconducting GaSb layer, and at the boundary of a semi-infinite InAsSb layer with air. InAsSb and GaSb have been applied in this work for mid-IR plasmonics with innovative materials, replacing the traditionally used noble metals. The properties and advantages of the HDSC will be discussed in detail in chapter 3. For the moment, we will only introduce the material parameters used for model calculations with these materials. A constant dielectric function was used for the insulators air ( $n = 1$ ) and GaSb ( $n = 3.77$ ). A Drude dielectric function, whose functional form was introduced in the collection of formula and definitions (equation 0.8) and which will be derived in chapter 3, was applied to model the highly doped InAsSb, the Drude parameters being  $\epsilon_\infty = 10.4$  and  $\omega_p = \frac{1.2 \times 10^{15}}{\sqrt{\epsilon_\infty}}$  rad/s.  $\gamma$  was set to zero to show the simplified case of a non-absorbing metal.  $\epsilon_\infty$  was chosen according to ellipsometry measurements on thin InAsSb films, and  $\omega_p$  corresponds to the plasma frequency of the experimentally reached highest doping level in our samples of around  $5 \times 10^{19} \text{ cm}^{-3}$ .

As the dielectric function of the highly doped InAsSb has no imaginary part in this simple model ( $\gamma = 0$ ), the in plane wave vector  $\beta$  diverges and a frequency gap opens between the surface plasmon frequency  $\omega_{\text{SP}}$  and the plasma frequency  $\omega_p$ . Due to the higher refractive index of GaSb compared to air, both frequencies are lowered and the frequency gap between both branches is wider. The SPP branch for both materials lies outside the lightline in the respective medium explaining the non radiative nature of the propagating SPPs.

### 1.2.2. SPPs in multilayer systems

The model case of the interface between two semi-infinite half spaces can be extended to more complex and more realistic systems. The approach to find the dispersion relation is similar. For example, for a layer extending from  $z = -a$  to  $z = a$  described by its dielectric function  $\epsilon_1$

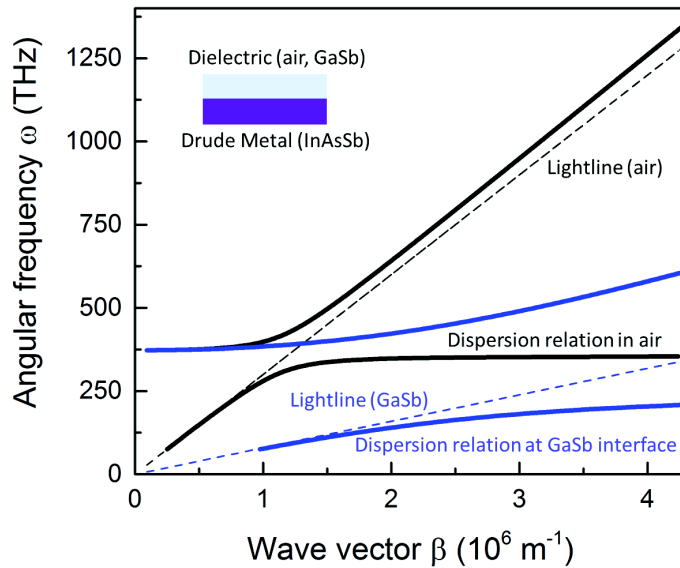


Figure 1.8.: Dispersion relation of a smooth interface between highly doped InAsSb and air (black lines) respectively GaSb (blue lines). The dashed lines indicate the lightline in the respective insulator. The lower branch to the right of the lightline corresponds to the propagating SPPs. As the highly doped InAsSb was modeled as material without damping  $\gamma = 0$ , the in-plane wave vector  $\beta$  diverges, reaching asymptotically  $\omega_{\text{SP}}$  and does not fold back towards smaller values in the frequency gap between  $\omega_{\text{SP}}$  and  $\omega_{\text{p}}$ .

sandwiched between two claddings  $\epsilon_{2,3}$  (see Figure 1.9), an approach is chosen in each region labeled  $i$ ,  $i = 1, 2, 3$  for the non-zero field components ( $E_{i_x}$ ,  $H_{i_y}$  and  $E_{i_z}$  for TM solutions).

Continuity conditions for  $E_x$  and  $H_y$  apply at both interfaces, yielding a system of four linear equations for four unknowns. Labeling the wave vector  $z$  component in each layer  $\kappa_i$ , the condition  $\kappa_i^2 = \beta^2 - \frac{\omega^2}{c^2}\epsilon_i$  from the wave equation still holds as for the two layer system, linking the  $z$  components and the  $x$  components ( $\beta$ ) of the wave vectors. Solving the linear equation system yields an implicit expression for the dispersion relation [Mai07]:

$$e^{-4\kappa_1 a} = \frac{\frac{\kappa_1}{\epsilon_1} + \frac{\kappa_2}{\epsilon_2} \frac{\kappa_1}{\epsilon_1} + \frac{\kappa_3}{\epsilon_3}}{\frac{\kappa_1}{\epsilon_1} - \frac{\kappa_2}{\epsilon_2} \frac{\kappa_1}{\epsilon_1} - \frac{\kappa_3}{\epsilon_3}}, \quad (1.14)$$

containing the frequency dependence implicitly in the dielectric functions  $\epsilon_i$ . Using numerical solvers, the dispersion relation can be evaluated.

Two cases of the expression will be investigated here. First, if  $a$  goes to infinity, 1.14 reduces to the dispersion relation of the simple interface 1.12, yielding hence two uncoupled SPPs.

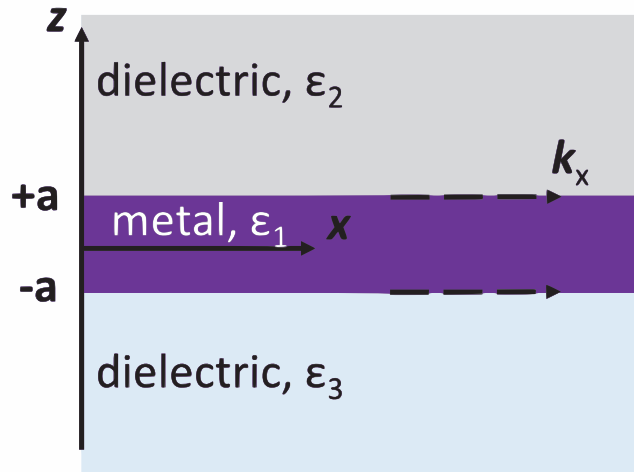


Figure 1.9.: Schematic of the geometry of a thin film forming interfaces with media described by  $\epsilon_{2,3}$ . The stratification of the system is in  $z$ -direction, and the in plane wave vector is  $k_x$ .

Second, in symmetric structures, where  $\epsilon_2 = \epsilon_3$  and  $\kappa_2 = \kappa_3$ , the expression splits into two conditions [Mai07, PSCE07]:

$$\tanh(\kappa_1 a) = -\frac{\epsilon_1 \kappa_2}{\epsilon_2 \kappa_1} \quad (1.15)$$

$$\tanh(\kappa_1 a) = -\frac{\epsilon_2 \kappa_1}{\epsilon_1 \kappa_2}. \quad (1.16)$$

The former expression corresponds to solutions with odd vector parity, that is, the component  $E_x(z)$  is an odd function, while  $H_y(z)$  and  $E_z(z)$  are even functions. Hence,  $E_x(z)$  changes its sign at the interface. The latter expression is a solution with even vector parity. Here,  $E_x(z)$  is an even function, whereas  $H_y(z)$  and  $E_z(z)$  are odd functions. Figure 1.10 illustrates the two branches from the conditions given above. The solution with odd vector parity is shifted to higher frequencies due to the interaction of electrons oscillating in phase at both interfaces while the even parity solution is shifted to lower frequencies, the electrons at both interfaces oscillating in anti-phase. For high  $k$  vectors, both expressions converge towards the SP frequency.

In the case of a thin metallic layer embedded in a dielectric (IMI structure),  $\epsilon_1$  is a frequency dependent (Drude) dielectric function, and  $\epsilon_{2,3}$  are positive constants. For thin layers, the confinement of the odd modes decreases, and the propagation length, inversely linked to the confinement, increases. These modes are called long range SPPs. The even mode evidences a high confinement in thin layers but has a short propagation length.

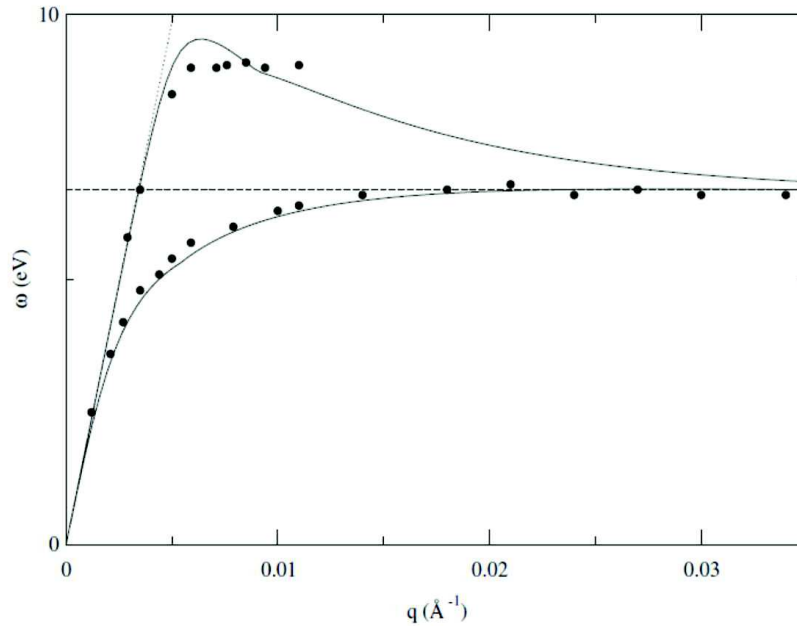


Figure 1.10.: Splitting of the SPP dispersion in a IMI structure in an upper and a lower branch. The structure is a 12 nm thick Al film in air. The circles represent electron spectrometry measurements reported by Pettit et al. [PSV75]. Solid lines correspond to the calculated dispersion in a layered system, using a Drude dielectric function for Al,  $\epsilon_2 = 1$  and  $\epsilon_3 = 4$  for the dielectric layers. The horizontal dashed line is the surface plasmon frequency  $\omega_{SP}$ . Figure from [PSCE07].

### 1.2.3. Excitation of SPPs in layered systems

As can be seen from Figures 1.6 and 1.8, the dispersion relation of SPPs in layered systems without coupling lies outside the light line. For a given energy, the in-plane component of the incident photon's wave vector is smaller than the one of a SPP. Thus, at a perfectly smooth interface, SPPs are non-radiative, they can neither be excited by light nor can the reverse process, an SPP giving rise to an emitted photon, take place. Coupling mechanisms via prisms or gratings allow to match the wave vectors of the photon and the SPP. More generally, any roughness of a surface, also in a less ordered fashion than for a grating, couples light to SPPs.

#### Prisms

Prisms allow to increase the wave vector of the incident light by a factor of  $\sqrt{\epsilon_{Pr}}$  as the incident light passes through the prism,  $\epsilon_{Pr}$  being the dielectric constant of the prism. Then, SPPs at an interface between a metal and a medium with lower refractive index than the prism, often air, can be excited by an evanescent wave. Two configurations are typically used, the Otto configuration and the Kretschmann-Raether configuration. In the Otto configuration (Figure 1.11A), light enters through the prism and impinges on an interface between the prism and the lower refractive



## 1. Overview of Plasmonics and Plasmons

index spacer (air). If this spacer layer is infinitely thick, total reflection takes place. For small thicknesses, an evanescent wave can traverse the spacer and excite a propagating SPP if the in-plane momentum of the photons  $k_x$  matches the in plane momentum of the SPP for an adapted incidence angle  $\Theta$ :

$$k_x = k\sqrt{\epsilon_{Pr}} \sin(\Theta) = \frac{\omega}{c} \sqrt{\frac{\epsilon_m(\omega)\epsilon_d}{\epsilon_m(\omega) + \epsilon_d}} = \beta = k_{SPP}, \quad (1.17)$$

$k = \frac{\omega}{c}$  being the free space wave vector of the photons. At the angle  $\Theta$  where this condition is fulfilled, a minimum in reflection is obtained. This is the so-called frustrated total reflection, i.e. uncomplete total refraction due to the energy transfer to the SPP that is excited.

The Kretschmann-Raether configuration is shown in Figure 1.11B. The metallic film is directly evaporated onto the prism, so that, similarly to the Otto configuration, an SPP can be excited on the metal-air interface. The metal serves as spacer layer through which the evanescent wave passes. In the original experiment of Kretschmann and Raether, the emission due to the SPP was measured [KR68], that is, the processus that SPP energy is transformed back to free space photons. In contrast, Otto measured the plasma resonance absorption [Ott68].

N.B.: In equation 1.17, the dispersion relation of the SPP on an interface formed by two semi-infinite media was used. Due to the presence of the prism (or grating, or any other real configuration), the dispersion relation is perturbed. In the equation, as in the following ones concerning coupling by gratings or roughness, the dispersion relation should be replaced by  $k_{SPP} = \frac{\omega}{c} \sqrt{\frac{\epsilon_m(\omega)\epsilon_d}{\epsilon_m(\omega) + \epsilon_d}} + \Delta\beta$ , where  $\Delta\beta$  is the term that accounts for the finite thickness of the metal and the presence of the prism (or grating, etc) [Hom06a].

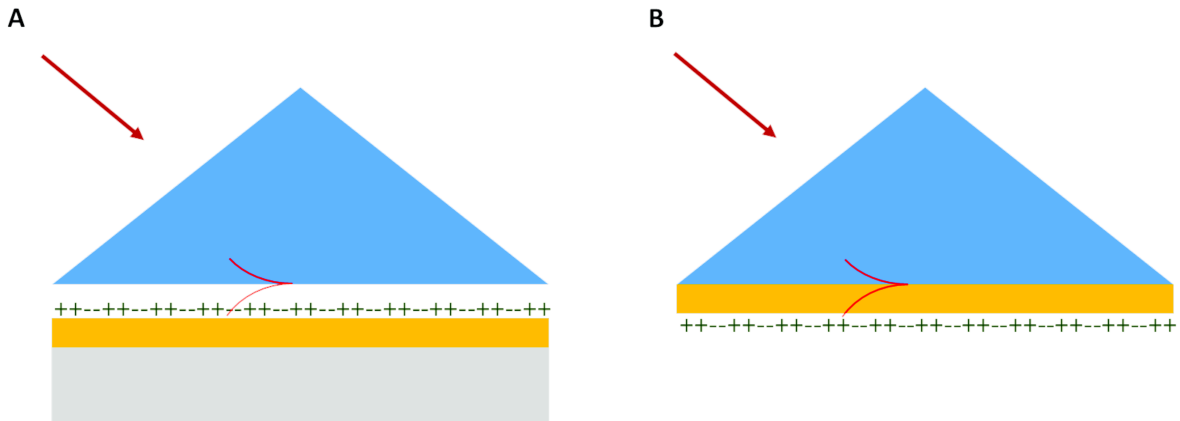


Figure 1.11.: Prism coupling. A. Otto configuration. An evanescent wave propagates through the air gap between the prism and the metallic film and couples evanescently to SPP modes of the metallic film. B. Kretschmann-Raether configuration. An evanescent wave propagates through the thin metallic film to couple to SPP modes on the outer boundary of the metallic film (interface with the lower refractive index medium, here air).

### Gratings

The purpose of the grating is again, as for the prism, to match the wave vectors. The principle used here is different: Due to the periodicity  $\Lambda$  of the grating, the dispersion relation might be reduced to an equivalent of the first Brillouin zone. Via an *umklapp* process, the grating may transfer additional momentum equivalent to an integer multiple  $m$  of the inverse grating vector  $\mathbf{G} = \frac{2\pi}{\Lambda} \hat{\mathbf{e}}_x$ :

$$k_x = \frac{\omega}{c} \sin \Theta \pm mG = \frac{\omega}{c} \sqrt{\frac{\epsilon_m(\omega)\epsilon_d}{\epsilon_m(\omega) + \epsilon_d}} = k_{\text{SPP}}. \quad (1.18)$$

The light incident with its wave vector  $\mathbf{k}$  is diffracted into a series of diffracted waves. The in-plane component of the wave vector is diffraction-altered by the grating and can excite the SPP when it equals the propagation constant of the wave vector. Figure 1.12 illustrates schematically the grating coupling.

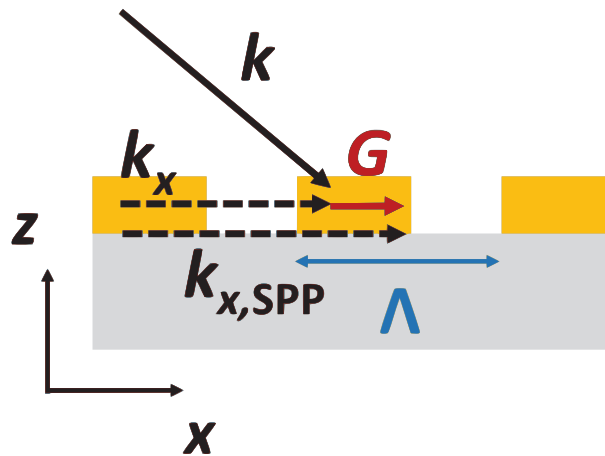


Figure 1.12.: Grating coupling: the in plane component  $k_x$  of the incoming light (wave vector  $\mathbf{k}$ ) is matched to the  $x$  component of the SPP by additional momentum from the grating vector.

### Roughness

Instead of the defined periodicity with the grating vector  $\mathbf{G}$  as shown above for the grating coupling, any perturbation of the smooth surface can introduce an additional momentum  $\Delta k_x$  that may allow to match the momentum of the incident light to the SPP:

$$k_x = \frac{\omega}{c} \sin \Theta \pm \Delta k_x = \frac{\omega}{c} \sqrt{\frac{\epsilon_m(\omega)\epsilon_d}{\epsilon_m(\omega) + \epsilon_d}} = k_{\text{SPP}}. \quad (1.19)$$

The case of rough surfaces was studied extensively by Raether [Rae80, Rae82, Rae86].

## Waveguides

Light guided in a dielectric wave guide can couple to an SPP when the light enters into a region with a thin metal film on top of the wave guide. The wave penetrates through the thin metallic film and couples with an SPP at the outer boundary of the metal film, as illustrated in Figure 1.13. Coupling is possible when the propagation constant of the wave guide mode equals the propagation constant of the SPP:

$$k_{x,\text{mode}} = k_{\text{SPP}}. \quad (1.20)$$

Indeed, the principle of waveguide coupling is similar to prism coupling.

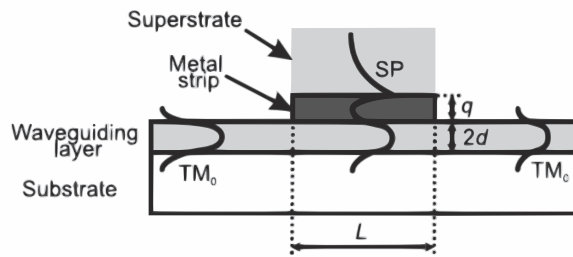


Figure 1.13.: Excitation of an SPP by a mode of a dielectric waveguide. Figure from [Hom06a].

## 1.3. Localized surface plasmon-polaritons (LSPs)

After the investigation of the surface wave solutions in geometries with translational invariance in plane we now turn to the systems without any translational symmetry. Individual metallic objects like nanoparticles sustain these type of plasmonic resonances. Due to the rupture of the symmetry, the SPPs are localized and can be excited by any wave vector  $\mathbf{k}$  and inversely also couple to outgoing light. That is, LSPs in particles are radiative modes which makes them often easier accessible as SPPs in layered systems which need the coupling mechanism described above. In the following, the formal solution to find the eigenmodes of spherical particles will be addressed. Then, a more descriptive approach, the quasi-static approximation, which is limited to the dipolar eigenmode, is presented.

### 1.3.1. Mie theory

In 1908, Gustav Mie derived a method to calculate rigorously the scattering and absorption cross sections for spherical particles [Mie08]. Modern formulations can be found in references [BW02, BH07]. Rigorous calculations of the scattering and absorption are possible for particles whose boundaries coincide with coordinate surfaces of a coordinate system in which the wave equation is separable [BH07]. Examples are, besides the already mentioned spheres, infinitely long cylinders,

## 1.3. Localized surface plasmon-polaritons (LSPs)

coated spheres, and ellipsoids [BH07]. Yet, these calculations, even for the spheres, necessitate computational power because the cross sections are given by infinite series.

In his original work, Mie intended to explain the different colors appearing in colloidal solutions of gold particles. Mie resonances were interpreted as surface plasmon oscillations of different multipole orders many years later [KZ70].

The general idea of Mie theory is to develop the electromagnetic fields inside and outside a spherical, metallic particle in series of vector functions that are solutions of the Helmholtz equation 0.9 in a spherical coordinate system. The vector functions  $\mathbf{M}$ ,  $\mathbf{N}$ , which are the solutions of the Helmholtz equation in the required coordinates, are normal modes of the sphere. They correspond physically to the electric and magnetic field created by a multipolar distribution of sources in the center of the particle [LE09]. Figure 1.14 shows illustrations of the lowest order normal modes.

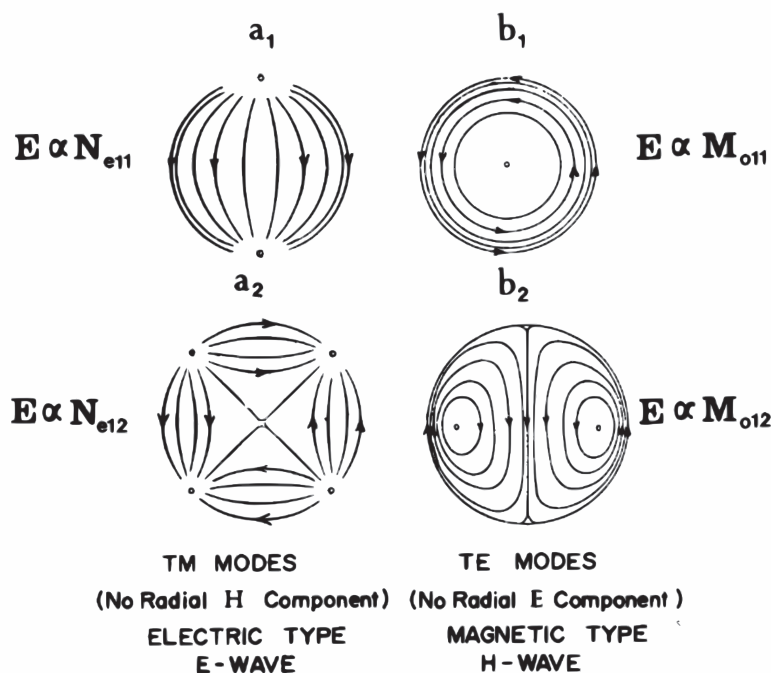


Figure 1.14.: Lowest order normal modes of a sphere. On the left are the modes without a radial magnetic field component  $\propto \mathbf{N}$ . Shown on the right are the modes without a radial electric field component  $\propto \mathbf{M}$ . The lines represent the electromagnetic field lines on the surface of a concentric imaginary sphere at a distance from the particle. The points where the field lines appear to converge to or diverge from are indeed no free charges but positions where the transverse field vanishes. The radial fields cannot be represented on a spherical surface, provoking the impression of what seems to be free charges. Figure from [BH07].

## 1. Overview of Plasmonics and Plasmons

The development of the electric field in the base of the spherical vector functions takes the form:

$$\mathbf{E} = \sum_{m=0}^{\infty} \sum_{n=m}^{\infty} B_{emn} \mathbf{M}_{emn} + B_{omn} \mathbf{M}_{omn} + A_{emn} \mathbf{N}_{emn} + A_{omn} \mathbf{N}_{omn}, \quad (1.21)$$

where  $\mathbf{M}_{e(o)}$  and  $\mathbf{N}_{e(o)}$  are the even (odd) spherical vector functions, generated by a potential function  $\Psi$  by

$$\mathbf{M}_{e(o)} = \nabla \times (\mathbf{r} \Psi_{e(o)}) \quad (1.22)$$

$$\mathbf{N}_{e(o)} = \frac{1}{k} \nabla \times \mathbf{M}_{e(o)}. \quad (1.23)$$

$\mathbf{r}$  is the radius vector and  $k$  the wave number.

The potential function  $\Psi$  is a solution of the scalar wave equation and is found by separating this scalar wave equation into a radial and two angular contributions ( $r$ ,  $\Theta$ ,  $\varphi$ ). It has the form

$$\Psi = \text{spherical Bessel function}(kr) \cdot \text{Legendre function}(\Theta) \cdot \text{trigonometric function}(\varphi).$$

The incident electric field  $\mathbf{E}_{\text{inc}}$ , the field inside the sphere  $\mathbf{E}_{\text{in}}$  and the scattered field  $\mathbf{E}_{\text{sc}}$  are developed in such series.

The incident field, physically set by the experimental conditions, is imposed by developing the desired wave form in the base of the spherical vector wave functions. As a typical example, a linear polarized plane incident wave  $\mathbf{E}_{\text{inc}} = \mathbf{E}_0 e^{ikr \cos(\Theta)} \hat{\mathbf{e}}_x$  is assumed, the polarization direction is along  $\hat{\mathbf{e}}_x$ . In the case of the plane incident wave, many coefficients in the series expansion vanish due to the orthogonality of the functions contained in the spherical vector harmonics and the trigonometric functions that express the cartesian unit vector  $\hat{\mathbf{e}}_x$  in spherical polar coordinates. This drastically simplifies the determination of the coefficients for the scattered field and the field inside the sphere. Notably, the summation over two indices reduces to one single index. The two remaining sets of series expansion coefficients for each field will be called  $a_n$  and  $b_n$  for the scattered field, and  $c_n$  and  $d_n$  for the field inside the sphere.

The continuity of the tangential electric and magnetic field components at the sphere's boundaries implies

$$E_{\text{inc},\Theta} + E_{\text{sc},\Theta} = E_{\text{in},\Theta} \quad E_{\text{inc},\varphi} + E_{\text{sc},\varphi} = E_{\text{in},\varphi} \quad (1.24)$$

$$H_{\text{inc},\Theta} + H_{\text{sc},\Theta} = H_{\text{in},\Theta} \quad H_{\text{inc},\varphi} + H_{\text{sc},\varphi} = H_{\text{in},\varphi} \quad \text{at } r = a. \quad (1.25)$$

These four equations allow to find the four unknown coefficients  $a_n$ ,  $b_n$ ,  $c_n$  and  $d_n$  in the series expansion of the scattered field  $\mathbf{E}_{\text{sc}}$  and the field inside the sphere  $\mathbf{E}_{\text{in}}$  by systems of linear equations.

## 1.3. Localized surface plasmon-polaritons (LSPs)

For the scattered field, which is the interesting case as it allows to express the scattering and absorption cross section (see below), the coefficients take the form

$$a_n = \frac{\nu\psi_n(\nu x)\psi'_n(x) - \psi_n(x)\psi'_n(\nu x)}{\nu\psi_n(\nu x)\chi'_n(x) - \chi_n(x)\psi'_n(\nu x)} \quad (1.26)$$

$$b_n = \frac{\psi_n(\nu x)\psi'_n(x) - \nu\psi_n(x)\psi'_n(\nu x)}{\psi_n(\nu x)\chi'_n(x) - \nu\chi_n(x)\psi'_n(\nu x)}. \quad (1.27)$$

In these expressions, a nonmagnetic medium with  $\mu = 1$  was assumed.  $\nu = \frac{k_{\text{in}}}{k}$  is the relative refractive index,  $x = ka$  is the size parameter ( $a$  being the radius of the sphere),  $\psi_n(kr)$  and  $\chi_n(kr)$  denote the Riccati-Bessel functions, associated to the spherical Bessel functions that appeared in the potential function of the spherical vector harmonics  $\mathbf{M}$  and  $\mathbf{N}$ .

The final step is to derive the scattering and absorption cross section of the spherical particle from the fields expressed by their series expansion. Knowing the fields  $\mathbf{E}_{\text{sc},\text{in}}$  and also  $\mathbf{H}_{\text{sc},\text{in}}$  derived from  $\mathbf{E}$  using Maxwell's equations, the time averaged Poynting vector  $\mathbf{S} = \frac{1}{2}\text{Re}(\mathbf{E} \times \mathbf{H}^*)$  is calculated. The asterisc \* denotes the complex conjugate. The power scattered by the particle is given by

$$P_{\text{sc}} = \int \mathbf{S}_{\text{sc}} \cdot \hat{\mathbf{e}}_r dA, \quad (1.28)$$

which, normalized to the incident power  $S_{\text{in}} = \frac{1}{2}\sqrt{\frac{\epsilon}{\mu}}|E_0|^2$ , yields a scattering cross section [BH07]

$$\sigma_{\text{sc}} = \frac{2\pi}{k^2} \sum_{n=1}^{\infty} (2n+1)(|a_n|^2 + |b_n|^2). \quad (1.29)$$

Analogously, the extinction is given by

$$P_{\text{ext}} = \int \mathbf{S}_{\text{ext}} \cdot \hat{\mathbf{e}}_r dA, \quad (1.30)$$

where  $\mathbf{S}_{\text{ext}} = \frac{1}{2}\text{Re}(\mathbf{E}_{\text{inc}} \times \mathbf{H}_{\text{sc}}^* + \mathbf{E}_{\text{sc}} \times \mathbf{H}_{\text{inc}}^*)$  is the term that arises because of the interaction of the incident and the scattered wave [BH07]. The extinction cross section is then [BH07]

$$\sigma_{\text{ext}} = \frac{2\pi}{k^2} \sum_{n=1}^{\infty} (2n+1)\text{Re}(a_n + b_n). \quad (1.31)$$

Finally, the absorption cross section is the difference of the previous two cross sections

$$\sigma_{\text{abs}} = \sigma_{\text{ext}} - \sigma_{\text{sc}}. \quad (1.32)$$

These analytical expressions allow to calculate the optical spectra of a sphere, given its radius and dielectric function. An implementation of the Mie series expansion is available in the open source software Mieplots [Lav]. This tool was used to calculate the scattering, absorption and extinction cross sections of spheres of different diameter with the material parameters of highly

## 1. Overview of Plasmonics and Plasmons

doped InAsSb. In Figure 1.15, the scattering (black dashed line) and absorption cross section (black solid line) as a function of wavelength is displayed for highly doped InAsSb spheres of different sizes in vacuum ( $n = 1$ ). The Drude parameters of InAsSb were used as indicated in section 1.2.1 ( $\epsilon_\infty = 10.4$ ,  $\omega_p = \frac{1.2 \times 10^{15}}{\sqrt{\epsilon_\infty}}$  rad/s) but this time with a finite damping parameter  $\gamma = 1 \times 10^{13}$  rad/s. The value was extracted from reflectance measurements on uncorrugated InAsSb layers.

For small radii  $a$ , the spectrum is dominated by a sharp absorption peak at the dipole mode resonance frequency. Scattering becomes important for bigger spheres. It is furthermore found that the resonance red-shifts when the size parameter increases, that is, when higher order terms in the series become non-negligible. Big spheres are dominated by scattering (Figures 1.15E and F). Besides the plasmonic modes, they display dielectric scattering features below the plasma wavelength, resulting in a complex scattering spectrum. Absorption contributes less for these spheres with dimensions similar to the wavelength but there is still the sharp feature at the dipole mode of the sphere.

### 1.3.2. The quasi-static approximation

The expressions derived by Mie are analytically exact, but on the other hand not very intuitive. However, for small particles compared to the incident wavelength, it is possible to expand the functions in the Mie expressions in terms of the size parameter  $x = ka$  and to retain only leading terms. This yields simple expressions that are quite useful to get an idea of the main contributions to the scattering and absorption spectrum. Besides, there is an equivalence between this case of particles that are small compared with the incident wavelength and particles embedded in a uniform static electric field. If the particle is sufficiently small, the phase variation of the external electric field can be neglected over the particle, making it hence the analogue of a particle in a spatially uniform field, as illustrated in Figure 1.16.

Instead of solving the full electromagnetic problem, an electrostatic solution is calculated, retaining however the frequency dependent dielectric function of the material. Because of this analogy, this method is called quasi-static or electrostatic approximation. It can be shown that a sphere in an electrostatic field is equivalent to an ideal dipole [BH07]. When a time-harmonic oscillating dependence is adopted to the spatially uniform field, the ideal dipole radiates, that is, scatters light back into the surrounding medium. From the scattered and absorbed powers obtained from the electrostatic solution, the absorption and scattering cross sections are derived [BH07]:

$$\sigma_{\text{sc}} = \pi a^2 \frac{8}{3} x^4 \left| \frac{\epsilon - \epsilon_d}{\epsilon + 2\epsilon_d} \right|^2 \quad (1.33)$$

$$\sigma_{\text{abs}} = \pi a^2 4x \text{Im} \left( \frac{\epsilon - \epsilon_d}{\epsilon + 2\epsilon_d} \right). \quad (1.34)$$

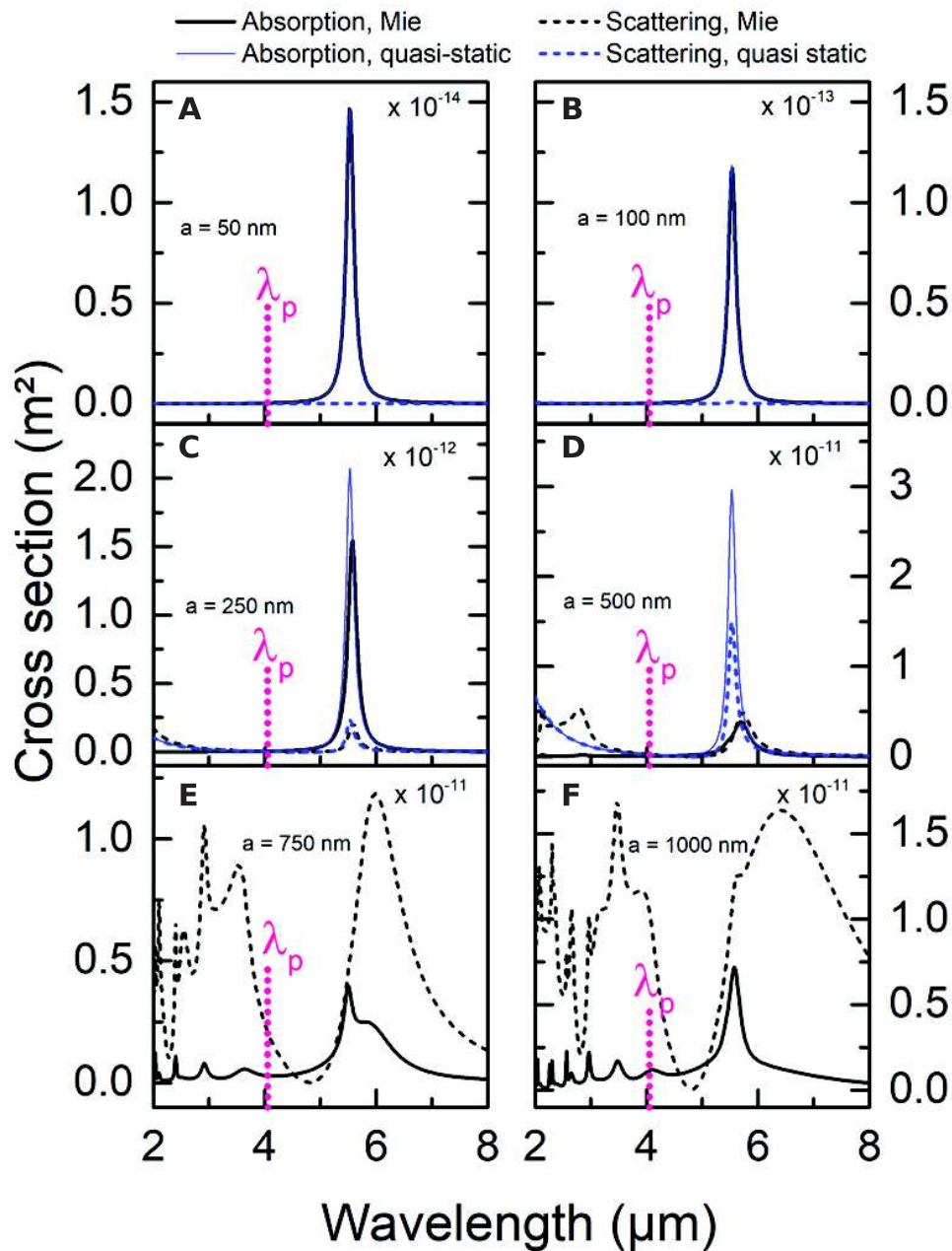


Figure 1.15.: Scattering (dashed lines) and absorption cross sections (solid lines) as a function of wavelength for highly doped InAsSb spheres of different radii  $a$  (A: 50 nm, B: 100 nm, C: 250 nm, D: 500 nm, E: 750 nm, F: 1000 nm) calculated using a Mie solver (black lines) and the quasi-static approximation (blue lines). The spectral position of the plasma wavelength  $\lambda_p$  of the HDSC is indicated in each graph. Note the different orders of magnitude indicated in each graph.



## 1. Overview of Plasmonics and Plasmons

We dropped here the index in the dielectric function of the metal  $\epsilon_m$  and will only write  $\epsilon$  in the following. Both expressions display resonant behavior when  $\epsilon + 2\epsilon_d$  tends to zero. This is fulfilled when

$$\text{Re}(\epsilon(\omega)) = -2\epsilon_d, \quad (1.35)$$

and  $\text{Im}(\epsilon(\omega))$  is small. Equation 1.35 is the dipolar resonance condition of a sphere, as indicated in Table 1.1. It is also called the Fröhlich condition.

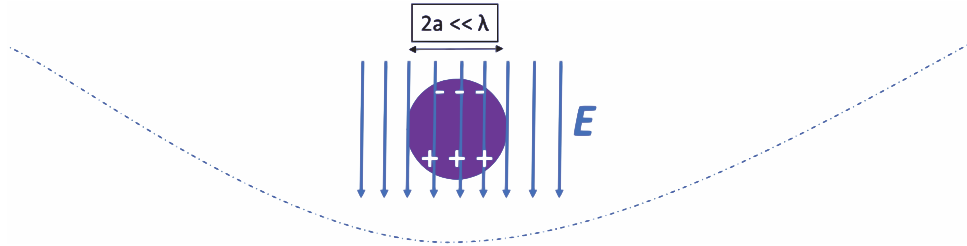


Figure 1.16.: For spheres that are small compared to the wavelength, the phase of the electric field varies negligibly over the sphere radius giving rise to the conditions of the quasi-static approximation.

In Figure 1.15, quasi-static calculations using the same material parameters are shown associated to the Mie calculations for the spheres of smaller diameter (Figures 1.15A-D). For the investigated mid-IR spectral range, the validity of quasi-static calculations reaches up to particles with diameters around 100 nm. As can be seen in Figures 1.15A and B, the quasi-static calculation corresponds to the Mie calculation. For larger particle sizes, we see that the quasi-static treatment approaches the limits of its validity. For the largest investigated particles, the approximate calculations do not even resemble the exact ones (see Figure 1.15D). For this reason, they are not shown in Figures 1.15E and F. Especially, the order of magnitude is strongly overestimated due to the proportionality factor which is  $a^6$  for the scattering (note the  $x^4$  dependence, where the size parameter  $x$  is proportional to the radius  $a$ ), and  $a^3$  for the absorption cross section.

The quasistatic spectra are dominated by the absorption and scattering maximum at the pole of the fraction. The Fröhlich condition  $\epsilon(\omega) = -2\epsilon_d$  is met here and yields the dipolar resonance. In the framework of the quasi-static approximation, the spectral position of this resonance is independent of the size of the sphere. The size impacts only the amplitude of the cross section.

### 1.4. Surface plasmon-polaritons in nanostructured matter

Beyond the described model systems such as the smooth interface or spherical particles, plasmonic modes exist also in nanostructured matter. Nanostructured matter can be understood as nanoparticles or inverse nano"particles", *e.g.* nanoslits, of well-defined shape arranged in an ordered fashion on a substrate.

#### 1.4. Surface plasmon-polaritons in nanostructured matter

The calculation of the normal modes in these nanostructured systems is not as straightforward as in the case of spherical, isolated particles or the smooth layered system from which possibly the nanostructure is fabricated. An electrostatic treatment for the modes of particles is possible for different kinds of geometries but constitutes an approximation, especially for larger particles. Moreover, the impact of the substrate on which particles might be arranged has to be incorporated to obtain the optical response comparable to experimental measurements.

For periodic nanostructured matter, different methods exist to calculate the optical response of the system. If the periodicity is small compared to the wavelength, effective medium approaches provide a possible solution. Instead of modeling an inhomogeneous medium consisting of different materials, a homogenized layer with mean properties calculated from the permittivities and the volume fractions, the so-called effective medium, is considered [Mar16].

To obtain a full solution of Maxwell's equations for periodic systems, especially for systems where the typical feature size is in the range of the wavelength, numerical methods are applied. Some of them are rigorous methods, which means that there exists a resolution parameter in the model, that, when it goes to infinity, will yield an exact solution [Rum]. Due to computational resources, the resolution parameter has however always a finite value.

Examples for rigorous numerical methods are the transfer matrix method (TMM), the rigorous coupled wave analysis (RCWA), the finite element method (FEM), the finite-difference frequency-domain method (FDFD), and the finite-difference time-domain method (FDTD). While the TMM is limited to layered systems without in plane periodicity, and the RCWA to periodic structures only, the latter three methods can be applied to model arbitrarily shaped, periodic or isolated complex structures (FDFD mainly in two dimensions) [Rum]. To model the optical response and the electric field distributions from the nanostructured matter investigated in this manuscript, we opted for the FDTD method. As a time-domain method, it allows to easily calculate the optical response under illumination with a broadband source. This is useful to find resonance frequencies of the system. Moreover, there are no restrictions on the modeled geometry, or on the modeled materials, unless in terms of introducing instabilities leading to artifacts in or divergences of the solution. Disadvantages of the FDTD method are the resolution of curved surfaces and the relatively high simulation time, especially in highly resonant devices. Details on the method can be found in chapter 4 and the appendix B.

Nanostructured matter sustains LSPs due to the rupture of symmetry and the confinement of the SPP to a limited particle. Additionally, in periodic structures, diffractive phenomena like grating orders, also called Rayleigh anomalies, or propagating SPP, allowed due to the array periodicity, may appear. In Figure 1.17, the conditions of the Rayleigh anomaly are schematized.

The Rayleigh anomaly occurs at a wavelength where the grating period matches the effective wavelength [HvHB<sup>+</sup>17]

$$\Lambda = \lambda_{\text{eff}} = \frac{\lambda}{n}, \quad (1.36)$$

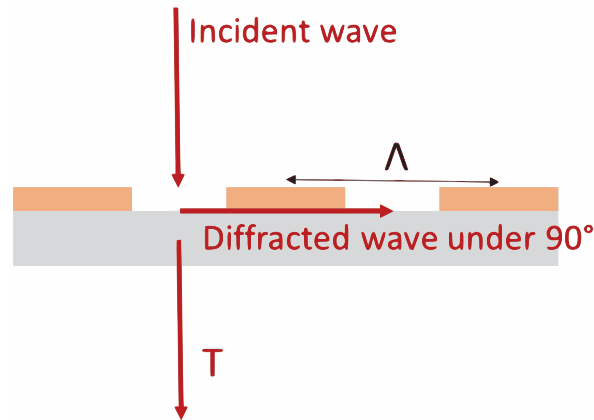


Figure 1.17.: Schematic illustration of the condition giving rise to Rayleigh anomalies. The (here normal) incident light is diffracted in the plane of the grating so that this grating order becomes radiative.

where  $\lambda$  is the free space wavelength and  $n$  the refractive index of the substrate. Indeed, at this condition, a grating order which is up to this periodicity evanescent, becomes radiative. It corresponds to a wave that is diffracted at an angle of  $90^\circ$  into the plane of the interface.

The interaction of LSPs sustained by individual particles and diffractive modes (Rayleigh anomalies or grating orders), linked to the array, was reported in the literature [HvHB<sup>+</sup>17, AYA<sup>+</sup>09, HMSB16]. It has furthermore been shown that inverse nanostructures, that is, holes of defined shape in a metallic layer, couple via propagating SPPs on the metal-substrate interface [HTN<sup>+</sup>15]. In chapter 7 of this manuscript, we investigate the coexistence of LSP and diffractive grating modes in the case of InAsSb nanoantenna arrays.

## 1.5. Summary

In this chapter, the basic theoretical elements of plasmons and surface plasmons were assembled. The characteristics of the bulk plasmon, the bulk plasmon-polariton, as well as the localized and propagating surface plasmon-polariton with its asymptotic form, the surface plasmon, were described. The modes of interest for plasmonics, SPPs, were identified and their dispersion relation was investigated in more detail. Notably, it was shown how the dispersion relation at an interface of two infinitely extended materials is found. The generalization to multilayer systems, notably a thin layer sandwiched between two halfspaces was then given. Propagating SPPs display a dispersion relation lying outside the light cone, making them non-radiative. Under some experimental conditions using phase matching between the incident wave and the SPP wave vector, propagating SPPs can nevertheless be excited. Namely, light is coupled to SPPs using prisms, gratings, surface roughness of the film in which the SPP is excited or waveguides. Next, turning to the localized form of SPPs, the LSPs in the special case of spherical particles,

corresponding to their normal modes, were introduced by means of Mie's theory. It was shown how the incident electromagnetic field on the particle, as well as the fields inside the particle and scattered by the particle are developed as series of the normal modes of a sphere. The scattering, absorption and extinction cross sections of the sphere of fixed size and defined material properties were obtained based on the series expansions. To achieve a more intuitive idea on how the scattering and absorption cross section depends on the material properties of the particle, the quasi-static (or electrostatic) approximation was addressed, which describes appropriately the dipolar plasmonic mode of a spherical particle small compared to the wavelength. Finally, the SPPs and diffractive modes sustained by nanostructured matter were assessed. Methods were discussed that can be applied to study the optical response of complex nanostructured matter where analytical solutions as for the smooth interface or the spherical particles are not available.



## 2. Generalities of Biosensors and Plasmonic Biosensors

In this chapter, the field of biosensors will be explored in a wider context. Biosensors rely on different approaches how they measure signals, for example optically or electrically. These approaches for the transduction in biosensors are presented. Also, the different biorecognition elements, that is, the ligands which bind the analyte molecules, are discussed. Then, we will concentrate on the optical sensing methods that rely on plasmonics. Surface plasmon resonance (SPR) sensing and surface enhanced spectroscopies are investigated. The state of the art in the domains of SPR sensing and surface enhanced infrared spectroscopy (SEIRA) is presented. The chapter terminates with a presentation of the project this thesis is concerned with and the definition of the objectives.

### 2.1. Introduction to biosensors

Biosensors are applied to detect biological analytes via a biochemical binding reaction. Their scope of application is large, reaching from medical analysis, control and development of pharmaceuticals, food safety up to environmental monitoring, defense and security [TT14, DLJH06].

In the medical domain, it is of interest to detect biomarkers like circulating tumor cells, cell free DNA and RNA, metabolites, peptides, and proteins for an early-stage diagnosis of illnesses [BCKT12, VH06], or pathogens like bacteria and viruses [MCCS12], among other biological substances. Quite established biosensors for medical applications exist for the detection of the small metabolite glucose as an indicator for civilization diseases like diabetes or cancer [CSR<sup>+</sup>12, MCCS12]. As a future trend, wearable sensors for real-time monitoring are being developed [CPN<sup>+</sup>14], including biological and chemical sensing of bodily fluids [CMO12]. The requirement is to be little invasive, unobtrusive, functional and easy to use to reach the necessary acceptance as a real-life solution for potential users [CMO12].

A quantitative analysis of drug compounds and the monitoring of drug - biocomponent interaction are requested for pharmaceutical control and drug development [PKE12].

Food contaminants need to be detected to avoid foodborne diseases. Foodborne pathogens include bacteria, viral and fungal cells, proteins, for example those secreted from infectious bacteria, and low molecular weight compounds [LTJ06, BSGO09].

## 2. Generalities of Biosensors and Plasmonic Biosensors

The content of pesticides, heavy metal salts, phosphates, nitrates and other substances in water, soil and air caused by environmental pollution with toxic chemicals has to be determined for environmental control [BT04, DH06].

Explosives like trinitrotoluene (TNT) need to be detected in a context of defense and security applications [DH06].

Conventional chemical analytical procedures for the detection of these substances, from small molecules to living organisms, are typically time-consuming and require sophisticated equipment operated by skilled personnel [BT04]. Conventional analysis methods for organic analytes include the extraction of the analyte by liquid-liquid extraction or liquid-solid extraction, followed by gas chromatography or high-performance liquid chromatography, coupled to a detector system, for example mass spectrometry or fluorescence detection, among other detection techniques [BT04]. Detection methods for inorganic compounds include for example atomic absorption spectrometry, optical emission spectrometry or X-ray fluorescence spectroscopy [BT04] after an adapted pretreatment of the samples. These conventional analysis methods are often the official methods for quality control of samples. Details on each of the methods can be found in reference [BT04].

Established biological techniques are the culturing of bacteria, polymerase chain reaction (PCR), and immunoassays [BSGO09]. Culturing of bacteria serves to amplify the number of cells for subsequent ocular inspection or analysis by biochemical or nucleic-acid based assays [BSGO09]. PCR is used to amplify only the number of pathogen specific nucleic acids, followed by sequencing. A common form of immunoassays is the enzyme-linked immunosorbent assay (ELISA). It can be used for the detection of antigens (short for antibody generators). Antigens in unknown quantity from a sample are immobilized on a solid support. The specific antibody is needed for detection of the antigen. To do so, the antibodies are added to the assay, so that they bind to the antigens. The antibodies are linked to an enzyme that serves as a label. Indeed, when the substrate of the enzyme is added to the assay, it will trigger typically a color change of the assay. Between each step, non-specifically bound antibodies are washed off the assay. While being sensitive and accurate, ELISAs require a lengthy preparation time, specialized personnel to perform the steps and a relatively large amount of sample ( $> 5$  ml) [BLZ<sup>+</sup>17].

Biosensors constitute a complementary approach for analysis where neither the complex equipment nor the skilled personnel is available, for point-of-care applications, on-site control and continuous monitoring by faster, simpler, or cheaper methods. This can also serve as indicator if a specific analysis by conventional methods needs to be performed.

Biosensors consist of [DH12a, Ani14]

- a biorecognition system, where a biochemical binding reaction takes place,
- a transducer, where the binding event is transformed into a physically measurable signal
- a read-out of the signal.

Figure 2.1 schematizes the components of biosensors.

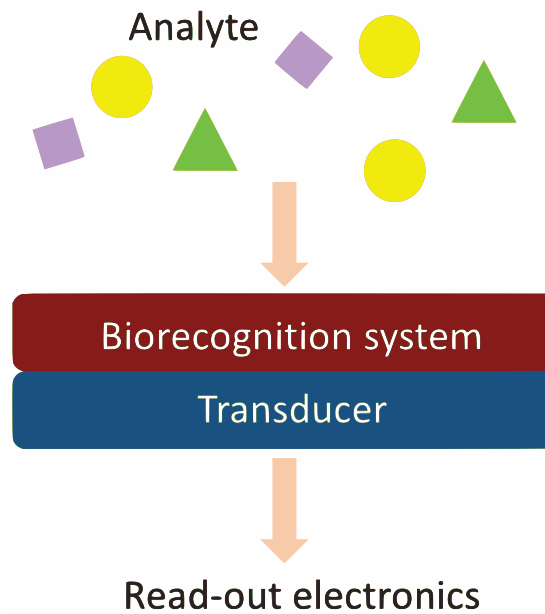


Figure 2.1.: Schematic illustration of a biosensor consisting of a biorecognition system, a transducer and the read-out of the signal.

In the next two sections, the biorecognition system and the transducing methods will be investigated in more detail.

## 2.2. The biorecognition element

### The binding reaction

In order to observe a specific binding reaction, a recognition ligand is immobilized on the sensor surface. The role of this ligand is to bind molecules that shall be detected, the so-called analyte, in a sample. Figure 2.2 shows a simplified schema of the binding reaction.

The specificity of the sensor depends strongly on the ligand, notably whether it binds to many different molecules or only to the requested analyte. Different classes of substances can be used as biorecognition ligand: enzymes, antibodies, fragments of antibodies and antibody mimetics, single stranded DNA (ssDNA), RNA and aptamers, lipids or living cells [BT04, MCCS12, dVB14, LM06].

The biotin-streptavidin system will be described in the following as a concrete example for surface binding reactions. Biotin (vitamin H) is a small molecule acting as ligand to bind the bacterial protein streptavidin (SA) (Figure 2.3). Biotin-SA serves as a model system for the study of high affinity protein-ligand interactions [CKLH11] and is also an excellent model system for the validation of biosensors [HV02]. The binding is highly specific and is one of the strongest non-covalent interactions in nature [CKLH11].



## 2. Generalities of Biosensors and Plasmonic Biosensors

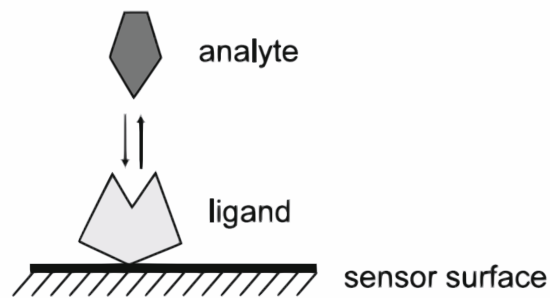


Figure 2.2.: The biorecognition element, labeled ligand in the schema, is immobilized onto the sensor surface. The analyte available in a solution binds (reversibly) to the biorecognition ligand. (Figure from [LM06]).

Biotin is immobilized on the transducer by a linker molecule. For example, to attach biotin to a gold surface, molecules with a carboxylic acid terminal group are used as linker [HV02]. The biotinylated surface is then exposed to a solution containing SA. The binding of the SA molecule, illustrated in Figure 2.3, leads to a modification of the refractive index which is read out by optical sensing methods (see section 2.3.3).

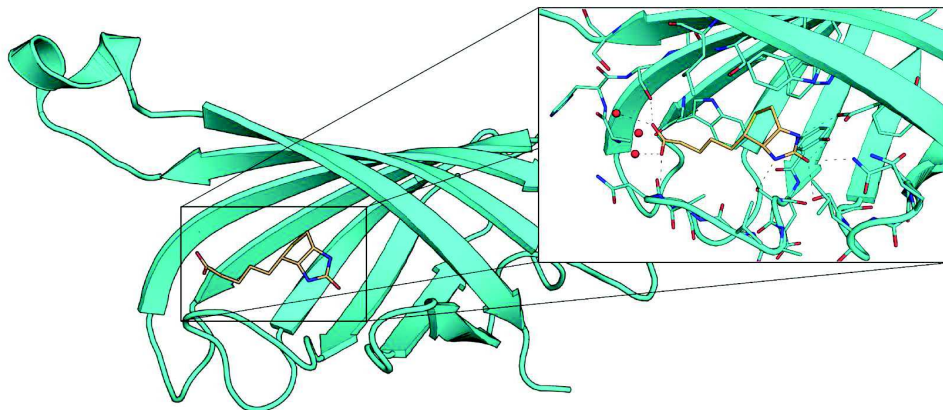


Figure 2.3.: Illustration of the biotin-SA system. The inset shows a zoom of the region where the SA molecule binds to biotin (illustrated in yellow). Displayed are the amino acids contained in the SA molecule that interact with biotin. Dashed lines depict hydrogen bonds.

### Detection formats

For some analytes, especially medium to large size molecules, it is possible to directly measure the signal induced by the binding of the analyte to the biorecognition element, but for small molecules, signals can indeed be too weak. For this reason, different direct and indirect detection formats exist. In direct methods, the sensor response is produced by the analyte binding to the

sensor. Meanwhile, in indirect methods, the analyte induces merely a change in the state of a secondary system component, which then triggers the sensor response [DLJH06].

Besides the already mentioned immediate detection of the analyte binding to the ligand (see Figure 2.4A), other direct detection formats are sandwich assays (Figure 2.4B) and competitive assays (Figure 2.4C). In a sandwich assay, for example with antibodies, the analyte is captured by an immobilized antibody on the sensor surface and then a second antibody in solution binds to the analyte at another epitope to produce a measurable signal. This can improve the limit of detection and verifies that the bound analyte is the right one and not an unspecific binding reaction. Moreover, the sandwich antibody can carry a label to further reduce the limit of detection.

In competitive assays, a known concentration of a competitor molecule is added to the analyte solution. The competitor binds also to the ligand but produces a stronger signal than the actual analyte, because it is linked to a larger protein, for example. If there are very few analyte molecules present, more competitor molecules can bind to the ligand binding sites. So, the signal of competitor binding is inversely proportional to the analyte concentration.

Inhibition assays constitute an indirect detection format. They consist of more steps than the other detection formats. The sample is preincubated with an antibody of known concentration for the target analyte. Moreover, an analyte derivative is immobilized on the transducer. The sample mixed with the antibody is then injected. Unreacted antibody binds to the immobilized analyte derivative (see Figure 2.4D). A high amount of unreacted antibody indicates a low concentration of analyte in the sample. This also means that this high amount can bind to the analyte derivative, yielding a strong signal at the transducer. Consequently, as for the competitive assay, the signal is inversely proportional to the analyte concentration, making this more complex technique interesting for small concentrations.

### Limitations

Biosensors rely on the activity of the biorecognition element for specific binding. One limiting factor is consequently the stability of the biorecognition ligand under storage conditions. In complex samples, biofouling such as protein deposition on the sensor surface, can be a problem [DH12a]. It can be overcome by using antifouling layers [BCKT12]. Non-specific binding remains the limiting factor for all biosensors for real samples [VCK12]. Techniques with high specificity like surface enhanced Raman scattering (SERS) or SEIRA can be helpful to deal with the non-specific binding, to confirm the presence or absence of the target molecule and theoretically reduce the limit of detection of real samples by several orders of magnitude.

## 2.3. Transducing methods

The most important and wide spread transduction methods are the electrochemical and optical approaches [BT04]. Besides, there exist other techniques relying on piezoelectric, thermometric

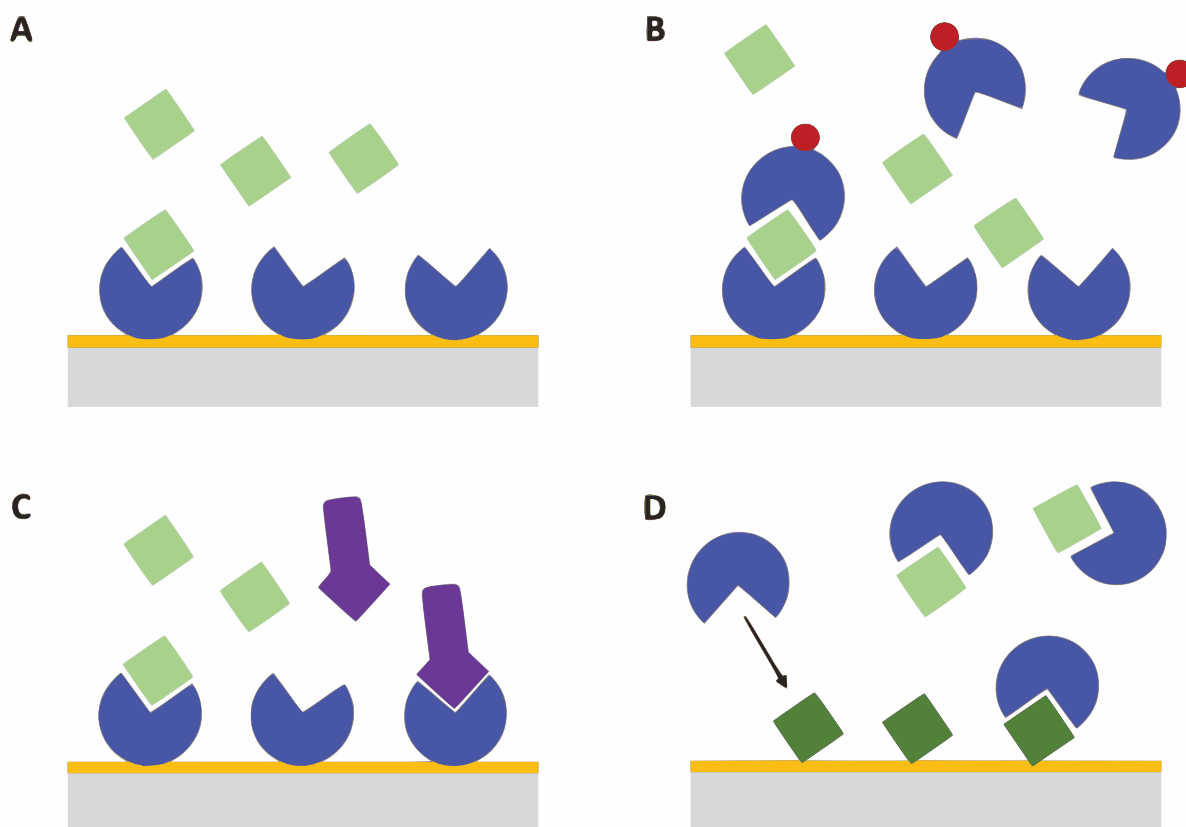


Figure 2.4.: Detection formats. A. Direct binding of the analyte (green squares) to the biorecognition element (blue circle segments). B. Sandwich assay. A second, eventually labeled biorecognition elements binds to another epitope of the analyte. C. Competitive assay. A competitor molecule (purple symbols) competes with the analyte for binding pockets. D. Inhibition assay. The preincubated sample is flowed over the sensor functionalized with an analyte derivative (dark green squares). Unreacted biorecognition molecules bind to the analyte derivative.

and magnetic transducers [BSGO09, BCKT12]. In the following, an overview of the frequently used electrochemical transduction methods, piezoelectric transducers and some selected optical sensing methods is presented.

### 2.3.1. Electrochemical transduction

Electrochemical transducers convert the binding event into an electrical signal. Several ways exist to measure this electrical signal. One distinguishes between amperometric (also called voltammetric), potentiometric and impedimetric platforms [VCK12]. These transducers typically use a configuration based on a three-electrode cell consisting of a working electrode, a reference electrode and a counter electrode [VCK12], as schematized in Figure 2.5. In amperometric sensors, a current arising from the oxidation or reduction of an electroactive product at the

working electrode is measured. A potential difference between the working electrode, where the binding reaction takes place, and the reference electrode is measured in a potentiometric setup. Impedimetric sensors measure changes of the impedance resulting from an interaction between the analyte with a receptor, using electrochemical impedance spectroscopy (EIS) [VCK12, BT04, dVB14].

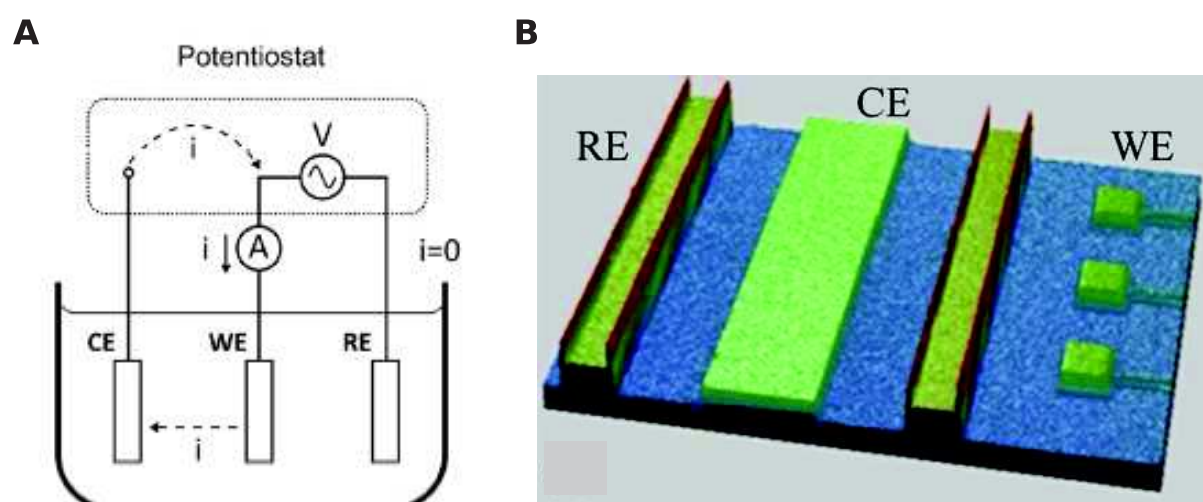


Figure 2.5.: A. Schematic diagram of a three-electrode cell consisting of a working electrode (WE), a counter electrode (CE) and a reference electrode (RE). The potential of the WE with respect to the RE is controlled by adjusting the current between WE and CE. Figure from [Car14]. B. Example of an integrated sensor chip with integrated WE, RE and CE. Figure from [BLZ<sup>+</sup>17].

Specifically, the potentiometric detection method allows to cover large concentration ranges of analyte (due to the logarithmic concentration - potential dependence whereas the amperometric method has a linear relationship, which reduces the accessible concentration range but improves the resolution. Impedimetric transducers can provide sensitivities comparable to optical methods [BT04].

Advantages of electrochemical transducers are their short response time, the ease of operation, low costs, long term stability, low power requirements, the capability for miniaturized designs [CPN<sup>+</sup>14, dVB14], requiring only small operating volumes [VCK12]. Electrochemical transduction is unaffected by the turbidity or visible absorption of samples [DH12b]. Electrochemical electrodes can be fabricated easily, for example by screen printing [BSGO09, PM08], so that a mass production is possible. Indeed, amperometric biosensors for glucose monitoring hold a large share of the biosensor market and were besides the first commercialized biosensors [HFE<sup>+</sup>16].

Nanomaterials as electrode material have drastically reduced the achievable detection limits of electrochemical biosensors [HFE<sup>+</sup>16].

### 2.3.2. Piezoelectric transduction

Piezoelectric transducers measure the changes in the mass of a thin film when a binding reaction takes place on the surface of a piezoelectric crystal or a quartz crystal microbalance. An electric field applied to the piezoelectric quartz creates an acoustic wave within the crystal whose frequency changes upon increase of its mass. Piezoelectric biosensors are label-free and can thus measure kinetics of a reaction in real-time [Tom12]. They are independent of the optical properties of the media, can also detect changes in the viscosity and viscoelasticity at the biointerface and can be combined with other transduction techniques [PKE12]. Further advantages are the simplicity and their low cost. However, piezoelectric transducers are intrinsically non-specific and react to any mass that binds to the surface.

### 2.3.3. Optical transduction

In optical biosensors, the information is carried by photons instead of electrons, eliminating accordingly sources of error due to electrical measurements [CSR<sup>+</sup>12]. Many different ways for the read-out are possible, as the binding event can generate a change in absorbance, reflectance, scattering, fluorescence, polarization or refractive index of the sample [MMP12]. The detected effects can be generated by the analyte itself, by the matrix of the sensor, or by a marker like fluorescence labels [BT04]. Labeled methods achieve often higher sensitivity, whereas label free methods are easier to prepare, require less modification of the system and are appropriate for real-time monitoring. While classical techniques such as absorbance or fluorescence are rather volume sensitive, techniques based on evanescent waves like SPPs are more surface sensitive [BT04]. Optical sensors probe samples in a nondestructive manner. This can be of interest for medical analysis. With regard to the number of optical methods, we will limit a detailed description on the surface plasmon resonance (SPR) sensing which exploits the change of the refractive index and the surface enhanced spectroscopy techniques, in sections 2.4 and 2.5.

### 2.3.4. Comparison of the transduction methods

Table 2.1 concludes this overview of different transduction methods by indicating the advantages and inconvenients of the transduction approaches addressed above. As the methods have quite some differences, a consistent comparison is not straightforward, especially in terms of the limits of detection or sensitivity because they tend to be evaluated by different approaches. Based on recent reviews [PZT<sup>+</sup>13, HFE<sup>+</sup>16, DVK16, Poh17], an overview of the properties is shown and a non-exhaustive list of references where particularly high sensitivity or a very low limit of detection (LOD) was reached are given. A lookahead of the plasmon based sensing approaches is already contained in the table, but they will be discussed in more detail below. The major advantage of SEIRA compared to the other methods is its intrinsic specificity applicable for the identification of molecules.

Transduction method	Label-free	Low-cost	Miniaturization	Simplicity	Specificity	References Sensitivity / LOD
Electrochemical	Yes	Yes	+++	Yes	relies on electrode functionalization	Protein detection of fM concentration and aM concentration in sandwich assays [BKS <sup>+</sup> 13]
Piezoelectric	Yes	Yes	+++	Yes	intrinsically non-specific	Detection of human matrix metalloproteinase 9 with a QCM aptasensor, concentration 100 pg/ml (1.2 pM) in buffer [SDC <sup>+</sup> 15]
Fluorescence spectroscopy	No	No	++	No (labeling necessary)	detection of the label	Detection of 17 $\beta$ -estradiol using fluorescently labeled aptamers with an evanescent wave optical fiber sensor, LOD 2.1 nm (0.6 ng/ml) [YLG <sup>+</sup> 12]
SPR	Yes	No	+ (prism coupling)	No	relies on surface functionalization	Detection of concentrations down to 1 pM with commercialized Biacore S200 system [Bia]
LSPR	Yes	Yes	+++	Yes	relies on surface functionalization	Detection of single binding events of short nucleic acid strands (< 1 kDa) [BFV14]
SEIRA	Yes	No	+	No	<b>intrinsically specific</b>	Detection of 25 zeptomole of ODT molecules [NHW <sup>+</sup> 17]

Table 2.1.: Comparison of different transduction methods.

## 2.4. Surface plasmon resonance (SPR) and localised surface plasmon resonance (LSPR) sensors

### 2.4.1. Principle of SPR and LSPR sensors

As discussed in chapter 1, the plasmon resonance frequency of propagating SPPs and LSPs depends on the refractive index of the surrounding medium. (L)SPR sensors exploit this dependency. Due to a biochemical binding event or simply due to the presence of a material on the surface of a plasmonic structure, the refractive index is modified and the plasmon resonance frequency shifts. The evanescent field of the plasmon resonance is especially sensitive to the immediate vicinity of the plasmonic resonator.

In an SPR sensor, a light wave excites a propagating SPP, usually by one of the coupling schemes described in section 1.2.3, that is, by prisms, gratings, or wave guiding. The change in refractive index due to the presence of a substance or a binding reaction will alter the coupling condition between the light wave and the SPP. The measured signal can be a change of the coupling angle, the resonance wavelength, the intensity, the polarization state or the phase shift of the wave that has excited the SPP [HP06]. The first three, illustrated in Figure 2.6, are the most frequently used approaches [PH06]. Depending on the read-out, the instrumentation is different. For example, to measure the coupling angle, monochromatic light is sufficient, but the incident angle needs to be variable. For a measurement of the wavelength shift, a collimated broadband light source and a spectrometer are needed whereas the incidence angle is kept fixed. A variant of SPR sensing, namely SPR imaging (SPRi), offers moreover a spatial information. Using a constant angle and wavelength, a map of the reflectance intensity as a function of the position on the surface is acquired [WV07].

Following the definition by Homola and Piliarik [HP06], SPR sensors can either be direct, which means that the measurand, typically the refractive index, affects directly the output signal. Indirect sensors intend to measure for example the concentration of an analyte, that generates a change in the refractive index as an intermediate quantity, which is then read out by the transducer. Biosensors are typical examples of indirect sensors.

Advantages of SPR (bio)sensors are their sensitivity, the linearity between input and output signal, the resolution (the smallest change in measurand that can be detected), the good reproducibility, the dynamic range, and the low limit of detection [HP06].

Biosensing with LSP has been proposed for its advantages over the standard SPR configuration based on propagating SPP on flat surfaces [AHL<sup>+</sup>08]. LSP can be directly excited without need for momentum matching with the incident light wave. Ideally, only a simple, small, light, robust and low cost equipment for reflection or transmission spectroscopy is needed to perform LSPR sensing [HV02]. The sensing volume is smaller for LSP than for SPP where the decay length of



## 2.4. Surface plasmon resonance (SPR) and localised surface plasmon resonance (LSPR) sensors

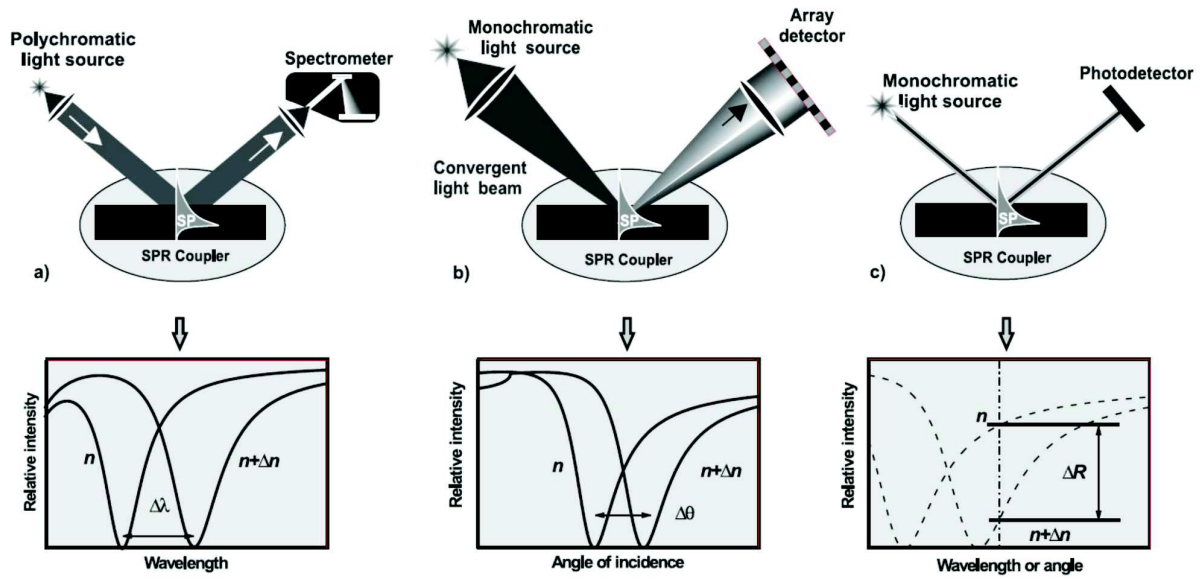


Figure 2.6.: Instrumentation and read-out for different SPR sensing approaches based on the modulation of a) the coupling wavelength, b) the coupling angle, c) the light intensity. Figure from [PH06].

the electromagnetic field is in the range of hundreds of nanometers for SPR sensing at visible wavelengths [WV07].

Benchmarks of (L)SPR sensors are the limit of detection, that is, the smallest quantity of analyte that produces a measurable change, and that can be detected with reasonable certainty, and the sensitivity.

Sensitivity is generally defined as the ratio of the change in the sensor output to the change in the measurand [HP06]:

$$S = \frac{\partial Y}{\partial X}, \quad (2.1)$$

where  $X$  is the measurand (for example the refractive index or the analyte concentration) and  $Y$  the respective quantity used as read-out (plasmon wavelength, coupling angle, intensity).

For indirect sensors aiming at measuring concentrations the sensitivity to a concentration is defined accordingly to the general expression

$$S_c = \frac{\partial Y}{\partial c}. \quad (2.2)$$

The refractometric sensitivity is

$$S_{\text{RI}} = \frac{\partial Y}{\partial n} = \frac{\delta Y}{\delta n_{\text{eff}}} \frac{\delta n_{\text{eff}}}{\delta n_b}, \quad (2.3)$$

where  $n_{\text{eff}}$  is the effective refractive index probed by the SPP and  $n_b$  the refractive index induced by the analyte molecules binding to the biorecognition element.



## 2. Generalities of Biosensors and Plasmonic Biosensors

In the second step, the general expression has been separated into an instrumental contribution  $\frac{\delta Y}{\delta n_{\text{eff}}}$ , which depends on the method of excitation of the SPP, and the sensitivity of the effective refractive index experienced by the SPP to the refractive index induced by the binding of the analyte molecules  $\frac{\delta n_{\text{eff}}}{\delta n_{\text{b}}}$ .

(L)SPR sensors typically need to be calibrated to know their response to a refractive index modification. Over narrow ranges of bulk refractive index change  $\Delta n$ , the sensor response is often linear or can be approximated as linear [JCC<sup>+</sup>98, MH11]. Mayer and Hafner deduce this analytically from the resonance condition's dependence on the refractive index of the surrounding medium for geometrically simple systems like a small sphere [MH11].

For wavelength based readout, which is the most frequently used especially in the case of LSPR sensors, we can hence write

$$\Delta\lambda = S_{\text{RI}}\Delta n = S_{\text{RI}}(n_{\text{final}} - n_{\text{initial}}), \quad (2.4)$$

where the refractive index sensitivity  $S_{\text{RI}}$  is the local slope, or in case of linearity the global slope.

For adlayers of uniform thickness, there is an effective refractive index  $n_{\text{eff}}$  instead of the bulk refractive index  $n_{\text{final}}$ .  $n_{\text{eff}}$  should be the properly weighted average of the individual refractive indices of the adlayer material and the initial medium. Using a weighting factor proportional to the intensity of the light, for an exponentially decaying field, this results in [JCC<sup>+</sup>98]

$$n_{\text{eff}} = n_{\text{initial}} + (n_{\text{a}} - n_{\text{initial}}) \left(1 - \exp\left(\frac{-2d}{l_d}\right)\right), \quad (2.5)$$

where  $n_{\text{a}}$  is the refractive index of the adlayer material,  $d$  is the layer thickness and  $l_d$  is the characteristic decay length of the electromagnetic field.

Inserting this expression for the effective refractive index yields [JCC<sup>+</sup>98, WV07]

$$\Delta\lambda = S_{\text{RI}}(n_{\text{eff}} - n_{\text{initial}}) = S_{\text{RI}}(n_{\text{a}} - n_{\text{initial}}) \left(1 - \exp\left(\frac{-2d}{l_d}\right)\right). \quad (2.6)$$

This relationship allows for example to determine the thickness of an adlayer when the sensitivity is already calibrated [JCC<sup>+</sup>98].

Another quantity derived from the sensitivity, and important for an evaluation of the sensing capabilities is the figure of merit defined as [MH11]

$$\text{FOM} = \frac{S}{\text{FWHM}}, \quad (2.7)$$

taking into account the resonance's full width at half maximum (FWHM). For SPR readout, it is beneficial if the resonances are narrow because shifts are more clearly detectable when the resonance maximum is sharply defined.

## 2.4. Surface plasmon resonance (SPR) and localised surface plasmon resonance (LSPR) sensors

Further details on SPR sensing can be found in the reviews and books by Homola [Hom06b, Hom08], and for LSPR sensing in the reviews by Willets and Van Duyne [WV07], or Mayer and Hafner [MH11].

### 2.4.2. State of the art

SPR sensing is a detection technique that has already made its way to commercialization. The Swedish company Biacore (now Protein research GE Healthcare Life Sciences) commercialized integrated table top systems for SPR sensing. The SPR substrates are thin smooth gold films deposited on glass slides. Propagating SPPs are excited in a Kretschmann-Raether configuration. These commercialized systems are used as standard analysis tools for example in drug development [KCB<sup>+</sup>16, CKF<sup>+</sup>17]. Their most sensitive device, Biacore S200, is adapted for sample concentrations down to 1 pM [Bia]. In a review dating back from 2008, Homola indicates several examples where concentrations below 1-100 pg/ml of pesticides could be detected, below 1 ng/ml of staphylococcal enterotoxins, below 1-10 ng/ml of antibiotics, and below 1-100 ng/ml of cancer markers and antibodies [Hom08], using commercial systems such as Biacore devices or others, or custom-built sensors. Lowest concentrations were typically detected using an inhibition array format. In terms of resolution of the devices, SPR sensors based on prism coupling reach values in the range of  $10^{-7}$  to  $10^{-8}$  RIU whereas sensors based on grating coupling have a slightly lower performance, reaching resolutions of  $10^{-6}$  to  $10^{-7}$  RIU [Hom08], and references therein.

The inconvenient of sensors based on prism coupling is their bulkiness. This sets some limits to miniaturization. At research level, other geometries have been proposed. Objectives are a better suitability for on-chip integration [Bro12], improved sensitivities and the potential to be used for SPR imaging for multiplexing at different sensing sites [Bro12].

In research articles which focus on sensor design without application to real samples of a specific substance, it is more common to evaluate the sensitivity, eventually the figure of merit, and rather seldom the measured concentration or the resolution of refractive index, as it is done in more biologically relevant work. Making a good comparison of different devices is therefore often not straightforward.

A plasmonic interferometer structure made of circular grooves concentric with a central aperture was proposed by Gao *et al.* [GXZ<sup>+</sup>13]. Propagating SPPs are launched at each groove and interfere at the central focusing point. The periodicity of the grooves has to be chosen in accordance with the working wavelength. The readout is done using a simple inexpensive transmission spectroscopic setup. Tracking the wavelength shift of the central interometric peak, the sensitivity is evaluated to 470 nm/RIU and the resolution is  $1.55 \cdot 10^{-6}$  RIU. The structure has a small footprint, so that an integration of multiple structures on one chip is possible. Using an intensity based readout is possible and allows for multiplexing. A similar structure but with a linear instead of circular geometry of the grooves was subsequently proposed, yielding nearly the same sensitivity of 490 nm/RIU for a working wavelength of 660 nm and 470 nm/RIU at 650 nm,

## 2. Generalities of Biosensors and Plasmonic Biosensors

with figures of merit of 35 and 67, respectively, due to the narrow linewidths of approximately 10 nm.

Vincenti *et al.* investigated a structure made of square gold patches supporting plasmonic resonances and Fabry-Perot like resonances with electric field localization in the slits between the patches [Sto12]. The interaction of these resonant modes gives rise to a plasmonic band gap. Based on the shift of the plasmonic band edge, the sensitivity is evaluated to 650 nm/RIU. Due to the very sharp feature, the theoretical figure of merit,  $FOM = 150 \text{ RIU}^{-1}$ , is very high. In experiment, it reduces to  $32 \text{ RIU}^{-1}$  due to the incidence angle range which broadens the resonance, which is nevertheless considerably good.

Bog *et al.* developed an analytical method to optimize the coupling efficiency to SPPs in one-dimensional periodic gratings and applied this to a sinusoidal grating [BHM<sup>+</sup>12]. Experimentally they determined a sensitivity of 630 nm/RIU, with this rather conventional SPR sensing approach based on grating coupling.

Around the years 2009 - 2010, SPR sensors for the IR spectral range have been proposed [Che09, VDLG10]. It is of interest to exploit the strong refractive index variation associated to molecular absorption lines in this spectral range to obtain stronger SPR shifts. Cleary *et al.* suggested different materials as a host for the SPPs, such as doped Si, CuSnS, graphite, antimony and bismuth [VDLG10]. Chen investigated in a numerical study the performance of a silicon based sensor made of an undoped grating implanted in a doped Si-substrate, and evaluated the instrumental contribution to the sensitivity ranging from 900 - 17200 nm/RIU depending on geometrical parameters and the Si doping level [Che09]. DiPippo *et al.* also promote mid-IR SPR sensing and judge the higher penetration depth of the evanescent field of the SPP in this spectral range as an advantage to probe larger biological samples [DLP10]. Their design proposition consists of a periodic highly doped Si grating embedded into an undoped Si wafer, similar to the device proposed by Chen, to allow coupling to the SPPs yet having a smooth surface for controlled binding of the analyte. Based on the simulated values, the sensitivity was evaluated to 3020 nm/RIU for a 100 nm thick analyte layer. An experimental demonstration of the proposed lateral embedded doping profile was achieved by Wasserman's group in 2013 [RSL<sup>+</sup>14]. Kuznetsov *et al.* fabricated a mid-IR sensor made of a Ga-doped ZnO grating which allows free space coupling to propagating SPP [KSJ<sup>+</sup>16]. An experimentally determined sensitivity of 4900 nm/RIU and a FOM of 12 were reported.

LSPR sensing has the advantage to be inherently free of elaborate coupling schemes and does not require any particular geometry for the excitation of resonances, but can be operated using simple experimental setups. Moreover, while SPR sensing based on propagating SPPs is more volume sensitive due to the decay length into the dielectric of roughly  $\lambda/2$ , LSPR sensing is more surface sensitive, because the decay length of the electric field around nanoparticles is rather in the range of tens of nanometers in the visible spectral range [Bro12]. While the bulk sensitivity of LSPR sensors is typically smaller, they respond better to changes in their immediate vicinity [Bro12].

## 2.4. Surface plasmon resonance (SPR) and localised surface plasmon resonance (LSPR) sensors

LSPR sensors exist also as commercialized systems, for example the LSPR chips marketed by LambdaGen which consist of nanostructures, metallic thin films [Lam]. Femtomolar sensitivities are achieved with this system.

In research, LSPR sensing has been reported with a variety of nanoparticles and nanostructured substrates [AHL<sup>+</sup>08]. A particle-based approach was adopted by Kazuma *et al.* [KT14]. Polydisperse Ag nanoparticles with a large extinction band were prepared. By removal of one specific size using photochemical methods, that is, the oxidation of the particles due to electron transfer to the TiO<sub>2</sub> substrate, an extinction dip is created. This dip should ideally lie at the highest possible wavelength within the transparency window where the best sensitivities can be reached. A sensitivity to refractive index variations of 360 nm/RIU was reported. The system was furthermore validated in real-time measurements of SA binding. Single gold nanoparticles were recently applied to monitor dynamics of biomolecular systems with high temporal and spatial resolution. Namely, the attachment of so-called Min proteins from a lipid membrane on a gold nanorod was monitored by Lambertz *et al.* [LMH<sup>+</sup>16].

Baaske *et al.* demonstrated the detection of single binding events of nucleic acid strands using a plasmon enhanced whispering gallery mode (WGM) microcavity [BFV14]. A gold nanorod is loaded onto the WGM cavity to locally enhance the electric field. The nucleic acid strands are contained in a nmolar solution but the measured signal originates from a single binding event.

Many further examples of particle based LSPR sensing can be found in the review by Mayer and Hafner [MH11]. The bulk sensitivity of LSPR is indicated therein to be in the range of 10<sup>2</sup> nm/RIU.

The following approaches are based on nanostructured substrates supporting LSPR. An early biological relevant demonstration of LSPR sensing was presented by Haes *et al.* [HCKVD05]. The presence of an illness marker of Alzheimer's disease in human brain extract and cerebrospinal fluid was detected using LSPR sensing with a sandwich assay format. The LSPR shift over the concentration range from 1 fM to 10 μM of the illness marker was measured.

Making the resonance narrow for ideal read-out, described by a high FOM, is of interest to improve sensing. Fano resonances, arising in plasmonic structures due to the coupling of a bright to a dark mode, can be applied to achieve this. Cetin and Altug proposed asymmetric ring-disk structures and reached a sensitivity of 650 nm/RIU and a comparatively high FOM of 72 [CA12]. A sensitivity in similar magnitude, 520 nm/RIU, was reached by Zhao *et al.* yet with a drastically lower FOM of 2.9, using hole-mask colloidal nanolithography as low cost and large area technique [ZZBG12]. Mesch *et al.* proposed a sensor read-out at the third harmonic frequency instead of at the fundamental LSPR frequency to improve the measured signal strength [MMHG16]. The plasmonic spectrum at the third harmonic frequency is narrower than at the fundamental one, which is advantageous to have a strong variation in an intensity based readout at a fixed frequency. The sensor signal was hence found to be stronger when exploiting the third harmonic generated in a gold nanoantenna array. The limit of detection for the variation of the refractive index  $n$  is 10<sup>-3</sup> RIU. Butet *et al.* investigated in a numerical

## 2. Generalities of Biosensors and Plasmonic Biosensors

study the second harmonic (SH) signal from a gold nanodolmen structure supporting Fano resonances [BM14]. The symmetry of the scattered electromagnetic wave at the SH changes with a refractive index modification. For an array of  $10 \times 10$  structures, the authors report a resolution of  $10^{-5}$  RIU.

Combining (L)SPR and surface enhanced spectroscopy, such as SERS or SEIRA (see below), has been proposed to provide an additional means of molecular identification [AHL<sup>+</sup>08] and demonstrated in several works [PKA<sup>+</sup>11, SSZ<sup>+</sup>16]. Both effects are based on plasmonic resonances and hence occur jointly and can be observed under appropriate conditions. Pryce *et al.* reported sensitivity values ranging from 1190 to 3370 nm/RIU using a gold split-ring resonator metamaterial, with different size unit cell elements, as LSPR sensing substrate and demonstrated furthermore the enhancement of vibrational features by post fabrication tuning of the resonances to be in resonance with the molecular vibration. Being capable of predicting the LSPR shift for a plasmonic system exposed to a small perturbation such as a molecular layer is of interest to determine the sensitivity and performance of the plasmonic structure as sensor. Yang *et al.* derived an analytical formula that expresses the change of the complex eigenfrequency of LSPRs due to a small perturbation [YGL15]. Their formalism necessitates a Maxwell quasi normal mode solver for practical calculations. Weiss *et al.* applied perturbation theoretical methods to calculate the refractive index sensitivity of dipolar and quadupolar modes in periodic nanostructure arrays [WMS<sup>+</sup>16].

Acimovic *et al.* developed an integrated LSPR lab-on-a-chip system with advanced microfluidics for 32 parallel sensing sites in 8 microfluidic channels [AOS<sup>+</sup>14]. LSPRs are excited in a gold nanorod array. The system was applied to detect clinically relevant biomolecules such as cancer markers in a 50% human serum sample. The smallest measurable concentration of human alpha-feto-protein (AFP), which is a protein with a mass of 70 kDa, is 500 pg/ml corresponding to picomolar concentration levels. This is as good as the limit of detection of the commercial Biacore system based on propagating SPPs, as discussed above. Particularly high sensitivity and FOM were reported by Sreekanth *et al.* [SAE<sup>+</sup>16]. Using a hyperbolic metamaterial made of stacked gold and Al<sub>2</sub>O<sub>3</sub> layers, which supports bulk plasmon-polariton modes coupled in via a 2D grating as top layer of the stack, a sensitivity of 30000 nm/RIU was reached for NIR wavelengths and around 13300 for modes at visible wavelengths. The corresponding FOMs for various visible and NIR wavelengths range from 108 to 590. The sensor proved to be applicable also for low weight molecules at picomolar concentration levels.

### 2.5. Surface enhanced spectroscopy techniques

The study of the vibrational energy levels is an efficient technique to detect and identify molecules. Vibrational spectroscopy measures the characteristic Raman or IR absorption lines of the molecules present in a sample. Complementary information can be obtained from the inelastic Raman scattering and the direct absorption of IR radiation, as these techniques obey different

## 2.5. Surface enhanced spectroscopy techniques

selection rules. While both techniques are important analytical tools and provide exceptional selectivity, they suffer from a major drawback. Indeed, the interaction cross section with the incident radiation is very low. For IR absorption, the reason for the weak interaction cross section is the large mismatch between the typical dimensions of the incident, micrometric radiation and the nanometric molecules. Raman scattering has a low probability compared to elastic (Rayleigh) scattering. To give an idea of the efficiencies of both processes, the weak IR absorption cross section is still 9 orders of magnitude higher than the Raman cross section [Aro06].

Surface enhanced vibrational spectroscopy techniques introduce plasmonic structures as additional component besides the molecules and the electromagnetic radiation. The excitation of SPPs allows to confine the incident electric field into a small volume around the plasmonic nanostructure and consequently to enhance the electric field. Molecules placed in these hotspots interact more efficiently with the electromagnetic radiation, mediated by the plasmonic resonance, as described later in more detail in the case of surface enhanced infrared absorption (SEIRA).

The surface enhancement effect of the Raman intensity has first been discovered on rough gold films in 1974 [FHM74]. Surface enhanced Raman spectroscopy (SERS) has since then become a hot topic. SEIRA was first described a few years later, in 1980 [HKT80]. The SEIRA effect was also ascribed to IR surface phonon-polaritons [Aro06], as the plasmonic resonances of not particularly structured rough metallic films lie in the visible, or to the tail of the plasmonic resonance which reaches out into the IR [Osa01]. Nowadays it is possible to fabricate structures sustaining sharp plasmonic resonances in the IR spectral range. SEIRA has achieved less attention compared to SERS, as the signal enhancement is not as spectacular as for SERS, but this is mainly due to the extremely weak Raman cross section and to the nonlinearity of the Raman scattering. The scale on which molecules are probed is different for SERS and SEIRA, the SERS signal being proportional to  $|E|^4$  yielding a nanometric probe extension, against an  $|E|^2$  dependency in SEIRA, probing molecules rather at the scale of a few tens of nanometers. Nevertheless, SEIRA is of great practical interest and an enhancement which might seem small compared to SERS, might be sufficient to detect minute amounts of molecules. In the following section, SEIRA spectroscopy will be presented.

### 2.5.1. Principles of SEIRA

#### IR spectroscopy and the origin of the vibrational spectra

Molecular vibrations can be excited when molecules absorb IR radiation. Indeed, the typical energies of IR radiation corresponds to the energy of molecular vibrations, determined by the mass of the atoms constituting the molecule and the spring constant representative of their chemical bond, as schematically shown in Figure 2.7A. IR spectroscopists divide the IR spectral range into the functional group (4000 - 1500  $\text{cm}^{-1}$ ) and the fingerprint spectral range (1500 - 500  $\text{cm}^{-1}$ ) [Dur02, HYR<sup>+</sup>13]. While the former indicates which functional groups are present in the molecule, the latter allows to specifically identify the molecule. Figure 2.7B shows an



## 2. Generalities of Biosensors and Plasmonic Biosensors

overview of the energy ranges where the vibrations of several chemical bonds of organic molecules can typically be found.

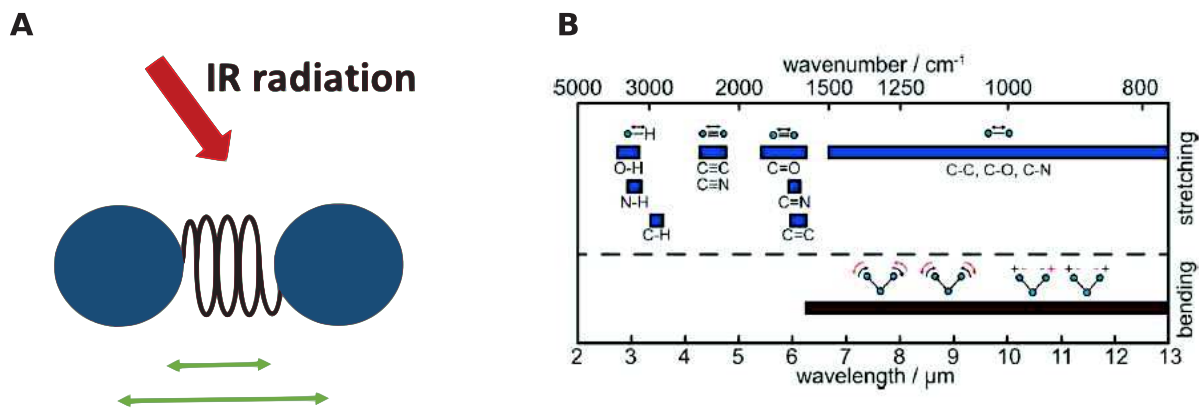


Figure 2.7.: A. Illustration of IR absorption and excitation of a molecular vibration. B. Overview of characteristic IR vibrations of molecules. Figure from [HYR<sup>+</sup>13].

The total energy of molecules can be partitioned into contributions from the electronic, vibrational, rotational and translational motion [Aro06]:

$$E_{\text{molecular}} = E_{\text{electronic}} + E_{\text{vibr}} + E_{\text{rot}} + E_{\text{transl}}.$$

These energies are quantized. Using the adiabatic approximation, that is, the separation of electronic and nuclear motion, and considering an isolated molecule (no external potential) which is furthermore fixed in space ( $E_{\text{transl}} = 0$ ), allows to treat the wave functions of electrons and nuclei separately, and to obtain Schrödinger equations for the electronic and the nucleic energy eigen values. A second separation of wave functions yields Schrödinger equations for the vibrational and the rotational energy eigenvalues. Calculated vibrational spectra of molecules can be obtained solving these equations for example by *ab initio* or density functional theory methods, which are common methods of quantum chemistry.

Not all possible vibration modes can be observed in a measured spectrum. It depends on the symmetry of the molecule if modes are allowed or forbidden. When the molecule vibrates, the dipole moment  $\mathbf{p}$ , which is initially defined by the charge distribution at equilibrium, will change. Each of the three components of the dipole moment vector  $\mathbf{p}$  can be expanded in a series

$$p_i = p_{0i} + \left( \frac{\partial p_i}{\partial q} \right)_0 + \dots, \quad (2.8)$$

where  $q$  is the normal coordinate, and neglecting all higher order terms. The coupling of the electric dipole to an external electric field is given by the operator

$$\mathcal{H} = -\mathbf{p} \cdot \mathbf{E}. \quad (2.9)$$

The probability of absorption is proportional to the square of the transition dipole moment matrix element  $|\langle \psi_{\nu'} | \mathbf{p} \cdot \mathbf{E} | \psi_{\nu} \rangle|$ .

If the vector of the dipole moment is not orthogonal to the electric field and if one of the three first derivatives  $\frac{\partial p_i}{\partial q_0}$ ,  $i = 1, 2, 3$  is nonzero, the matrix element is also different from zero and the molecular vibration is observable in IR spectra. For Raman active modes, the polarizability tensor is the decisive parameter instead of the dipole moment. For this reason, Raman scattering and IR absorption obey different selection rules so that some modes are Raman active but not IR active and vice versa. Hence, Raman and IR spectroscopy and equally their surface enhanced versions are complementary.

### Electromagnetic and chemical effect in SEIRA

Rough metallic surfaces or engineered plasmonic nanoantenna substrates enhance the interaction of IR light and the molecules, that is, they increase the absorption cross section of the molecules in their vicinity, when the molecules are placed in the zones where the electric field is enhanced due to the plasmonic resonances. This can be deduced from the coupling operator (equation 2.9), where the local electric field enters linearly. The infrared absorption is then proportional to the electric field intensity  $|E|^2$  [Osa01]. The field enhancement in engineered antennas is the strongest spectrally close to the plasmonic resonance. It can furthermore be reinforced by the lightning rod effect, the geometrical electric field enhancement at highly curved features of the nanoantennas or the grains in a rough metallic film [ZSM05]. For rough metallic films, there is a broader resonance, typically in the visible spectral range, but with a tail extending into the IR region [Osa01]. The enhancement of signals is found to be strongest for molecules placed within a distance of 5 nm from the surface [Osa01]. Besides this electromagnetic effect, there are also chemical effects for analytes chemisorbed on the SEIRA substrate. The role of chemical effects is not as well understood as the electromagnetic effects. It is assumed that, contrariwise to physisorbed molecules, the electronic structure of a molecule changes when it is chemically bound [MP17], modifying the dipole moment of the molecule.

### Resonant SEIRA

The principle of resonant SEIRA is to use well defined plasmonic resonances that are spectrally tuned to the molecular vibrations. This exploits the fact that the electric near field enhancement is strongest close to the plasmonic resonance wavelength, typically measured as far field quantity. This approach necessitates tailored nanoantennas that sustain a plasmonic resonance at a targeted wavelength. Moreover, the SPR shift induced by the attachment of the analyte needs to be anticipated. Resonant SEIRA was introduced in 2008 by Neubrech *et al.* [NPC<sup>+</sup>08]. In an initial demonstration, gold nanorod antenna prepared by electrochemical deposition were used for the detection of octadecanethiol (ODT). Spectroscopic investigation of single nanorods was performed using synchrotron radiation. The tuning and detuning for different antenna lengths was investigated. The best tuning ratio between the nanoantenna resonance and the molecular



## 2. Generalities of Biosensors and Plasmonic Biosensors

vibrations allowed to detect 50 attogram of molecules located in the hotspots of the nanoantennas, corresponding to approximately 105000 molecules (less than 1 attomol).

### SEIRA enhancement factor

For the quantification of a SEIRA substrate, it is possible to indicate the number or the mass of molecules contributing to a signal. For nanoantenna arrays, the number is often given per antenna where indeed many antennas and molecules contribute to the actual signal, hence improving the signal-to-noise ratio. Another quantity to evaluate the performance of a SEIRA substrate is the enhancement factor defined as [NHW<sup>+</sup>17]

$$\text{EF} = \frac{I_{\text{SEIRA}}}{I_0} \frac{A_0}{A_{\text{SEIRA}}}, \quad (2.10)$$

where  $I_{\text{SEIRA}}$  is the enhanced vibrational signal strength,  $I_0$  the strength of the unenhanced signal,  $A_0$  is the area (volume) covered (filled) with molecules and  $A_{\text{SEIRA}}$  the active surface (volume) where high field enhancement is achieved.

This definition is related to the number of molecules contributing to the signal. It is assumed that the enhanced signal originates mainly from molecules located in the hotspots of the nanoantennas, neglecting all other molecules whose contribution is weak. For the reference measurement, one assumes that all molecules contribute to the measured signal. Using the condition of equally distributed molecules, this can be expressed as done above by considering the areas (volumes) containing the molecules.

But already the ratio of the enhanced to the unenhanced signal gives valuable information on the performance of a sensor.

The definition of the enhancement factor and consequently the values given in publications need to be critically investigated. Indeed, there is no clear and universal definition of the hotspot and its area. Often it is extracted from numerically calculated electric field profiles but then it still depends on assumptions above which value the field can be considered as strongly enhanced. Mayerhöfer *et al.* [MP17] argue moreover that the definition of the enhancement factor is more pertinent in the case of antennas covered with chemically bound monolayers than for continuous films covering the whole surface of a nanoantenna substrate. Furthermore, the reference experiment to extract  $I_0$  has to be chosen carefully.

### Interaction between plasmonic and molecular excitations, Fano-like line shape

The line shapes of the vibrational features found in resonant SEIRA differ from the typical Lorentzian bands of unenhanced transmission or absorption spectra. The phase dependent electromagnetic interaction between the large plasmonic resonance and the narrow vibrational feature yields asymmetric line shapes. These can be explained using a Fano type interaction [Fan61]. The line shape stems from the constructive and destructive interferences of a continuum (the broad plasmonic resonance) and a discrete resonance (the narrow molecular absorption) which are two available excitation path ways. The asymmetric intensity profile can be modeled by the

expression

$$I \propto \frac{q\gamma + \omega - \omega_0}{(\omega - \omega_0)^2 + \gamma^2}, \quad (2.11)$$

where  $\omega_0$  is the resonance frequency,  $\gamma$  is the damping rate and  $q$  is the Fano-parameter accounting for the asymmetry.

Alternatively, to use a more intuitive model for the interaction and the resulting line shapes, a coupled harmonic oscillator model can be applied [AAA15, NHW<sup>+</sup>17]. As the plasmonic resonance interacts strongly with the incident light, it is described as bright mode. The molecular absorption interacts so weakly with the incident light that it can be described as dark mode. It is driven by the coupling to the plasmonic resonance. The signal that is measured of this coupled system is hence the imprint of the absorption line on the plasmonic resonance, so that different line shapes may arise. Figure 2.8 visualizes the coupled harmonic oscillator system and the different coupling and damping rates. In the schematic, blue symbols (mass, spring) belong to the bright mode A and red symbols to the dark mode P.  $k_A$  and  $k_P$  denote the spring constants,  $\mu$  the coupling constant in the coupled masses on springs model,  $\gamma_A$  and  $\gamma_P$  the damping rates. The external driving force  $\mathbf{F} = -g\mathbf{E}_{\text{inc}}$  acts on mass  $m_A$ .

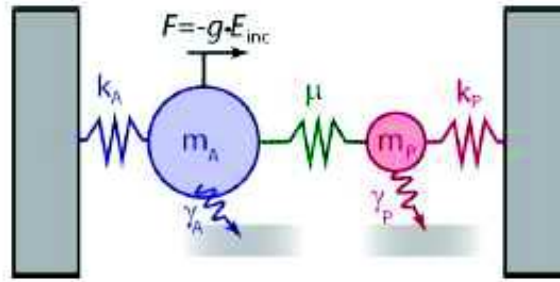


Figure 2.8.: The system of the plasmonic resonance and the molecular absorption seen as coupled harmonic oscillators. The blue big mass (bright mode A) on a spring symbolizes the plasmonic resonance, which is driven by the external force  $F$ . The red small mass (dark mode P) stands for the molecular absorption which does not interact directly with the external field but is driven by the coupling to the plasmonic resonance, with coupling constant  $\mu$ . Damping is also indicated by the rates  $\gamma_A$  and  $\gamma_P$ . Figure from [AAEA13].

Furthermore, the resulting line shape when the plasmonic resonance couples to the molecular absorption is also determined by intrinsic properties of the plasmonic resonator itself and depends on the ratio of the external (radiative) damping and the intrinsic material absorption of the plasmonic resonator. The formalism of the temporal coupled mode theory (TCMT) can account for the resulting line shape [AAEA13], where actually the molecular absorption band is observed as a modulation on top of the plasmonic spectrum. For a plasmonic resonance spectrally aligned with the absorption feature, the line shape can vary from a dip, like an electromagnetically induced transmission (EIT), to an additional peak on top of the plasmonic resonance, an electromagnetically induced absorption (EIA), as shown in Figure 2.9B. Analyzing first the

## 2. Generalities of Biosensors and Plasmonic Biosensors

plasmonic resonance alone, it is damped intrinsically in non-radiative pathways, described by the rate of intrinsic damping  $\gamma_{A0}$  and radiatively, by sending out radiation into the far field, accounted for by the rate of external damping  $\gamma_{Ae}$ . The temporal dependence of the amplitude  $A$  can be expressed by

$$\frac{dA}{dt} = i\omega_A A + (\gamma_{A0} + \gamma_{Ae})A + \kappa s_+, \quad (2.12)$$

where  $\omega_A$  is the resonance frequency and  $\kappa s_+$  is a driving term of the resonance, with  $s_+$  the amplitude of the incoming wave and  $\kappa$  its coupling rate to the plasmonic resonance (see also Figure 2.9A). The outgoing traveling waves are described by

$$s_- = -s_+ + \kappa A. \quad (2.13)$$

The amplitudes of the mode and of the traveling waves are normalized so that  $|A|^2$  and  $|s_{(+,-)}|^2$  correspond to the energy stored in the mode and in the incoming and outgoing waves respectively.

The rates  $\kappa$  and  $\gamma_{Ae}$  are related due to time-reversal symmetry in the system and energy conservation by

$$\kappa = \sqrt{2\gamma_{Ae}}, \quad (2.14)$$

in the case of a system with a single input / output port for the traveling waves.

The peak absorption for a bright mode at its resonance frequency  $\omega_A$  can be found from these equations [AAEA13]

$$\mathcal{A} = \frac{4\gamma_{Ae}\gamma_{A0}}{\gamma_{Ae} + \gamma_{A0}}. \quad (2.15)$$

The absorption is maximal when radiative and internal damping contribute equally. This corresponds to the critical coupling point in Figure 2.9C. In the next step, the molecule enters into play. A simplified approach is to consider the molecule as a small increase of the internal damping rate  $\gamma_{A0}$ , as the coupling to the molecular vibration adds an additional nonradiative decay pathway with a rate  $\gamma_\mu$ . Due to this shift  $\gamma_{A0} \rightarrow \gamma_{A0} + \gamma_\mu$ , the peak absorption moves a little bit to the left along the coupling curve. In the under-coupled regime, going to the left means decreasing the peak absorption, which accounts for the dip appearing in the spectrum (blue curve in Figure 2.9B). Close to the critical coupling point, the variation of the peak absorption is quite small (green curve in Figure 2.9B). Finally, in the over-coupled regime, increasing the internal damping rate means increasing the peak absorption, thus explaining the additional peak in the red curve in Figure 2.9B. A minimum modulation occurs when moving the absorption from the right shoulder of the peak to its opposite point in the left shoulder, as shown in [AAEA13]. An important result of the TCMT treatment is that the magnitude of the absorption feature is not necessarily a monotonically increasing function, of for example the electric field enhancement provided by the plasmonic resonator, but depends also on the internal properties as the damping rates due to absorption and scattering.

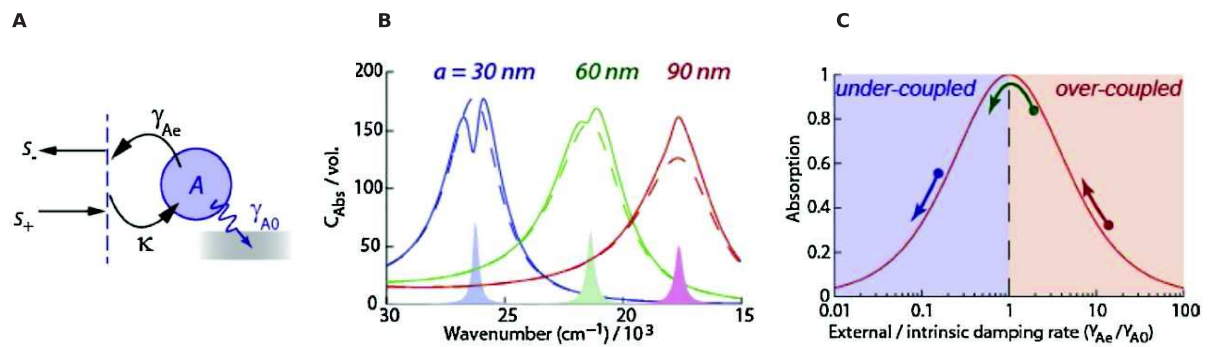


Figure 2.9.: A. Model used in the framework of the temporal coupled mode theory. The oscillator is damped radiatively with rate  $\gamma_{Ae}$  and nonradiatively with rate  $\gamma_{A0}$ . The incoming and outgoing waves have amplitudes  $s_+$  and  $s_-$ .  $\kappa$  is the coupling rate of the incoming wave to the plasmonic resonance. B. Different coupling regimes for plasmonic resonances aligned with an absorption feature. Depending on the resonator size (here prolate spheroid with major half axis  $a$ ), the damping is dominated by absorption or scattering, leading to an undercoupled (blue), a critically coupled (green) and an overcoupled (red) regime. C. Coupling curve indicating the peak absorption at the resonance frequency of the oscillator depending on the ratio of external to internal damping. Adding a molecular layer is equivalent to increasing slightly the internal damping rate, moving left on the curve as indicated by the arrows. The peak absorption can thus decrease (under-coupled regime), vary only little (critically coupled) or increase (over-coupled). Figure from [AAEA13].

### 2.5.2. State of the art

The nanofabrication technologies nowadays available allow to fabricate precisely tailored plasmonic nanoantenna substrates for SEIRA, which constitute the current state of the art. Using plasmonic resonances spectrally tuned to the vibrational lines, instead of non-resonant enhancement on rough metallic films, has been an important milestone in the field of SEIRA. Research aims at finding the best conditions for maximal enhancement of the vibrational features. Different approaches have emerged to further improve SEIRA substrates.

Firstly, the shape of the nanoantenna can be considered. Linear nanoantenna (see Figure 2.10A) have the advantage that the wavelength scaling with their length is well known [Nov09, WAAG<sup>+</sup>11, AAA15], and that they further confine the electric field due to the lightning rod effect [ZSM05], which can be considered as an off-resonance enhancement effect improving the resonant enhancement [MP17]. They have been applied many times in SEIRA experiments [NPC<sup>+</sup>08, AYA<sup>+</sup>09, PNW<sup>+</sup>10, WAAG<sup>+</sup>11, DND<sup>+</sup>12, AAEA13, NBG<sup>+</sup>14], owing to their simplicity and good performance.

Studies on the tuning and detuning of the resonance frequency  $\omega_{\text{resonance}}$  with the molecular absorption feature  $\omega_{\text{vib}}$  have been performed with the linear nanoantenna [NPC<sup>+</sup>08, VHN<sup>+</sup>14]. Vogt *et al.* [VHN<sup>+</sup>14] demonstrated that the best tuning ratio  $\omega_{\text{vib}}/\omega_{\text{resonance}}$  is slightly inferior to 1. This can be explained considering that the far field maxima of the plasmonic resonance, which is typically measured in experiments, is slightly blue-shifted from the near field maximum. This follows from a driven damped harmonic oscillator model for plasmonic resonances [ZN11]. The difference between near field and far field maximum depends on the damping of the system. Because this shift might be insignificant for the relatively large plasmonic resonances, a subset of the authors of [VHN<sup>+</sup>14] however advice, as a rule of thumb, to use a spectral match between the plasmonic resonance and the absorption feature [NHW<sup>+</sup>17].

Another off-resonant technique to further amplify the electric field enhancement often applied in combination with linear or other, differently shaped nanoantennas is the confinement of the field in a nanogap between the antennas [PNW<sup>+</sup>10, NWK<sup>+</sup>12, BZK<sup>+</sup>13, HJCT14, HNV<sup>+</sup>14], see Figure 2.10B. The nanogap serves as hotspot and the signal arising from this zone is highest [DND<sup>+</sup>12]. The fabrication of nanogaps is not a trivial task and needs often a serial fabrication technique like electron beam lithography [WAAG<sup>+</sup>11, BYZ<sup>+</sup>15], which can be combined with photochemical methods [NWK<sup>+</sup>12], or ion beam milling [MWA<sup>+</sup>14]. Hoffmann *et al.* [HJCT14] proposed a technique to fabricate bowtie antenna with nanogaps (Figure 2.10C) on large surfaces by nanosphere lithography combined with a double step metallic evaporation under different tilt angles. To better funnel the light into a gap, linear nanoantenna combined with fans have been proposed [BYZ<sup>+</sup>15], shown in Figure 2.10D. Going towards the goal of single molecule detection, the fan shaped nanogap antennas, furthermore placed onto a reflective substrate (whose benefits will be discussed later) allowed to detect 20-200 zeptomole of ODT (corresponding to approximately 6 to 60 attogram, or 12400-124000 ODT molecules) using a standard micro-FTIR

setup. The electric field intensity enhancement was evaluated to  $10^5$  using electromagnetic simulations.

Other popular nanoantenna shapes besides the already mentioned ones are for example monopole antenna [AYA11] (see Figure 2.10E) and split ring resonators (SRRs, see Figure 2.10F and G) [CZP<sup>+</sup>09, CZN<sup>+</sup>12, CLC16]. Monopole antenna typically consist of the antenna element perpendicular to a ground plate and would hence need three-dimensional fabrication techniques. Adato *et al.* replaced the ground plate by a nanorod as wire reflector [AYA11], the whole structures being oriented flat on the substrate. SRR make use of gaps and have a smaller footprint than linear nanoantenna for similar resonance wavelengths. This allows for higher surface coverage with antennas. Cubukcu *et al.* [CZP<sup>+</sup>09] reported on the detection of approximately 22000 ODT molecules, that is, 40 zeptomoles (approximately 11 attogram), located in the nanogap of their SRR. Asymmetric SRRs (A-SRR) have the advantage of two gaps. The segments of the rings are of different length to create the asymmetry. Different SRR types (A-SRRs, c-shaped, u-shaped, and crescent-shaped SRRs) have been compared by Chae *et al.* [CLC16]. A-SRRs provided the strongest SEIRA enhancement in their study. Related structures to the SRRs are dolmen-type structures which are combinations of perpendicularly oriented long and short bars [WKA<sup>+</sup>12, PKA<sup>+</sup>11]. They typically feature Fano-type resonances by coupling a dark mode of the plasmonic antenna to a bright mode, so that narrow resonances with high quality factors can be excited. To allow the dark mode to become bright, an asymmetry needs to be introduced into the structure. The short horizontal bar, like the one in Figure 2.10H, breaks the symmetry.

Cross shaped nanoantenna, see Figure 2.10I, have also been investigated [BZK<sup>+</sup>13, CYNH16]. Crosses can be understood as a pair of linear nanoantennas at right angles making them polarization insensitive [MP17]. Using different arm lengths for each linear nanoantenna pair, it is possible to excite plasmon resonances at different wavelengths to cover a larger part of the IR spectral range. Cerjan *et al.* [CYNH16] proposed asymmetric crosses made of aluminum using moreover an internal calibration of signal strength by exploiting the  $\text{Al}_2\text{O}_3$  phononic vibration, because a thin layer of oxide forms naturally on the antenna. One of the antenna pairs can be matched to its vibrational frequency, while the other one is tuned to the vibration of the targeted molecules.

Besides the particle based substrates, inverse nanostructures, for example nanoslits (Figure 2.10J) instead of linear nanoantenna, have its interest for SEIRA [HWBG13, HTN<sup>+</sup>15, CYG15]. Inverse structures are similar to the aperture gratings which display extraordinary optical transmission [GVMMEK10]. The optical response of an inverse structure is linked to their positive counterpart by Babinet's principle. The reflectance spectrum of the particle based structure resembles the transmission spectrum of its corresponding inverse structure when the light polarization is rotated of  $90^\circ$ . According to Babinet's principle, the electric and magnetic field components commute between the particle based structure and its inverse aperture. Huck *et al.* [HTN<sup>+</sup>15] compared nanoslits to their positive counterpart, the linear nanoantennas, and found that the slit provided superior signal strength. This is mainly due to the larger hotspot



## 2. Generalities of Biosensors and Plasmonic Biosensors

volume accessible in the slit center. While finding higher signal intensity, the enhancement factor was 7 times smaller for the slit, due to the larger hotspot (enhancement factor 93400 for nanoantennas against 13500 for slits)<sup>1</sup>. Dolmen-type inverse nanoapertures (Figure 2.10K) were studied by Cheng *et al.* for the detection of vibrational lines of PMMA [CYG15]. The authors report a sensitivity in the zeptomolar range and indicate an enhancement factor of 163000. The electric field distribution in slits and the accessibility of the hotspots seems advantageous for good signal enhancement.

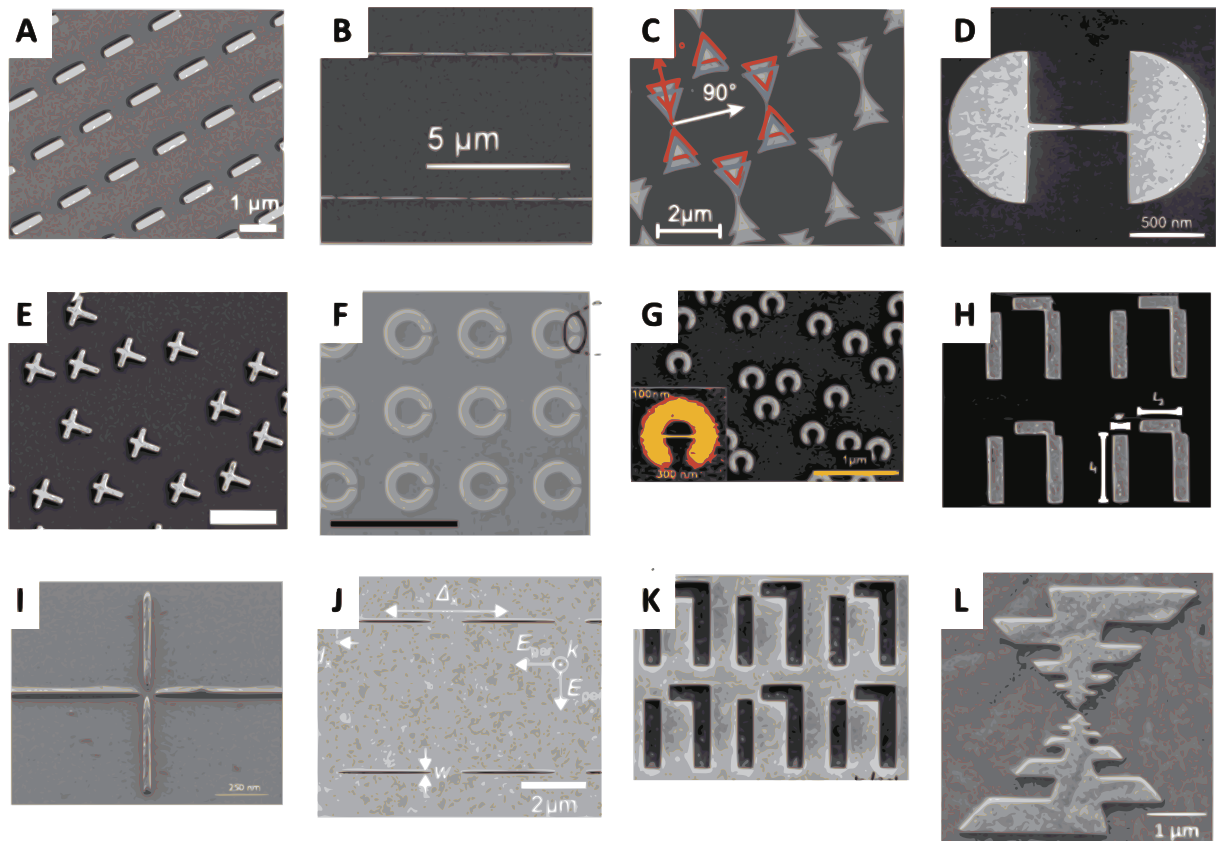


Figure 2.10.: Overview of different geometric designs of nanoantennas used for SEIRA substrates. A. Isolated linear nanoantenna. Figure from [NHW<sup>+</sup>17]. B. Array of linear nanoantennas [AYA<sup>+</sup>09]. C. Nanogaps between linear nanoantenna [VHN<sup>+</sup>14]. D. Bowtie nanoantenna with small gaps fabricated by NSL [HJCT14]. E. Fan-shaped nanoantenna pair with gap [BYZ<sup>+</sup>15]. F. SRR antenna array [CZP<sup>+</sup>09]. G. Crescent-shaped SRR [CZN<sup>+</sup>12]. H. Dolmen-type structure [WKA<sup>+</sup>12]. I. Cross-shaped nanoantenna [CYNH16]. J. Nanoslit array [HTN<sup>+</sup>15]. K. Inverse dolmen-type structure [CYG15]. L. Log-periodic multifrequency antenna pair [ARS<sup>+</sup>13].

1. This example of different enhancement factors for the inverse and particle based structures underlines the issue of the enhancement factor as a kind of figure of merit for signal enhancement. The best enhancement factor might not simply provide highest signal enhancement but be linked to a tiny hot spot area.

The spectral position of the plasmonic resonances can be drastically shifted using substrates with different refractive indices. This constitutes hence a degree of freedom to tailor the optical properties of a SEIRA substrate. Hoffmann *et al.* covered the spectral range from 3-13  $\mu\text{m}$  using differently large antennas on diverse substrates [HYR<sup>+</sup>13]. Brown *et al.* [BYZ<sup>+</sup>15] proposed an additional metallic layer underneath a dielectric spacer and the plasmonic antennas, providing an additional enhancement due to scattered wave interference from the metallic layer. This strategy is also employed to create perfect absorber (PA) structures, which are usually fashioned from a metal-insulator-metal (MIM) structure, the topmost metal layer being patterned with nanoantennas [LSS<sup>+</sup>13, CDI<sup>+</sup>15] or inverse structures [MP17]. At the resonance, reflectance and transmittance go both to zero, yielding a structure with absorption near 1. Tailoring the effective optical constants of the PA, the impedance of the structure is matched to the free space, which minimizes reflection. At the same time, transmission is suppressed due to the back reflector. Chen *et al.* [CAA12] used monopole antennas fashioned into the topmost layer of a MIM system with two different arm lengths to obtain a dual band PA structure. They could detect widely separated vibrational modes of PMMA thin films.

Placing nanoantennas on pedestals allows to decrease the effective refractive index of the surrounding material of the nanoantennas and increases the accessible sites for molecules inside the active zone of strongest electric fields [CEA14, HTN<sup>+</sup>15].

Collective array resonances have been exploited to increase the SEIRA signal [AYA<sup>+</sup>09, BWG<sup>+</sup>15]. As discussed in section 1.4, plasmonic antennas arranged in regularly spaced arrays allow to observe Rayleigh anomalies (grating orders). Combined with gold nanoantennas, which scatter dominantly in the IR spectral range, an enhancement of the SEIRA signal was observed for periodicities just below the critical one at which the evanescent grating order becomes radiative [AYA<sup>+</sup>09]. The plasmonic far field response is spectrally narrowed due to the collective resonances. The authors report on the detection of 300 zeptomole of silk fibroin proteins distributed over the whole array, corresponding to 145 molecules per antenna (approx. 90 attogram), and give an enhancement factor of  $10^4$  to  $10^5$ . The applied effect of collective resonances for IR absorption enhancement was named CEIRA for collectively enhanced IR absorption. Weber *et al.* [WAAG<sup>+</sup>11] investigated the far field coupling of linear nanoantenna in longitudinal and transverse directions separately. Due to the dipolar emission pattern of the linear nanoantenna, the transverse direction is the more critical one. Bagheri *et al.* [BWG<sup>+</sup>15] indicate an enhancement factor of 14000 for a nanoantenna array with an ideally chosen periodicity in both in plane directions, fabricated by direct laser writing. Besides, Rayleigh anomalies tuned to plasmonic resonances were also applied for THz enhanced transparency [HvHB<sup>+</sup>17]. Collective resonance effects in indium tin oxide (ITO) nanoantenna arrays were analyzed by Abb *et al.* [AWP<sup>+</sup>14]. The resonance wavelength was found to be independent of the array spacing, contrariwise to gold nanoantenna arrays. The lower sensitivity to long range interaction provides the possibility to densely arrange the nanoantennas without altering the optical response.



## 2. Generalities of Biosensors and Plasmonic Biosensors

While ITO nanoantennas prove to be ideal for densification, they however provide lower field enhancement than equal gold nanoantennas because of high internal losses.

Apart from the electric field enhancement, the contribution of scattering and absorption to the extinction of the nanoantennas is an important point for an optimization of the signal enhancement, as already mentioned in the context of the TCMT theory above. The proportion of scattering and absorption accounts also for the findings obtained with the ITO nanoantenna arrays and their reduced long range interactions [AWP<sup>+</sup>14]. Besides the results from Adato *et al.* [AAEA13] using the analytical TCMT, Neuman *et al.* [NHV<sup>+</sup>15] presented a numerical study in which they state that antennas with approximately equal scattering losses and internal absorption losses, that is, critically coupled antennas, provide an optimal spectral contrast of the SEIRA signal. According to the results of Adato *et al.* [AAEA13] it has however to be noted that the design of the loss channels of the antenna should not lead to the case with minimal signal contrast when the amplitude passes from the right shoulder of the coupling curve to its exact opposite position in the left shoulder (see Figure 2.9C).

Multiband plasmonic antennas have been proposed by some authors. Besides the already mentioned asymmetric cross antennas [CYNH16] using one band for self-calibration, and the dual-band PA [CAA12], Chen *et al.* [CCSO15] presented a wafer scale template stripped sample exploiting gap plasmons between Au ribbons and an Ag underlayer. Using ribbons of different width, they obtained a large band resonant structure, as a superposition of the individual resonances. Aouani *et al.* [ARS<sup>+</sup>13, ASR<sup>+</sup>13] proposed log-periodic trapezoidal optical antennas (Figure 2.10L) for broadband SEIRA. The advantage of this antenna design is, compared to the asymmetric structures with more than one hotspot or the wafer size structure proposed by Chen *et al.* [CDI<sup>+</sup>15], that the light is concentrated in the center between the two antenna arms for all resonance frequencies, that is, there is only one single hotspot where the analyte needs to be localized.

The best reported value so far achieved using SEIRA is the detection of 15000 chemisorbed ODT molecules (25 zeptomol) on a gold nanoantenna, corresponding to 7 attograms per antenna [NHW<sup>+</sup>17]. The corresponding enhancement factor is  $3 \times 10^6$ . This high value was reached using nanoantennas fabricated from monocrystalline gold platelets which improves the material quality compared to the evaporated metals typically used in combination with electron beam lithography fabrication. A high material quality is indeed a relevant approach to reduce additional, undesired internal losses and to improve the plasmonic properties.

Integrating plasmonic SEIRA substrates in devices is a critical point to enable real-time kinetic measurements, and ideally in the natural environment of the analyte molecules, for example aqueous environments for biomolecules. Adato *et al.* [AAEA13] proposed an integrated cell combining the plasmonic nanoantennas on an IR transparent substrate with a flow cell, working in reflectance geometry with light coming from the substrate side. The so-called plasmonic internal reflection geometry avoids the high loss of light intensity due to the OH bending modes of the water molecules, concealing possibly the vibrational lines of the analyte molecule. The

functionality of the integrated cell was proven using the biotin-SA molecular binding. The enhancement factor was evaluated to 7700. The same geometry was applied in order to detect the spectral signatures of lipid bilayers [LEW<sup>+</sup>16].

A consideration that needs to be addressed in the context of SEIRA spectroscopy are the light sources. Brilliant light sources like synchrotron radiation or quantum cascade lasers (QCLs) provide higher spectral power density than the standard thermal light sources (globars) used in FTIR spectroscopy. Spectroscopy of single gold nanorods [NKL<sup>+</sup>06] and later the use of these nanorod antennas for SEIRA of ODT molecules [NPC<sup>+</sup>08] with good signal to noise ratio was enabled by the use of IR synchrotron radiation. Hasenkampf *et al.* [HKS<sup>+</sup>15] demonstrated an experimental IR spectroscopy setup based on a tunable QCL. Compared to standard FTIR spectroscopy, the setup operates 2 - 3 orders of magnitude faster. The bandwidth is limited (1170 - 1300 cm<sup>-1</sup>), but nevertheless sufficiently large to tune the laser over the spectral width of the vibrational features.

All work presented above, apart from the example of the ITO nanoantenna array, has been realized with metals, mainly gold and silver and to a lower extent aluminum. Some studies on SEIRA with alternative plasmonic materials can be found. A more detailed state of the art on plasmonic materials will be given in the next chapter, here we will focus on some examples where alternative materials have been applied for SEIRA. Law *et al.* applied InAs disks fabricated by nanosphere lithography to detect absorption lines of a 50 nm thick PMMA layer. This was probably the first demonstration of III-V semiconductor materials for SEIRA spectroscopy. A quantification of the SEIRA enhancement is unfortunately not given. The SPR shift is 71 cm<sup>-1</sup> for a sample with high doping level and its resonance at shorter wavelength, and 44 cm<sup>-1</sup> for a sample with lower doping level, corresponding to approximately 600-700 nm.

PMMA was also the target analyte whose vibrational lines were enhanced in the work employing the ITO nanoantenna array [AWP<sup>+</sup>14]. For a 50 nm thick PMMA layer, a vibrational signal contrast close to 8 % is found using ITO nanoantenna dimers, which is comparable to single gold antenna. Despite these results of the ITO nanoantenna arrays, the material does not seem to be the material of choice for sensing due to the high internal losses and the weaker field enhancement compared to gold [GWDM15]. The increased bandwidth compared to gold and the transparency in the visible are nevertheless advantages compared to gold to create metamaterials [GWDM15]. Current work of the same research group applies ITO for space technology [MSdG<sup>+</sup>17].

Germanium nanoantennas were investigated by Baldassarre *et al.* [BSF<sup>+</sup>15] and applied to detect an absorption line of the polymer polydimethylsiloxane (PDMS). The antennas have micrometric dimensions. A resonance located on the surface of the antenna is tuned to be in resonance with the PDMS absorption line. Using a Ge nanoantenna dimer with improved electric field enhancement inside the gap, an enhancement factor of 2 orders of magnitude is reported. In general, Ge shows limitations to reach short wavelengths, due to the limited carrier incorporation.

Graphene supports surface plasmon-polaritons in the THz to IR spectral range, with a tunability of the resonance wavelength by the doping level and by electrostatic gating. Extremely high

## 2. Generalities of Biosensors and Plasmonic Biosensors

field enhancement and confinement has been shown for LSPs in graphene ribbons. Rodrigo *et al.* [RLJ<sup>+</sup>15] found that 90% of the mode energy is confined in a distance of 15 nm from the graphene ribbon interface, whereas for linear gold nanoantenna an equal amount of energy is distributed over a distance of 500 nm from the interface. Li *et al.* [LYF<sup>+</sup>14] reported a 5-fold signal enhancement of the vibrational strength of the carbonyl vibration of PMMA achieved by the graphene nanoribbons. They moreover investigate the SPR shift induced by the modification of the refractive index and indicate a sensitivity of 2650 nm/RIU. The saturation of the shift is a means to determine the electric field decay. The LSP shift saturates well below 100 nm, indeed the authors indicate a value of 20 nm which is in accordance with the value given by Rodrigo *et al.* [RLJ<sup>+</sup>15]. Choosing an adapted substrate, for example CaF<sub>2</sub> instead of the often used SiO<sub>2</sub> or hexagonal boron nitride (h-BN), suppresses the undesired plasmon-phonon coupling [HYZ<sup>+</sup>16]. For an 8 nm thin film of polyethylene oxide, a 20 fold signal enhancement of the vibrational signatures is reported for graphene ribbons on CaF<sub>2</sub>.

More details on resonant SEIRA using different types of nanoantenna substrates, covering to a small extent also SEIRA with alternative plasmonic materials, can be found in the recent reviews by Neubrech *et al.* [NHW<sup>+</sup>17] and Mayerhöfer and Popp [MP17].

### 2.6. Biosensor concept of the project Supreme B (Localized Surface Plasmon Resonance in highly doped Semiconductors for Infrared Biosensing)

The project Supreme B aims at developing a metal free plasmonic biosensor based on highly doped semiconductor material. Si-doped InAsSb is used to replace traditional metals like gold, silver or aluminium that have good plasmonic properties in the visible spectral range but approach the perfect conductor limit at higher wavelengths. InAsSb can be grown lattice matched onto GaSb substrates, which account also for a strong refractive index contrast. Previously, it has been demonstrated that InAsSb:Si nanostructures on GaSb sustain plasmonic resonances [NCR<sup>+</sup>12]. One of the objectives of the project is to determine nanostructures that are particularly adapted for the sensing applications, that is, nanostructures providing high electric near field enhancement and strong field confinement. Ideally, a large spectral range throughout the infrared should be covered, so that an adapted structure for the targeted analyte can be found. Yet, these nanostructures should ideally be fabricated by large scale nanopatterning methods so that it is interesting for low cost, industrial applications. Another goal of the project is the development of surface chemistry on the semiconductors, which is less mastered than the well-studied thiol-based surface chemistry on gold. Furthermore, the integration with a microfluidic circuit shall be demonstrated. A schematic representation of a sensor device is shown in Figure 2.9. This thesis is mainly concerned with the design of the plasmonic resonator structure which serves as the sensor's transducing element.

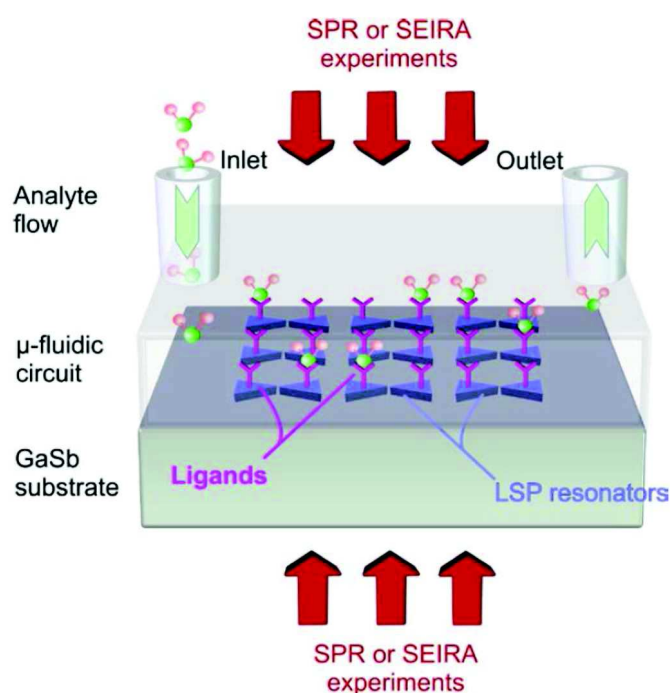


Figure 2.11.: Schematic illustration of an integrated, metal-free plasmonic biosensor based on SPR sensing and SEIRA spectroscopy.

## 2.7. Summary

In this chapter, the range of applications of biosensors was presented and put into context with standard chemical analysis methods. Biosensors were defined as devices consisting of a biorecognition element where an analyte binds to, a transducer and a read-out unit. Biorecognition ligands need to have a high affinity to bind the analyte. Different classes of biological substances can be used as biorecognition ligand: enzymes, antibodies and derivatives, nucleic acids, receptors like biotin, or whole microorganisms. Next, electrochemical, piezoelectric and optical transduction methods were discussed. Then, the surface plasmon based optical methods SPR sensing and SEIRA were investigated in detail. SPR sensing relies on the dependence of the surface plasmon frequency on the refractive index of the medium in vicinity of the plasmonic structure. It can be implemented using either propagating or localized SPP. The refractive index resolution of SPR is superior to LSPR ( $10^{-7}$ - $10^{-8}$  RIU for SPR against  $10^{-6}$  RIU for LSPR sensing [Hom08, BM14]) but at the cost of lower surface sensitivity due to a longer decay length of the electric field and a more complicated instrumentation because of the coupling conditions.

SEIRA belongs to the surface enhanced vibrational spectroscopy techniques, together with the complementary technique SERS. It exploits the enhancement of the electric field in proximity of the structure supporting surface plasmon resonances. The confined electric field leads to an increase in the interaction cross section for the molecular absorption of IR light due to coupling

## 2. Generalities of Biosensors and Plasmonic Biosensors

with the plasmonic resonance. Resonant SEIRA is the current state of the art, using antennas with plasmonic resonances spectrally matched to the molecular vibrational features. Several approaches to obtain maximum signal enhancement have been investigated in the literature, including the geometrical design of the nanostructures, the consideration of the best tuning ratio between the plasmonic and the vibrational resonance, the choice of the substrate, collective array resonances, the contribution of scattering and absorption to the extinction of the nanoantenna, or alternative materials for the plasmonic nanostructures.

## 3. Alternative Materials for Plasmonics

Materials are characterized by their dielectric function  $\epsilon$ , often also called relative permittivity, which indicates how the material interacts with electromagnetic fields of various frequencies. Notably, metals have a negative dielectric function in the spectral range where we describe their compartment as typically metallic (e.g. high reflectivity). The negative real part of the dielectric function results from the collective oscillations of the free carriers [LYRW13], the plasmons sustained by the metal. Inversely, a negative real part of the dielectric function is the necessary condition for plasmon excitation. The imaginary part of the dielectric function is related to losses in the material. Noble metals like gold and silver are standard plasmonic materials, especially for the visible spectral range. Silver has the advantage of lower losses compared to gold, which features several interband transitions in the visible range that are at the origin of its characteristic color. The inconvenient of silver is its reactivity with oxygen. In the IR spectral range, both materials have dielectric functions with strongly negative real parts, approaching the perfect conductor behavior with little penetration of electromagnetic fields into the metal. Moreover, the imaginary part of their dielectric function is high, due to ohmic losses. Indeed, the high carrier density in these metals causes these losses as a result of electron-electron scattering. Because of the perfect conductor-like optical response, their resonances can rather be described as antenna resonances than as a plasmonic effect [LYRW13]. Instead of using the traditional metals for the IR spectral range, it is of interest to mimic the dielectric function of the metals in the visible with engineered metals in the targeted spectral range, but without the undesired interband losses. Highly doped semiconductors can be described as «designed »metals [LATW12], with lower carrier density yielding a plasma frequency in the IR and at the same time less ohmic losses.

In this chapter, the definition of the dielectric function will be revised. As a typical model for dielectric functions of metal-like materials, the Drude model is presented. It is then discussed why alternative materials other than the noble metals are needed for plasmonics, focusing especially on the IR spectral range. A state of the art of these alternative materials is presented, highlighting the III-V semiconductors. To conclude this chapter, a comparison of highly doped InAsSb with gold is performed in terms of the electric field enhancement at mid-IR wavelengths.

### 3.1. The dielectric function

The dielectric function  $\epsilon$  is the response function describing how a material reacts to an electromagnetic field. More precisely, it links the electric field  $\mathbf{E}$  with the electric displacement vector  $\mathbf{D}$  in matter. The constitutive relations or material equations in the case of linear, isotropic

### 3. Alternative Materials for Plasmonics

and nonmagnetic materials have been given in equations 0.5-0.7. We are especially interested in the first of the constitutive relations, equation 0.5:

$$\mathbf{D} = \epsilon_0 \epsilon \mathbf{E}.$$

This equation shows that an electric field  $\mathbf{E}$  produces an electric displacement  $\mathbf{D}$  inside the material which is proportional to the field. The proportionality constant at each frequency is the permittivity  $\epsilon = \epsilon_0 \epsilon$ . Besides this multiplicative relation, the macroscopic fields  $\mathbf{E}$  and  $\mathbf{D}$  from Maxwell's equations can be linked by an additive relation involving the electric polarization  $\mathbf{P}$ :

$$\mathbf{D} = \epsilon_0 \mathbf{E} + \mathbf{P}. \quad (3.1)$$

With

$$\mathbf{P} = \epsilon_0 \chi \mathbf{E}, \quad (3.2)$$

where  $\chi$  is the dielectric susceptibility, it follows that

$$\mathbf{D} = \epsilon_0 (1 + \chi) \mathbf{E}. \quad (3.3)$$

Comparing with equation 0.5, it can be seen that

$$\epsilon = 1 + \chi. \quad (3.4)$$

In general, the dielectric function is complex and is written as

$$\epsilon(\omega) = \epsilon'(\omega) + i\epsilon''(\omega). \quad (3.5)$$

An equivalent description of the optical properties can be given using the complex refractive index

$$N = n + ik. \quad (3.6)$$

The quantities are linked by the following relations [BH07]

$$\epsilon'(\omega) = n^2 - k^2, \quad (3.7)$$

$$\epsilon''(\omega) = 2nk. \quad (3.8)$$

And inversely,

$$n = \sqrt{\frac{\sqrt{\epsilon'^2 + \epsilon''^2} + \epsilon'}{2}}, \quad \text{and} \quad (3.9)$$

$$k = \sqrt{\frac{\sqrt{\epsilon'^2 + \epsilon''^2} - \epsilon'}{2}}. \quad (3.10)$$

## 3.1. The dielectric function

$n$  is related to the phase velocity and  $k$  to the attenuation of plane waves in matter<sup>1</sup>. Depending on the context, either the description with the complex dielectric function  $\epsilon(\omega)$  or with the optical constants  $n$ ,  $k$  is preferred, for example  $n$  and  $k$  for considerations about wave propagation and  $\epsilon(\omega)$  to account for the microscopic mechanisms responsible for optical effects [BH07].

The optical response may strongly depend on the frequency. Various effects, due to core electrons, free electrons or the crystal lattice, may dominate the different spectral ranges. Figure 3.1 gives an example for the different contributions over the frequency ranges in the case of an ideal nonconductor (without Drude term). At lowest frequencies, contributions to the dielectric functions originate from permanent dipoles in matter, vibrational oscillators and electronic oscillators. Going to higher frequencies, the permanent dipoles cannot follow the oscillating field. Their contribution to the dielectric function drops out. The initial, static value of the dielectric function decreases to the value labeled  $\epsilon_{0,v}$  in Figure 3.1, at frequencies that are low compared to characteristic frequencies of lattice vibrations (phonons). Increasing the frequency throughout the frequency region of lattice vibrations,  $\epsilon'$  oscillates and then drops to the low frequency limit for core electron vibrations labeled  $\epsilon_{0,e}$ . In case of a materials with free electrons, there would be an additional contribution in a range around the lattice vibrational frequency region [AS11]. At highest frequencies, the optical properties of the material are mainly influenced by the core electrons. When all the electronic modes are exhausted,  $\epsilon'$  drops to the high frequency value  $\epsilon_\infty$ , in Figure 3.1  $\epsilon_\infty \approx 1$ .

If the dielectric function is known for all frequencies, it describes all light-matter interactions of the material in question. This is however rarely the case. So, it is often simpler to divide the dielectric function into the different contributions under the premise that there are no strong interactions between the contributions (adiabatic approximation). If we consider for example the three main contributions to the dielectric function of semiconductors [AS11], the dielectric function can be written as

$$\epsilon(\omega) = \epsilon_{\text{lattice}}(\omega) + \epsilon_{\text{free carriers}}(\omega) + \epsilon_{\text{interband}}(\omega). \quad (3.11)$$

Then, if some contributions are negligible within a frequency range or can be accounted for by a constant value, it is sufficient to model only the dominant part, eventually including all other contributions in a constant term. The excitation of plasmons is linked to the free carriers. This is why a model for the response of the free carriers (Drude model), if applicable with a dielectric background, is sufficient to describe the dielectric function appropriately in many materials. If the material displays phonons in the same frequency range as the plasmons, a combined model with a plasmon and a phonon contribution must be applied [ZMHW15] to take into account phonon-plasmon strong coupling. In the following, the Drude model for the free carrier response is derived from the more general Lorentz polarizability model.

1. The imaginary part  $k$  of the complex refractive index should not be confounded with the in-plane wave vector  $k$  which is unfortunately designated by the same symbol in the standard literature.



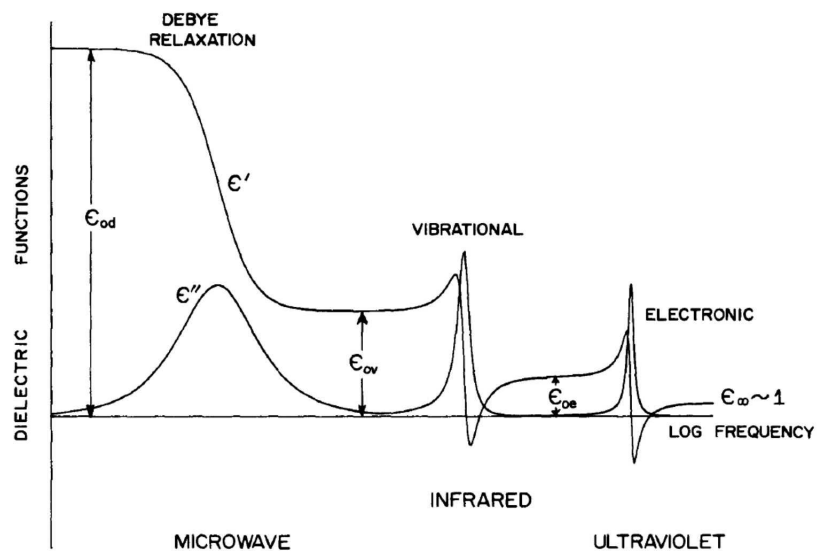


Figure 3.1.: Schematic diagram of the frequency variation of the dielectric function, exemplary for an ideal nonconductor. At lowest frequencies, there are contributions from permanent electric dipoles which drop out once the dipoles cannot follow the oscillation frequency of the field. Beyond the frequency region of lattice vibrations, the dielectric function drops again when the oscillations of the ions cannot follow the frequency of the field. Finally, there is the contribution from electronic vibrations. When all electronic vibrations are exhausted, the dielectric function drops to 1. The schema is for an ideal nonconductor so that there is no Drude term. Figure from [BH07].

### 3.1.1. The Drude model

The Drude model is a special case included in the extension of the model made by Lorentz. The latter is a classical theory describing electrons or ions in polarizable matter as harmonic oscillators acted upon by a linear restoring force and a damping force, driven by an electromagnetic field as external force. The equation of motion of the Lorentz model is

$$m\ddot{x} + b\dot{x} + Kx = e\mathbf{E}_{\text{local}}, \quad (3.12)$$

where  $x$  is the displacement from equilibrium of the oscillator,  $m$  is the mass of the oscillator and  $e$  the elementary charge,  $b$  the damping constant, and  $K$  the spring constant.

Electrons near the Fermi level in metals are considered as free, as they can be excited into other energy and momentum states by absorption of considerably low energy photons. To account for this in the harmonic oscillator model, the spring constant is set to zero, yielding the equation of motion of the Drude model (also called Drude-Lorentz model):

$$m\ddot{x} + b\dot{x} = e\mathbf{E}_{\text{local}}. \quad (3.13)$$

The eigenfrequency of transverse oscillations is then zero in a system without an external driving force, because there is no restoring force<sup>2</sup>.

For a time-harmonic driving field  $\mathbf{E}(t) = \mathbf{E}_0 \exp(-i\omega t)$  with frequency  $\omega$  the solution for the displacement is

$$\mathbf{x}(t) = \frac{-e}{\omega^2 + i\gamma\omega} \mathbf{E}(t), \quad (3.14)$$

with  $\gamma = \frac{b}{m}$ . In the model applied to electrons as oscillators,  $m$  is the electron mass and  $e$  the electron charge.

The induced dipole moment in a single oscillating electron is

$$\mathbf{p} = e\mathbf{x}. \quad (3.15)$$

For a collection of  $N$  oscillators per unit volume, this leads to the polarizability

$$\mathbf{P} = N\mathbf{p} = Ne\mathbf{x} = \frac{\omega_p'^2}{\omega^2 + i\gamma\omega} \epsilon_0 \mathbf{E}, \quad (3.16)$$

where we have defined the plasma frequency

$$\omega_p'^2 = \frac{Ne^2}{m\epsilon_0}. \quad (3.17)$$

---

2. This is different in the case of SPPs where the surface creates the necessary restoring force by the charge image, giving it a nonzero eigenfrequency.

### 3. Alternative Materials for Plasmonics

Employing the image of the electron gas moving against a fixed background of positive ions, we can interpret the plasma frequency as follows. The density of positive charges  $N_{\text{ions}} = N$  is constant in a defined volume. At equilibrium, the density of electrons is also  $N$ . When the electrons are displaced from equilibrium, for example due to an external electric field, a non-uniform charge distribution arises, creating an internal electric field that tries to restore equilibrium. The electrons moving in this field acquire momentum and overshoot the equilibrium position, so that an oscillation of the electrons takes place. If damping is neglected, a longitudinal oscillation is allowed as solution when  $\omega = \omega'_p$ . This is the bulk plasmon (see chapter 1), as a collective motion of the free electrons, due to long range interaction via the Coulomb force between electrons. In case of damping, the oscillation frequency is complex:  $\omega = \omega'_p - i\frac{\gamma}{2}$  (for  $\omega_p'^2 \gg \gamma^2$ ) [BH07], which means that the oscillation decays over time [LE09].

Equation 3.16 is a particular expression of the linear relation between the polarizability and the electric field (equation 3.2) for a free electron metal, from which the dielectric function of the Drude metal can be deduced:

$$\epsilon = 1 + \chi = 1 - \frac{\omega_p'^2}{\omega^2 + i\gamma\omega}. \quad (3.18)$$

The polarizability considered until here is the one caused by the free electrons. In real materials, there is also a residual polarization due to the positive background of the ion core, which can be accounted for by their permittivity at high wavelength  $\epsilon_\infty$ , which is different from 1 for diverse materials. The dielectric function is then

$$\epsilon = \epsilon_\infty - \frac{\omega_p'^2}{\omega^2 + i\gamma\omega}. \quad (3.19)$$

For doped semiconductor materials, it is more appropriate and convenient to redefine  $\omega_p$  as it was done below equation 0.8 [LE09, LPW13, ZMHW15]:

$$\omega_p^2 = \frac{Ne^2}{m^*\epsilon_0\epsilon_\infty} = \frac{\omega_p'^2}{\epsilon_\infty}, \quad (3.20)$$

where  $m^*$  is the effective electron mass. The plasma frequency  $\omega_p'$  is normalized by the square root of the high frequency permittivity  $\epsilon_\infty$ . We then have

$$\epsilon(\omega) = \epsilon_\infty \left(1 - \frac{\omega_p^2}{\omega^2 + i\gamma\omega}\right). \quad (3.21)$$

The dielectric function is zero at  $\omega_p$ , that is, the spectral signature due to  $\epsilon(\omega_p) = 0$  will be at the energy  $\hbar\omega_p$ . The plasma frequency normalized to the high frequency permittivity is sometimes called cross-over frequency, maintaining the definition 3.17 for the plasma frequency [NSB13, GKBS15].

## 3.2. Why are alternative materials for plasmonics needed?

Gold and silver are known as standard materials for plasmonics. Principal milestones have been discovered based on these noble metals. The real part of their dielectric function is negative at visible wavelengths as their plasma frequency lies in the ultraviolet, allowing to excite plasmons from visible wavelengths on. The high DC conductivity, which at the same time means reduced ohmic (resistive) losses [NSB13] compared to other metals, is the reason for the choice of gold and silver for plasmonics. While silver has a higher resonance quality than gold due to lower losses, it is chemically not stable, due to room temperature oxidation and sulfidation, contrariwise to gold which excels in terms of chemical stability but whose resonance quality is lower [GKBS15]. Nevertheless, both materials, gold and silver, suffer from several drawbacks.

1. Even the two metals of choice, yet better than others, display considerable resistive losses at visible and IR wavelengths [BA11]. Other loss mechanisms are also present at these optical frequencies: Besides the resistive intraband losses, interband losses occur notably for gold below 600 nm [LE09]. Scattering losses due to the metal film quality, like its granularity and surface roughness, add to this [NSB13]. This is notably a problem in patterned metal films [KB12].
2. The plasma frequency of metals is fixed, preventing a tunability of the optical properties. For some applications like transformation optics and hyperbolic material, it is desired to have approximately same absolute values of the relative permittivity of the metal and the dielectric, with opposed sign. Large negative values of the metal permittivity are hence undesired [NSB13, BA11].
3. Gold and silver are not compatible with standard silicon fabrication techniques and are thus not adapted for plasmonic on-chip integrated devices [Edi15, NSB13, KB12].

According to diverse authors, these points have hampered real life applications of plasmonics in some of its possible application fields [LATW12, GKBS15]. Only very inefficient processes, like Raman scattering, can benefit from the improvement achieved by lossy plasmonic elements [Khu15].

Especially the loss issue of metals was addressed in the literature [Khu15, KS12, KB12]. Following the description therein, it is derived in the following why, considering the conservation of energy, sub-wavelength confinement requires materials with negative permittivity and moreover, that loss is inherent in sub-wavelength structures.

Figure 3.2 schematizes an electromagnetic mode oscillating in an optical cavity with characteristic length  $a$ , which is larger than half the wavelength in the medium (Figure 3.2a) or smaller than this (Figure 3.2b). Sub-wavelength confinement is achieved in the small cavity with oscillating charges (Figure 3.2c).

From considerations on Maxwell's equations, the ratio of magnetic and electric energy  $u_M$ ,  $u_E$  can be estimated [KB12]:

$$\frac{u_M}{u_E} \approx \left(\frac{\pi n a}{\lambda}\right)^2. \quad (3.22)$$

### 3. Alternative Materials for Plasmonics

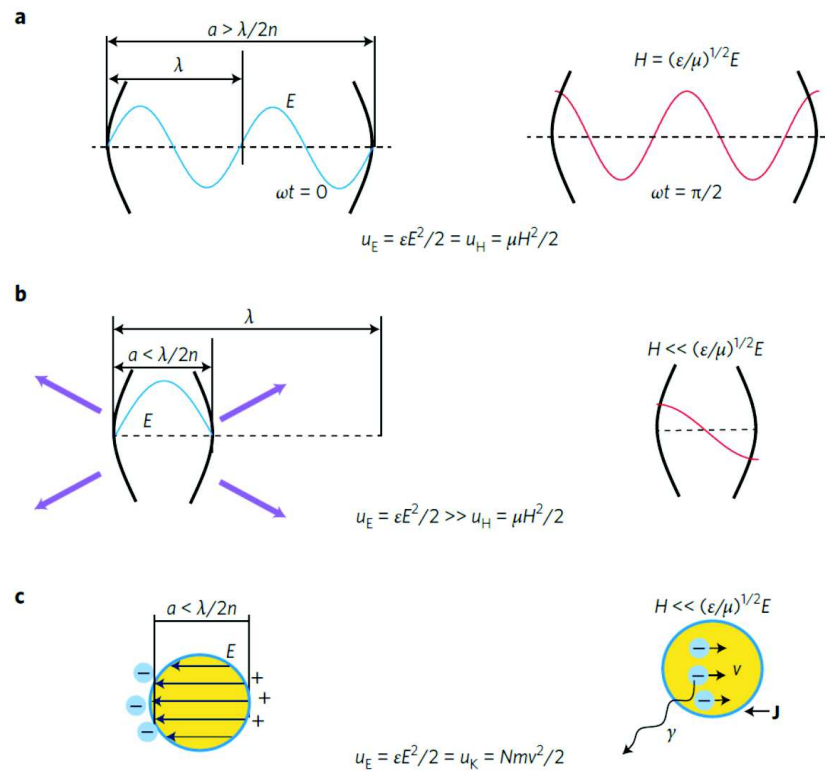


Figure 3.2.: Energy balance in photonic and plasmonic structures. a. Optical cavity with dimensions larger than half the wavelength  $\frac{\lambda}{2n}$ . Self-sustained oscillations are possible as the energy can alternate between electric (left) and magnetic (right) energy. b. Energy radiates out of the cavity with dimensions  $a < \frac{\lambda}{2n}$  because the magnetic energy is too small. c. Free carriers restore the energy balance by the kinetic energy of the carriers, allowing for sub-wavelength confinement. Figure from [Khu15].

### 3.2. Why are alternative materials for plasmonics needed?

In resonators with  $a > \frac{\lambda}{2}$ , a balance between  $u_M$  and  $u_E$ , and self-sustained oscillations are possible. Energy flows from the magnetic to the electric form, like in a classical mass on a spring oscillator where the energy is half of the time stored in form of kinetic and the other half stored in form of potential energy. When  $a \ll \lambda$ , the magnetic energy is much smaller than the electric energy. Because the energy cannot be stored in magnetic form in the cavity, it radiates out of it, in accordance with the diffraction limit (Figure 3.2b). However, the energy conservation can be restored when the energy of the kinetic motion  $u_K$  of carriers, which is  $90^\circ$  out of phase with the electric field and hence in phase with the magnetic energy, is taken into account. Then the energy relation is

$$u_K + u_M = u_E \quad (3.23)$$

and self-sustained oscillations are in turn possible. The kinetic energy is large enough only for materials with free carriers, or in polar dielectrics when ions are driven beyond their resonance frequency, which is the case only in the *reststrahlenband*<sup>3</sup>. The real part of the dielectric function is negative in both cases. In short, when the free carriers carry enough kinetic energy to restore the energy balance between magnetic and electric energy, modes with subwavelength confinement are possible, as illustrated in Figure 3.2c.

Half of the oscillation period, the energy is hence stored in form of the motion of the free electrons. This motion is however damped with the rate of electron scattering in the material, which makes this energy form highly dissipative. The conduction electrons are scattered into higher energy states due to collisions with lattice vibrations, electrons, surface states and defects. Photons account for the necessary energy for these electron scattering processes, so that finally all these phenomena are forms of absorption. For absorption of higher frequency photons, even more electrons, not only those close to the Fermi level, contribute. Moreover, interband electronic transitions set on for higher frequencies, without need for momentum matching contrary to the processes mentioned above. In metals, there is a relatively large density of states (DOS) to accept the electrons scattered into higher energy states, which is the reason for the high damping rate (see Figure 3.3). Materials with low DOS are favorable because they reduce the absorption losses.

As losses cannot be completely avoided, their effects should at least be minimized. Three main approaches can be found in the literature [BA11, KB12]:

- **Engineering the size or shape** of the plasmonic structure to have little penetration of the electromagnetic wave in the metal.
- Use **gain media** to compensate losses.
- Use **alternative low loss plasmonic materials** other than the traditionally used noble metals.

The first approach leads to a weak confinement, because it is necessary for sub-wavelength confinement, to have energy stored in form of the kinetic energy of the oscillating electrons, where it is dissipated, as discussed above. The use of gain media turned out to require unrealistically

---

3. The frequency band between the transverse optical phonon and the longitudinal optical phonon in polar dielectrics.

### 3. Alternative Materials for Plasmonics

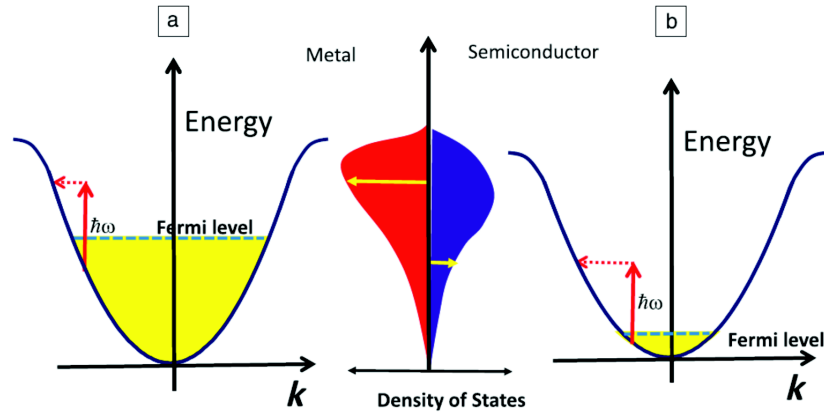


Figure 3.3.: Band diagram and density of states of (a) a metal and (b) a highly doped semiconductor. The lower density of states in the semiconductor reduces the loss. Figure from [KB12].

high current densities for compensation of the loss [KS12]. The use of alternative materials for plasmonics seems to be the most fruitful idea. Besides the reduction of losses, alternative materials can be tunable / modulable. One way is to increase the carrier density in semiconductors, the complementary approach is to reduce the free carrier density in metals for example by alloying [NSB13]. Also this alternative material approach is not completely free from drawbacks. With increasing doping level in semiconductors, the losses that are initially low in an undoped reference material also increase due to the introduction of defects. Similarly, alloying of metals introduces disorder in the crystalline structures and hence increases the losses due to electron scattering at defects.

Depending on the targeted spectral range, different materials can be most advantageous. The real part of the dielectric function of the material under consideration in the required spectral range must be negative but for many applications not too high in absolute value.

Figure 3.4 from reference [BA11] displays an overview of possible materials for plasmonics classified by their carrier concentration and carrier mobility. The carrier concentration must be high enough to obtain a negative dielectric function and is ideally tunable. A low carrier mobility means high losses. As a third axis, the interband losses are displayed. They are undesired as they introduce additional loss channels. The ideal material in its respective spectral range would therefore lie in the bottom plane at the very left [BA11]. Although a perfect material does not exist, it can be seen that for the mid-IR spectral range, III-V semiconductors are quite well placed, having an appropriate carrier concentration for the mid-IR and one of the highest carrier mobilities of the displayed materials.

In the next section, the achievements obtained with several of the alternative plasmonic materials displayed in Figure 3.4 will be discussed. We will detail especially the doped semiconductors

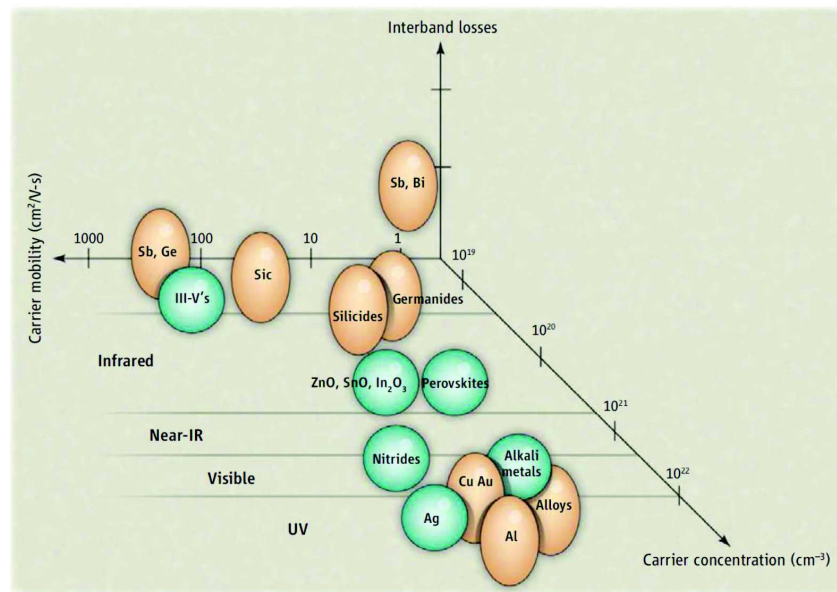


Figure 3.4.: Classification of potential materials for plasmonics by their carrier concentration, carrier mobility and interband losses. Spherical, green bubbles represent materials with low interband losses, and elliptical beige bubbles represent those with larger interband losses in the corresponding part of the electromagnetic spectrum. Figure from [BA11].

and notably on InAs(Sb) as one of the most promising candidates for plasmonics in the mid-IR spectral range, which is the spectral range that we are particularly interested in in this work.

### 3.3. State of the art of alternative materials for plasmonics

Doped semiconductors for plasmonics are based on the approach of increasing the carrier density to obtain metallic optical properties in the spectral range of interest. The accessible spectral range is hence limited by the maximum doping level. The frequency corresponding to the bandgap of the semiconductor should be higher than the frequency where plasmonic behavior is achieved, to avoid interband transitions.

Silicon and germanium have the advantage of being standard materials in semiconductor technology, hence their fabrication and processing is well studied. Excitation of propagating and localized surface plasmons in the IR has been demonstrated with doped Si [SMP<sup>+</sup>11, GJSD11, CBF15, BCF16], and doped Ge and GeSn [Sor10, SHC12]. Plasmonic Ge structures have been employed for sensing [BSF<sup>+</sup>15] and more recently for higher harmonic generation [DLTSP16, FRG<sup>+</sup>17]. The dopant solubility in Ge is lower than in Si and the background permittivity of Ge is higher, so that Ge is limited to longer wavelengths compared to Si. Both materials would however need extremely high carrier incorporation to display plasmonic properties at telecommunication wavelengths [NSB13], making them finally rather mid-IR plasmonic materials.



### 3. Alternative Materials for Plasmonics

Highly doped III-V semiconductors have also been investigated for mid-IR plasmonics [LATW12, LLW14, LYW13]. An InAs / GaSb system for plasmonics has first been proposed in 2011 [LN11]. InAs has the advantage of a high carrier incorporation, offering the shortest plasma wavelength among common semiconductors [LN11]. Doping densities up to several  $10^{19} \text{ cm}^{-3}$  have been experimentally shown [LATW12], and densities up to  $10^{20}$  have been predicted [Tok90]. The unusual high Fermi level stabilization point, that is, the point beyond which additional dopants act as acceptors instead of donors and thus lead to a compensation, is the reason for these high possible doping densities [Tok90, LATW12]. For the epitaxial growth of InAs on GaSb substrates, the incorporation of a few percent of Sb allows an improved crystalline quality due to the latticed matched growth conditions [NCR<sup>+</sup>12] while maintaining the possibility of high carrier incorporation as in InAs. Another advantage of InAs and InAsSb is the low effective electron mass, which increases the plasma frequency. InAs and the lattice matched alloy InAsSb on GaSb are consequently interesting materials for the mid-IR spectral range. LSPR in InAs disks were studied for sensing applications [LYRW13]. A multilayer epitaxial structure made of highly doped InAs and undoped InAs as spacer was studied as a perfect absorber structure [LLW14]. A more fundamental investigation of the ultrafast dynamics of SPPs in weakly doped InAs showed its potential to be used as material for ultrafast optical modulators for SPPs in the mid-IR spectrum [WMM<sup>+</sup>14]. Already before being used in plasmonics, superlattices based on InAs materials (InGaAs and AlInAs) have been applied as metamaterials displaying negative refraction [HSB<sup>+</sup>09].

Bound surface polariton modes were observed in Sb [CMS<sup>+</sup>12]. While the authors describe these modes to be similar in all respects to SPPs, they however occur at positive values of the real part of the dielectric function. It might be assumed that the observed modes are Brewster modes (see section 1.1.3).

To go to higher frequencies, other material systems than the III-V semiconductors are necessary. For short mid-IR wavelengths and the near-IR, transparent conducting oxides (TCOs) show adapted properties [SLG<sup>+</sup>13]. In general, TCOs have large band gaps, making them transparent in the visible spectral range. High doping levels in the range of  $10^{21} \text{ cm}^{-3}$  are possible [AWP<sup>+</sup>14] which lead to the high DC conductivity of the TCOs. Due to the high doping, TCOs display metallic properties in the near-IR. Advantages are the well mastered deposition techniques, the fabrication and a possible integration, and as for the semiconductors detailed above, the tunable plasma frequency by the doping level [NSB13]. Naik *et al.* [NSB13] studied the optical properties of Al- and Ga-doped ZnO (AZO and GZO), and those of indium tin oxide (ITO), which are probably the most established TCOs. AZO displays the lowest losses due to the better crystalline quality, followed by ITO and GZO. GZO and ITO allow in return a higher carrier incorporation. Nanostructuring of the TCOs has been demonstrated [KSJ<sup>+</sup>16, AWP<sup>+</sup>14, NSB13] as well as the epitaxial growth of nanorods [LN11]. Propagating SPPs excited in a Kretschmann configuration on thin ITO films were investigated by Rhodes *et al.* [RCE<sup>+</sup>08] and Dominici *et al.* [DMB<sup>+</sup>09]. A GZO SPR sensor based on propagating SPPs was proposed by Kuznetsov *et*

*al.* [KSJ<sup>+</sup>16] reaching a sensitivity of 4900 nm/RIU. Abb *et al.* demonstrated SEIRA using an array made of ITO nanoantennas and showed that an ultradense packaging of the antennas in arrays is possible because of the reduced long range interactions in the dominantly absorbing nanoantennas [AWP<sup>+</sup>14]. However, the field enhancement is low, due to relatively high losses in ITO which makes the material less favorable for sensing applications. Negative refraction using a plasmonic hyperbolic metamaterial based on stacked AZO/ZnO has been shown [NLK<sup>+</sup>12]. The dynamic tunability of the plasma frequency in AZO using an electric field at the surface of the film was demonstrated [PMS<sup>+</sup>14].

2D material like graphene find also application in plasmonics. Graphene sustains SPPs in the mid-IR to THz spectral range. Graphene provides high electric field confinement and enhancement, low losses and the possibility to actively tune the plasma frequency by electrostatic gating. More details on graphene plasmons can be found in the review by Low *et al.* [LA14]. Graphene nanoribbon structures have been applied for biosensing [LYF<sup>+</sup>14], the tunability by electrostatic gating has been exploited to spectrally match the absorption lines with the plasmonic resonance [RLJ<sup>+</sup>15]. Another plasmonic 2D material, black phosphorus, has been investigated in a numerical study by Liu *et al.* [LA16]. Similar to graphene, strong field confinement and enhancement can be achieved. Due to its in plane crystalline structure, it exhibits anisotropic properties in the absorption spectra which can be exploited in optical polarization selective structures.

Transition metal nitrides like TiN and ZrN have been studied for plasmonics in the visible spectral range as an alternative to gold and silver [GBS14, GKBS15, GSB15], using the approach of metals with reduced carrier density. They are refractory materials, that is, they are stable at high temperature. TiN and ZrN exhibit plasmonic properties similar to gold, which can also be anticipated by the similar color indicating that the dielectric functions are alike. Due to this property, TiN and ZrN are even used in jewellery as cheaper replacement of gold. Concerning the dielectric functions, gold has a slightly higher absolute value of the real part and a marginally lower imaginary part of the dielectric function, which makes it advantageous from a purely material property point of view. Yet, considering the temperature resistance of the transition metal nitrides, with melting points above 2000°C and the mechanical and chemical stability (disregarding a tendency to formation of a native oxide on the surface), they can be advantageous for certain applications. TiN is biocompatible, material deposition and fabrication are well mastered and is compatible with CMOS technology. Triangular shaped TiN antennas for heat assisted magnetic recording applications have been investigated by Guler *et al.* [GKBS15] yielding very similar performance in terms of electric field enhancement and confinement and scattering spectra compared to gold. TiN nanoparticles have been used as local heat sources [GNN<sup>+</sup>13]. Kinsey *et al.* experimentally validated an optical interconnect made of an IMI structure with TiN as metal at telecommunication wavelengths [KFN<sup>+</sup>14]. Second harmonic generation in TiN nanoantenna arrays has recently been demonstrated [GBS<sup>+</sup>16].

### 3. Alternative Materials for Plasmonics

Different metals for plasmonics were assessed in the review by West *et al.* [WIN<sup>+</sup>10]. Indeed, silver and gold are already the most favorable metals with regard to the material properties. Other metals display generally higher losses. Platinum and palladium could be interesting for their catalytic activity. Copper, characterized by its high conductivity is comparable to gold concerning the losses and a cheaper alternative. However, device fabrication with copper is challenging. Aluminum was used in some recent applications such as color printing [TZZ<sup>+</sup>14] and sensing [CYNH16, CDI<sup>+</sup>15]. While displaying broader resonances than gold in the visible range, and a quite different dielectric function, the IR optical properties are similar to the noble metals [CYNH16]. Aluminum is the third most abundant material on earth, is sustainable and cost-effective making it an interesting alternative to the noble metals. It can furthermore extend plasmonics to the UV spectral range. The native oxide layer can be exploited beneficially [CYNH16, TZZ<sup>+</sup>14]. Alloying gold with other metals is another strategy to modify the optical properties [NHS<sup>+</sup>14].

Alkali metals have been investigated with regard to their plasmonic properties. The losses of sodium and potassium are comparable to silver [WIN<sup>+</sup>10]. Khurgin and Sun performed a theoretical study showing that sodium with a stretched unit cell displays the band structure of an «elusive lossless material» [KS10]. The drawback of alkali metals is their extreme reactivity in ambient condition necessitating special storage conditions [WIN<sup>+</sup>10] and making them impractical for real life applications. Sterl *et al.* proposed the earth alkaline metal magnesium for active plasmonics in the visible spectral range [SSW<sup>+</sup>15]. Magnesium disks were capped with a catalytic Pd layer. When exposed to hydrogen gas, magnesium hydride is formed and the LSPR vanishes, a reaction that can be reversed by exposure to oxygen. Magnesium is relatively reactive but once a native oxide layer is formed on the exposed surfaces of the nanodisks, the properties remain stable over reasonable time scales. A similar switching behavior between a plasmonic state and the suppression of the plasmonic resonance has been shown in yttrium hydride antenna arrays upon hydrogen exposure making them a potential building block for active plasmonics [STS<sup>+</sup>14].

This overview of different materials used in plasmonics underlines the manifold of possibilities to find adapted material with respect to a specific spectral range, applications and the respective requirements needed for the application in question.

#### 3.4. Plasmonics in the mid-IR spectral range

The spectral range where plasmonics was initially applied is the visible, where nanophotonic applications make use of plasmonic effects. The mid-IR in itself is a spectral range of interest in diverse domains as it encompasses vibrational and, at again lower energies, rotational absorption resonances of various molecules. Moreover, it is the spectral range of thermal radiation of biological objects. Also, the mid-IR has been proposed as an appropriate spectral range for free space optical communication. Naturally, the mid-IR is of interest for sensing using the characteristic absorption or the thermal signatures. Mid-IR plasmonics finds hence application for chemical and biological

### 3.5. Comparison of the dielectric functions and the electric field enhancement: InAsSb and gold

optical sensing, as already mentioned in chapter 2, for the detection and control of thermal emission, and to go further, also in communication applications for light guiding, especially in connection with mid-IR lasers as the quantum cascade laser (QCL) [LPW13]. Potential users of mid-IR plasmonics come from the domains of security and defense, communication, environmental, industrial, medical, or chemical control and fundamental science. This manuscript focusses on mid-IR plasmonics for biological and chemical sensing, as detailed in chapter 2. According to the assessment of alternative materials for plasmonics in different spectral ranges, we apply highly doped InAsSb for mid-IR plasmonic (bio-)sensors.

### 3.5. Comparison of the dielectric functions and the electric field enhancement: InAsSb and gold

In the remainder of this chapter, we perform a comparison in terms of electric field enhancement achieved at mid-IR wavelengths by a gold resonator and an InAsSb resonator, considering the different optical properties of the noble metal and the HDSC. With regard to the targeted applications, SPR sensing and SEIRA, electric field enhancement is one of the key parameters. However, record achievements for SEIRA have been achieved with gold nanostructures which exploit different effects as for example sharp tips for additional field enhancement, nanogaps, both off-resonant enhancement mechanisms, or an ideal ratio of scattering and absorption. The objective here is to show that the basic material properties of InAsSb resonators, compared to an equivalent resonator structure made of gold, are favorable for mid-IR plasmonics and might be more adapted than gold. We also underline that the doped semiconductors try to reproduce the optical properties of noble metals that the latter display in the visible, simply shifted to another spectral range.

To begin with, Figure 3.5 displays the real and imaginary parts of the dielectric function of gold, with material data taken from Palik [Pal02], and InAsSb with different plasma frequencies. InAsSb was modeled as before in chapter 1 by a Drude model, using  $\epsilon_\infty = 10.4$ , and for simplicity with a same damping parameter  $\gamma = 1 \times 10^{13}$  rad/s for all plasma frequencies, chosen according to experimental observations for samples of the highest doping level [TGC<sup>+</sup>14]. InAsSb is metallic only above approximately  $5 \mu\text{m}$ . Both real and imaginary part are drastically lower for the InAsSb in the mid-IR spectral range compared to gold. The low imaginary part means lower losses compared to gold, which is partly explained by the reduced carrier density. Moreover, the high mobility of the carriers in InAsSb is an advantage. The low real part is beneficial for some applications where it is needed to have the same magnitude as the dielectric constant in dielectrics but with opposite signs, such as hyperlenses and transformation optics. The low real part allows however for a certain penetration depth into the material, which leads to dissipation of the energy, due to the energy storage in the form of kinetic motion of the free electrons [KB12, Khu15]. Yet, this yields a strong confinement, compared to gold where less energy is dissipated due to the weak penetration of electromagnetic fields into the material. The propagation length of SPP on

### 3. Alternative Materials for Plasmonics

gold is higher, but the electromagnetic fields are also less confined. Furthermore, the natural resonance frequencies  $\omega_{\text{SP}}$  and  $\omega_{\text{dipolar mode}}$ , given in Table 1.1 (see chapter 1) lie in the mid-IR for InAsSb. Moreover, it can be seen that the dielectric functions of gold in the visible spectral range and the Drude dielectric functions for InAsSb in the mid-IR are similar.

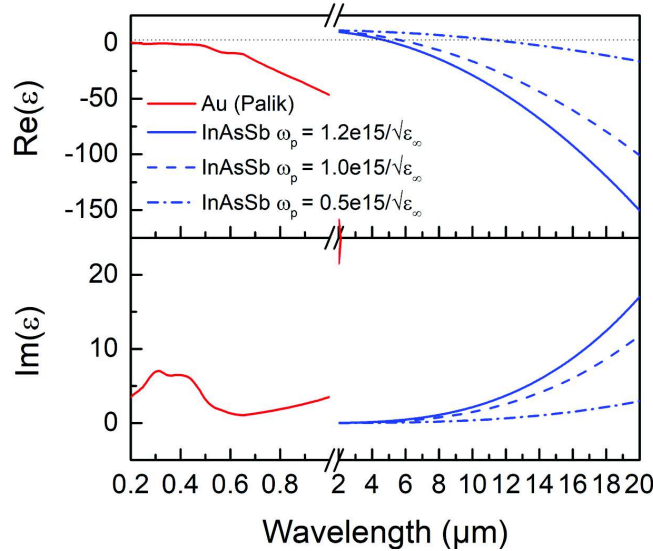


Figure 3.5.: Real and imaginary part of the dielectric function for gold (material data taken from Palik), and InAsSb, modeled by a Drude model with  $\epsilon_{\infty} = 10.4$ , damping  $\gamma = 1 \times 10^{13}$  rad/s and the plasma frequencies  $\omega_p$  as indicated.

A basic assessment of the electric field enhancement can be performed using the quasi-static approximation (see section 1.3.2), valid for small spherical particles of the investigated material, with diameters  $a \ll \frac{\lambda}{10}$ . The field inside and close to the small spherical particle in a dielectric medium, around its LSP frequency is calculated by the relation

$$E_{\text{in}} = \frac{3\epsilon_d}{\epsilon(\omega) + 2\epsilon_d} E_0, \quad (3.24)$$

where  $\epsilon_d$  is the dielectric constant of the surrounding medium, and  $\epsilon$  the dielectric function of the metallic material which forms the particle,  $E_0$  is the incident field and  $E_{\text{in}}$  the field inside and at the surface of the particle. In the case of a purely real dielectric function of the metallic material, this expression diverges at the Fröhlich condition (equation 1.35). The imaginary part of the dielectric function limits the magnitude of the maximum electric field. In Figure 3.6, the quasi-static field enhancement was calculated for gold, silver and InAsSb spheres, sufficiently small for a validity of the model (see also section 1.3.2, using material data from Johnson and Christy [JC72] and a Drude model with the parameters  $\epsilon_{\infty} = 10.4$ ,  $\omega_p = \frac{1.2 \times 10^{15}}{\sqrt{\epsilon_{\infty}}}$  rad/s and  $\gamma = 1 \times 10^{13}$  rad/s. While silver is better than gold for visible plasmonics regarding only the optical properties, InAsSb is nearly as good as silver in its respective spectral range. Clearly

### 3.5. Comparison of the dielectric functions and the electric field enhancement: InAsSb and gold

higher field enhancement compared to gold is obtained. A similar comparison for different other materials can be found in [NSB13]. These evaluations are however limited to the spectral range around the Fröhlich resonance condition due to the quasistatic treatment where the actual size and shape of a material, which can shift the resonance frequency, is not considered.

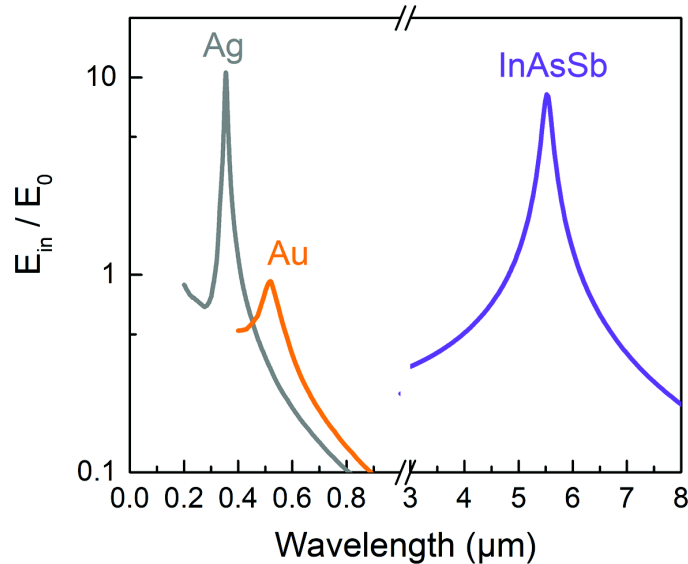


Figure 3.6.: Electric field enhancement calculated using the quasistatic approximation for silver, gold and InAsSb spheres in their respective spectral range. Material data for silver and gold were taken from Johnson and Christy [JC72], while a Drude model with parameters  $\epsilon_\infty = 10.4$ ,  $\gamma = 1 \times 10^{13}$  rad/s and  $\omega_p = \frac{1.2 \times 10^{15}}{\sqrt{\epsilon_\infty}}$  rad/s was used for InAsSb. The dielectric function of the surrounding medium  $\epsilon_d$  was taken to be 1.

Beyond the quasi-static approximation, a concrete example of a plasmonic resonator on a substrate is investigated in the following. An InAsSb nanoribbon sustaining a LSPR at  $10 \mu\text{m}$  was exemplarily chosen. To have equal conditions for the comparison of the electric field enhancement at this wavelength, it was first of all needed to determine the scattering maximum of gold ribbons of different width, so that all further calculations could be performed with a structure resonant at  $10 \mu\text{m}$  as our exemplary InAsSb plasmonic resonator. The results presented in the following were obtained by FDTD simulations. A detailed description of the method and the models is given in chapter 4. Here the presentation will be limited to the results. Figure 3.7 shows the scattering maximum for a single gold ribbon placed on different substrates, modeled by a constant dielectric function as indicated in the graph. As expected, a linear scaling with the ribbon width is found, the dashed lines corresponding to linear fits. Due to the high refractive index of GaSb, the width of the ribbon is smaller compared to low index substrates for same resonances. From the fit we deduce that an approximately 1600 nm large gold ribbon on GaSb provides the targeted resonance frequency.



### 3. Alternative Materials for Plasmonics

Using the same substrate, GaSb, for the gold and the InAsSb resonator, the electric field distribution was calculated. Figure 3.8A compares the electric field profiles obtained for the gold and the InAsSb resonator and highlights also their different geometric footprints (ribbon widths 1600 nm against 260 nm). The maximal values are indicated in the figure, both models being calculated with same FDTD parameters, notably the meshsize, for good comparability. Due to the high imaginary part of gold at IR wavelengths, we notice that the electric field does practically not penetrate into the metal. Besides, we note a higher confinement for the HDSC. This can be seen more clearly in Figure 3.8B, where a section parallel to the resonator - substrate interface is shown, at a distance of 1 nm above it. The maximum value is roughly one order of magnitude higher. The decay length of the electric field, which we define here as the distance from the resonator edge where the field has decayed to  $e^{-1}$  of its maximum value, is 2.75 nm for the InAsSb resonator and 10.25 nm for the gold resonator, considering the field profile in the plane 1 nm above the interface which is shown in Figure 3.8B. In conclusion, considering only the properties concerning the electric field enhancement, InAsSb provides higher absolute field enhancement values and stronger confinement with a nearly 4 times shorter decay length.

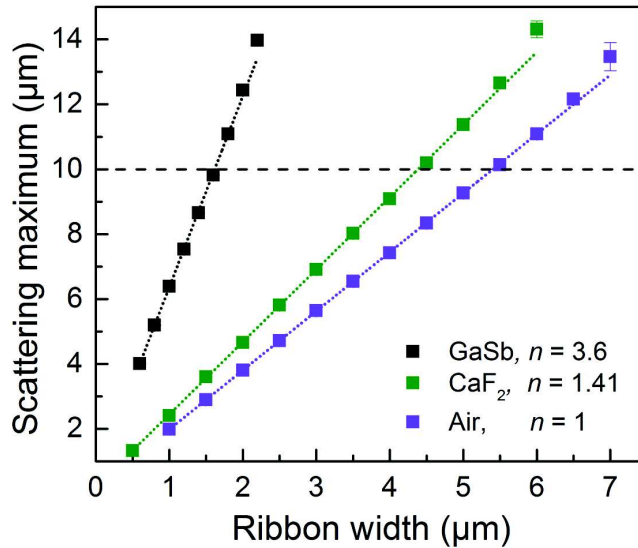


Figure 3.7.: Scattering maximum of single gold ribbons on different substrates. The ribbon width  $w$  is varied in order to find a scattering maximum at  $10 \mu\text{m}$ .

A similar comparison has been shown by Law *et al.* for (1) gold and InAs spheres of different sizes at their respective resonance wavelength and (2) for a perfect electrical conductor sphere and an InAs sphere of same diameter [LYRW13]. Figure 3.9, adapted from reference [LYRW13], shows the field enhancement derived from quasistatic calculations. Figure 3.9A displays the gold sphere with 52 nm diameter at its (quasi-static) resonance. Field enhancement is obtained

### 3.5. Comparison of the dielectric functions and the electric field enhancement: InAsSb and gold

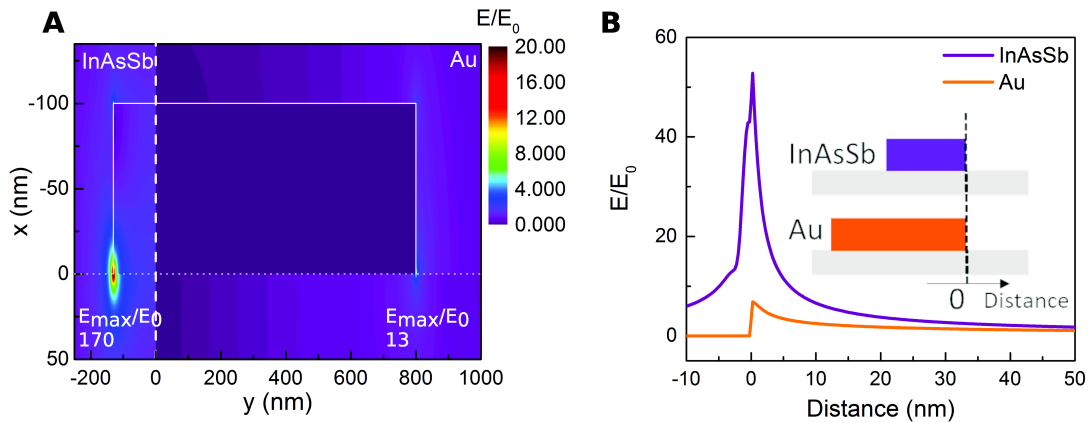


Figure 3.8.: A. Electric field profile at resonance,  $10 \mu\text{m}$ , for an InAsSb ribbon (left) and a gold ribbon resonator (right) on GaSb substrate. Note the increased footprint for the gold resonator. B. Cut through the field profile 1 nm above the substrate-resonator interface.

which is decreased due to large interband losses near the plasma frequency, and hence near the resonance frequency of the gold sphere. The field enhancement is weaker as for the InAs sphere at its resonance, here  $6 \mu\text{m}$ , shown in Figure 3.9C. Figures 3.9B and C compare spheres of same size at the same wavelength, the resonance wavelength of InAs. The gold sphere is represented as a perfect electrical conductor. The weak enhanced field around the sphere is due to nonresonant scattering and is clearly much weaker than for the InAs at resonance. As in our example, it is shown that InAs(Sb) is beneficial for strong field enhancement in the mid-IR spectral range.

It was argued in reference [NHW<sup>+</sup>17] that the electric field enhancement achieved with semiconductor structures is lower than for gold nanostructures, due to the penetration depth into the metal. Contrariwise to this, we have shown here that despite the penetration into the metal, the field reaching into the surrounding space of the resonator is strongly enhanced and accessible for analyte molecules or layers. For the equivalent structure types, the field enhancement is clearly stronger in the case of the HDSC. In reference [MBGP<sup>+</sup>17], the field penetration into an analyte layer surrounding the semiconductor structures is illustrated for different doping levels of the semiconductor. Indeed, it is most advantageous to have the highest doping level to obtain less penetration into the semiconductor material and stronger penetration into the analyte layer. The highest doping level makes this possible due to the higher absolute value of  $\text{Re}(\epsilon)$  at a fixed wavelength when the plasma frequency is higher.

A second point addressed in [NHW<sup>+</sup>17] is that absorption dominates the optical properties at frequencies close to the plasma frequency  $\omega_p$ , which might be unfavorable compared to gold nanoantennas that dominantly scatter at mid-IR wavelengths. Appropriate geometrical antenna design could help to find ideal proportions of absorption and scattering also in HDSC antennas, to further improve them besides their good field enhancement properties.



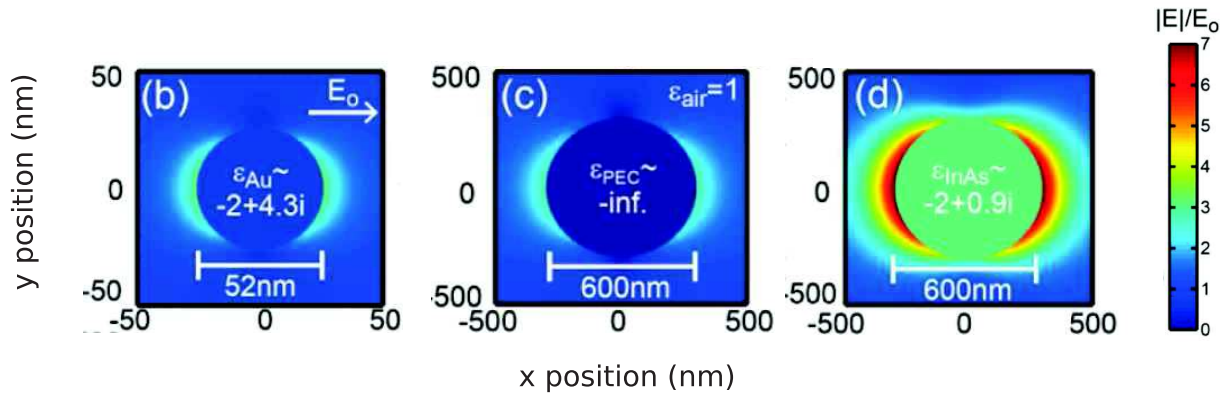


Figure 3.9.: Field enhancement in gold and InAs spherical particles calculated using the quasistatic approximation. Figure from [LYRW13]. A. Gold sphere with 52 nm diameter at resonance,  $\lambda = 520 \text{ nm}$ . Au material data from Johnson and Christy. B. Perfect electrical conductor sphere with 600 nm diameter at  $6 \mu\text{m}$  (off resonance). C. InAs sphere with 600 nm diameter at resonance,  $6 \mu\text{m}$ . InAs is modeled by a Drude model with  $\lambda_p = 5.5 \mu\text{m}$  and  $\gamma = 2 \times 10^{13} \text{ rad/s}$ .

### 3.6. Summary

This chapter dealt with the optical properties of metals and HDSC materials. To give the necessary theoretical background, the definition of the dielectric function as response function of a material to an electric field was summarized. The Drude model was introduced as it is used throughout this manuscript to model the dielectric function of the HDSC. In the framework of the Drude model, the optical properties are mainly influenced by free electrons while the background polarizability is considered by a constant. Next, the drawbacks of noble metals for plasmonics were discussed. For the visible spectral range, they have limitations, such as ohmic losses, a fixed plasma frequency prohibiting tunability, and an incompatibility with standard CMOS technology. These limitations need to be improved for real-life applications in the diverse fields where plasmonics has been proposed to be beneficial. Notably the losses, yet lower than in many other metals, are problematic. In the IR, the optical properties differ quite strongly from the visible spectral range due to the scaling of the dielectric function. The real part of the dielectric function is large and negative so that noble metals approach the perfect electrical conductor behavior. The high imaginary part signifies high losses. The most appealing approach to improve plasmonics are alternative materials with lower losses than the noble metals. The carrier density, carrier mobility and additional loss channels such as interband transitions can be used as criteria to assess the suitability of a material for plasmonics. The carrier density determines the spectral range where the material displays plasmonic compartment, the carrier mobility should be high, because this means low intraband losses, and additional loss channels should be completely avoided.

An overview of the research achievements with different types of materials for plasmonics was then given. Two complementary approaches are 1) incorporating carriers into semiconductors to make them metallic, 2) reducing the carrier density in noble metals to reduce losses. The first group includes materials such as III-V semiconductors, Si, Ge, TCOs, and 2D materials like graphene and black phosphorus. The second group includes principally the transition metal nitrides and metal alloys. The advantages and downsides of the diverse alternative material have been assessed, giving also some examples of applications where the materials were already successfully used. After this general description of plasmonics for various spectral ranges, the mid-IR was highlighted as the remainder of this manuscript is concerned with mid-IR plasmonics using highly doped InAsSb. The last part of this chapter showed a comparison of the optical properties of InAsSb and gold, starting from general considerations like the dielectric functions and the field enhancement using the quasi-static approximation for spherical particles. Then, using FDTD calculations, an example was shown for field enhancement at mid-IR wavelengths with an InAsSb and a gold ribbon resonator where the advantages of InAsSb for strong field enhancement and confinement could be approved. The maximal field enhancement for InAsSb is about one order of magnitude higher and the decay length of the electric field is a factor of nearly 4 smaller. Moreover, due to the smaller geometric footprint ( $w = 260$  nm versus 1600 nm) of the InAsSb resonators for a same resonance wavelength, a higher densification of resonators on a substrate is possible.



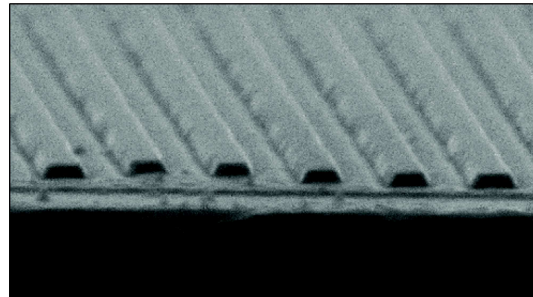
## Part II

# Simulations, fabrication and optical characterization of HDSC plasmonic nanostructures

*Periodic structures..*



*.. formed naturally*



*..fashioned by nanotechnological methods*



## 4. Simulation of a 1D Periodic Grating Structure and Parameter Optimization

Electromagnetic simulations of plasmonic nanostructures help to target optimal geometries preliminary to the sample fabrication and help to understand which parameters have the strongest impact on the optical response. In addition, they are also useful for the validation of experimentally observed effects. In this chapter, the basic model used for calculations of the optical response and the electric field profiles of the plasmonic resonator structures is introduced and applied to first investigate the impact of different geometric parameters and then to study the performance for sensing. This chapter is restricted to 2D simulations which are fully applicable to the grating structures, invariant along one direction. An extension to 3D simulations is presented in the next chapter.

### 4.1. Elaboration of a FDTD model for a parameter study

The finite-difference time-domain (FDTD) method is a numerical approach to solve Maxwell's equations, simplified to finite differences instead of derivatives. A short description of the FDTD method is given in the appendix B. It is a useful tool to simulate the optical properties of a given structure, detailed by its geometry and its constituting materials. Once the electromagnetic field vectors are known throughout the calculation zone, it is possible to deduce various optical properties of the structure, for example the reflection and transmission spectra. These can be compared to experimentally measured far field spectra. Also, electromagnetic field distributions can be displayed, allowing to distinguish resonances with different electric field profiles in a structure and to obtain information on the electromagnetic near field such as the electric field hotspots.

A commercially available FDTD software, Lumerical FDTD Solutions version 8.12, was used to obtain the results presented in the following sections. Models were established for the simulation of periodic grating structures and also for isolated nanoresonators. Taking the example of the 1D periodic grating, the influence of different geometric parameters on the optical response was explored. Then, the objective was to optimize the structure design for a targeted wavelength range for sensing.

In the following, the basic model used for the parameter study in periodic structures will be presented. Once this basic model validated, it was applied for the variation of the geometric

#### 4. Simulation of a 1D Periodic Grating Structure and Parameter Optimization

parameters. It was also reused with slight modifications, for example additional layers, to simulate a transducer exposed to an analyte.

A schema of the simulated structure and the unit cell is shown in Figure 4.1. Due to the invariance of the structure in the  $z$ -direction, it is sufficient to use a 2D model, assuming the third dimension to be infinitely extended (Figure 4.1A). The geometric structure consists of an InAsSb ribbon on a GaSb substrate. The variable geometric parameters of the grating are the ribbon width  $w$ , thickness  $t$  and pitch  $\Lambda$ , as indicated in Figure 4.1B. To model the materials, a constant refractive index  $n = 3.6$  [Ada89] was applied for the substrate, in later models it was modified to 3.77, based on more recent material data measured by the M-lines technique, using waveguide modes [RBL<sup>+</sup>15].

A Drude dielectric function, see equation 0.8, with  $\epsilon_\infty = 11.7$ ,<sup>1</sup>  $\omega_p = \frac{1.2 \times 10^{15}}{\sqrt{\epsilon_\infty}}$  rad/s and  $\gamma = 1 \times 10^{13}$  rad/s, was assigned to the n-doped InAsSb. The plasma frequency  $\omega_p$  corresponds approximately to the highest doping levels that have been achieved in the epitaxially grown InAsSb layers. Curves of the dielectric function with similar parameters ( $\epsilon_\infty = 10.4$  instead of 11.7) are shown in chapter 3 (see Figure 3.5). The main influence of the lower  $\epsilon_\infty$  on the plasmonic spectrum is a blue-shift of the resonances, also due to the higher plasma frequency. For the qualitative analysis shown in the following, the same global behavior is expected but the actual resonance wavelengths might be slightly shifted. Hence, if one tried to adjust experimental data using the values indicated above, this might give a fit that does not perfectly match experimental data.

A broadband plane wave source injects the initial electric field distribution from above the plasmonic structure. Its bandwidth is 1-15  $\mu\text{m}$ , the longest wavelength being most critical for the convergence and the dimensioning of the model. In most models, normal incidence was investigated as it simplifies the broadband simulations. Reflection and transmission monitors, measuring the power transmitted through their surface, were placed in between the source and the plasmonic structure and in the substrate below the grating, respectively.

Perfectly matched layer (PML) boundaries were used at the limits of the calculation zone in the direction of initial plane wave propagation. At such boundaries, all incident energy is absorbed so that no energy is scattered back into the calculation zone when the dimensioning of the model is sufficiently large and convergence is achieved. To take into account the periodicity of the structure, Bloch or periodic boundaries were applied as lateral boundaries for the unit cell. For normal incidence, periodic boundaries are appropriate. To reduce the calculation time and the data volume, symmetry planes were applied combined with periodic boundaries. The periodic boundaries replicate the field at the edges of the simulation region to reinject it in the next cell. In the case of oblique incidence, the whole unit cell has to be calculated with Bloch boundary conditions. The Bloch boundary conditions apply a phase correction at the edges of

---

1. In the initial models, the value  $\epsilon_\infty = 11.7$  was used, which has been found experimentally for thick InAsSb layers. In later models it was modified to 10.4 in accordance with more recent ellipsometry measurements on thin layers.

the unit cell because the field in vicinal unit cells is not exactly periodic, but dephased due to the oblique incidence.

The interfaces of the plasmonic resonator with its environment are modeled precisely when a fine mesh is applied enveloping the resonator and its interfaces with other materials. Also, a fine mesh is necessary when thin layers are present in the model in order to have a sufficient number of mesh cells within this material layer. For these reasons, a mesh override was used covering the resonator and its surroundings. The typical size of the mesh cells was 1 nm, in some detailed models, especially with thin layers, 0.25 nm. Staircase or «conformal variant 0» mesh refinement techniques were applied, which are adapted for metallic interfaces. For a staircase mesh refinement, only the material properties at the precise position where the field vector is calculated are considered, whereas conformal mesh refinement techniques use a rigorous description with Maxwell's integral equations near the interfaces. This is more precise but can be delicate to use when metallic materials are involved. The conformal variant 0 mesh refinement excludes metallic interfaces from the conformal meshing, but applies it anywhere else.

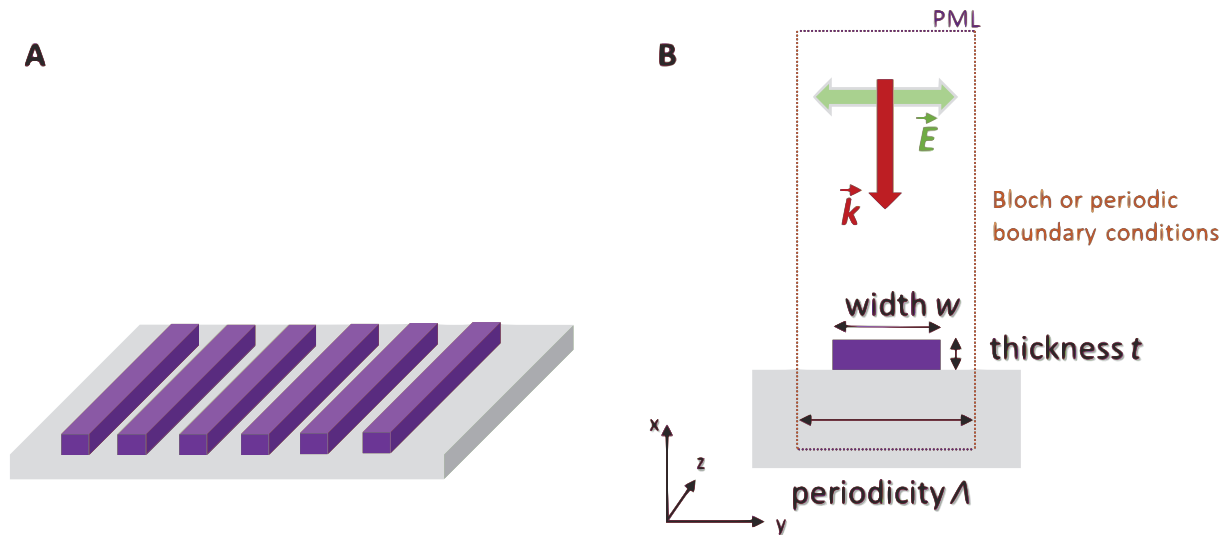


Figure 4.1.: A. Schematic of the grating structure. B. Sketch of the modeled unit cell, indicating the geometric parameters and boundary conditions.

Isolated structures are investigated by a total-field scattered-field (TFSF) approach. The physical structure is modeled as indicated above. The TFSF source is a box that separates the computation region into two regions, one that contains the total field, that is, the incident field and the scattered field, and one that contains only the scattered field. Placing transmission monitors within the zone of the total field, in a non-absorbing medium, around the geometric structure, allows to deduce the absorption cross section of the structure by calculating the absorbed power. The absorbed power is obtained using the transmission through the monitors around the structure, the source power and its intensity. The same type of evaluation, concerning the scattered power respectively, inside the scattered field zone yields the scattering cross section.



#### 4. Simulation of a 1D Periodic Grating Structure and Parameter Optimization

For isolated nanostructures, these are the pertinent quantities instead of the transmission and reflection. The scattered wave by a particle is the analogous quantity to the sum of transmission and reflection by a slab [BH07]. As there is no periodicity, the computation region in the TFSF model is completely surrounded by PML boundaries.

### 4.2. Study on the geometrical parameters

For several applications, plasmonic nanoantennas are required that display their spectral signature at a precise wavelength or in a defined spectral band. For example, SEIRA using resonantly tuned nanoantennas (resonant SEIRA [NHW<sup>+</sup>17]), has proven to be beneficial compared to SEIRA on arbitrarily fashioned rough surfaces, non-resonant SEIRA, where the enhancement effect has initially been discovered [HKT80], as discussed in detail in chapter 2. Similar considerations apply to SERS, where the nanoantennas should favor a high electric field enhancement at the excitation frequency but also at the frequency of the stokes or anti-stokes Raman emission [LE09, LVV<sup>+</sup>16]. Likewise, for plasmonic color printing, plasmonic nanoantennas displaying resonances at the desired wavelength to obtain a particular color in a plasmonic pixel are needed, often achieved by variation of the size of the antennas [TZZ<sup>+</sup>14, RPAB14].

Using traditional plasmonic materials like gold and silver, the common way to tailor the resonance wavelength of a nanoantenna is to change the size or shape of the antenna [BZK<sup>+</sup>13, NP13, BGN14], to use substrates of different refractive indices [HTN<sup>+</sup>15, HYR<sup>+</sup>13], apply alloys of materials [WIN<sup>+</sup>10, NHS<sup>+</sup>14] or to exploit near- or far field coupling interaction for resonance tuning [AYA<sup>+</sup>09, WAAG<sup>+</sup>11, HNV<sup>+</sup>14]. With «designed» plasmonic materials [LYRW13, LATW12, ZMHW15] it is possible to adapt the dielectric function using different doping levels in order to tune the resonances. Nevertheless, size and shape are important parameters to tailor the nanoantennas once the material has been grown. In the following, we investigate the influence of different geometric parameters on the optical properties. Using a simple type of structure, a grating made of HDSC ribbons on a substrate, the impact of the ribbon width and thickness is first investigated. The grating period was fixed at 500 nm. This small periodicity is interesting for high densification of the ribbons which generates marked signatures in the reflectance spectra. Besides, periodicities around this range can still be fabricated by large scale nanopatterning methods like interferential lithography.

In the simulated reflectance spectra, two peaks, associated to the excitation of LSPR, can be observed. From the electric field distribution shown in Figure 4.2, it can be deduced that the high energy resonance, labeled  $\omega_{\text{top}}$ , is mainly located on the top corners of the ribbon, at the air - HDSC interface. The strong resonance at low energy, labeled  $\omega_{\text{bottom}}$ , is linked to a confinement at the corners at the HDSC - substrate interface. From estimations and approximate expressions for the surface plasmon frequency, this assignment is evident as the surface plasmon frequency is higher when the refractive index of the contiguous medium is lower, as shown exemplary for some simple geometries in chapter 1, table 1.1.

Increasing the ribbon width for a constant ribbon thickness red-shifts the principal, low-energy LSPR peak  $\omega_{\text{bottom}}$  displayed in the reflectance spectra, as shown in Figure 4.3A. As the confinement is relaxed due to the larger extension of the ribbon, the oscillation frequency of the LSP, driven along the width axis of the nanoribbon, decreases, as schematically illustrated in Figure 4.3B. Similarly to the frequently applied gold nanorod antenna [HTN<sup>+</sup>15, NKL<sup>+</sup>06, BDN09], we first observe a zone of linear scaling between nanoribbon width and the LSPR wavelength. But when the ribbon width approaches the grating periodicity, near field interactions between vicinal nanoribbons arise yielding a deviation from the linear scaling. When approaching the limiting case of the uncorrugated HDSC layer, no resonance can be excited as the coupling conditions are not satisfied for normal incident light from free space. Hence, the resonance wavelength diverges for large ribbons.

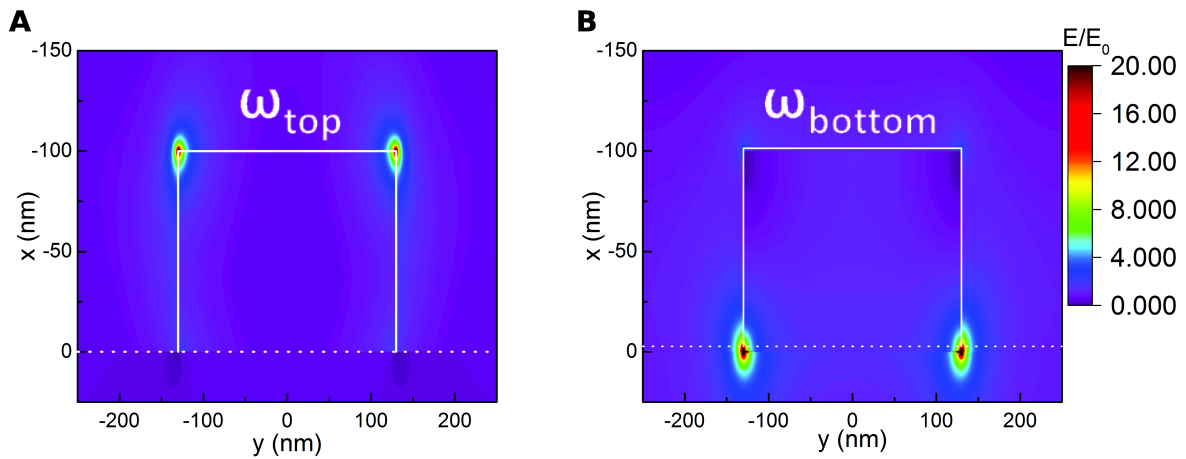


Figure 4.2.: A. Electric field profile associated to the high energy peak  $\omega_{\text{top}}$ , close to the plasma frequency  $\omega_p = \frac{1.2 \times 10^{15}}{\sqrt{11.7}}$  rad/s (respectively the plasma wavelength  $\lambda_p = 5.4 \mu\text{m}$ ), in the reflectance spectra. The field is mainly localized at the top corners. B. Electric field profile associated to the low energy peak  $\omega_{\text{bottom}}$ , which is the stronger spectral signature in the reflectance spectra. The field is confined at the resonator corners at the interface with the substrate.

If, for a constant ribbon width, one decreases the thickness of the grating, it can be observed that the principal LSPR peak red-shifts. The shift is particularly strong for the thinnest simulated ribbons (50 nm to 60 nm), gradually decreases and tends to saturate when reaching thicknesses of 200 nm and above (Figure 4.3C). From this observation, it can be assumed that the resonance position is influenced by an interaction of the plasmonic resonance  $\omega_{\text{top}}$  at low wavelength, localized at the interface with the air. As in a layered system (see section 1.2.2), an interaction between upper and lower interface resonances is possible for sufficiently thin layers. In the layered system, the dispersion of one resonance is shifted to lower energies whereas the other one deviates to higher energies. In the plasmonic grating, the high energy resonance  $\omega_{\text{top}}$  located at the upper interface is obstructed by the proximity to the plasma frequency  $\omega_p$ . Hence, it cannot

#### 4. Simulation of a 1D Periodic Grating Structure and Parameter Optimization

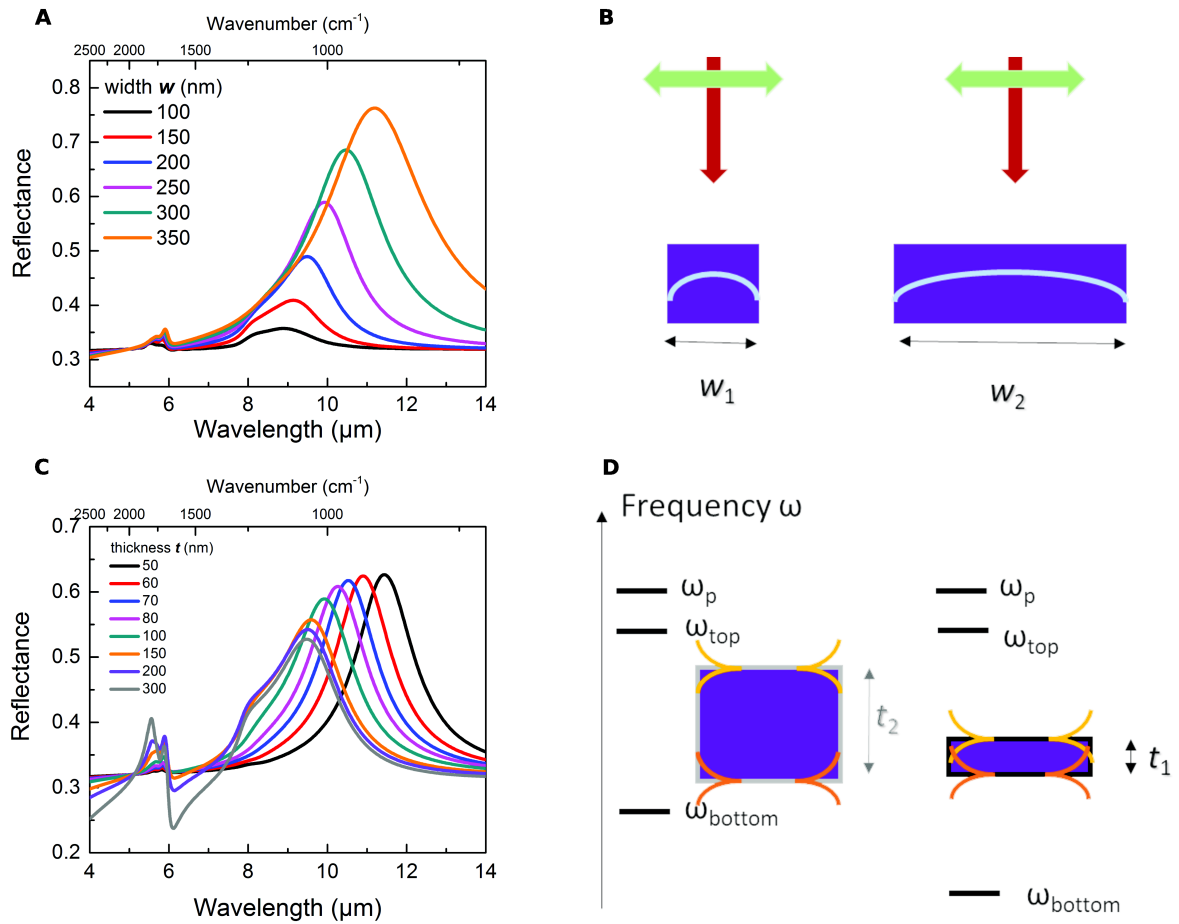


Figure 4.3.: A. Exemplary reflectance spectra of 100 nm thick ribbons of different ribbon width  $w$ . B. Illustration of the impact of the ribbon width on the resonance wavelength. Larger ribbons have a lower resonance frequency due to lower confinement, yielding a longer wavelength of the standing wave. C. Exemplary reflectance spectra of 250 nm large ribbons of different thickness  $t$ . D. Illustration of the impact of the ribbon thickness on the resonance wavelength. Higher ribbons have a lower resonance frequency due to the repelling interaction with the resonance at high energy.

deviate towards higher energies. The interaction thus repels the low energy resonance  $\omega_{\text{bottom}}$  to again lower energies, shown in the schematic in Figure 4.3D. Concerning the intensities, we note an attenuation of the low energy resonance  $\omega_{\text{bottom}}$  while the high energy resonance  $\omega_{\text{top}}$  becomes considerably more marked when the thickness is increased. When the nanostructure is thick, the light couples less to the resonance  $\omega_{\text{bottom}}$  localized at the interface with the substrate, attenuating the reflectance intensity reached at the maximum of the low energy resonance.

To clarify the nature of the different modes and their extension through the structure, electric field profiles were calculated for a thin and a thick structure, at the resonances extracted from the black (50 nm) and the gray (300 nm) curve in Figure 4.3C. Figure 4.4 shows the field profiles corresponding to the thin structure in the left column and those corresponding to the thick structure in the right column. The ribbon cross section and the substrate is displayed by the white lines. We distinguish two resonances with distinct field profiles at short wavelength. Using a simplified image, the lowest wavelength mode (Figures 4.4A and B) is a Fabry-Perot like mode propagating along the vertical interfaces of the grating's ribbons with the air, corresponding to the model detailed in [LT10]. According to the model, this mode shifts as a function of thickness. This shift is however rather observable for much thicker layers. As a consequence of the comparatively thin gratings, the mode is rather weak in the two investigated cases here, yet it can be seen that its spectral signature increases clearly comparing the 300 nm thick grating to the 50 nm thick grating. The field profiles shown in Figures 4.4C and D correspond to the LSP situated at the air-InAsSb interface oscillating in the horizontal direction, labeled  $\omega_{\text{top}}$  above. Due to the energetic proximity of the Fabry-Perot mode and the mode  $\omega_{\text{top}}$ , the distinction into the horizontal and the vertical direction is an over-simplification and in fact there might be hybridisation between them. At highest wavelength, we again recover the field profile of the mode  $\omega_{\text{bottom}}$ , the LSP localized at the interface between the grating and the substrate. Comparing the thin and the thick grating, it can be seen that the two LSP resonances are pinned to their respective interface and are therefore well separated for the thick grating, whereas for the thin grating the field extends around the ribbons, indicating the interaction of the LSP at the upper and the lower interface.

4. Simulation of a 1D Periodic Grating Structure and Parameter Optimization

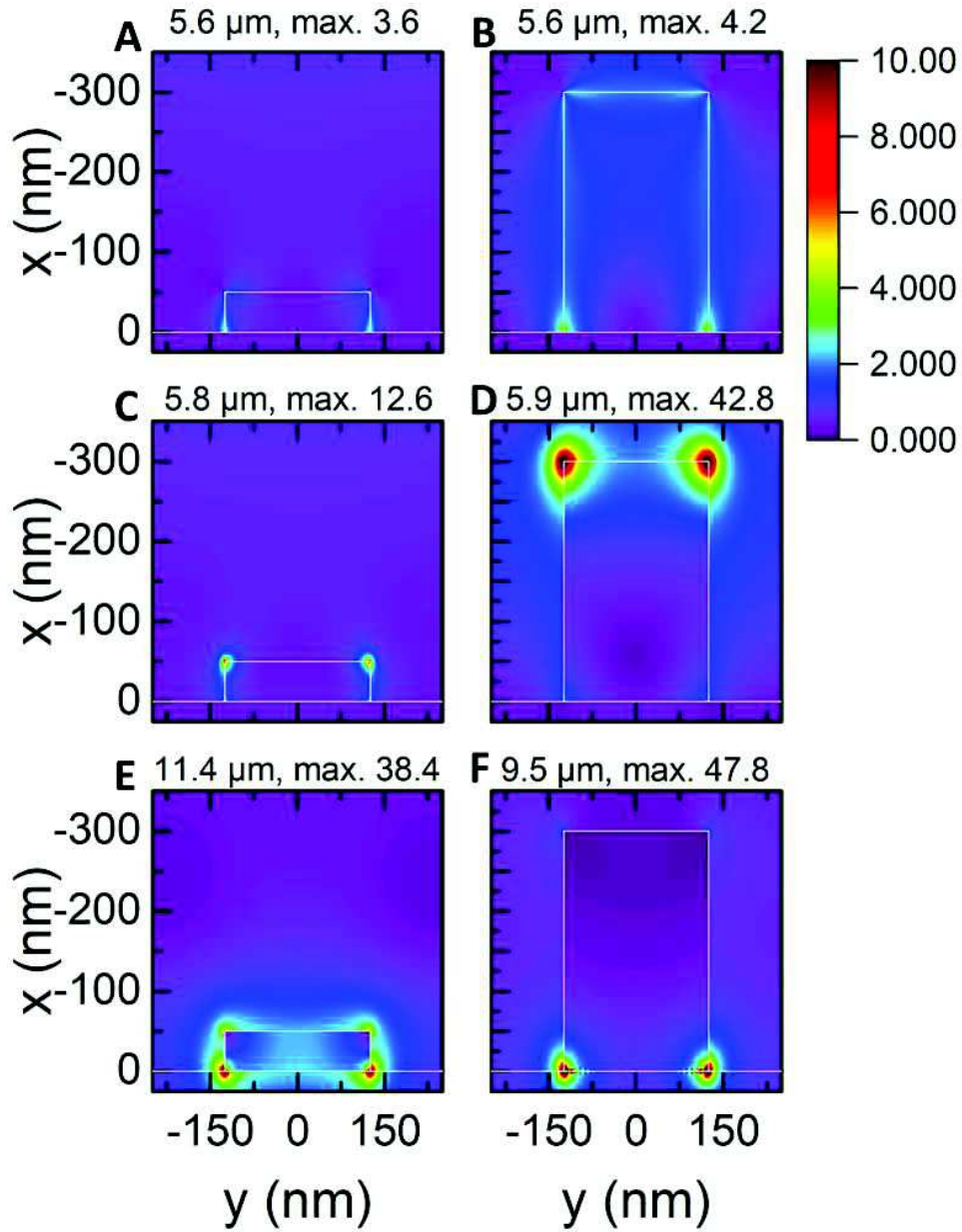


Figure 4.4.: Electric field profiles at the spectral positions of the resonances extracted from Figure 4.3C, for a 50 nm thick grating (left) and a 300 nm thick grating (right). A. and B. Fabry-Perot like mode. C. and D. LSP at the air-InAsSb interface. E. and F. LSP at the substrate-InAsSb interface. The interfaces of the grating are delimited by the white lines. The wavelength and the maximum electric field value are indicated for each profile.

Figure 4.5 displays the resonance position for various sets of geometric parameters and resumes the described observations of red-shifting LSPR for increasing ribbon width and also red-shifting LSPR for thin ribbons where an interaction with the mode confined at the interface with the air can arise. By the simple choice of a set nanoribbon width and thickness, several resonance wavelengths can be reached. It is hence possible to tailor an adapted grating structure when a plasmonic spectral signature at a targeted wavelength is required.

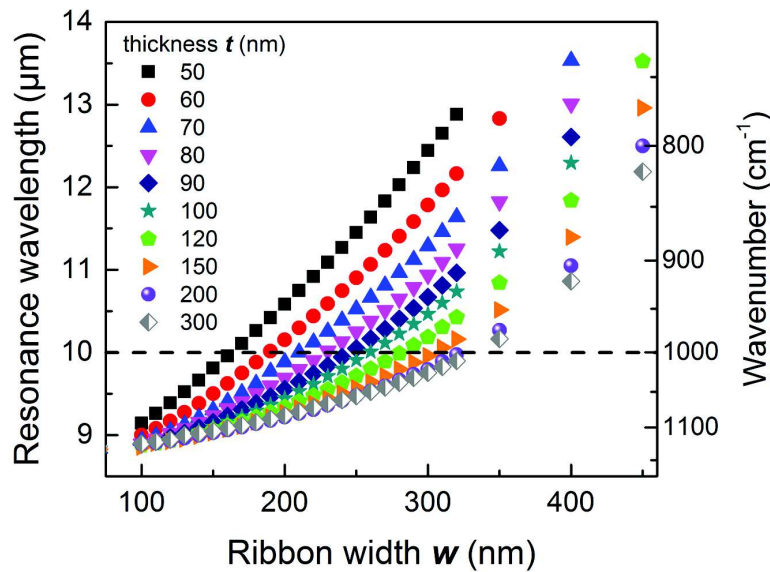


Figure 4.5.: Resonance maximum as a function of the geometric parameters ribbon thickness  $t$  and width  $w$ . The pitch is 500 nm. Choosing an adapted set of parameters  $(t, w)$ , various wavelengths throughout the mid-IR spectral range can be reached.

Next, the influence of the periodicity on the resonance wavelength is studied. For simplicity, the other parameters will be kept constant. Figure 4.6A shows the reflectance spectra of a 100 nm thick and 260 nm large ribbon with varying periodicity as indicated. For the smallest investigated periodicity of 300 nm, both LSPR,  $\omega_{\text{top}}$  and  $\omega_{\text{bottom}}$ , are considerably red-shifted. The gap between two ribbons is only 40 nm wide so that near field interactions across the gap take place. The interaction can be illustrated by two electric dipoles oscillating in phase. The resulting force on the oscillating charges is reduced, because the field created by the charge distribution in the neighboring ribbon is antiparallel to the electromagnetic force generated by the incident light. This lower driving force on the electron plasma translates into a reduced LSPR frequency [RHL<sup>+</sup>03, SWZ<sup>+</sup>03, NOP<sup>+</sup>04, LWC<sup>+</sup>12]. Increasing the gap size, the interaction and hence the red-shift decreases until saturation where impacts of neighboring ribbons on each other vanish, as shown in Figure 4.6B. Furthermore, increasing the periodicity, the overall reflectance intensity decreases since the size of the resonator stays the same but the unit cell size increases.



#### 4. Simulation of a 1D Periodic Grating Structure and Parameter Optimization

Effectively, there is less material that scatters light at the LSPR wavelength. Densification of the nanoribbons is hence of interest to obtain strong reflectance signals.

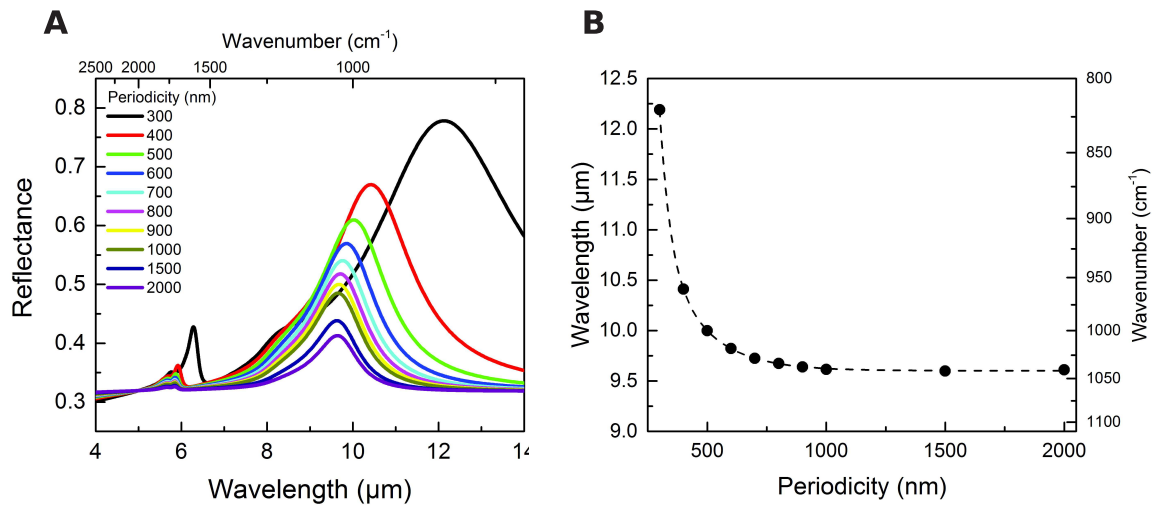


Figure 4.6.: A. Reflectance spectra of a grating with 100 nm thick and 260 nm large ribbons for varying periodicity. B. LSPR wavelength extracted from panel A for the low energy resonance  $\omega_{\text{bottom}}$ . A constant LSPR wavelength is reached when the LSPR in neighboring ribbons do not interact due to large separations.

### 4.3. Optimization for sensing around 10 $\mu\text{m}$

In the previous section, it was shown that by choosing a set of geometric parameters, it is possible to reach a LSPR wavelength between approximately 9 to 14  $\mu\text{m}$ , in the mid-IR spectral range, for a given material composition. To go further, it is of interest to know which one of these structures displaying their far field LSPR maximum at the wavelength  $\lambda_1$ , generates the maximum electric field enhancement. The objective of the next section is to determine if an optimized structure exists, exemplary at the target wavelength 10  $\mu\text{m}$ . LSPRs at 10  $\mu\text{m}$  can reasonably be reached with gratings fabricated from highly doped InAsSb. Also, this wavelength is at the center of the spectral region of the characteristic molecular fingerprint vibrations (1500 - 500  $\text{cm}^{-1}$ ) [CG02], so that it can be necessary to have resonant nanostructures for SEIRA at these wavelengths to detect molecules by their characteristic spectra<sup>2</sup>.

In order to evaluate the field enhancement compared to the incident electric field strength, the norm of the electric field  $|\mathbf{E}|$  was measured within a square with 50 nm side width centered at the ribbon's corner close to the substrate, where the field hotspot is located, and averaged over this investigated zone. The averaging attenuates effects originating from singularities generated by the FDTD simulation at the material interfaces. Figure 4.7A displays the averaged electric

<sup>2</sup>. Some examples of characteristic molecular vibrational spectra are shown in chapter 8, for the substances that were used in sensing experiments.

field around the hotspots extracted from the field profiles at  $10\mu\text{m}$  as a function of the variable geometric parameters ribbon width and thickness. We especially investigate the structures with far field reflectance maxima at  $10\mu\text{m}$ , marked by the black line in Figure 4.7A. They are a priori best candidates due to their resonant nature at the targeted wavelength, if the shift between the far field maximum and the near field maximum is neglected [VHN<sup>+</sup>14, ZN11]. More precisely, the shift between the near field and far field maximum is determined by the damping of an oscillator:  $\omega_{\text{near field}} = \sqrt{\omega_0^2 - \frac{\beta^2}{2}}$ , where  $\omega_0$  is the natural frequency of the oscillator and  $\beta$  the damping [ZN11]. As the intrinsic damping parameter  $\gamma$  for InAsSb is relatively low, it is reasonable to neglect the shift.

Indeed, the structures with far field maxima at  $10\mu\text{m}$  are in the center of the red zone in Figure 4.7A, where highest field enhancement at  $10\mu\text{m}$  is achieved. In Figure 4.7B, the field enhancement of only the resonant structures is extracted and displayed with higher resolution. We will designate the resonant structures in the following by their ribbon thickness indicating the related width to obtain a resonance maximum at  $10\mu\text{m}$  in table C.1 in the appendix. Indeed, the thinnest nanostructures reach relatively low field values, but from approximately 100 nm ribbon thickness upwards, the field strength is only slowly growing with ribbon size. It should nevertheless be kept in mind that thick gratings are difficult to fabricate, especially when it is needed to etch small apertures into a thick layer, as will be detailed in chapter 6. From a technological point of view, a grating thickness of around 100 nm seems favorable notably as the increase in field strength for thicker gratings is weak and might even not be completely reached because of deviations between the physically realizable structure and the simulation.

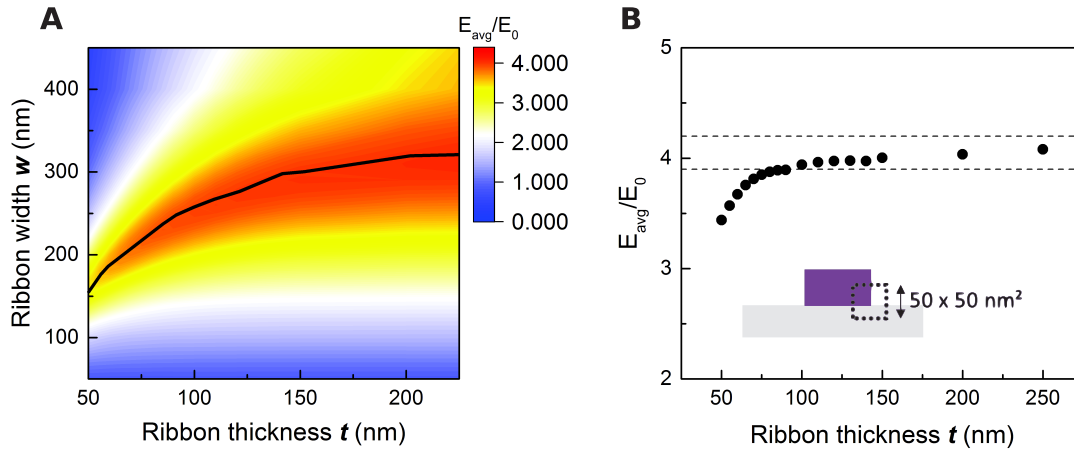


Figure 4.7.: A. Averaged electric field in a zone of  $50 \times 50 \text{ nm}^2$  around the ribbon corner for various parameter combinations ribbon thickness and width ( $t$ ,  $w$ ). The black line indicates the structures displaying a far field reflectance maximum at  $10\mu\text{m}$ . B. Detailed evaluation of the resonant structures at  $10\mu\text{m}$ . The inset schematizes in which zone the averaged field value was calculated.



#### 4.4. Modeling a refractive index sensing transducer

Having investigated the variability of the resonance position depending on the geometrical parameters and the associated field enhancement obtained at the exemplary wavelength of  $10\ \mu\text{m}$ , we will now model the response to a material layer covering the plasmonic resonators. This is another prerequisite to determine an ideal structure for sensing. As shown above, the electric field enhancement obtained for structures with a far field resonance at  $10\ \mu\text{m}$  is relatively stable when the resonators have a certain thickness. Two limiting cases can be pictured when modeling material layers on the resonators. In the first case, the plasmonic structure could be embedded into a halfspace of material, corresponding to a thick bulk material layer. The sensitivity of SPR sensors is defined with respect to a variation of the bulk refractive index  $n$  as indicated in chapter 2, in equation 2.4. On the other hand, biosensors are intended to measure smallest quantities of material. So, the more interesting case is the one of monolayers and thin films.

Simulations allow to estimate the impact of the layer thickness on the magnitude of the LSPR shift. The thickness dependence was evaluated for three exemplary geometries among the resonant structures, one 70 nm thick, one 100 nm thick and finally one 150 nm thick grating. The calculated reflectance curves of the 100 nm thick grating covered with different layer thicknesses of analyte material are shown in Figure 4.8A.

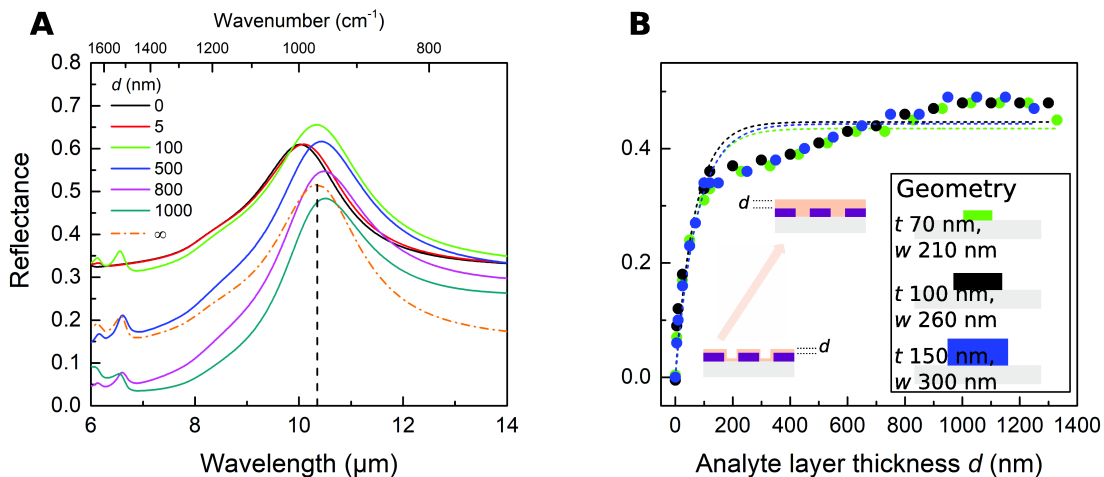


Figure 4.8.: A. Set of reflectance curves of the 100 nm thick grating covered with different layer thicknesses of analyte material. To calculate the orange dashed curve, light is incident from a constant refractive index background with  $n = 1.61$ , so that there is one interface less than in the other calculations. B. Resonance wavelength shift as a function of the analyte layer thickness, investigated for different plasmonic grating geometries, as indicated in the inset. The grating periodicity is 500 nm. The geometry of the conformal analyte layer is shown in the schematics. Dashed lines correspond to fits using equation 2.6.

The resulting resonance wavelength shift as a function of the layer thickness, for all three exemplary gratings, is displayed in Figure 4.8B. The adlayer was modeled as a conformal layer surrounding the plasmonic grating. The material of the adlayer was modeled by a constant refractive index  $n = 1.61$ , corresponding to the refractive index of octadecyl phosphonic acid (ODPA), a molecule used in surface chemistry.

In Figure 4.8B, it can be seen that the LSPR shift increases particularly strongly on deposition of nanometric layers. It increases almost linearly with the analyte layer thickness up to approximately 100 nm. Then, for thicker layers, a saturation is reached. This behavior corresponds to the description given in [JCC<sup>+</sup>98] with a linear response regime for small thicknesses and an exponential decay for thicker films. All three investigated geometries of the grating display equivalent qualitative behavior. When the analyte layer thickness exceeds the thickness of the grating, there is a discontinuity in the model which has to be considered as a modeling artefact. As illustrated in Figure 4.9, the evanescent electromagnetic wave encounters two interfaces, one between semiconductor and analyte layer and a second one between analyte layer and air, when the layer thickness  $d_1$  is smaller than the grating thickness, but only one interface when the layer thickness  $d_2$  exceeds the grating thickness. We suppose that this produces the artefact of a sudden change of the slope of the curve.

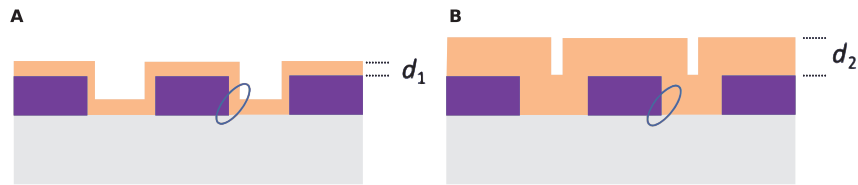


Figure 4.9.: A. Schematic of the grating structure with a conformal analyte layer of thickness  $d_1 < \text{ribbon thickness } t$ . B. Schematic in the case of an analyte layer thickness  $d_2 > t$ .

The confined electric field at the ribbon corners probes the refractive index of the medium through which it extends. In this way, the field encounters an effective refractive index, averaging over its extension, as shown in equation 2.6. A fit function according to equation 2.6 was applied to extract the bulk sensitivity  $S_{\text{RI}}$  and the decay length  $l_d$  of the electric field. Following values were obtained:

- Geometry 1:  $t = 70 \text{ nm}$ ,  $w = 210 \text{ nm}$ :  $S = 710 \pm 20 \text{ nm/RIU}$ ,  $l_d = 140 \pm 20 \text{ nm}$
- Geometry 2:  $t = 100 \text{ nm}$ ,  $w = 260 \text{ nm}$ :  $S = 730 \pm 20 \text{ nm/RIU}$ ,  $l_d = 130 \pm 20 \text{ nm}$
- Geometry 3:  $t = 150 \text{ nm}$ ,  $w = 300 \text{ nm}$ :  $S = 730 \pm 20 \text{ nm/RIU}$ ,  $l_d = 150 \pm 20 \text{ nm}$ .

Within the range of error, the results agree well for the three structures. Typical decay lengths are in the range of 25 - 50 % of the wavelength of light for the noble metal SPR systems [JCC<sup>+</sup>98]. We underline that the decay lengths found for the LSPR in the HDSC structures is only about 1 - 2 % of the mid-IR wavelength of operation. This is in accordance with the findings in chapter 3 of stronger confinement of the electric fields in highly doped InAs compared to gold.

#### 4. Simulation of a 1D Periodic Grating Structure and Parameter Optimization

However, it can be seen that the fits have some shortcomings. As explained in [JCC<sup>+</sup>98], the model relies on a linear sensor response to changes in the bulk refractive index. It should be assumed that this might not be satisfied here.

As we found a strong dependence on the layer thickness, we will in the following indicate the associated layer thickness for a sensitivity, when saturation has not yet been reached. We introduce

$$S_d^* = \frac{\Delta\lambda(d)}{\Delta n}, \quad (4.1)$$

analogously to the bulk refractive index sensitivity  $S$ .

To evaluate the bulk sensitivity of the resonant structures without need to calculate the complete sensor response curve, we evaluate in a simplified model with a homogeneous bulk medium of constant thickness of  $1 \mu\text{m}$  the thickness dependent sensitivity  $S_{1\mu\text{m}}^*$  which is in a regime where saturation is reached, so that we can approximately use  $S_{1\mu\text{m}-t}^* \approx S$ . (That is, the adlayer thickness is indeed  $1 \mu\text{m} - t$  due to the simplification applied in the model.) For all resonant structures, we find sensitivity values of  $900 \pm 20 \text{ nm}$ , with no clear trend indicating if small or large ribbons in a grating are beneficial (Figure 4.10). The variations around the mean value might stem from the evaluation of only discrete parameter sets in the model. Compared to the sensitivity obtained from the fit of the full response curve, this data evaluation yields higher values, as the chosen thickness is situated in a regime where the fit underestimates the actual values.

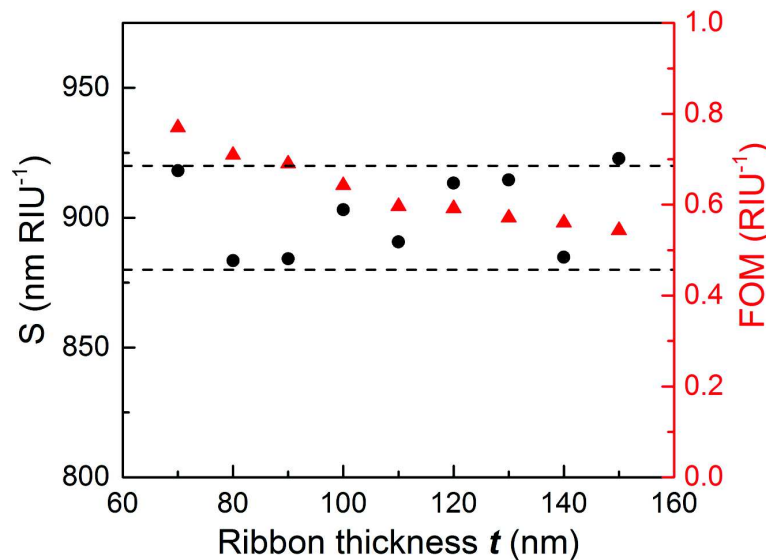


Figure 4.10.: Sensitivity  $S$  and figure of merit FOM evaluated for the structures that are resonant at  $10 \mu\text{m}$ .

As an additional parameter, the FOM as defined in equation 2.7 is evaluated. As the resonances broaden with increasing width of the grating's ribbons, the FOM decreases over the investigated range of structures (Figure 4.10). Admittedly, the need for a sharp resonance is in contrast to the requirements for SEIRA where large resonances are demanded to cover a wide spectral range. However, a narrow resonance signifies a high quality factor of the resonator and small intrinsic losses, which is the case for InAsSb plasmonics as discussed in chapter 3. It might be ideal to find a compromise for SPR and SEIRA applications combined on a same platform, with a medium FOM.

Indeed, drastically higher FOMs can be found in the literature (see section 2.4.2), especially for systems that are particularly optimized for SPR sensing exploiting extremely narrow resonances or Fano-like lineshapes. Considering the combined use as SEIRA and SPR platform, the FOM is however only one factor, while other properties should as well be considered. For SEIRA it can indeed be interesting to have some margin to cover vibrational lines within the resonance width.

## 4.5. Modeling absorption enhancement - estimating the SEIRA effect

The thickness dependence study for quantification of the SPR shift was performed using a lossless material modeled by a constant, real refractive index  $n$ . In the following, a model will be presented to evaluate the enhancement of narrow absorption features. A Lorentz-oscillator material model was assigned to the nanometric layer (typically 2 nm). It is described by the functional form:

$$\epsilon(\omega) = \epsilon_{\infty} - \frac{\epsilon_{\text{Lor}}\omega_0^2}{\omega_0^2 - 2i\delta_0\omega - \omega^2}, \quad (4.2)$$

with the high-frequency dielectric function  $\epsilon_{\infty} = 2.59$ , the Lorentz permittivity  $\epsilon_{\text{Lor}} = 0.01$ , the resonance frequency  $\omega_0 = 1.88 \times 10^{14}$  rad/s and the linewidth  $\delta_0 = 3 \times 10^{10}$  rad/s. The high-frequency dielectric function  $\epsilon_{\infty}$  is equal to the refractive index of the dispersionless material used for the SPR shift models ( $n = 1.61$ ). The resonance frequency  $\omega_0$  corresponds to a free space wavelength of  $10 \mu\text{m}$  and the linewidth  $\delta_0$  was taken as a typical value for molecular vibrations. The Lorentz permittivity  $\epsilon_{\text{Lor}}$  was chosen as fit parameter to yield a weak vibrational feature in a model of the nanometric layer on an unstructured GaSb substrate.  $\epsilon_{\text{Lor}}$  is related to the oscillator strength. In order to achieve convergence in the model with this sharp resonance, the calculation time was increased to 10000 fs. However, some oscillations around the resonance peak persist, indicating that the field has not yet completely decayed. This is a normal behavior for multi-cavities system, where the field oscillates between the cavities and decreases slowly.

Real materials are characterized by several absorption features, corresponding for example to IR-active molecular vibrations, yielding the characteristic spectrum of the molecules constituting the material. They can be modeled by a sum of Lorentz-oscillators, weighted by the oscillator strength. In this simple model, we will focus on a single absorption feature.

#### 4. Simulation of a 1D Periodic Grating Structure and Parameter Optimization

At the wavelength of the absorption feature, the imaginary part  $k$  of the refractive index displays a Lorentzian peak, as shown in Figure 4.11. This is consistently linked via the Kramers-Kronig relations to a strong variation of the real part  $n$ , which passes through a minimum and a subsequent maximum as a function of wavelength. Around absorption features, materials display anomalous dispersion, that is, an increase of the refractive index with increasing wavelength.

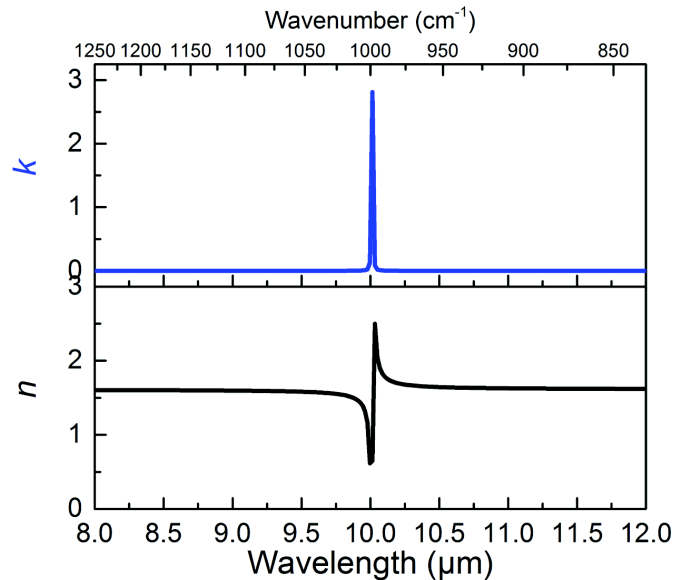


Figure 4.11.: Real and imaginary parts  $n$  and  $k$  of the refractive index used to model a material with an absorption feature at  $10 \mu\text{m}$ .

Firstly, we investigate the reflectance spectra when the thin, absorbing layer is placed onto the plasmonic resonators, with the polarization orientated perpendicular to the grating so that the LSPR can be excited. Furthermore, reflectance spectra on an uncorrugated InAsSb layer and on a GaSb substrate are calculated and compared to an analogous model but with a constant refractive index thin layer (Figure 4.12A). On uncorrugated layers (InAsSb or GaSb), the absorption feature is very weak. On the contrary, the absorption feature is clearly visible when exploiting the plasmonic effects of the nanostructure. To quantify the signal enhancement of the absorption feature, the ratio of the reflectance curve with absorbing layer and the reflectance curve with a constant refractive index layer is calculated. The LSPR shift induced by the refractive index modification is hereby considered, so that the data treatment only extracts the vibrational signal. This data treatment procedure is adapted from experimental data evaluation similar to the literature [HNV<sup>+</sup>14], where however a data adjustment of the reflectance curve excluding the vibrational features is taken to remove the (plasmonic) background, as it is not realistic to have a material with the same refractive index but without absorption features as reference. Using the reflectance spectrum calculated with a constant refractive index layer has the same effect as using the smoothed plasmonic background as correction curve. The extracted signal strength

on the GaSb substrate and the 100 nm thick InAsSb layer on GaSb substrate is less than 1%, as indicated in Figure 4.12B. In contrast, we find a signal strength of 9.3% on the plasmonic grating. A more than 30-fold increase of the signal strength is achieved.

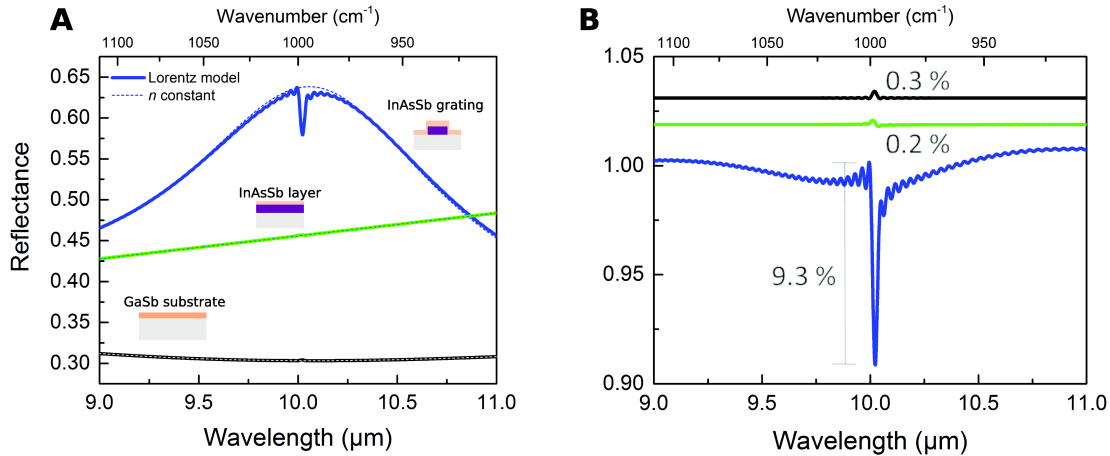


Figure 4.12.: A. Reflectance spectra in a reduced spectral range of a plasmonic grating (blue curve), a 100 nm thick uncorrugated InAsSb layer (green curve) and a GaSb substrate (black curve) coated with a 2 nm thin layer displaying an absorption feature at 10  $\mu\text{m}$ . The dashed lines indicate the reflectance of the respective structure coated with a non-absorbing layer. B. Extracted vibrational signals from A.

The interaction between a large and a narrow resonance leads to a Fano-type interaction [Fan61], which becomes manifest by the line shape of the resonance. Depending on the phase relation between the large and the narrow resonator, a narrow vibrational line appears as a zig-zag, a dip, or a maximum superposed on the plasmonic resonance. When we use the same material model, but on differently large ribbons, we observe these line shapes (Figure 4.13A). We furthermore evaluate that the absorption feature is most enhanced ( $\geq 9\%$ ) for resonators with 220 nm to 280 nm ribbon width (Figure 4.13B), signal strengths being indicated next to each signal. When the absorption feature is rather off-resonance, it is less enhanced. In Figure 4.13C, the signal enhancement is indicated as a function of the ribbon width. From literature it can be deduced that often a slight detuning of the vibrational feature towards higher wavelength than the plasmonic resonance maximum is beneficial [VHN<sup>+</sup>14]. This can be explained by the near field maximum, essential for the surface enhancement, which is slightly red-shifted from the far field maximum. Therefore, gratings with ribbon widths yielding a far field resonance at wavelengths shortly below 10  $\mu\text{m}$  might be most efficient, for example the grating with 220 nm large ribbons. To account for the drop in vibrational signal enhancement for the 240 nm large ribbons, two effects may be considered. First, this drop might be due to a numerical artifact arising from the superposed oscillations which complicate the extraction of the peak-to-peak distance of the vibrational feature. Second, it would be of interest to investigate how the scattering rate and the absorption rate evolve with the ribbon width. This would allow to situate the plasmonic

#### 4. Simulation of a 1D Periodic Grating Structure and Parameter Optimization

«oscillators» on the coupling curve shown in Figure 2.9C. The reduced signal contrast for the 240 nm large ribbon could for example arise from an unfavorable placement on the coupling curve.

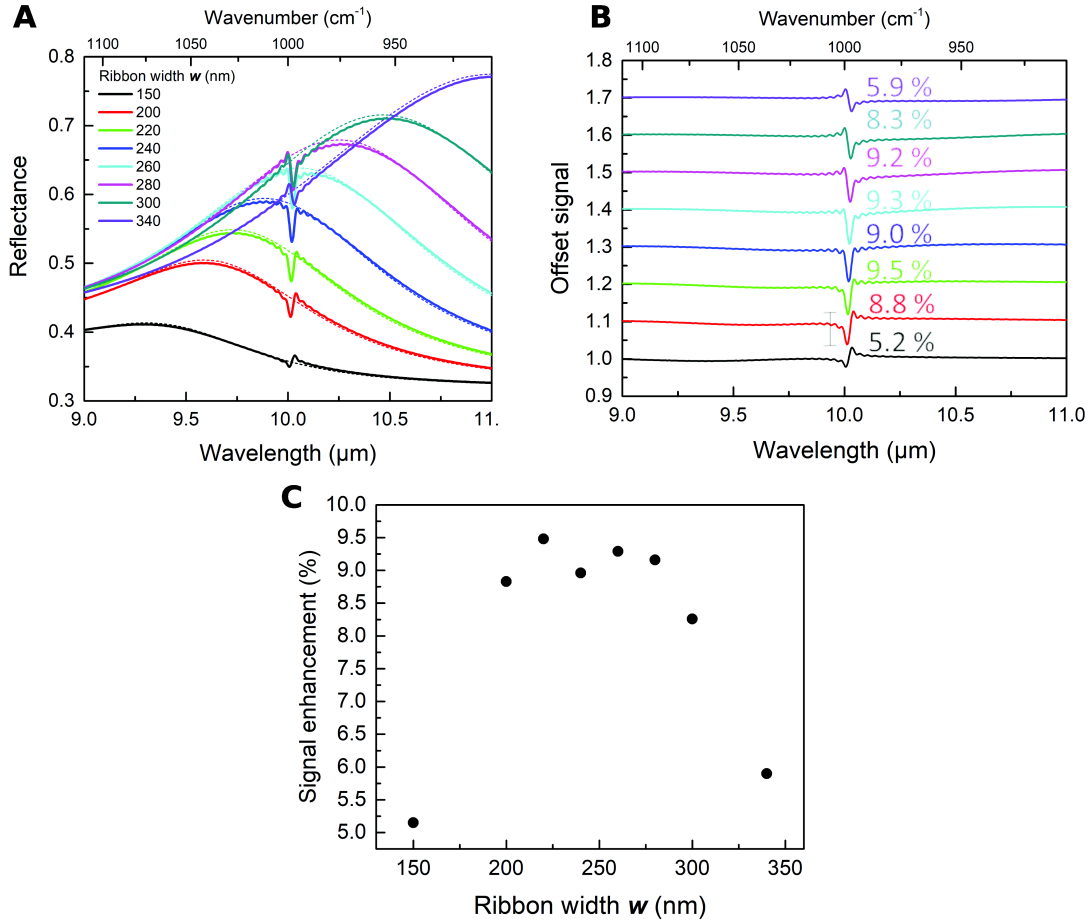


Figure 4.13.: A. Reflectance spectra in a reduced spectral range of plasmonic gratings with different ribbon width coated with a 2 nm thin layer displaying an absorption feature at  $10 \mu\text{m}$ . Thin, dashed lines are analogous simulations of the grating coated with a 2 nm thin, non-absorbing layer. B. Extracted vibrational signals from A. C. Signal enhancement as a function of the ribbon width.

Furthermore, using the extracted signal strengths, the SEIRA enhancement factor (equation 2.10) can be evaluated. The vibrational signal on the uncorrugated InAsSb layer is taken as reference signal:  $I_0 = 0.2\%$ . To estimate the active surface per unit length, the calculated field profile shown in Figure 3.8 can be employed. The unit cell is 500 nm large and we assume that the electric field is enhanced within a range of 10 nm to both sides of the ribbon. Per unit length, this yields a ratio  $\frac{A_0}{A_{\text{SEIRA}}} = \frac{500}{2 \cdot 10} = 25$ . Table 4.1 summarizes the obtained enhancement factors for each ribbon width. Values up to  $\approx 1200$  are reached which is in the range of state-of-the-art



Ribbon width /nm	Signal increase factor $I/I_0$	Enhancement factor
150	26	650
200	44	1100
220	47.5	1188
240	45	1125
260	46.5	1163
280	46	1150
300	41.5	1038
340	29.5	738

Table 4.1.: Signal increase factors and enhancement factors for differently large ribbons

values but rather in the lower regime possibly due to the simplicity of the structure which does not exploit any particular off-resonant effects such as the lightning rod effect.

## 4.6. Summary

In this chapter, a FDTD model was presented which was applied to perform a numerical study on one-dimensional periodic gratings. Notably, the impact of the geometric parameters on the optical response, on the achieved electric field enhancement and on the performance for SPR sensing and SEIRA was studied. The choice of the geometric parameters is an appropriate way to target diverse resonance wavelengths throughout the mid-IR spectral range. A grating with large ribbons displays its resonances red-shifted compared to gratings with narrow ribbons. A red-shift of the principal LSPR is also observed for thin gratings where the low energy LSPR peak is repelled due to interactions with the LSPR at higher energy, with its electric field hotspots localized at the surface of the grating. The periodicity of the grating impacts the spectral position of the resonances only in the case that the gap between neighboring ribbons is sufficiently small to allow interactions between them. This also red-shifts the resonances, as explained by the coupled dipole model. Besides, periodicity is important in terms of the achieved reflectance intensity. Densification is favorable to obtain high reflectance signals. With these results at hand, an optimization study for sensing at a target wavelength, exemplary  $10\ \mu\text{m}$ , was performed. In terms of the electric field enhancement at  $10\ \mu\text{m}$ , we found that it weakly increased with increasing resonator geometrical cross section. At the same time, this would imply structures that are technologically difficult to fabricate. A reasonable compromise was obtained for 100 nm thick structures. To conclude this chapter, models were presented that allow to quantify the performance for LSPR sensing and SEIRA. Based on the numerical simulations, bulk sensitivities in the range of  $900 \pm 20\ \text{nm}/\text{RIU}$  were derived and vibrational signals in the range of 9% variation in the reflectance curve, yielding enhancement factors up to  $\approx 1200$ . Whenever necessary, simulations will be found to confirm and clarify experimental results in subsequent chapters, based on the models presented here.





## 5. Simulations of 2D Periodic Nanoantenna Arrays

After the investigation of the 1D periodic grating structures in FDTD simulations, we present in the following the model applied to study the optical properties of the 2D periodic nanoantenna arrays and isolated rectangular nanoantennas. First we compare the grating with the nanoantenna array structure and highlight the differences. Then, inspired from experimental results where different lineshapes, depending on the nanoantenna size and shape were observed (see chapter 7), some elements of a study on the geometrical parameters of the rectangular nanoantennas are presented. The model detailed in the following was moreover applied to verify experimental results, which will be presented together with the measurements.

### 5.1. FDTD models for the rectangular nanoantennas

To model the rectangular nanoantennas, it is necessary to apply a 3D FDTD model instead of the simpler and faster 2D model used in the previous chapter. Apart from the additional dimension, the model was constructed similar to the 2D one.

Figure 5.1 shows the modeled unit cell. A thick GaSb substrate with refractive index  $n = 3.77$  is used, on top of which is placed the InAsSb nanoantenna, modeled with a Drude dielectric function with typical parameters  $\epsilon_\infty = 10.4$ ,  $\omega_p = \frac{1.157 \times 10^{15}}{\sqrt{\epsilon_\infty}}$  rad/s and  $\gamma = 1 \times 10^{13}$  rad/s. A broadband source with a bandwidth of 1-25  $\mu\text{m}$  introduces the initial electromagnetic field distribution. Reflectance and transmittance monitors were used like in the 2D model, here extended to planes instead of linear monitors. Due to the higher requirements in data storage for the 3D model files, it is indispensable to apply symmetry planes and to actually calculate only one fourth of the unit cell. In combination with symmetry planes, periodic boundary conditions were used, and PML boundaries perpendicular to the source injection direction. The smallest mesh refinement cell size is 5 nm due to limitations concerning the file size. Analogously to the 2D model, a TFSF variant of the 3D model was established to simulate isolated nanoantennas.

### 5.2. Comparison of the 2D and the 3D FDTD model

To begin with, a grating structure was simulated using the 3D model to verify if it yields the same results as the simpler 2D model. This constitutes an additional proof besides the convergence check. Figure 5.2 shows the optical spectra obtained from the 2D and 3D models,

## 5. Simulations of 2D Periodic Nanoantenna Arrays

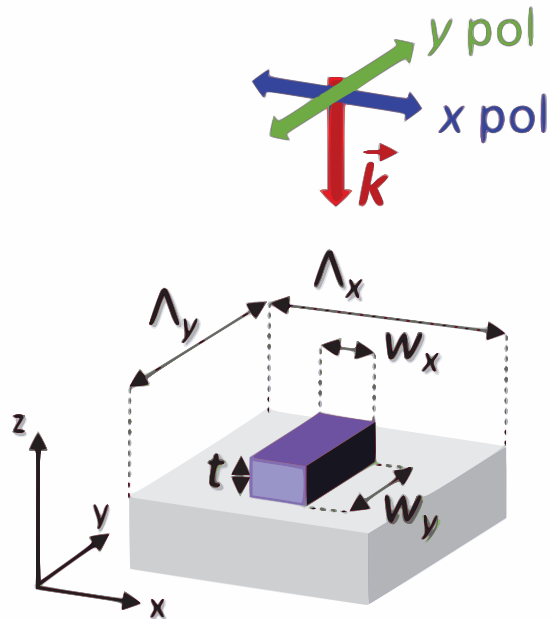


Figure 5.1.: Schematic of the modeled unit cell, indicating the geometric parameters and defining the directions of light polarization with respect to the nanoantenna orientation.

respectively, with light polarized parallel and perpendicular to the grating's ridges as indicated in the figure. Indeed, there is a small shift between the obtained resonance wavelength and a slightly lower reflectance intensity for the 3D model, while there is a good resemblance between both spectra. The deviation is most likely introduced by the lower accuracy of the mesh refinement around the resonator. The 3D model is limited to a mesh with  $dx = dy = dz = 5 \text{ nm}$ <sup>1</sup> due to the prohibitively high demand of computational resources. Precisely, the large extension of the unit cell and hence the high number of calculation nodes leads to a large amount of data stored for each model. Due to its qualitatively good agreement, the 3D model can be accepted for the following simulations.

Next, it is investigated what kind of differences are introduced in the optical spectra when adding a periodicity in the second in-plane direction. Maintaining the dimensions of the grating simulated in Figure 5.2 ( $w = 600 \text{ nm}$ ,  $t = 100 \text{ nm}$ ,  $\Lambda = 1.4 \mu\text{m}$ ), a square array with square patches of equal dimensions is compared to the grating in Figure 5.3. While the grating shows a strong polarization anisotropy, that is, LSPR excitation only under  $x$  polarization, the square array is insensitive to polarization and displays the same reflectance curve in both  $x$  and  $y$  polarization. The reflectance intensity is reduced due to a lower amount of highly reflecting metal-like material per unit cell. Moreover, and most importantly, the spectral position of the plasmon resonance shifts when the second dimension is added to the geometry. Indeed, it is not

1. At best, the  $dz$  mesh size can be slightly reduced if a very high resolution in the direction of the interfaces is imperatively needed.

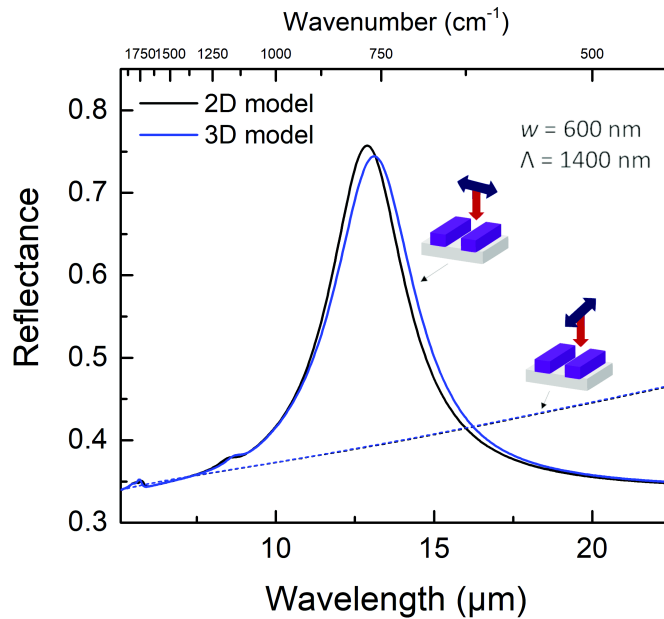


Figure 5.2.: Comparison of the reflectance spectra of a 1D periodic grating ( $\Lambda = 1.4 \mu\text{m}$ ,  $w = 600 \text{ nm}$ ) calculated using a 2D (black curve) and a 3D model (blue curve). The sketch in the inset shows the direction of the electric field vector for the corresponding spectra.

possible to reduce the square array to its 1D counterpart in order to determine the resonance wavelengths for each in plane direction independently, using the simpler and more efficient model. The spectral position of the resonance is influenced by the nanoantenna as an eigenmode of the system with its precise geometry. To study the impact of the lateral dimensions of the nanoantennas on the plasmonic resonances, a parameter variation was performed, whose results are shown in the next section.

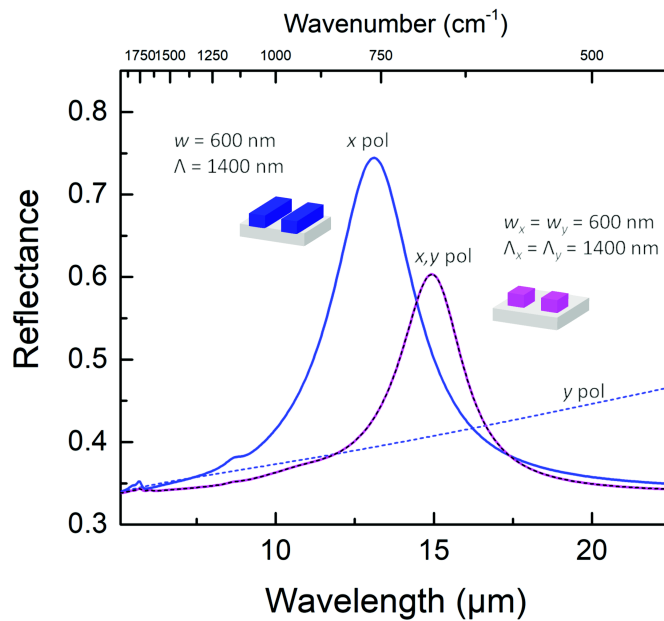


Figure 5.3.: Comparison of a 1D periodic grating ( $\Lambda = 1.4 \mu\text{m}$ ,  $t = 100 \text{ nm}$ ,  $w = 600 \text{ nm}$ ) and a square nanoantenna array ( $\Lambda_x = \Lambda_y = 1.4 \mu\text{m}$ ,  $t = 100 \text{ nm}$ ,  $w_x = w_y = 600 \text{ nm}$ ).

### 5.3. Study on the geometrical parameter of rectangular nanoantennas

Figure 5.4 shows the reflectance spectra under  $x$  and  $y$  polarization as defined above for different nanoantenna geometries on a square lattice of  $1.4 \times 1.4 \mu\text{m}^2$ . For simplicity, the square nanoantenna of  $600 \times 600 \text{ nm}^2$  is retained as reference point and additionally antennas with narrow and large  $w_y$  dimensions are shown.

Due to the rectangular shape, the spectra present a polarization anisotropy, with transverse (polarization along the short axis) and longitudinal resonances (polarization along the long axis) at distinct spectral positions. It is furthermore observed that the transverse resonance presents a marked shoulder peak, indicated by the arrows pointing to the green curve in Figure 5.4A and the dark blue curve in Figure 5.4B. Besides, a second resonance can also be seen in the longitudinal polarized spectra, especially well for the biggest resonator. Additional peaks in FDTD simulations are sometimes due to artifacts of the model. To verify that this is not the case here, an identical structure was simulated using another numerical method, namely the rigorous coupled wave analysis (RCWA)<sup>2</sup>. The spectrum is shown in the appendix D, confirming the FDTD results. It was furthermore investigated that the second resonance is not an effect of the periodicity by simulation of isolated structures, see below.

2. The RCWA calculations were performed by E. Centeno's group at the University Clermont Auvergne.

Concerning the spectral position, the longitudinal resonance shifts to longer wavelengths with increasing nanoantenna dimension  $w_y$  (Figure 5.4B), as expected, analogously to the 1D periodic gratings when the ribbon width is increased. In the transverse direction where the side length  $w_x$  is kept constant, the spectral position of the resonance shifts as well. This is in accordance with the observations of the comparison of the grating as infinitely long nanoantenna with the square antenna in Figure 5.3. With increasing dimension  $w_y$ , the transverse resonance shifts to shorter wavelength. A more detailed investigation of the dependence of the spectral position on the nanoantenna dimensions is shown below, using a simplified approach.

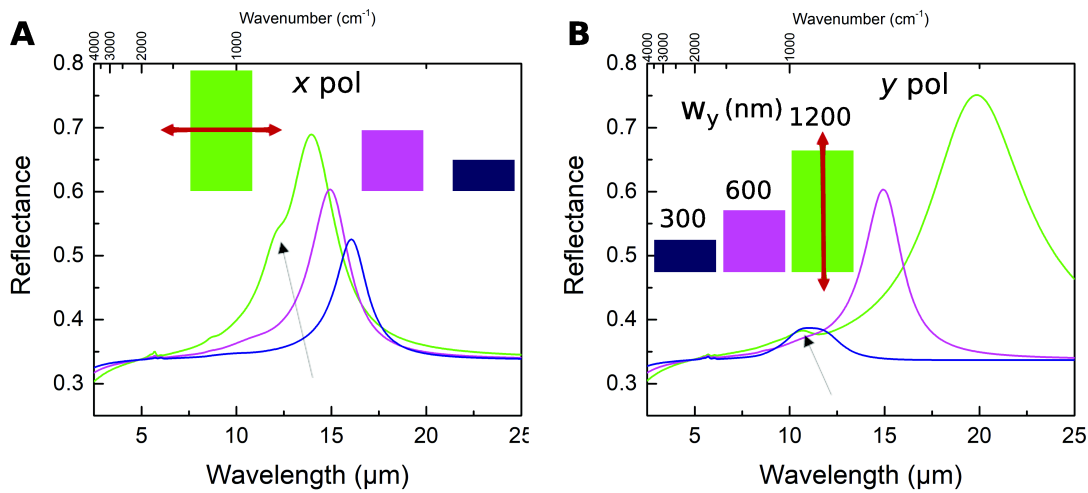


Figure 5.4.: A. Simulated reflectance spectra under  $x$  polarization for different nanoantenna dimensions  $w_x = 600$  nm,  $w_y = 300, 600, 1200$  nm as indicated in the inset, on a square array  $\Lambda_x = \Lambda_y = 1.4$   $\mu\text{m}$ . B. Simulated reflectance spectra under  $y$  polarization.

The 2D periodic grating contains many geometric parameter and moreover, when one of the antenna widths is large and approaches the size of the unit cell, interaction between nanoantennas sets on. To simplify the approach and reduce the number of parameters, an isolated rectangular nanoantenna can be studied instead of an array. Additionally, this allows to have access to the scattering and absorption cross sections separately, which can give insightful information. In Figure 5.5, the reflectance spectrum of square arrays with dimensions  $\Lambda_x = \Lambda_y = 1.4$   $\mu\text{m}$ , and side widths  $w_x$  and  $w_y$  as indicated in the figure legend are compared to the extinction cross section of isolated nanoantennas with the same side lengths  $w_{x,y}$ . For the antennas shown in Figures 5.5A and B, the line shape and spectral position of the resonances show a sufficient resemblance, but with a slightly larger resonance for the array. However, for big nanoantennas with dimensions close to the array periodicity, the resonance is shifted to higher wavelengths and broadened due to the near field interactions between nanoantennas (Figure 5.5C). For the non-interacting, smaller nanoantennas, the similarity between an array arrangement and the extinction spectrum of an isolated antenna is sufficient to retain the simpler isolated antenna model. In the case of

## 5. Simulations of 2D Periodic Nanoantenna Arrays

bigger antennas it is favorable to evaluate the single antenna spectrum to avoid the effects due to interaction. The single antenna extinction spectrum evidences furthermore the additional peaks mentioned above.

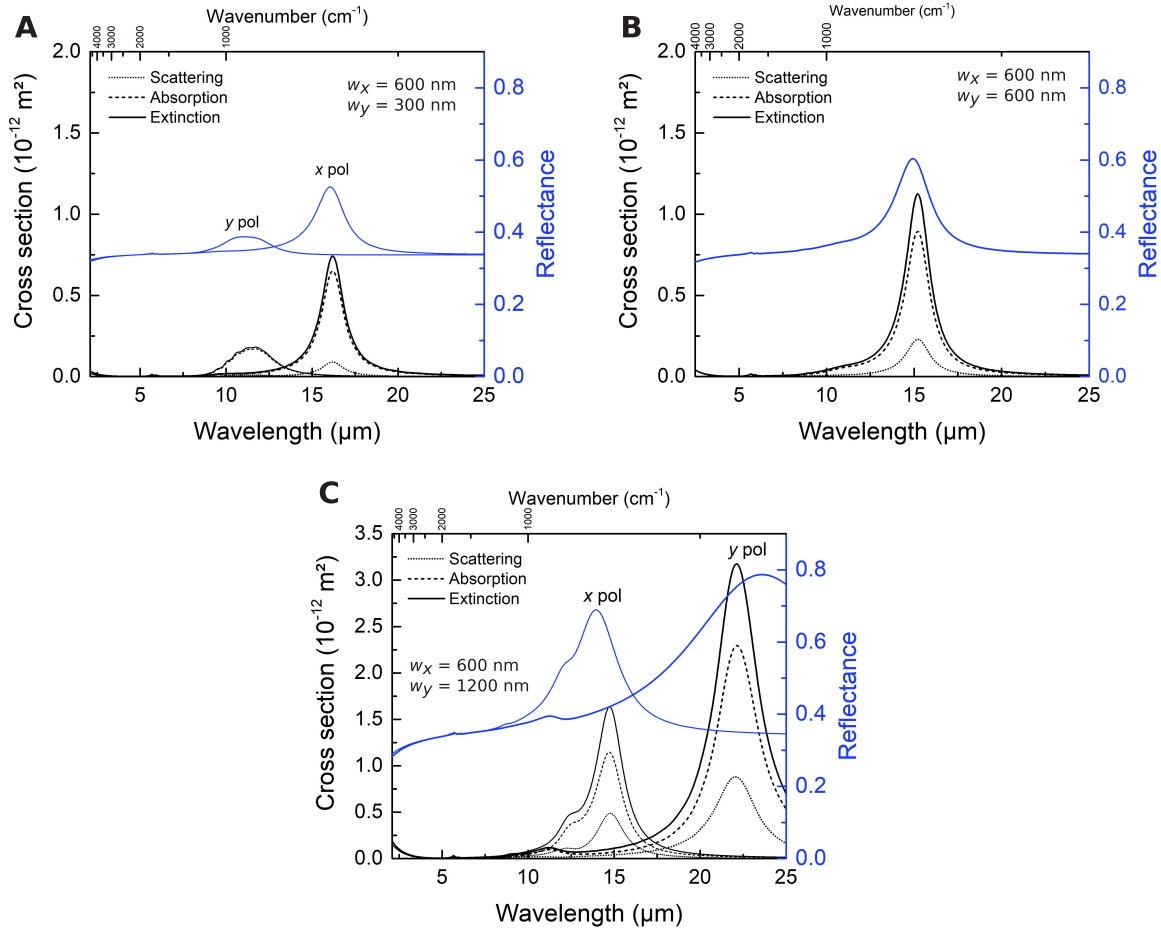


Figure 5.5.: Left  $y$  axis: Extinction, absorption and scattering cross section of an individual rectangular nanoantenna. Right  $y$  axis: Reflectance spectrum of a square array ( $\Lambda_x = \Lambda_y = 1.4 \mu\text{m}$ ) of the rectangular nanoantennas. Dimensions are A.  $w_x = 600 \text{ nm}$ ,  $w_y = 300 \text{ nm}$ , B.  $w_x = w_y = 600 \text{ nm}$ , C.  $w_x = 600 \text{ nm}$ ,  $w_y = 1200 \text{ nm}$ .

Figure 5.6 presents the resonance wavelengths of the principal (full symbols) and secondary (open symbols) resonances under  $x$  and  $y$  polarization as a function of the side length  $w_y$ , hence different nanoantenna aspect ratios. The resonance wavelength was extracted from extinction spectra of single nanoantenna. The side length  $w_x$  was kept constant at  $600 \text{ nm}$ . The spectral position of the secondary resonances have been extracted when possible but for some geometries they are very weak and not clearly identifiable, especially for small nanoantennas. A linear relationship is found between the principal resonance in  $y$  polarization and the belonging side length  $w_y$ . Under  $x$  polarization, the resonance wavelength decreases when the opposed side length  $w_y$  increases. While this effect is initially strong, that is, especially when  $w_y < w_x$ , the shift

saturates towards high  $w_y$ . The secondary resonance under  $x$  polarization contrarily increases with increasing  $w_y$ , making it more pronounced when approaching the main resonance, as shown exemplarily in the green curve in Figure 5.4A. It is easier to identify this secondary resonance when its spectral signature is superposed to the flanks of the principal resonance. Besides, the additional resonances can be observed more easily in the spectra of large nanoantennas. This might hint that these are higher order modes that enter into the spectrum when the antennas are sufficiently large to sustain them. As will be shown in chapter 7, additional resonances were also observed experimentally. While it was studied here how the resonance wavelength is influenced by the geometry of the nanoantenna for an exemplary case, it would be of interest for a more profound understanding to study the nature of the resonances.

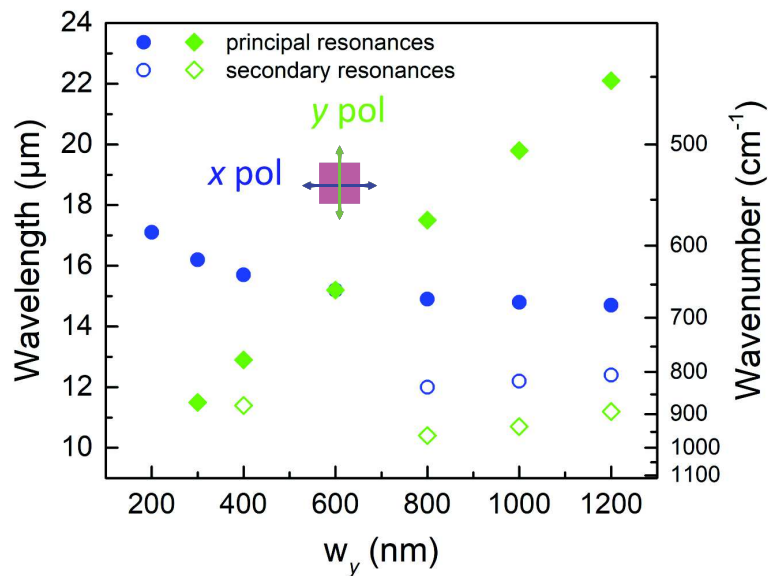


Figure 5.6.: Wavelength of the extinction maxima associated to principal and secondary resonances of rectangular nanoantennas for different geometric parameters of the nanoantenna.  $w_x = 600$  nm was taken as constant, and  $w_y$  so that the major axis is the  $x$  axis of the antenna in the left part of the figure and the  $y$  axis in the right part above 600 nm. The wavelengths of the secondary resonances could be extracted only for the largest geometries where a sufficient strength is reached.

## 5.4. Scattering and absorption of rectangular nanoantennas

Finally, it is analyzed how scattering and absorption contribute to the extinction of nanoantennas of different size. In Figure 5.7, the ratio of the scattering to the absorption cross section at the extinction maximum wavelengths is displayed. For all investigated geometries of the nanoantennas, absorption contributes significantly stronger so that the ratio of the cross sections



## 5. Simulations of 2D Periodic Nanoantenna Arrays

is inferior to 0.45. Increasing the side length  $w_y$ , the ratio increases, indicating a stronger increase of the scattering cross section compared to the absorption cross section. As can be seen from the example of spherical particles in the quasi-static approximation, the absorption cross section scales with the radius  $r^3$  whereas the scattering cross section scales with  $r^6$ . Qualitatively, also for other geometries the scattering cross section scales with a higher power of the geometrical dimensions than the absorption. Quantitatively, we do however not observe a  $w_y^3$  dependency for the ratio of the cross sections. Moreover, the ratio tends to saturate at least in the  $y$  polarized case. In general, if structures with a relatively high scattering cross section are required, larger nanoantennas tend to be beneficial. Furthermore, as the large nanoantennas sustain resonances at higher wavelengths, the operating regime is further away from the plasma frequency  $\omega_p$ , around which the extinction is dominated by absorptive losses. For comparison, gold nanoantennas operating in the IR spectral range, thus spectrally far from their plasma frequency, are often dominantly scattering because of the small penetration depth into the material. Very narrow nanoantennas can nevertheless be dominantly absorbing [NHV<sup>+</sup>15].

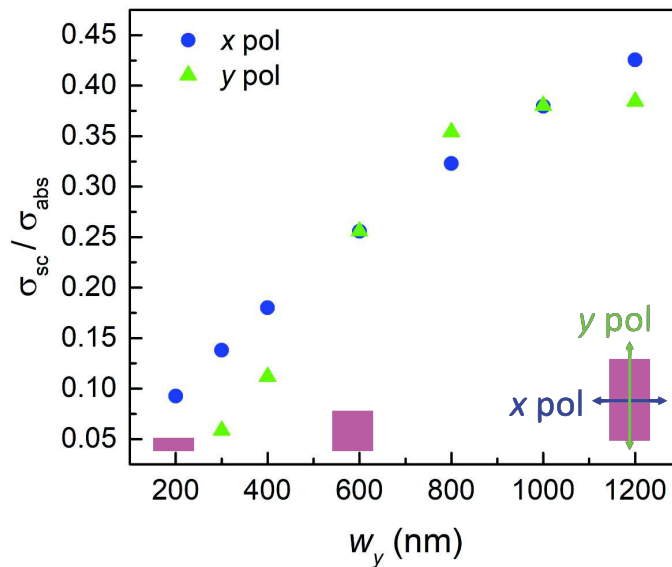


Figure 5.7.: Ratio of the scattering to the absorption cross sections for different nanoantenna geometries as indicated by the magenta symbols, for both polarization directions.

### 5.5. Summary

In this chapter, the 3D FDTD model used to simulate the optical properties of periodic nanoantenna arrays and isolated rectangular nanoantennas was presented. It was found that the optical properties of gratings and nanoantenna arrays of same geometric parameters along one

direction differ strongly so that a decoupling of the in-plane directions cannot be performed. The nanoantenna reflectance spectra feature polarization anisotropic spectra with LSPR excitation along both directions for rectangular geometries, or polarization insensitive spectra for square symmetry. Besides the principal resonances, smaller secondary resonances were evidenced which become most obvious when spectrally close to the principal resonance. This might possibly be only a question of visualization when the resonance is superposed to a sloped baseline. In general, the secondary resonances are also better observable in large nanoantenna structures due to higher oscillator strengths in the resonances. The periodic unit cell model was then reduced to a single nanoantenna to limit the number of parameters and exclude interaction effects between resonators. Analyzing the spectral position of the nanoantenna resonances, we found a linear scaling for the resonance along the antenna axis parallel to the polarization vector, and a decrease of the resonance wavelength for the polarization along the side with fixed length when the other dimension is increased. Both secondary resonances have however tendency to increase with increasing side length, so that the  $x$  polarized resonances (for variation of  $w_y$ ) spectrally approach each other for high aspect ratio nanoantennas, yielding the observed line shape with a strongly marked shoulder peak. The spectral position of the resonances as signatures of eigenmodes of the nanoantenna is influenced by both side lengths, as qualitatively described here. However, it would be of interest to better determine the nature of the resonances to give a more analytic image of the optical response. To conclude this chapter, the contributions of scattering and absorption to the optical response of the nanoantennas of different size were studied. As expected, the scattering cross section scales faster with the dimensions than the absorption cross section, but does not become the dominant contribution within the range of investigated geometries.



## 6. Technological methods for sample fabrication

In this chapter, two different approaches for the fabrication of plasmonic nanostructures made of highly doped InAsSb are presented. Their common feature is the suitability for large scale nanopatterning. The objective is to produce homogeneous patterns on large surface areas. Standard photolithography can be used to fabricate the plasmonic structures, but is limited to medium and large grating periodicities. Laser interference lithography (LIL) can go beyond these limitations and is applicable for structures with small periodicities. However, using photolithography makes it easier to control different ratios of ribbon width and periodicities, that is, grating filling factors, as they can be controlled directly by the pattern on the photolithography mask without need to modify the exposure time as it is the case for LIL.

All InAsSb layers are grown by solid source molecular beam epitaxy (MBE) in growth chambers Riber 412 or Riber Compact 21E. Te-doped, n-type GaSb substrates of crystalline orientation (1 0 0) are used. First, a non-intentionally doped GaSb buffer layer of around 200 nm thickness is grown, followed by 100 nm Si-doped, n-type InAs<sub>0.91</sub>Sb<sub>0.09</sub>. The antimony content allows lattice matching to the GaSb substrate, so that a good crystalline quality is obtained. The nanofabrication of the plasmonic structures is subsequently performed on the epitaxial InAsSb layers. In the following sections, the technological processes based on photolithography or LIL will be presented.

### 6.1. Fabrication process based on photolithography and chemical etching

Photolithography is a standard technique for device fabrication with feature sizes of several micrometers to hundreds of nanometers. The principle is to expose a photosensible polymer, a photoresist, deposited on the substrate, through a specific mask which is partly metalized and hence not transparent. The exposure with UV light alters the polymer molecules, so that they are either more or less soluble in a developer, for a positive respectively negative photoresist. More details on photolithography can be found for example in [YW05].

#### 6.1.1. Process flow

The process flow for sample fabrication consists of the following steps.

## 6. Technological methods for sample fabrication

1. Substrate preparation: The surface quality is inspected by optical microscopy and the sample is successively cleaned in acetone and isopropanol, rinsed with isopropanol and dried under nitrogen flow.
2. Photoresist deposition: A dehydration bake is performed on a hotplate at 120°C for 2 min, to evaporate liquid residues and organic pollutions. The sample is then covered with AZ MIR 701 (14 cps) photoresist, spread and spun at typically 4000 rpm for 30 s with 2 s acceleration ramp. Then, the solvent is expelled by a postbake at 90°C for 1 min 30 s.  
Pure AZ MIR 701 photoresist can be used for patterns with large pitches. With the spin parameters indicated above, an approximately 800 nm thick layer is obtained. To fabricate patterns with small pitches, diluted photoresist is preferentially used (AZ MIR 701 : AZ EBR (2 : 1)). The typical layer thickness is 380 - 400 nm.
3. Edge removal: The spin coating results in resist films with varying thickness close to the substrate edges, as can be seen from the interference fringes at these zones. For a correct exposure through the lithography mask with its grating pattern, a good contact between the mask and the substrate is needed without rough features generating air gaps of unequal thickness. At these air gaps, diffraction effects similar to Newton's rings formed around resist bumps can degrade the pattern. For this reason, the inhomogeneous resist film at the edges of the substrate is removed to leave only a smooth resist film in the center. This zone is covered by a shadow mask exposing only the edges. For the exposure, a Karl Süss MJB4 mask aligner is used. The exposure time for the flood exposure is 30 s. The resist is then removed in AZ 726 developer during 40 s.
4. Photolithography: We dispose of a mask with different grating patterns with periodicities ranging from 0.8  $\mu\text{m}$  to 12  $\mu\text{m}$  and ribbon widths ranging from 0.4  $\mu\text{m}$  to 6  $\mu\text{m}$ . The desired pattern is aligned with the resist film in the substrate center. To bring the sample and the mask in closest contact, a vacuum contact mode is applied. Then, the resist is exposed, the exposure time for different pattern types being indicated in Table 6.1. For the preparation of rectangular nanoantennas, the mask is rotated of 90° and a second exposure step is performed.
5. Resist development: First, the resist is hardened and thus made resistant to the subsequent chemical etching by a postbake at 110°C for 1 min. Then, the resist film is developed in AZ 726 developer for the time indicated in Table 6.1<sup>1</sup>.
6. Chemical etching: a solution of citric acid and hydrogen peroxide,  $\text{C}_6\text{H}_8\text{O}_7$  :  $\text{H}_2\text{O}_2$ , is highly selective between InAsSb and GaSb [DKB94]. Indeed, the kinetics for GaSb etching is so slow that the etching practically stops on arrival on the substrate. Citric acid is available in powder form. The citric acid crystals are dissolved in deionized water in a ratio of 1 g/ml to obtain a stock solution. The mixture with  $\text{H}_2\text{O}_2$  is prepared some minutes before the etching in a ratio of 2 : 1 (citric acid solution :  $\text{H}_2\text{O}_2$ ), and maintained in a

---

1. In case of ageing developer the time might need to be longer than the given values.

Pattern type	Exposure time	Development time	Etching time
Grating, large pitch (pure resist)	30 s	40 s	70 s
Grating, small pitch (pure resist)	35 s	40 s	70 - 75 s
Grating, diluted resist (2 : 1)	25 s	20 s	70 - 75 s
Crossed grating, diluted resist (2 : 1)	25 s (2×)	15-20 s	75 - 80 s

Table 6.1.: Fabrication parameters for different pattern types.

bath. After thermalization of the solution to 18 - 20°C, the sample is immersed into it and etched during the indicated time (typically 70 s - 80 s, see Table 6.1), then rinsed under deionized water and dried.

- Final cleaning: The photoresist is removed in an acetone bath followed by cleaning in isopropanol and drying.

Figure 6.1 illustrates the main steps of the process flow. Table 6.1 summarizes the fabrication parameters for different pattern types.

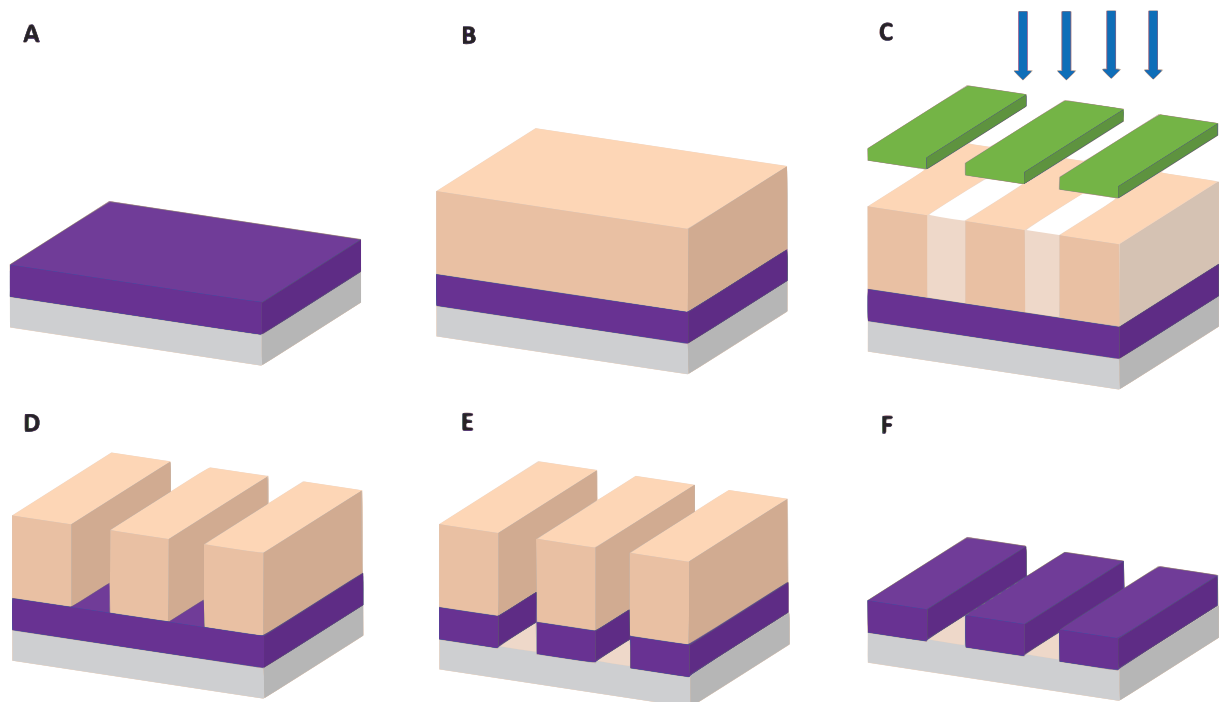


Figure 6.1.: Process flow for the sample fabrication by optical lithography and chemical etching. A. Substrate growth and preparation. B. Photoresist deposition. C. Edge removal and exposure by photolithography. D. Photoresist development. E. Chemical etching of InAsSb in citric acid :  $\text{H}_2\text{O}_2$ . F. Photoresist removal and final cleaning.

### 6.1.2. Calibration of the etching rate of InAs(Sb) using citric acid : $\text{H}_2\text{O}_2$

Selective etching of InAs against GaSb is possible using a citric acid : hydrogen peroxide ( $\text{C}_6\text{H}_8\text{O}_7 : \text{H}_2\text{O}_2$ ) solution [DKB94]. Etching proceeds through an oxidation-reduction reaction of  $\text{H}_2\text{O}_2$  with the semiconductor surface followed by a dissolution of the formed oxide by the citric acid. The process is limited by the chemical reaction rate, which means that the material removal rate depends on the rate of the chemical reaction at the surface [DKB94]. Characteristic for reaction rate limited processes is a linear proportionality of the etch depth with the etch time, a weak impact of agitation, a strong temperature dependence, a strong dependence on the relative proportions of the etch solution, and the formation of faceted surface structures during the etching [DKB94]. Most of these characteristics for the etching of InAsSb were observed.

DeSalvo *et al.* [DKB94] indicate an etching rate of  $90.5 \pm 1.7$  nm/min for InAs on GaAs substrate using a solution of  $\text{C}_6\text{H}_8\text{O}_7 : \text{H}_2\text{O}_2$  in a ratio of 2 : 1, at room temperature. Dier *et al.* [DLGA04] report an etching rate for InAs of  $92.8 \pm 2.8$  nm/min for the same ratio of the solution, at  $20^\circ\text{C}$ , and a slightly slower rate of  $88.9 \pm 3.0$  nm/min for  $\text{InAs}_{0.91}\text{Sb}_{0.09}$ . The rate for GaSb is evaluated to be  $0.84 \pm 0.04$  nm/min, yielding selectivities of 110 for InAs and 106 for InAsSb, while DeSalvo *et al.* report a selectivity of 97.6 between InAs and GaSb. The selectivity is here the ratio of the respective etching rates.

To validate the etching rate found in literature, a thick InAs layer was etched in the citric acid :  $\text{H}_2\text{O}_2$  solution. As indicated above, the etching rates of InAs and  $\text{InAs}_{0.91}\text{Sb}_{0.09}$  differ only slightly [DLGA04], so that the calibration with InAs can serve as an approximate reference for the etching of InAsSb which is used for the sample fabrication.

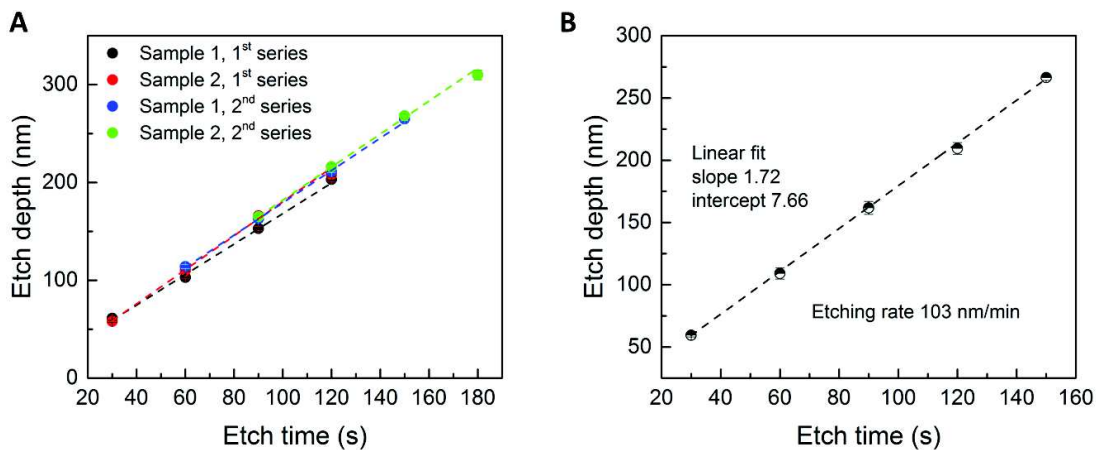


Figure 6.2.: Determination of the etch rate. A. Evaluation of individual sample series yielding the following etching rates: sample 1, 1<sup>st</sup> series:  $94 \pm 4$  nm/min, 2<sup>nd</sup> series:  $99 \pm 2$  nm/min; sample 2, 1<sup>st</sup> series:  $104 \pm 4$  nm/min, 2<sup>nd</sup> series:  $101 \pm 2$  nm/min. B. Evaluation of the averaged values, yielding an etching rate of  $103 \pm 1$  nm.

Photoresist gratings with  $2\ \mu\text{m}$  large ribbons and a periodicity of  $10\ \mu\text{m}$  were patterned onto an InAs substrate. Each patterned sample was divided into four pieces. These pieces were then etched in citric acid :  $\text{H}_2\text{O}_2$  solution for 30 - 120 s. As the temperature impacts strongly the etching rate, the recipient containing the etch solution was placed into a bath and the temperature of the acid was measured. The obtained etch depth was measured by profilometry (Veeco Dektak 150). The initially measured thickness of the photoresist was subtracted assuming that it is constant, that is, that the photoresist is inert to the citric acid solution. Then, to enlarge the range of data points, each sample was etched for additional 30 s for the pieces of the first sample respectively 60 s for the pieces of the second sample and again evaluated by profilometry. Figure 6.2A displays the individual data series, and Figure 6.2B the calculated averages. From the slope of the averaged curve, an etching rate of  $103 \pm 1\ \text{nm}/\text{min}$  is derived, which is slightly higher than what was found in the literature [DKB94, DLGA04]. The etching might be initially faster due to the possible presence of a surface oxide layer, before reaching a linear regime. This might also account for the positive intercept found in the linear fits.

Reflectance measurements using the micro-FTIR spectroscopy setup (as detailed in chapter 7) can be used to control if the etching time has been sufficient to completely open up the InAsSb layer. The evolution of the optical spectra after different etching times was investigated using a rectangular nanoantenna pattern (Figure 6.3). Measurements were performed on the same position on the sample surface under equal conditions. After each measurement, the sample was etched for additional 10 s in citric acid:  $\text{H}_2\text{O}_2$ . As the pattern was not protected by photoresist, the thickness of the pattern is also reduced, even if this is not the principal intention of the experiment.

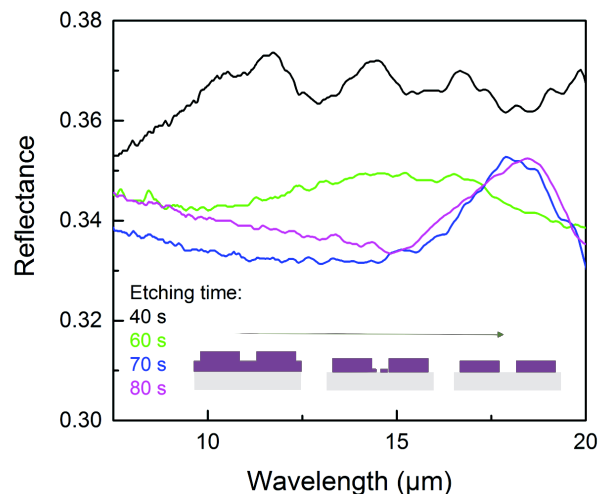


Figure 6.3.: Investigation of the reflectance spectra after the indicated etching times. A distinct LSPR is obtained for an etching time of 70 - 80 s.



## 6. Technological methods for sample fabrication

We observe that the plasmonic resonances are strongest for etching times of 70 - 80 s. For short etching times, the patterns are interconnected by the remainder of the InAsSb layer, which yields an oscillatory reflectance signal instead of a distinct LSPR. We suppose that the additional etching duration compared to the one derived from the etching rate calibration above is linked to the slightly slower rate for InAsSb compared to InAs. Moreover, it serves to clean all InAsSb residues between the patterns off the substrate so that the LSPR become sharper and stronger. Consequently, we propose to use a slightly prolonged etching time of 75-80 s for the sample processing. For patterns with small spaces between the features, the necessary etching time might also be impacted as the solution needs to penetrate into the apertures, so that the process might rather be diffusion limited.

Furthermore, we suggest performing a reflectance measurement during the sample fabrication, before removal of the lithography mask, as an additional technique to control the etch depth. The mask might introduce a slight shift due to its refractive index, and this especially for the high energy LSPR due to its presence on top of the nanostructures, like in SPR sensing experiments. The measurements allow to control if the optical spectrum resembles qualitatively the expected one, indicating that the InAsSb layer in between the patterns has completely been removed.

### 6.1.3. Results

In the following, some examples of samples fabricated by the optical lithography and chemical etching process are presented. Scanning electron microscope (SEM) images were acquired using a FEI SEM Inspect 50 or for high resolution images a Hitachi S4800 electron microscope at the Institut Européen des Membranes (IEM), Montpellier. In this chapter, the presentation is restricted to the structural characterization, the optical characterization of selected samples by FTIR spectroscopy follows in chapter 7.

Figures 6.4A-C display plasmonic gratings with periodicities ranging from 0.8 - 2  $\mu\text{m}$  in top view. Well defined ribbons are obtained. The width is reduced compared to the initially defined pattern due to lateral etching. Hence, the filling factor is smaller than the 50% on the lithography mask. Figures 6.4D-F show side views of some exemplary gratings. The verticality of the side walls is sufficient. The high-resolution image 6.4F indicates that a slight undercut profile is formed for this particular sample. In general, the etch profile depends on the crystalline orientation as discussed below.

Several 2D periodic nanoantenna arrays are shown in Figure 6.5. Figures 6.5A-D show overviews of the arrays, Figures 6.5E-H the corresponding detail views. The presented samples served to explore the feasibility of various dimensions. For the shown arrays, periodicities range from 0.4 - 6  $\mu\text{m}$ . The nanoantennas have typically rounded corners due to the proximity effects at the double lithographic exposure.

Figure 6.6A shows an image of the smallest fabricated nanoantennas. Due to the large pitch compared to the nanoantenna size and hence the low density of nanoantennas on the sample surface, the optical characterization yielded too weak signals. For this reason, it is favorable to

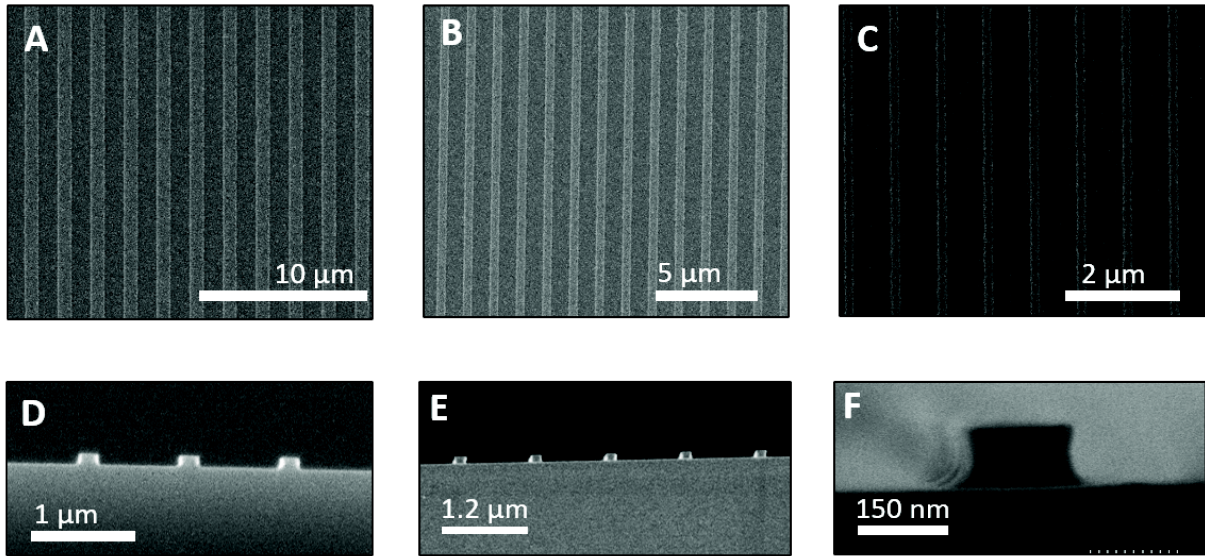


Figure 6.4.: SEM images of 1D periodic gratings fabricated by optical lithography and chemical etching. A-C: Top view. Dimensions are A.  $\Lambda = 2 \mu\text{m}$ ,  $w = 890 \pm 20 \text{ nm}$  (on mask  $w = 1 \mu\text{m}$ ); B.  $\Lambda = 1.4 \mu\text{m}$ ,  $w = 490 \pm 10 \text{ nm}$  (on mask  $w = 700 \text{ nm}$ ); C.  $\Lambda = 800 \text{ nm}$ ,  $w = 180 \pm 10 \text{ nm}$  (on mask  $w = 400 \text{ nm}$ ). D-F: Side view. Dimensions are D.  $\Lambda = 1 \mu\text{m}$ ,  $w = 200 \pm 30 \text{ nm}$  (on mask  $w = 400 \text{ nm}$ ), E. and F. (high resolution image)  $\Lambda = 1 \mu\text{m}$ ,  $w = 180 \pm 30 \text{ nm}$  (on mask  $w = 400 \text{ nm}$ ). High resolution images were acquired by D. Cot at the Institut Européen des Membranes (IEM).

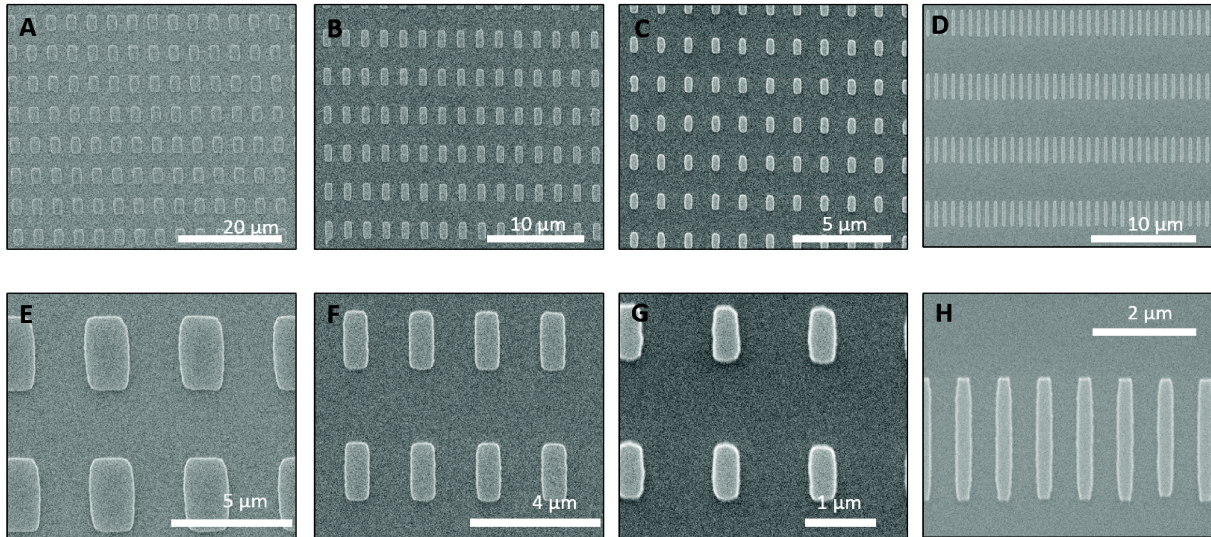


Figure 6.5.: 2D periodic nanoantenna arrays fabricated by optical lithography and chemical etching. A-D: Overview, E-H: Detail. Dimensions are A./E.  $w_x = 1900 \pm 20 \text{ nm}$ ,  $w_y = 3160 \pm 30 \text{ nm}$ ,  $\Lambda_x = 4 \mu\text{m}$ ,  $\Lambda_y = 6 \mu\text{m}$ . B./F.  $w_x = 770 \pm 10 \text{ nm}$ ,  $w_y = 1860 \pm 20 \text{ nm}$ ,  $\Lambda_x = 2 \mu\text{m}$ ,  $\Lambda_y = 4 \mu\text{m}$ . C./G.  $w_x = 850 \pm 10 \text{ nm}$ ,  $w_y = 420 \pm 10 \text{ nm}$ ,  $\Lambda_x = 0.7 \mu\text{m}$ ,  $\Lambda_y = 2 \mu\text{m}$ . D./H.  $w_x = 320 \pm 20 \text{ nm}$ ,  $w_y = 2480 \pm 20 \text{ nm}$ ,  $\Lambda_x = 0.8 \mu\text{m}$ ,  $\Lambda_y = 6 \mu\text{m}$ .



## 6. Technological methods for sample fabrication

opt for high dimensions in at least one direction, as shown exemplary in Figures 6.5D and H. A side view of the same antenna array is shown exemplary in Figures 6.6B and C. In spite of the cubic crystalline system, the lateral profiles are not the same along the orthogonal directions. Indeed, looking along the  $\langle 01-1 \rangle$  direction, a trapezoidal profile is found while the profile along the  $\langle 011 \rangle$  direction evidences straight edges with a slight undercut tendency [DKB94].

Lastly, we illustrate the effects arising from an air wedge between the mask and the sample. In Figure 6.7, several examples are shown from distorted patterns on a sample surface where Newton's rings interference fringes were strongly visible. The additional interference through the mask creates other shapes than the planned rectangles. A strong inhomogeneity on the surface of a single sample can arise and the pattern shape is not controllable.

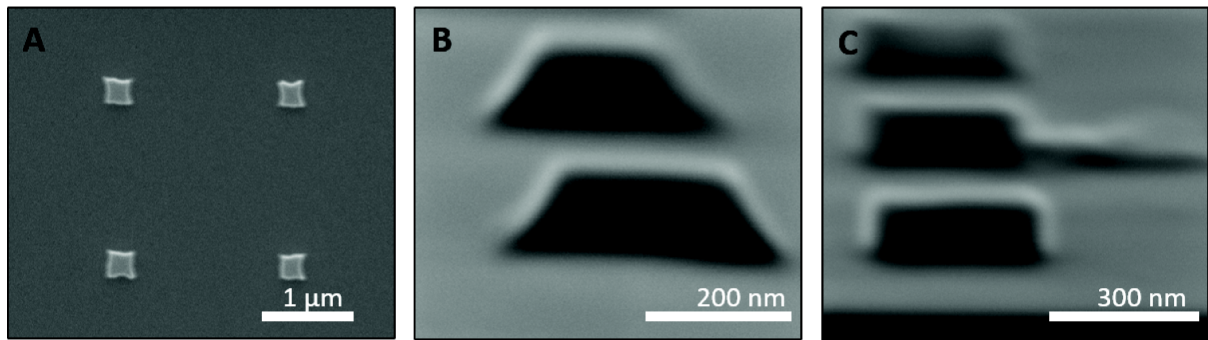


Figure 6.6.: 2D periodic nanoantenna array with dimensions  $w_x = 330 \pm 20$  nm,  $w_y = 320 \pm 20$  nm,  $\Lambda_x = \Lambda_y = 2 \mu\text{m}$ . B. and C. Side view along the  $\langle 01-1 \rangle$  direction, yielding a trapezoidal profile (B) and the  $\langle 011 \rangle$  direction, yielding a straight or slightly undercut profile (C).

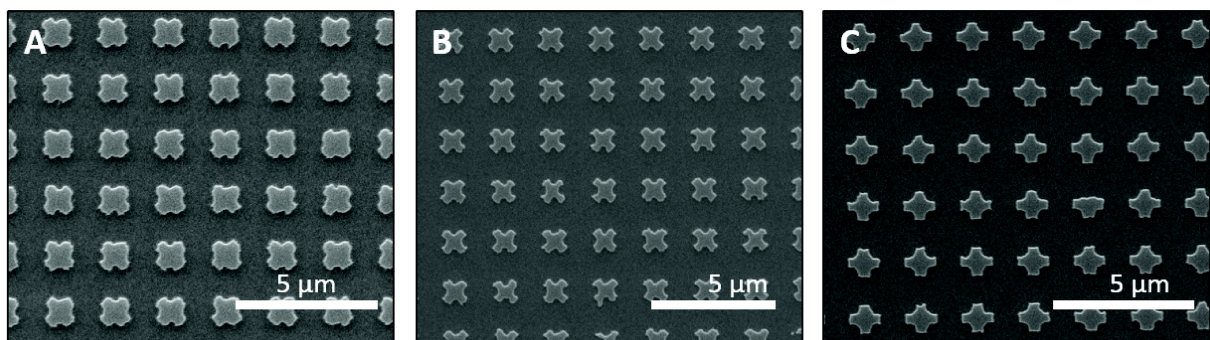


Figure 6.7.: Pattern distortion due to interferences arising from an inhomogeneous distance between the mask and the sample (Newton's rings).

## 6.2. Fabrication process based on laser interference lithography and plasma etching

### 6.2.1. Introduction to laser interference lithography

Laser interference lithography (LIL) or holography is a technique using the standing wave pattern formed by the interference of two or more coherent laser beams to expose a photoresist. It is based on the phenomenon of interference of coherent light sources described by T. Young in 1801 in his double slit experiment [BW02]. After the discovery of the laser in the 1960s, holograms began to be used for nanopatterning. LIL has many advantages compared to other nanofabrication techniques. The throughput is much higher than for serial writing techniques, it is a maskless technique preventing surface contaminations, it is applicable to large areas, it is inexpensive, and finally it allows to produce reconfigurable patterns of different periods, feature sizes and pattern shapes [SPK<sup>+</sup>14]. The bottleneck of LIL is the internal reflection in the photoresist layer, which causes undesired standing wave patterns in the vertical direction inside the photoresist layer. This can be controlled by antireflective layers below the photoresist [WAvW11].

To create the interference pattern, coherent laser light is split in two beams and recombined. This can be realized by a mirror creating a virtual image of the light source, using for example the Lloyd's or the Fresnel's mirror arrangements [BW02], shown in Figure 6.8A and B.

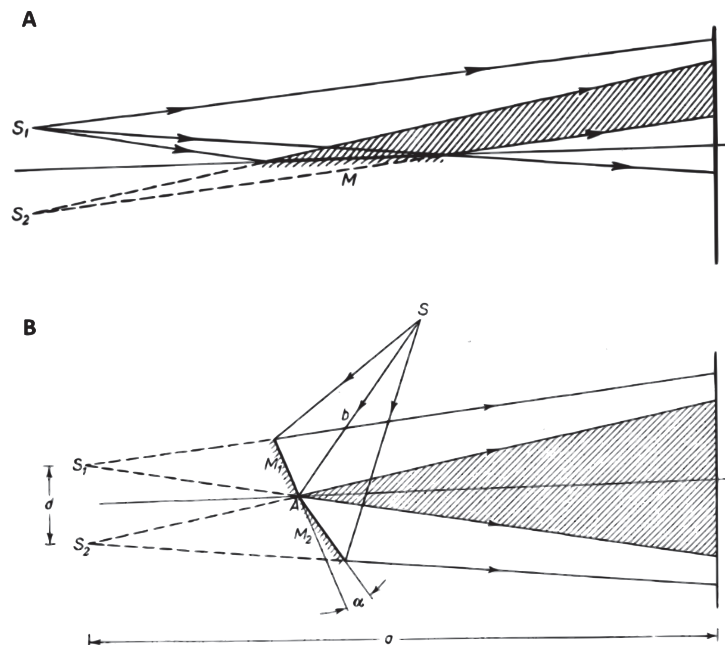


Figure 6.8.: A. Lloyd's mirror interferometer.  $S_1$  is the physical and  $S_2$  the secondary, virtual source. Virtual rays are depicted as dashed lines. B. Fresnel's mirror interferometer.  $S$  is the physical source and  $S_{1,2}$  virtual sources. Mirrors are denoted as  $M$ . Figure from [BW02].

## 6. Technological methods for sample fabrication

The Lloyd's mirror interferometer consists of a single mirror orthogonal to the sample holder placed onto a rotating stage which allows to control the incidence angle  $\Theta$  on the sample. It finds application for high resolution patterning. The Fresnel's mirror interferometer or the dual beam interferometer on the contrary can be used to expose large areas, because it produces an extended interference zone [WAvW11].

Using double exposures on a rotated sample, or the interference pattern of more than two laser beams, other periodic patterns than simple gratings can be created by LIL. Patterns fabricated by LIL find application wherever large area periodic structures are of interest, for example in 2D photonic crystals [Pro08], plasmonic nanoantenna arrays [BGN14] or Bragg gratings [Gai14].

### 6.2.2. The LIL setup

Figure 6.9 shows the optical pathway of the LIL setup available in Nanomir group at the University of Montpellier. It is based on a Lloyd's mirror interferometer. A coherent laser beam of the wavelength 405 nm with a Gaussian profile is used. A diverging beam is created by a convergent lens with a focal length of 19 mm and a pinhole with  $12.5 \mu\text{m}$  diameter placed in the beam path. After the focal point of the lens, where the pinhole is located, the beam diverges so that a sufficient beam diameter is obtained to illuminate the Lloyd's mirror interferometer. The lens and pinhole serve also for spatial filtering of the laser beam, in case of the presence of other modes than the fundamental one. A shutter in the beam path allows to control precisely the exposure time. The rotating stage can be removed from the beam path in order to control the interference pattern by two mirrors projecting an interference pattern onto a camera. The reason for this are instabilities of the laser, whose emission is not always monomode. The multimode image has a weak contrast between bright and dark interference fringes, and must be avoided for exposure.

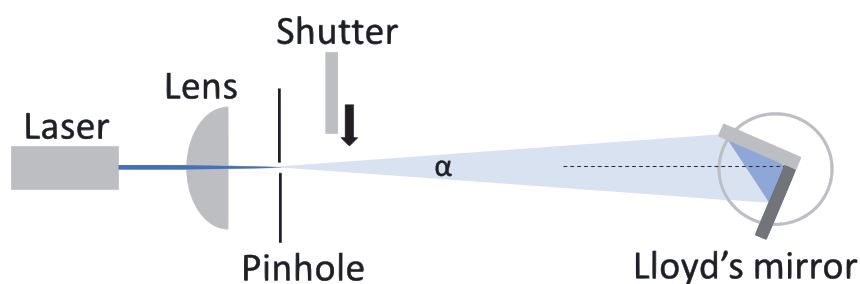


Figure 6.9.: Schema of the LIL setup. Not shown are the control mirrors (behind the Lloyd's mirror interferometer) projecting an interference pattern on a camera for the verification of the correct mode of operation of the laser.  $\alpha$  is the angle of the beam divergence.

Key parameters of LIL are the incidence angle onto the sample, the beam power, and the exposure dose [SPK<sup>+</sup>14], allowing to control periodicity and feature size.

**Incidence angle**

In Figure 6.10A, the incidence angles on the mirror and on the sample holder are indicated. For a plane wave, the rays are parallel and  $\Theta_1 = \Theta_2 =: \Theta$ .

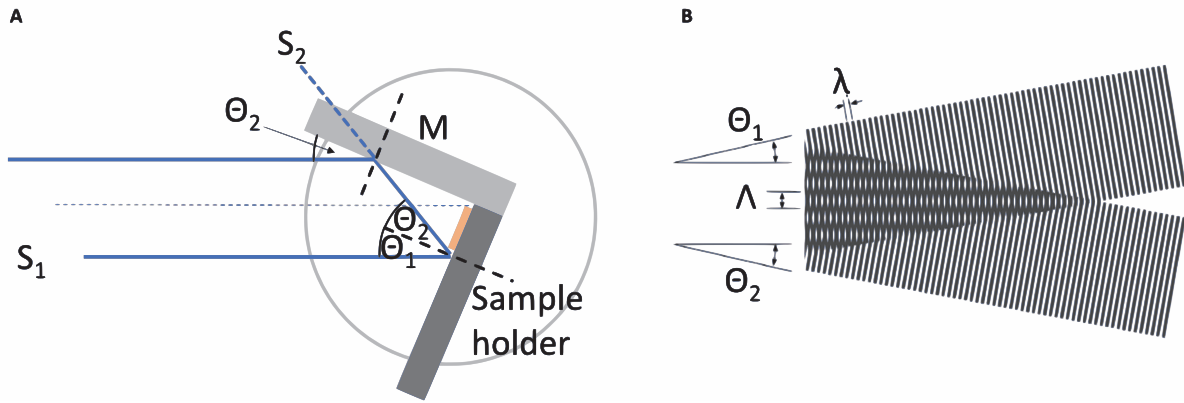


Figure 6.10.: A. Schematic of parallel incident rays on the Lloyd's mirror interferometer. The sources are labeled  $S_1$  and  $S_2$ .  $M$  denotes the mirror. B. Schematic of the interference pattern created by two coherent beams. Figure B. from [WAvW11].

The period of the interference pattern  $\Lambda$  is related to the incidence angles by the following expression, as illustrated in Figure 6.10B:

$$\Lambda = \frac{\lambda}{\sin(\Theta_1) + \sin(\Theta_2)}, \quad (6.1)$$

where  $\lambda$  is the wavelength of the laser. This simplifies in case of the plane wave to:

$$\Lambda = \frac{\lambda}{2 \sin(\Theta)}. \quad (6.2)$$

Figure 6.11 displays the graph of this expression, showing which incidence angle on the mirror is necessary to obtain the targeted periodicity. In practice, the calibration is given for the rotation angle of the goniometer serving as support for the mirror.

The divergence angle  $\alpha$  of the beam (see Figure 6.9) leads to an inequality of the angles  $\Theta_1$  and  $\Theta_2$ . Indeed, the angles are equal only at the intersection of the mirror and the sample holder. The expression of the error on the grating periodicity depending on the divergence angle  $\alpha$  can be found in [WAvW11]. In our setup, the sample must be placed close to the intersection with the mirror, because the intensity decreases fast with distance from the central axis. We will assume that at this point, the condition  $\Theta_1 = \Theta_2$  holds to a good approximation.

An estimation of the error on the grating periodicity due to deviations of the mirror or the sample holder from their mutually orthogonal position is given in reference [Gai14]. It will not be subject here as the exact value of the period for the plasmonic nanostructures is of less importance as for example for the fabrication of Bragg gratings.

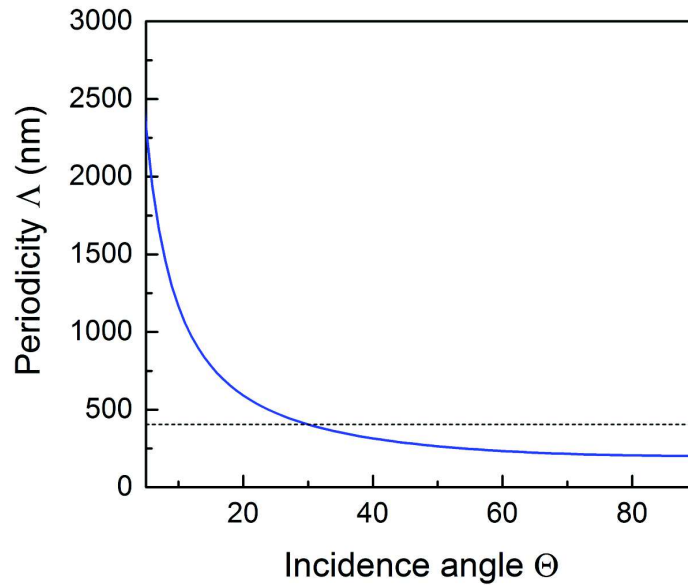


Figure 6.11.: Grating periodicity  $\Lambda$  as function of the incidence angle  $\Theta$ . The horizontal dashed line corresponds to the wavelength of the laser to show which range of incident angles is accessible.

### Beam power and effective power on the sample

The power measured in the center of the laser beam, before arrival on the Lloyd's mirror interferometer is typically  $P = 0.135 \text{ mW/cm}^2$ . The effective power received by the sample depends on the incidence angle  $\Theta$ :

$$P_{\text{eff}} = P \cos(\Theta). \quad (6.3)$$

The effective power allows to calculate the exposure time for a known exposure dose.

### Exposure dose

The exposure dose must deposit sufficient energy to transform the photoresist at the position of the bright fringes. If the deposited energy is above a certain threshold, the polymers of the positive photoresist modify their chemical structure and become soluble in the developer. As the photoresist shall not be modified at the dark fringes, it is necessary to have a strong contrast between the bright and dark fringes. The intensity in the interference pattern is given by

$$I_r = I_1 + I_2 + 2\sqrt{I_1 I_2} \cos\phi, \quad (6.4)$$

where  $\phi$  is the phase difference between the two beams. For beams with equal intensity  $I_1 = I_2 = I$  the maximal intensity is  $I_r = 4I$ , when  $\phi = 0 + 2\pi m$ ,  $m$  integer (bright fringes) and the minimal intensity is 0 for  $\phi = \pi + 2\pi m$  (dark fringes).

The manufacturer of the photoresist supplies the swing curve for the necessary exposure dose as a function of resist thicknesses in the range of  $0.8\ \mu\text{m}$  to  $1.2\ \mu\text{m}$ . Unfortunately, for thinner resist layers the necessary dose is not indicated. Using an extrapolation of the data points taken from the manufacturer's curve, we found a necessary dose of  $\approx 31\ \text{mJ}/\text{cm}^2$  for a  $400\ \text{nm}$  thick resist layer (see Figure 6.12). In [Gai14], the threshold dose for  $350\ \text{nm}$  was estimated to be  $20\ \text{mJ}/\text{cm}^2$ , which also complies with our extrapolation.

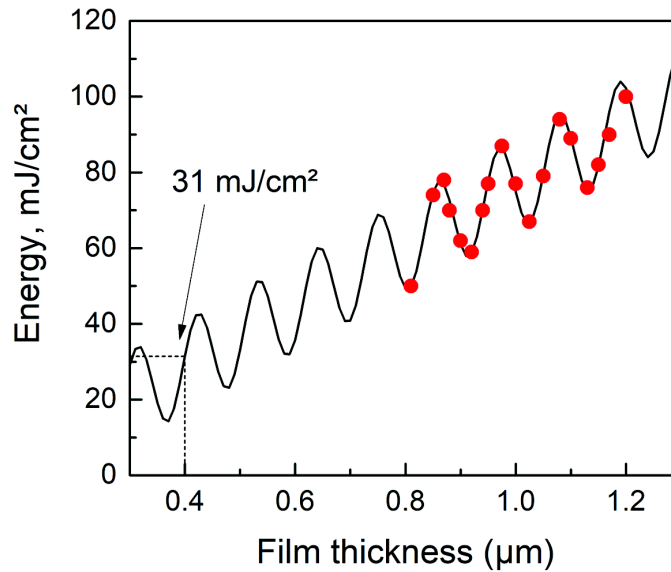


Figure 6.12.: Extrapolation of the swingcurve of AZ MIR 701 photoresist. The datapoints, taken from the resist supplier's data, from which the fit was obtained are displayed in red.

The exposure time can be estimated from the following formula:

$$W_{\text{threshold}} = 4I = 4P \cos(\Theta) t_{\text{exp}}, \quad (6.5)$$

where  $W_{\text{threshold}}$  is the threshold dose and  $t_{\text{exp}}$  the exposure time. Exposure times of around 1 min are obtained for incidence angles from  $1^\circ$  to  $20^\circ$ .

Nevertheless, due to the rough estimation of the threshold dose, exposure time tests were indispensable. Moreover, the threshold dose is reached only in the center of the bright fringes. A necessary time of 4 min was found in exposure time calibration tests, which exceeds considerably the estimated time. The risk of overexposure of the photoresist is that the pattern size is reduced [SPK<sup>+</sup>14]. A realignment of the interferometer allowed to decrease the exposure time.

#### Note on the internal reflection in the resist layer

The internal reflection on the photoresist - substrate interface can be a delicate point of LIL and is especially critical for strongly reflecting silicon or metal substrates [WAvW11]. However, as



## 6. Technological methods for sample fabrication

a SiO<sub>2</sub> layer below the photoresist is used which serves as hard mask, there is only a reduced refractive index difference between SiO<sub>2</sub> with  $n = 1.47$  at 405 nm wavelength and AZ MIR 701 with  $n = 1.70$  at 405 nm. This should reduce the effects compared to the direct contrast between the photoresist and the HDSC layer.

### Nonselective patterning

LIL is adapted for the patterning of large areas but is not selective. It is however useful to delimit the patterned zone to have an uncorrugated surface for a control of the subsequent etching by laser interference monitoring and eventually for reference measurements during the optical characterization. To selectively pattern only a part of the total sample surface, an optical lithography exposure step shielding the LIL pattern by a shadow mask can be added.

#### 6.2.3. Process flow

In the following, the process flow using LIL and plasma etching is indicated. The steps are also schematized in Figure 6.13. Several steps of the process flow are analogous to the process presented in section 6.1.1, and will only be shortly mentioned here for completeness. In this process, an additional step is the preparation of a solid mask made of SiO<sub>2</sub>. The photoresist alone seemed not adapted to obtain the favored etching profile [NG13]. Furthermore, it might melt during etching, so that wavy ribbons are produced. Also, as discussed above, it reduces the internal reflections at the photoresist - substrate interface due to a lower refractive index difference with the photoresist.

1. Substrate preparation: Cleaning with acetone and isopropanol, if applicable.
2. SiO<sub>2</sub> deposition: an environ 100 nm thick SiO<sub>2</sub> layer is prepared from precursors SiH<sub>4</sub> and N<sub>2</sub>O in an argon atmosphere using a plasma enhanced chemical vapor deposition (PECVD) chamber. The temperature of the growth chamber is 280°C. The thickness and quality of the SiO<sub>2</sub> is controlled by subsequent laser ellipsometry measurements.
3. Photoresist deposition: Diluted AZ MIR 701 (2 : 1 with AZ EBR) is spun at 4000 rpm for 30 s with 2 s acceleration ramp. To expel the solvent, a postbake is performed at 90°C for 1 min 30 s. The thin resist thickness obtained with diluted resist is needed to transfer the small patterns obtained by holography.
4. Interferential lithography: The samples are exposed in the set-up presented in section 6.2.2.
5. Definition of the patterned zone: A shadow mask is used to protect the pattern defined by LIL in the center of a sample. The unprotected photoresist is exposed by optical lithography during 30 s. The removal of the resist from the edges of the sample is useful as it will allow to use laser interference measurements on plane surfaces during the plasma etching steps.
6. Resist development: After a postbake at 110°C for 1 min, the resist is developed during 20 - 25 s using AZ 726 developer.

7. Plasma etching of the SiO<sub>2</sub>: The SiO<sub>2</sub> etching is performed in an inductively coupled plasma (ICP) reactive ion etching (RIE) reactor from Corial Plasma Processing Solutions. The standard recipe of the Centrale Technologique de Montpellier (CTM) for the etching of silicon, which is also applicable to SiO<sub>2</sub>, is used. The process gases are O<sub>2</sub> (20 sccm) and CHF<sub>3</sub> (100 sccm). The etch depth is controlled by laser interference measurements outside the patterned zone. This is necessary because the laser spot is larger than the pattern and can hence not be placed onto an opening in the photoresist mask. One complete oscillation of the laser signal corresponds to an etch depth of  $\frac{\lambda}{2n}$ , with  $\lambda$  the wavelength of the laser, here 633 nm, and  $n$  the refractive index of the material. For SiO<sub>2</sub>,  $n(633 \text{ nm}) = 1.457$  and one oscillation corresponds accordingly to 220 nm. Consequently, 100 nm correspond to slightly less than one half of the oscillation period. The signal stops oscillating when arriving on the InAsSb layer. Usual etching times are around 50 s.
8. Resist clean by oxygen plasma: The photoresist might suffer from deformations during the etching of the InAsSb in case the sample heats up. It is beneficial to clean the resist once the hard mask is defined to avoid any effect from melting photoresist. The sample is therefore exposed to an oxygen plasma using the ICP corial reactor and the standard recipe from CTM for resist cleaning. The rate being approximately 400 nm/min, we expose the sample for 1 min to remove the resist layer.
9. Plasma etching of the InAsSb: The InAsSb layer is etched using an Oxford instruments ICP-RIE reactor, which is entirely dedicated to the etching of antimonides. A chlorine plasma is used (see below for details). The ICP power is 100 W. A thermal contact between the sample and the support is provided to cool the sample to the support's temperature of 30°C. A Helium flow is introduced below the sample holder for thermalization. The laser interference signal is applied for in-situ control of the etching. Details on the recipe can be found in the following section.
10. Removal of the hard mask: The SiO<sub>2</sub> hard mask is removed using the same reactor (ICP-RIE Corial) and same recipe as already used for the definition of the mask. The etching time is 50 s.
11. Final cleaning: The processed sample is cleaned in acetone and isopropanol, particularly to remove the oil for the thermal contact from the bottom side.

#### 6.2.4. Plasma etching of InAsSb

For the small periodicities defined by LIL, we have chosen the approach of plasma etching because chemical etching reduces the lateral size of features due to its isotropy. That is, when 100 nm InAsSb are etched vertically to open up the layer until the substrate, the citric acid penetrates at the same time the lateral surfaces decreasing the initially defined pattern. Hence, wet etching is for small periodicities only applicable to thin InAsSb layers (approx. 50 nm). RIE is more anisotropic due to the bombardment with mainly vertically incident ions.

6. Technological methods for sample fabrication

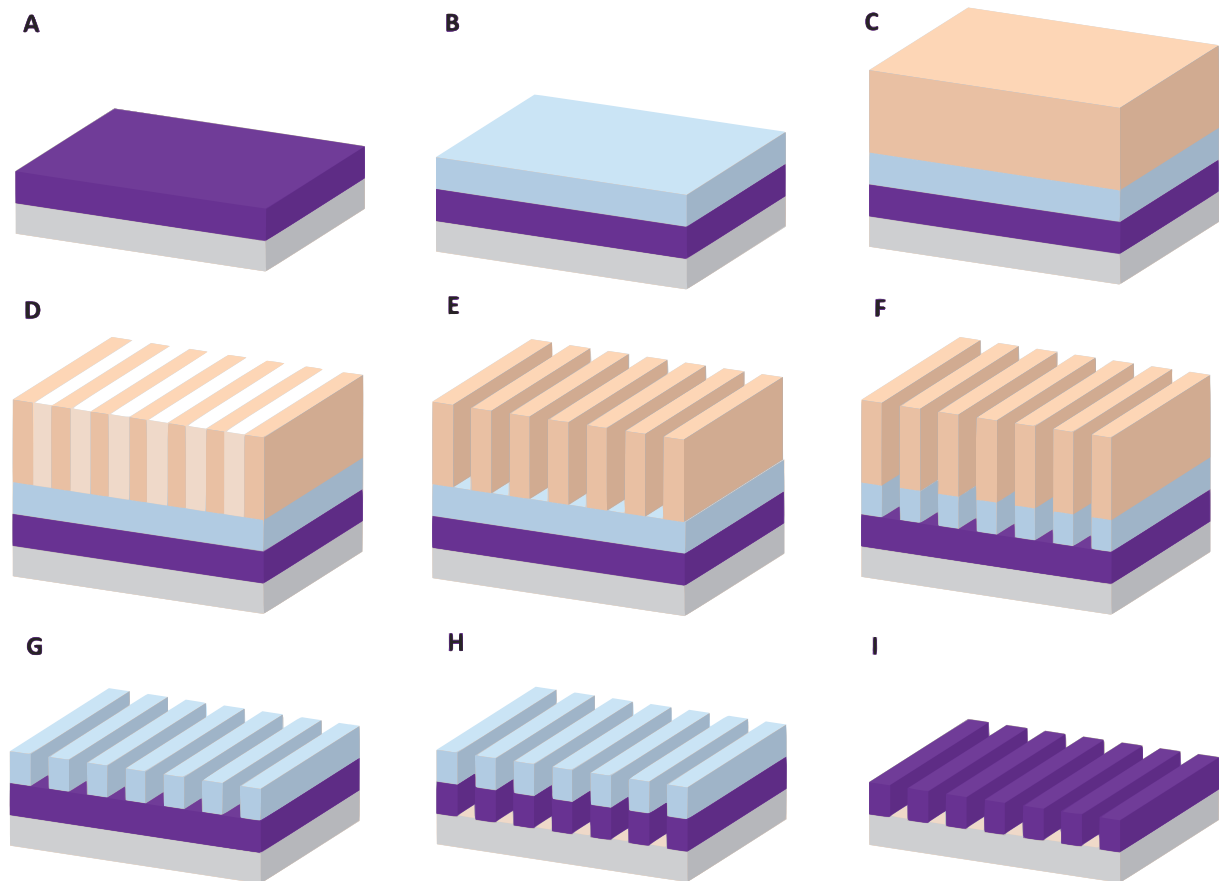


Figure 6.13.: Process flow for the sample fabrication by LIL and plasma etching. A. Substrate growth and preparation. B.  $\text{SiO}_2$  deposition by PECVD. C. Photoresist deposition. D. Exposure by LIL and definition of the patterned zone by photolithography. E. Development of the photoresist. F. Plasma etching of the  $\text{SiO}_2$  mask. G. Resist clean by oxygen plasma. H. Plasma etching of the InAsSb layer. I. Removal of the  $\text{SiO}_2$  mask by plasma etching and final cleaning.

Recipe	ICP power W	Thermal contact	Chiller °C	Helium backing	Etching rate nm/min
InAs etch	500	No	60	-	410
InAs etch 100 W	100	Yes	30	5.0 Torr	$40 \pm 10$

Table 6.2.: Recipes for plasma etching of InAs(Sb)

An Oxford Instruments ICP-RIE reactor is used. RIE uses a plasma, consisting of free electrons, ions, and reactive species to bombard the surface of a sample placed on the cathode of the system. The plasma is created by ionizing a gas mixture introduced via gas inlets into the reaction chamber. The ions are accelerated towards the sample and etch physically and also chemically, if reactive species are present, the sample's material. In an ICP-RIE reactor, the plasma is generated and confined by a radio frequency (RF) powered magnetic field using electromagnetic coils around the reaction chamber. The density of the plasma is hence increased and it is possible to separately control the ion energy by the RIE system and the ion density by the ICP generator [Ins].

The standard ICP-RIE recipe for the etching of InAs, indicated in Table 6.2, yields an etching rate of 410 nm/min and is hence too fast to obtain a controlled etching of 100 nm thin layers. In fact, the onset of the etching, at the initial plasma generation, cannot be precisely controlled.

To reduce the etching rate, the initial ICP power of 500 W was successively reduced, keeping the etching time constant at 1 min. We found that for 100 W at 1 min etching time, the InAsSb layer was not yet completely etched. The power of 100 W was consequently retained for the subsequent calibrations.

Table 6.2 compares the standard recipe for InAs with the recipe for slower etching. The process gases are the same for both recipes ( $\text{Cl}_2 : \text{CH}_4 : \text{H}_2$ ) with a flux of (5 : 5 : 7) sccm.

The etching tests were performed on epitaxially grown InAsSb layers on GaSb substrate patterned by LIL or optical lithography. Consequently, a general etch rate for InAsSb cannot be given, as, when exceeding 100 nm of etch depth, GaSb will be etched instead of InAsSb. However, we can calibrate the approximate time necessary to process our samples. An extrapolation using the data for depths below 100 nm can serve as a guiding value of the etching rate. From the acquired data, we estimate it to be approximately  $40 \pm 10$  nm/min.

Figure 6.14A displays the etch depth as a function of time. It was evaluated by profilometry and from SEM images in side view. We estimate the error of both methods to be in the range of 10 nm. The extrapolation curves using the data points associated to depths below 100 nm are also shown. Moreover, side-view SEM images of some of the samples from which the data points were obtained are shown.

Besides the calibrated etch rate, the laser interference signal retrieved from the sample surface during the processing can be used as an in-situ control of the etch depth. One oscillation of the

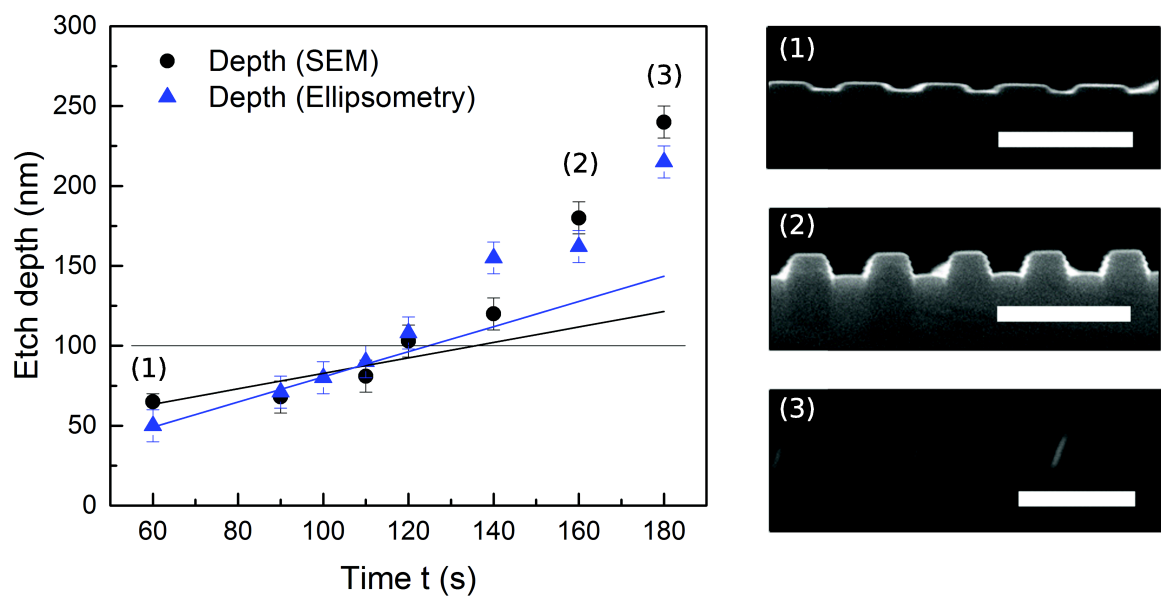


Figure 6.14.: Calibration of the etch depth using a chloride plasma. The depth was evaluated using profilometry (blue triangles) and SEM images (black dots). Solid blue and black lines correspond to linear fits of the first 4 data points (thicknesses below 100 nm). The SEM images for the indicated etching times labeled (1), (2) and (3) are shown. Scale bars are  $1\ \mu\text{m}$  in (1) and (2), and  $500\ \text{nm}$  in (3).

signal corresponds to 80 nm, for a refractive index  $n = 3.9$  for InAsSb at the laser wavelength 633 nm.

### 6.2.5. Results

In Figure 6.15, SEM images of a sample fabricated using the above described process are shown. Ribbons of homogeneous width are obtained, as displayed in the top views in Figures 6.15A and B. The side view in Figure 6.15C shows a slightly trapezoidal profile and hints furthermore that small InAsSb residues remained between the ribbons. The sample was etched for 2 min, a time that might need to be slightly increased to completely etch the InAsSb down to the substrate. Nevertheless, the optical characterization revealed the expected reflectance signal. Figure 6.16A shows the SiO<sub>2</sub> mask and Figure 6.16B the finalized InAsSb grating.

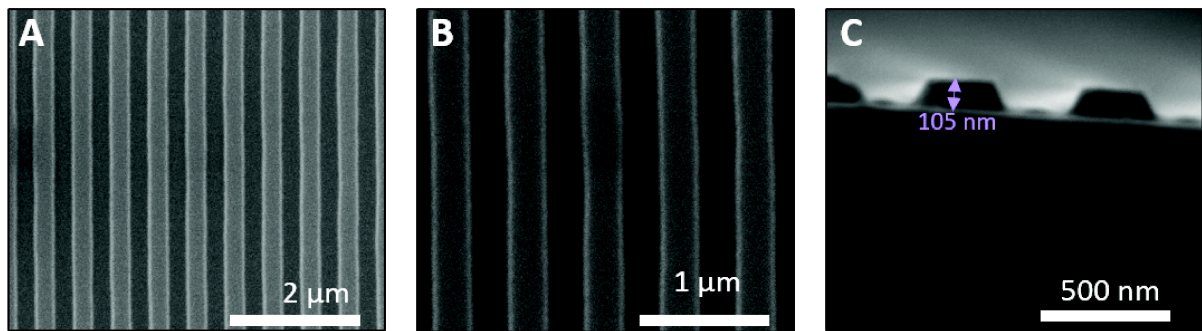


Figure 6.15.: 1D periodic gratings fabricated by LIL and plasma etching. A. Top view. Dimensions are  $\Lambda = 600 \text{ nm}$ ,  $w = 280 \pm 10 \text{ nm}$ . B. Detail of A. C. Side view, showing a slightly trapezoidal ribbon profile.

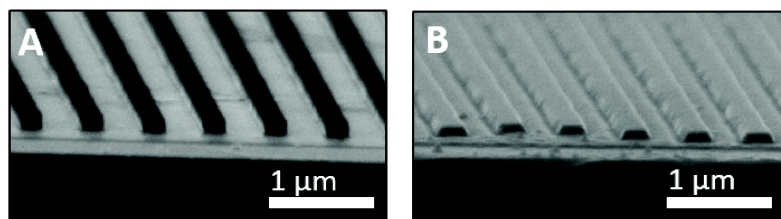


Figure 6.16.: A. Tilted view of the SiO<sub>2</sub> mask. B. Tilted view of the InAsSb grating.

### 6.2.6. Outlook on sample fabrication

While being generally a reliable and well mastered technique for large area sample patterning, instabilities of the laser provoking a multimode emission pattern limited the reproducible use of LIL with our setup.



## 6. Technological methods for sample fabrication

Several samples have been patterned by LIL using a setup based on a dual beam interferometer at the University of Technology of Troyes (UTT). This setup is advantageous to pattern larger surfaces than with the Lloyd's mirror setup. It is combined with a goniometric sample holder that allows to rotate precisely the sample for double exposures. However, if it is desired to vary the lattice parameter in subsequent exposures, a realignment of the setup is necessary. The exposure dose was varied using different exposure times. For the fabricated sample series, only the twice exposed resist spots dissolve in developer, resulting hence in a hole array. The diameter of the holes increases with exposure times until the holes merge and produce diamond shaped forms. Figure 6.17 shows some examples of fabricated samples. The InAsSb layer of is only 50 nm thick, enabling chemical wet etching also for small lattice parameters. The wet etching is also the origin for the resulting oval shaped holes due to its anisotropy for different crystalline directions. The samples are under study concerning their optical spectra. Ideally, the patterning by this LIL setup should be repeated with thicker InAsSb layers resulting in stronger optical resonances and combined with ICP-RIE.

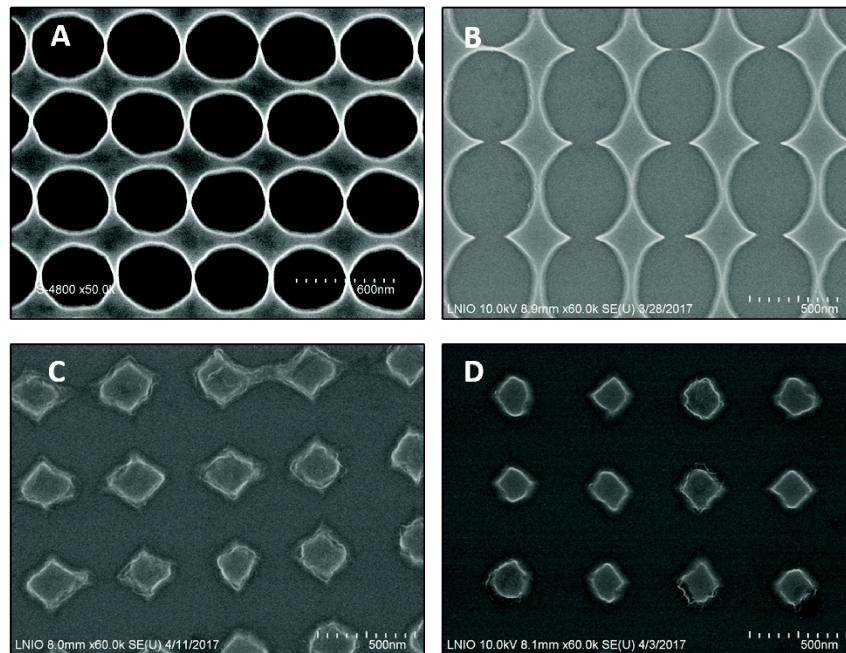


Figure 6.17.: Exemplary nanostructures fabricated by LIL using a setup based on a dual beam interferometer at the University of Technology of Troyes (UTT). The exposure time increases from A. to D. The period is constant for all samples,  $\Lambda \approx 500 \text{ nm}$ . Image A was acquired at the IEM, Montpellier by D. Cot, Images B-D were acquired at the UTT by A. Rumyantseva.

As an alternative to LIL, a technique with growing popularity can be applied, the Talbot lithography<sup>2</sup>. This technique relies on the Talbot effect, the formation of highly accurate self

<sup>2</sup>. At the Institute de l'Électronique et des Systèmes, the Talbot lithography is being developed by B. Charlot and R. Desgarceaux.

images of periodic objects at distances that are integer multiples of a fundamental unit, the Talbot distance  $Z_n = n\frac{2\Lambda^2}{\lambda}$  where  $\Lambda$  is the grating period and  $\lambda$  the wavelength of the light source. [IJC<sup>+</sup>09]. In planes at these distances, the phase shift cancels out and the diffracted waves by the periodic structure recreate its image. Using a polydimethylsiloxane (PDMS) template with a periodic pattern, this mask can be placed onto a photoresist-coated sample to transfer the periodic pattern. PDMS assures an ideal contact between the template and the photoresist layer due to its flexibility. The PDMS template itself is fabricated by LIL.

Some initial tests were performed with positive and negative photoresist, to obtain InAsSb disks or circular apertures in the InAsSb layer, as shown in the SEM images in Figure 6.18. The etching was performed using the ICP-RIE recipe as described above. While the presented structures have a relatively large array periodicity, there is potential to reduce it. In conclusion, Talbot lithography presents an appealing perspective for future fabrication of the periodic nanostructures.

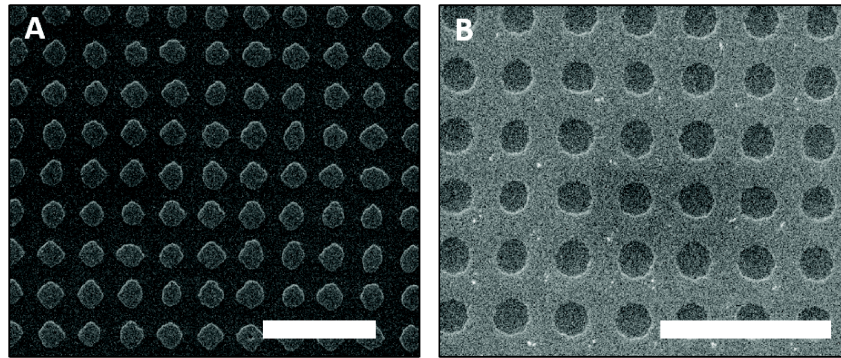


Figure 6.18.: Exemplary nanostructures fabricated by Talbot lithography and plasma etching. A. Sample fabricated using positive photoresist. The period is  $\Lambda = 1.8 \mu\text{m}$ , and the disk diameter  $d \approx 1.1 \mu\text{m}$ . B. Sample fabricated using negative photoresist. The period is  $\Lambda = 1.8 \mu\text{m}$ , and the aperture diameter  $d \approx 1.1 \mu\text{m}$ . Scale bars are  $5 \mu\text{m}$ .

### 6.3. Summary

In this chapter, two complementary recipes for the fabrication of plasmonic nanostructures from highly doped InAsSb layers on Gasb substrates were presented. First, a process based on photolithography and chemical etching, applicable for grating or array periodicities above 800 nm was presented. The major achievements were to adapt the standard photolithography process to small patterns by the use of diluted photoresist, modified exposure parameters and an amelioration of the contact between the mask and the sample in order to avoid additional interference patterns produced by photoresist bumps. The etch rate for InAs found in the literature was revised and an exemplary calibration on an InAsSb pattern was performed, evidencing the benefits of a slight increase of the etching time. We concluded this first part of the chapter with some examples



## 6. *Technological methods for sample fabrication*

of nanostructures fabricated by the process based on photolithography and chemical etching. Photolithography is an ideal method for the patterning of samples with comparatively large lattice parameters, but offers all the flexibility of the available masks. It is most adapted if a rectangular shape is required in double exposed samples, which is difficult to achieve with LIL.

Secondly, sample fabrication based on LIL was proposed, in order to achieve smaller periodicities and hence a densification of the plasmonic resonators. The principles of LIL were reviewed and the LIL setup based on a Lloyd's mirror interferometer was presented. The main parameters determining the pattern were investigated: incidence angle, laser power and exposure dose. The steps of the process flow were then indicated. The implementation of a plasma etching recipe adapted to etch thin InAsSb layers was then described. Compared to the standard recipe, the ICP power is reduced and a temperature control is applied. This second part was concluded by exemplary nanostructures fabricated by the proposed process. As an outlook, samples fabricated by LIL on a dual-beam interferometer setup were presented. This setup is advantageous to pattern larger surfaces than those which can be obtained by the Lloyd's mirror setup. This setup has furthermore the advantage of spatial filtering of the beams as last step before their arrival on the sample, avoiding consequently problems due to multimodal beams with improper interference patterns. Finally, Talbot lithography as a novel method for sample fabrication was proposed and the results of an initial test were presented. This method combines the possibility to fabricate patterns with small lattice parameters with the simplicity of photolithography.

## 7. Optical Characterization of Plasmonic Resonator Structures

In the previous chapters, the optical properties of plasmonic resonator structures were modeled by FDTD simulations. Furthermore, the technological processing for the fabrication of highly doped InAsSb nanostructures on GaSb substrates was presented. The successive step is the optical characterization and a comparison with the simulation results, if applicable. This chapter gives first an overview of the experimental setup before presenting the results obtained with different types of plasmonic resonator structures.

### 7.1. The experimental setup: Fourier transform infrared (FTIR) spectroscopy

#### 7.1.1. Principle of FTIR spectroscopy

IR spectroscopy is nowadays a routine analytical technique [CG02] thanks to the advent of FTIR spectrometers in the 1960s [Bru]. The FTIR spectrometer consists of a light source, an interferometer, a sample support, often inside a sample chamber with controlled atmosphere, a detector, and electronics for the conversion of the analog signal into a numeric one. The key element of the FTIR spectrometer is the Michelson interferometer, schematically shown in Figure 7.1. The light beam emitted by the source is collimated and then separated by a beam splitter. One beam is routed onto a fixed mirror while the other beam is reflected by a movable mirror. This introduces a phase difference between both beams which interfere when rejoining each other on the beam splitter. If, for a given frequency of light, the path difference is a multiple of the wavelength, constructive interference takes place. For a path difference  $\Delta x$  that is a half-integral multiple of the wavelength, the beams cancel out. A monochromatic light source produces a sinusoidal curve as interferogram:

$$I(\nu, \Delta x) = S(\nu) \cos(2\pi\nu\Delta x), \quad (7.1)$$

where  $S(\nu)$  is the intensity at the wavenumber  $\nu$ . For a continuous light source, all contributions from different wavelengths are summed up:

$$I(\Delta x) = \int_0^{\infty} (S(\nu) \cos(2\pi\nu\Delta x) d\nu). \quad (7.2)$$

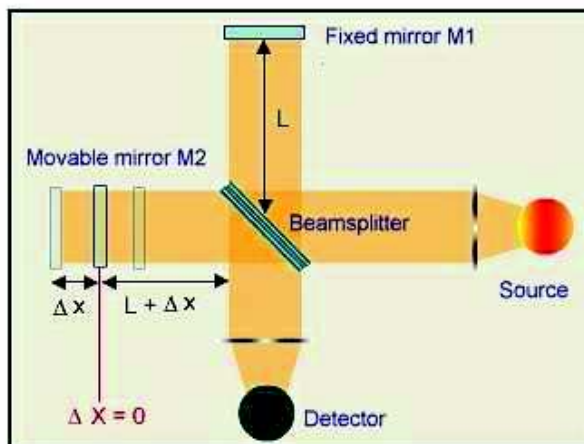


Figure 7.1.: Schematic of a Michelson interferometer. Figure from [Bru].

If the two mirrors are at equal distances, there is constructive interference for all wavenumbers. This corresponds to the central peak of an interferogram. As the path difference varies for different positions of the movable mirror, each wavelength undergoes constructive and destructive interferences. The interferogram contains therefore the entire information for all wavelengths emitted by the source. The detector measures the interferogram  $I(\Delta x)$  as signal. To obtain a spectrum  $I(\nu)$  as a function of wavenumber, the Fourier transform is applied to obtain the single channel intensity. In order to measure relative signals as the reflectance or transmittance of a sample, one single channel spectrum is measured on a reference sample, a strongly reflecting gold mirror for reflection measurements or an empty beam path in the case of transmission. The single channel spectrum from the sample is then normalized to the reference spectrum to obtain the relative signals.

To resolve spectral lines that appear at a distance  $d$  in terms of wavenumbers in the spectrum, a sufficient resolution is necessary. Typical resolutions in FTIR spectroscopy are around  $4\text{ cm}^{-1}$ , but it can be reduced to higher resolutions, the minimum resolution in the used setup being  $0.5\text{ cm}^{-1}$ . The resolution is obtained by a longer optical retardation, that is, the maximum oscillation amplitude of the movable mirror. For a theoretical resolution  $d$  a displacement  $x = \frac{1}{d}$  is necessary. For example,  $x = 2\text{ cm}$  is needed to reach a resolution of  $0.5\text{ cm}^{-1}$ .

The FTIR spectrometer presents several advantages compared to dispersive spectrometers which measure the intensity at each wavelength sequentially, using dispersive elements like prisms or gratings. Notably, there is the simultaneous acquisition of all spectral information in one acquisition, the Fellgett's or multiplexing advantage [Fel49]. Furthermore, a higher throughput of radiation is possible due to circular apertures in the optical path instead of slits used in dispersive spectrometers. This is the so called Jaquinot's advantage. The intrinsic wavenumber scale of FTIR interferometers is very precise due to an internal calibration with an alignment

laser (Connes' advantage). The Fellgett's together with the Jaquinot's advantage, *viz.* the short acquisition time per spectrum allowing to accumulate several spectra, and the high radiation intensity due to the circular beam, are the reason for the good signal-to-noise ratio in FTIR spectroscopy.

### 7.1.2. Description of the experimental setup used for the optical characterizations

The optical characterization was performed using a Bruker Vertex 70 FTIR spectrometer, equipped with the following accessories:

- Hyperion 3000 microscope for micro-FTIR measurements

Selected spots on a nanopatterned surface can be characterized by micro-FTIR measurements. The incident beam is focalized by a microscope objective (x15 magnification,  $NA$  0.4 or x36 magnification,  $NA$  0.5) on the sample surface. In the reflectance configuration, the signal is collected by the same objective, while in transmission configuration, a similar objective below the transparent sample collects the transmitted light. Using the x15 objective, the spot size is approximately  $150 \times 150 \mu\text{m}^2$ . This field can be reduced by knife-edge apertures shifted into the beam path, typically to  $100 \times 100 \mu\text{m}^2$ .

Besides the classical microscope objective, an attenuated total reflection (ATR) objective is available (x20 magnification,  $NA$  0.6). The light beam is incident through a germanium crystal with a refractive index of 4.0, increasing the  $NA$  of the objective. The passage from the high index material to lower index analytes gives rise to total reflection conditions. The evanescent wave impinging on the sample can excite propagating SPPs using the Otto configuration (see section 1.2.3). Due to the evanescent nature of the wave, ATR measurements are highly sensitive to the distance between the crystal and the sample.

Moreover, a grazing incidence reflection (GIR) objective can be used to analyze thin layers deposited on highly reflecting samples. The incidence angle ranges between  $54$  and  $84^\circ$ . The configuration improves the interaction of the incident IR beam with the sample. Notably, for this setup the measured signal is proportional to the square of the reflectance of the sample.

- A home-built reflectance setup with variable incidence angle from normal incidence up to grazing incidence ( $0^\circ$  -  $85^\circ$ )

This experimental setup is used to characterize large nanostructured surfaces especially for precise incidence angles and under oblique incidence. Hence it can give access to resonances that are not observable in nearly-normal incidence. The experimental setup consists of flat and hemispherical mirrors mounted on rotating arms, as shown in Figure 7.2. The collimated light beam from the internal MIR globar source of the FTIR spectrometer is routed to the mirror M1 of the setup, which in turn reflects it onto the hemispherical mirror M2, that focalizes the beam onto the sample placed onto the sample holder. The signal from the sample is collected by a second hemispherical mirror M3 and routed towards the detector

## 7. Optical Characterization of Plasmonic Resonator Structures

by mirror M4. A parabolic mirror is placed behind the rotating arm setup, to focalize the signal onto the entrance slit of the detector.

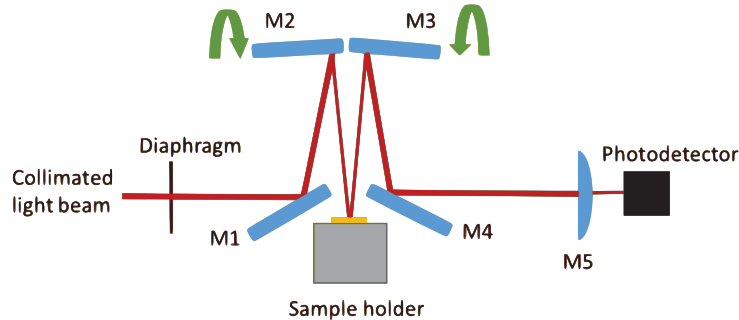


Figure 7.2.: Schematic beam path of the reflectance setup with variable incidence angle. The incidence plane is nearly perpendicular to the image plane; the mirrors rotate around the axis coplanar of the image plane. M1 and M4 are flat mirrors, M2 and M3 are spherical mirrors. M5 is a parabolic mirror that focalizes the beam onto the entrance aperture of the photodetector. For simplicity it is drawn here as a convergent lens.

- A home-built reflectance setup with a fixed incidence angle of  $60^\circ$  for the FTIR's internal sample chamber ("Brewster" setup)

This setup is similar to the above one, but is limited to a fixed incidence angle so that the complete setup is small enough to fit into the internal sample chamber of the FTIR. It is mainly used to determine the spectral position of the Brewster mode [TGC<sup>+</sup>14], the leaky, propagating mode close to the plasma frequency, observable also on uncorrugated HDSC layers. The plasma frequency and subsequently, via a calibration curve, the doping level can be determined by these measurements.

An overview of the different experimental setups is shown in Figure 7.3.

The FTIR spectrometer is equipped with a global MIR light source. Globars are SiC filaments heated at several  $1000^\circ\text{C}$  so that they emit blackbody radiation. Other sources are a tungsten lamp for the near-IR spectral range and a water cooled Hg lamp for the far-IR.

Several detectors are available for measurements in different spectral ranges and with the different accessories. For micro-FTIR measurements, a wide band mercury-cadmium-telluride (MCT) photoelectric detector is principally used, covering the spectral range from  $25000\text{ cm}^{-1}$  -  $450\text{ cm}^{-1}$ . Imaging of sample surfaces is possible due to a focal plane array (FPA), with a cut-off at  $800\text{ cm}^{-1}$ . The other internal and external measurement setups can be combined with pyroelectric deuterated triglycine sulfate (DTGS) detectors ranging from  $12000\text{ cm}^{-1}$  -  $125\text{ cm}^{-1}$  and  $12000\text{ cm}^{-1}$  -  $20\text{ cm}^{-1}$ , a MCT detector for the spectral range from  $12000\text{ cm}^{-1}$  -  $700\text{ cm}^{-1}$  that outranges the DTGS detectors in terms of sensitivity, but is limited towards high wavelengths, and a silicon bolometer for the far-IR spectral range from  $650\text{ cm}^{-1}$  -  $5\text{ cm}^{-1}$ . In appendix E, an overview of the different configurations and the respectively covered spectral ranges is shown, also indicating the spectral ranges of the different beam splitters which additionally impose limits to the accessible spectral range.

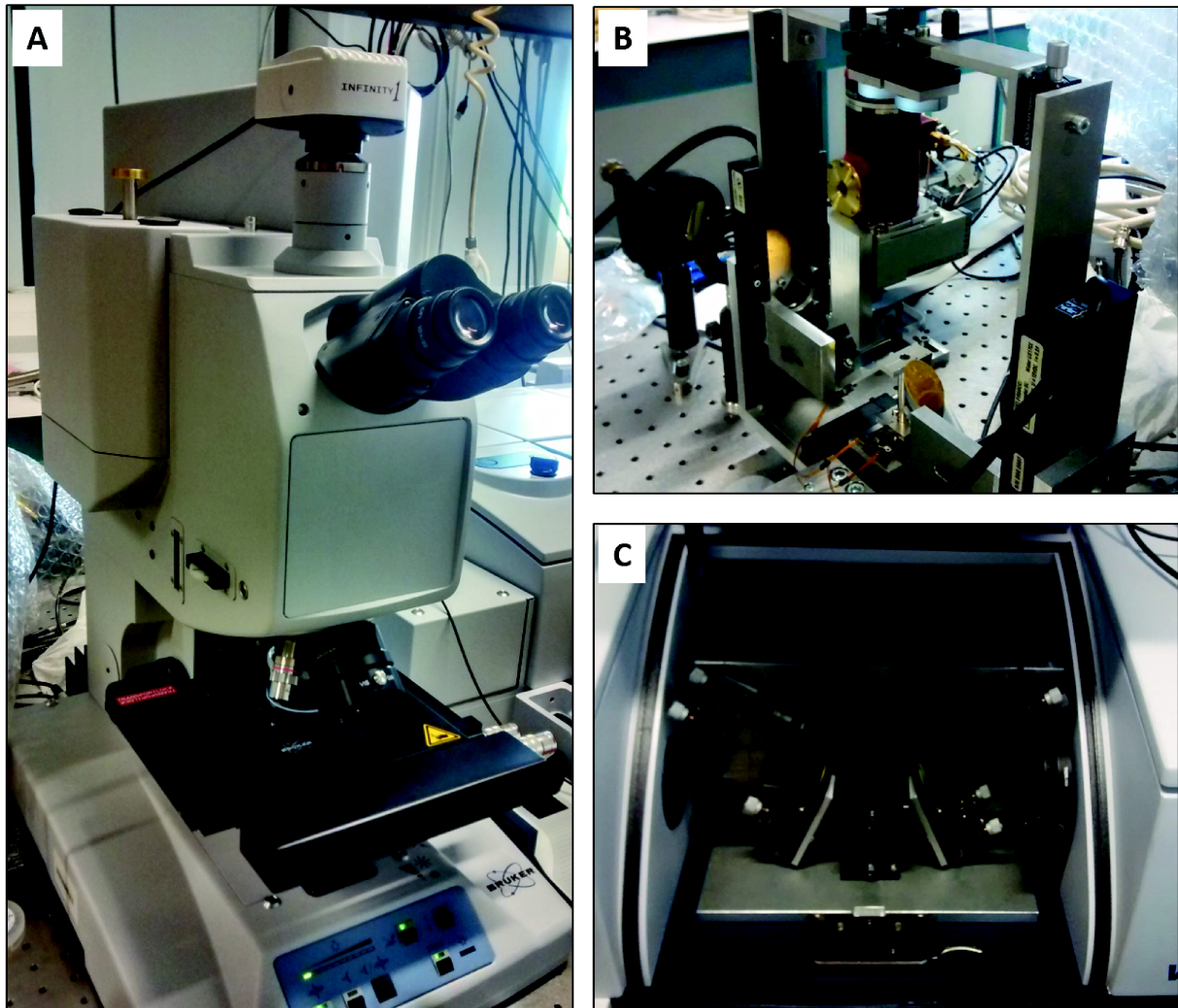


Figure 7.3.: A. Hyperion 3000 microscope with mounted 15x objective, GIR objective and 4x sample positioning objective. B. Home-built oblique incidence reflectance setup. C. "Brewster" setup.

## 7.2. Optical characterizations of 1D periodic plasmonic gratings

### 7.2.1. Localized plasmon resonances in 1D periodic plasmonic gratings

The first design proposition for the plasmonic resonator structure investigated in this manuscript are gratings made of InAsSb on GaSb substrates. They have been studied in detail by numerical simulations (chapter 4). The structure can be fabricated using the available photolithography masks or a single holographic exposure. Experimentally, they show the advantage of strong spectral signatures as there is a high amount of metal-like material that scatters and absorbs the incident light, due to the quasi-infinite extension of the grating's ribbons in one direction.



## 7. Optical Characterization of Plasmonic Resonator Structures

Figure 7.4 shows the reflectance spectra acquired from a plasmonic grating sample. As in the numerical simulations (see chapter 4), a principal LSPR is observed, in the exemplary structure at  $12.7 \mu\text{m}$ . The high energy peak, which we labeled  $\omega_{\text{top}}$  in chapter 4, is relatively weak for 100 nm thick gratings according to simulations, and is experimentally below the noise level. The LSPR can only be excited when the electric field vector has a component perpendicular to the grating's ridges. If the electric field vector is parallel to the ridges, the electrons are driven along the direction in which they can move infinitely, assuming the theoretical case of an infinitely extended grating. Practically, LSPR might be found at very high wavelength, as the ribbons are finite, but are in this case not in the investigated spectral range. For this reason, no plasmonic excitation can be observed under parallel polarization, apart from a weak signal at the initial position of the LSPR under perpendicular polarization, due to imperfections of the polarizers.

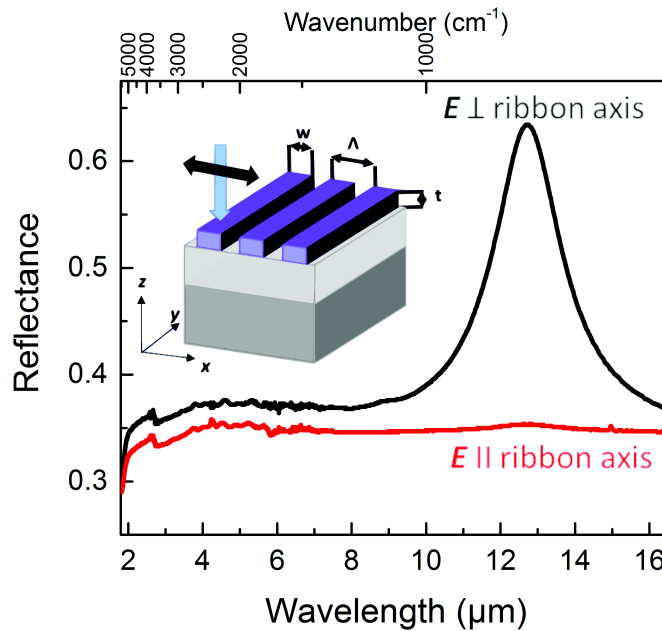


Figure 7.4.: Reflectance spectra of a plasmonic grating with dimensions  $\Lambda = 2 \mu\text{m}$ ,  $w \approx 500 \text{ nm}$ ,  $t = 100 \text{ nm}$ . The inset shows a schema of the structure indicating the geometric parameters and the polarization vector for excitation of the LSPR.

A plasmonic grating with dimensions similar to the one studied in simulations ( $\Lambda = 500 \text{ nm}$ ,  $w = 360 \text{ nm}$ ,  $t = 100 \text{ nm}$ ) was investigated under oblique incident light. The ribbon width  $w$  was measured at the interface with the GaSb substrate. Due to a slightly trapezoidal shape, the ribbon width on the surface of the grating is narrower. This and the slightly too high values for the Drude parameters in simulations are probably the reason for the differences in the spectra between the simulated and the physical structure.

An experience using oblique incident light allows to confirm the assumption that the SPPs excited in the here investigated 1D periodic gratings have localized character. Figures 7.5A and B

show measurements with light incident under different angles. The sample was orientated so that the grating is perpendicular to the incidence plane, as indicated in the schema (Figure 7.5C). In this configuration, TM polarized light can excite the SPPs. The resonance maximum is centered at  $10.1 \mu\text{m}$  and does not shift upon variation of the incidence angle. In fact, the dispersion relation of the SPP is flat, so that we confirm its localized character by these measurements. Indeed, the resonance in the optical spectra is linked to a LSP excited in the ribbon shaped particles placed onto a substrate. For the grating with small periodicity  $\Lambda$ , the flat dispersion can also be explained by the fact that the reciprocal grating vector  $G = \frac{2\pi}{\Lambda} \approx 12.6 \times 10^6 \text{ m}^{-1}$  for  $\Lambda = 500 \text{ nm}$ , is so large that the coupling condition, see equation 1.18, is only satisfied at very large in plane  $k$ -vectors where the dispersion of the propagating SPP becomes flat (Figure 1.8). This type of SPP has a large local density of states and a slow velocity, indeed all the characteristics of the LSP.

Moreover, when increasing the incidence angle, a decrease of the overall reflectance intensity is found for the TM polarized measurements (Figure 7.5A). This can be explained by the Fresnel equation for TM polarized light. Considering an interface between two half space media and oblique incident polarized light coming from medium 1, the reflection coefficient is given by [BW02]:

$$R_{\text{TM}} = \left( \frac{|n_1 \sqrt{1 - (\frac{n_1}{n_2} \sin(\Theta_i))^2} - n_2 \cos(\Theta_i)|}{|n_1 \sqrt{1 - (\frac{n_1}{n_2} \sin(\Theta_i))^2} + n_2 \cos(\Theta_i)|} \right)^2, \quad (7.3)$$

with  $n_{1,2}$  the refractive indices of the first medium respectively second medium and  $\Theta_i$  the incidence angle. When  $\Theta_i$  increases, the reflection coefficient decreases until the Brewster angle  $\Theta_B$ , from which on it increases, as shown in Figure 7.5D, where the reflection coefficient was exemplary calculated for an air - GaSb interface. The Brewster angle was evaluated to be at  $75.1^\circ$ . Furthermore, a phase shift in the reflected light takes place for incidence angles greater than the Brewster angle, yielding an inversion of minima and maxima in the spectra. In TE polarization, the reflection coefficient is given by

$$R_{\text{TE}} = \left( \frac{|n_1 \cos(\Theta_i) - n_2 \sqrt{1 - (\frac{n_1}{n_2} \sin(\Theta_i))^2}|}{|n_1 \cos(\Theta_i) + n_2 \sqrt{1 - (\frac{n_1}{n_2} \sin(\Theta_i))^2}|} \right)^2. \quad (7.4)$$

This expression increases monotonically as a function of  $\Theta_i$ . This is also found in the measurement series in TE polarization where only a flat spectrum without plasmonic excitation is obtained. Until  $75^\circ$  incidence angle, the reflectance intensity increases as confirmed by the Fresnel coefficients. For the two spectra at highest angles, the intensity drops due to a vignetting effect. Indeed, the spot size at grazing incidence is relatively large, often larger than small samples as in our specific case.



## 7. Optical Characterization of Plasmonic Resonator Structures

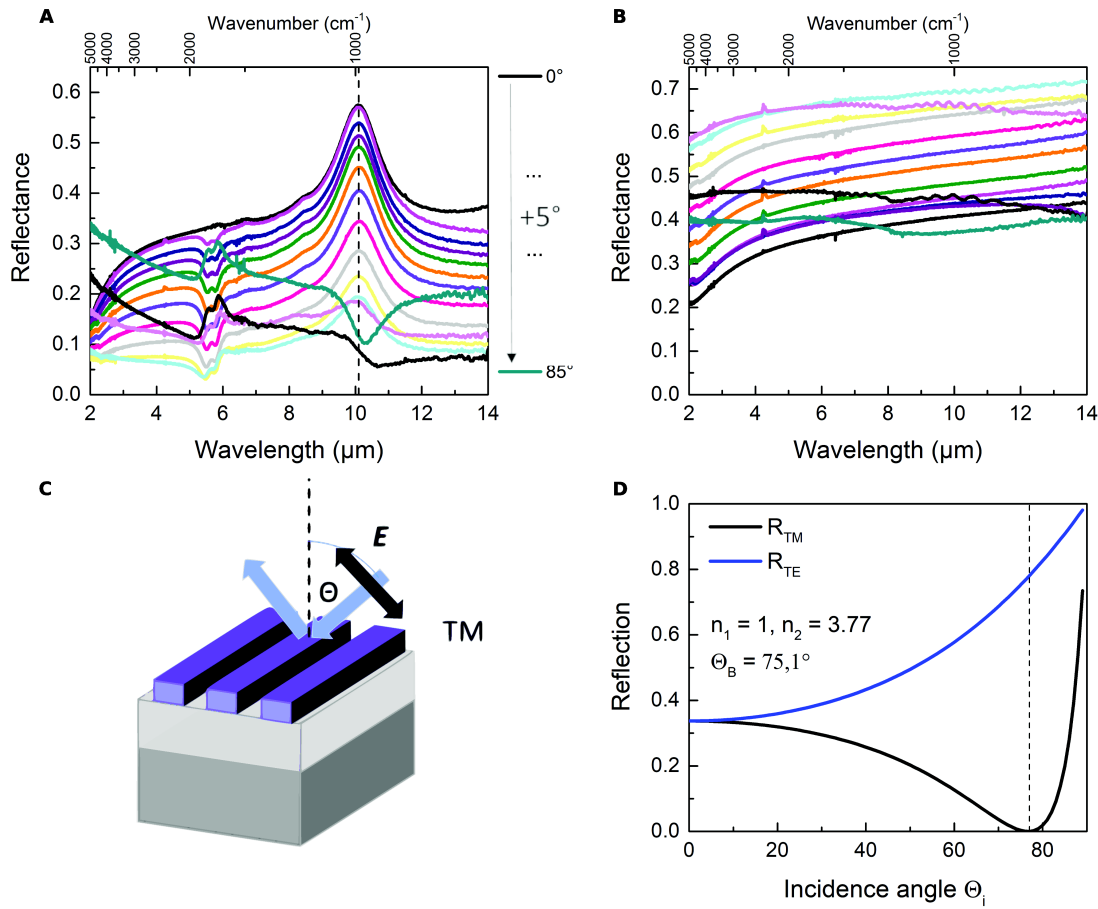


Figure 7.5.: A and B. Reflectance spectra obtained under oblique incidence of a plasmonic grating with dimensions  $\Lambda = 500$  nm,  $w = 360$  nm and  $t = 100$  nm. The grating's ridges are orientated perpendicular to the incidence plane. A. TM polarization B. TE polarization. C. Schema indicating the orientation of the grating with respect to the incidence plane. The electric field vector in TM polarization has a component perpendicular to the ribbons' axes, allowing the excitation of LSPR. D. Calculated Fresnel coefficients for an air - GaSb interface. The corresponding refractive indices and the Brewster angle are indicated in the Figure.

We now come back to a detail observed in Figure 7.5A. While in normal incidence there is only a very weak feature corresponding to the high energy LSPR ( $\omega_{top}$ ) found in simulations, for non-normal incidence, two dips can be observed at shorter wavelength. Beyond the Brewster angle, they transform into peaks due to the phase shift. To investigate in detail the origin of these spectral signatures, simulations were performed including electric field profiles at the wavelength of the spectral features. In Figure 7.6A, the experimental curve measured at  $40^\circ$  incidence angle is shown with according FDTD simulations in oblique incidence. The dip at highest energy corresponds to the Brewster mode, the propagative mode for positive values of the dielectric function  $\epsilon(\omega)$  just above the zero crossing. This spectral feature allows to deduce the plasma frequency by optical measurements, on uncorrugated or corrugated doped layers [TGC<sup>+</sup>14]. It is

identified by its field profile, shown in Figure 7.6B, where the electric field penetrates into the material. The plasma frequency used in simulations is slightly higher than the one of the sample (see Figure 7.5A), resulting in the shifted spectral position between simulations and experiment. The field profile of the second spectral signature is shown in Figure 7.6C. In chapter 4, the Fabry-Perot like mode spectrally close to the LSPR on the surface was already mentioned. In oblique incidence, it is possible to excite a Fabry-Perot like mode with an antisymmetric field profile in the component  $E_x(x)$  [LT10], as schematized in Figure 7.7. This mode is forbidden in normal incidence because it is necessary to have an electric field component parallel to the vertical interfaces between the HDSC and the air to excite it. Due to the spectral proximity of this Fabry-Perot like mode and the LSPR at the upper interface of the grating, they are not clearly separable. The increase of the spectral signature with increasing angle hints however that the antisymmetric mode on the vertical interfaces contributes to it, being mixed with the LSPR at the upper interface, especially due to the low thickness of the investigated grating.

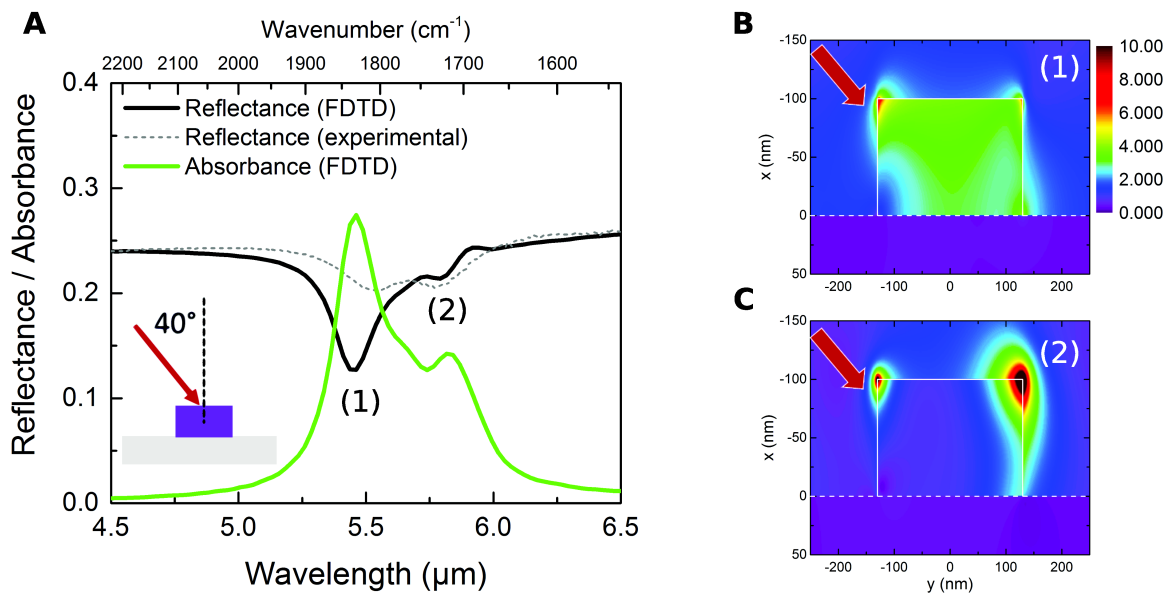


Figure 7.6.: A. Measured and calculated reflectance under  $40^\circ$  incidence evidencing dips corresponding to the Brewster mode and the antisymmetric LSPR. B. Field profile at the wavelength of the Brewster mode ( $5.45 \mu\text{m}$ ). The direction of light incidence is indicated by the red arrow. C. Field profile at the wavelength of the antisymmetric LSPR ( $5.8 \mu\text{m}$ ).

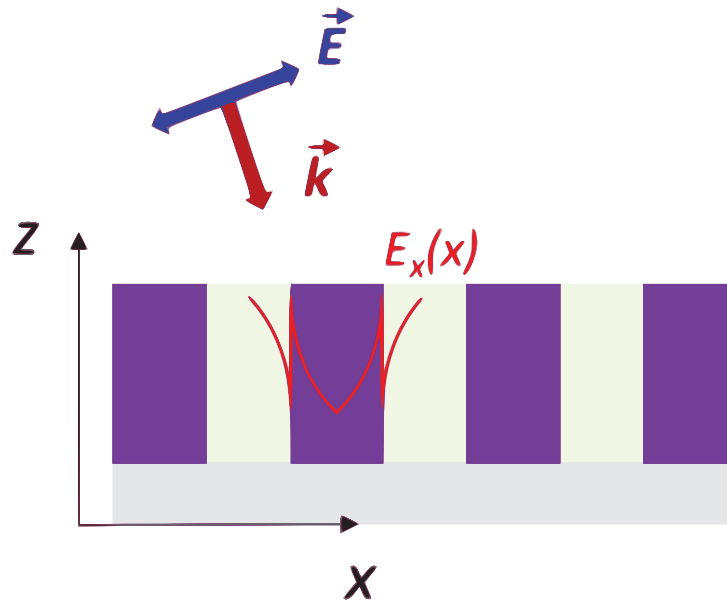


Figure 7.7.: Schematic of the field profile associated to the antisymmetric mode. The red lines indicate the field profiles corresponding to the component  $E(x)$ .

### 7.2.2. Tunability of the LSPR by the geometry and the doping level

Based upon the simulations shown in Figure 4.5, the tunability of the low energy LSPR throughout the mid-IR spectral range due to different geometries can be anticipated. Experimentally, this has been demonstrated for different ribbon widths [MBGP<sup>+</sup>16], at constant thickness of 100 nm and also constant periodicity of  $2\ \mu\text{m}$ , that is, in a configuration where the periodicity does not have an impact on the LSPR wavelength. The nanostructures have been fabricated by optical lithography and chemical etching, using the recipe indicated in section 6.1.1. Moreover, the doping level of the InAsSb layers has been varied in different sample series. This constitutes another possibility to control the LSPR wavelength. The carrier density modifies the plasma frequency  $\omega_p$  and consequently the LSPR whose frequency depends on the plasma frequency. Figure 7.8 displays the redshift of the LSPR for increasing ribbon width and the blueshift for increasing doping level. The tunability of the plasma frequency is one of the advantages of semiconductor materials for plasmonics.

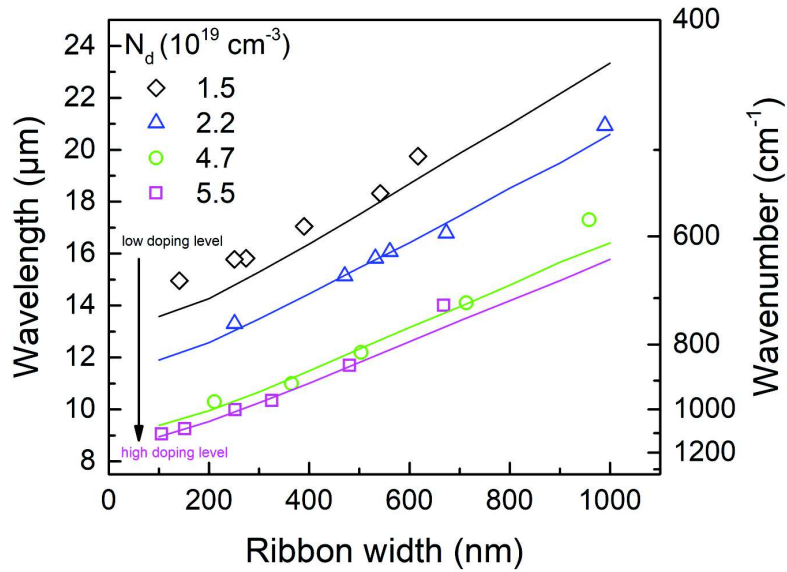


Figure 7.8.: Tunability of the LSPR wavelength using the ribbon width or the doping level as parameters. The ribbon thickness  $t = 100$  nm and the grating periodicity  $\Lambda = 2 \mu\text{m}$  are constant.

## 7.3. Optical characterizations of 2D periodic plasmonic nanoantenna arrays

### 7.3.1. Exploring possible geometries

In the following, we continue the investigation of the optical properties with the structure design presented in simulations in chapter 5, the 2D periodic arrays of rectangular nanoantennas. An overview and a detailed SEM image as well as a schematic are shown in Figure 7.9. The nanoantenna arrays were fabricated by optical lithography and wet etching. As mentioned in the previous chapter, the fabrication process comprises an additional lithographic exposure compared to the fabrication of the gratings. Adding one spatial dimension to the nanoantennas allows to excite LSPR for both polarization directions, contrariwise to the 1D periodic grating.

Several nanoantenna arrays, differing in antenna size and periodicities, were fabricated and investigated by FTIR spectroscopy. Some exemplary reflectance spectra are shown in Figure 7.10. The nanoantennas have a rectangular shape. In consequence of the anisotropy of the side lengths  $w_x$  and  $w_y$ , strong polarization dependence of the optical response is expected [DLYE04, GVMMEK10]. Clearly, this can be observed in the four examples shown in Figure 7.10. LSPR can be excited in both polarizations at different spectral positions. If there is only a little difference between the side lengths as for the array in Figure 7.10A, the LSPR in  $x$  and  $y$  polarization overlap, whereas they can be spectrally well separated for very anisotropic antennas

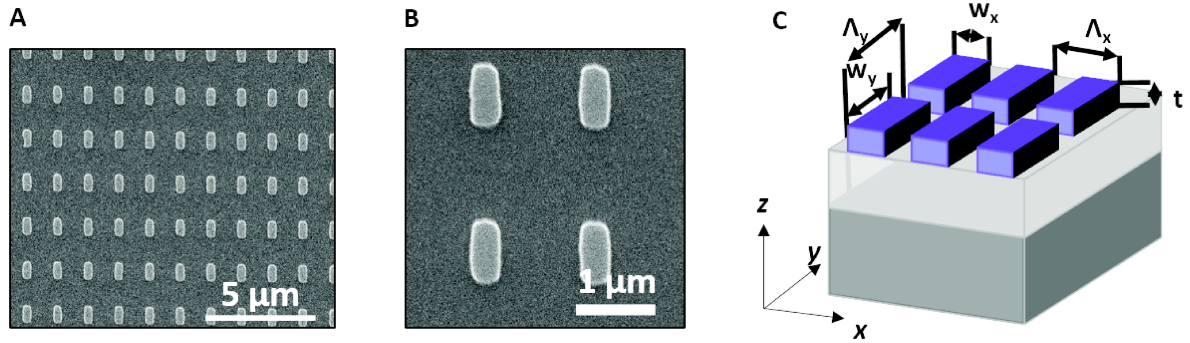


Figure 7.9.: A. 2D periodic rectangular nanoantenna array. B. Detail of A, displaying the rectangular shape with rounded corners. C. Schematic representation of the nanoantenna array, indicating all geometric parameters, thickness  $t$ , side lengths  $w_{x,y}$  and periodicities  $\Lambda_{x,y}$  in  $x$  and  $y$ -directions, respectively.

as in Figure 7.10D. Taking Figure 7.10B as example, the reflectance spectra of an array with periodicities  $\Lambda_x = 1.4 \mu\text{m}$ ,  $\Lambda_y = 2.0 \mu\text{m}$  of nanoantennas with side lengths  $w_x = 400 \pm 30 \text{ nm}$  and  $w_y = 810 \pm 30 \text{ nm}$ , one strong reflectance peak is revealed at  $\lambda_l = 16.8 \mu\text{m}$ , attributed to the longitudinal LSPR of the nanoantennas. Under  $x$  polarization, two peaks at  $\lambda_t = 11.7 \mu\text{m}$  and  $\lambda_t' = 10.4 \mu\text{m}$  are observed. These transverse LSPR, associated to the short axis of the nanoantennas, are at smaller wavelength than the longitudinal LSPR [NFK<sup>+</sup>09]. The reflectance intensity is weaker, due to the smaller dipole moment, or higher depolarization factor, of the transverse LSPR [BGN14, NFK<sup>+</sup>09, DBT<sup>+</sup>13].

The particular line shape varies for the different examples of nanoantenna arrays. In Figure 7.10A, a weak additional resonance at shorter wavelength than the principal one is observed in the  $x$  polarized spectrum. In Figure 7.10B, there is an inversion between the intensity of the resonances observed under  $x$  polarization. We assume that the origin of the particular line shape is linked to the aspect ratio of the nanoantennas, as discussed in chapter 5. The antennas in Figures 7.10C and D are so big that their longitudinal resonance maximum is outside the accessible spectral range of the MCT detector used for micro-FTIR spectroscopy. However, in Figure 7.10C, the weak additional resonance is observed in  $y$  polarization; in Figure 7.10D for both polarizations. This confirms experimentally the observations seen in the simulated spectra of chapter 5.

### 7.3.2. Polarization switchable resonances

In the following, we investigate the transition between the excitation of longitudinal or transverse LSPR using intermediate polarizations not aligned with the main axes. The angle  $\psi$  between the  $y$  axis (long axis of the rectangular nanoantennas) and the polarization vector is varied in steps of  $\pi/16$  rad. Measurements were performed with the sample whose reflectance

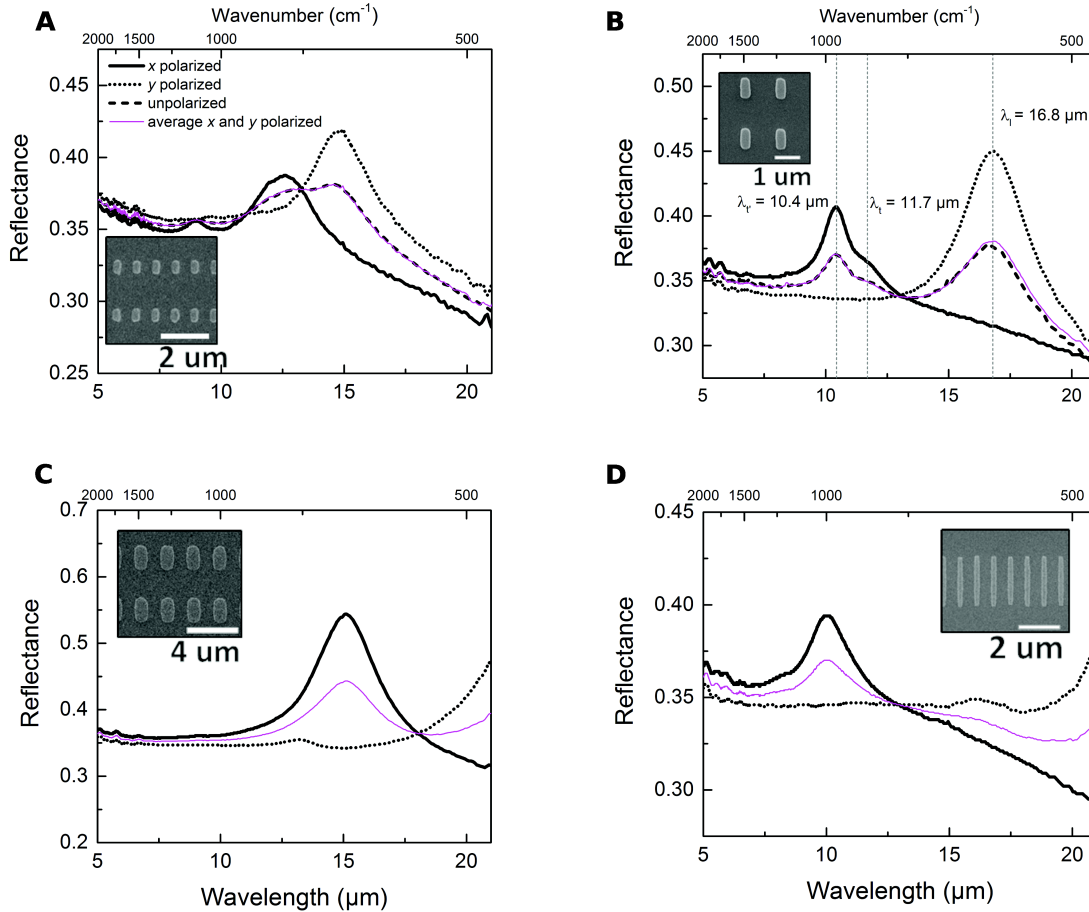


Figure 7.10.: Exemplary reflectance spectra of rectangular nanoantenna arrays obtained with light polarized along the short axis ( $x$  axis) and the long axis ( $y$  axis) of the resonators and with unpolarized light. An average of the polarized reflectance curves is also shown. SEM images of the corresponding nanoantenna array are shown in the insets. Dimensions of the nanoantenna arrays are A.  $w_x = 330 \pm 20$  nm,  $w_y = 560 \pm 30$  nm,  $\Lambda_x = 0.8 \mu\text{m}$ ,  $\Lambda_y = 2 \mu\text{m}$ ; B.  $w_x = 400 \pm 30$  nm,  $w_y = 810 \pm 30$  nm,  $\Lambda_x = 1.4 \mu\text{m}$ ,  $\Lambda_y = 2 \mu\text{m}$ ; C.  $w_x = 1.05 \pm 0.03 \mu\text{m}$ ,  $w_y = 1.97 \pm 0.03 \mu\text{m}$ ,  $\Lambda_x = 2 \mu\text{m}$ ,  $\Lambda_y = 4 \mu\text{m}$ ; and D.  $w_x = 270 \pm 20$  nm,  $w_y = 2.44 \pm 0.08 \mu\text{m}$ ,  $\Lambda_x = 0.8 \mu\text{m}$ ,  $\Lambda_y = 6 \mu\text{m}$ .

## 7. Optical Characterization of Plasmonic Resonator Structures

spectra are shown in Figure 7.10B. From the spectra measured at diverse polarization angles, the longitudinal and transverse LSPR wavelengths were extracted and the intensity value at these wavelengths was plotted against the polarization angle  $\psi$  (Figure 7.11). Note that a baseline correction was performed to extract the variation of the LSPR intensity without considering the reflection from the substrate. Therefore, the reflectance of a bare GaSb substrate at the investigated longitudinal and transverse resonance wavelengths was subtracted. Figure 7.11 indicates that by changing the polarization it is possible to switch between the longitudinal and transverse LSPR. The intensity of the longitudinal resonance decreases while the transverse resonances become more pronounced when increasing the polarization angle from  $0^\circ$  to  $90^\circ$ . The transition between the limiting cases can be fitted by cosine squared functions, with the maximum reflectance value extracted from the measurement. This behavior is coherent with Malus's law. The dipole-like pattern in the polar plot confirms the polarization dependence [MZY<sup>+</sup>09]. The polarization vector can be decomposed into components parallel and perpendicular to the long axis of the nanoantenna. When the component is large, the associated resonance is strong. Using an intermediate polarization direction or unpolarized light as it has been shown in Figures 7.10A and B, it is possible to excite simultaneously both LSPR as a superposition of the orthogonal polarization directions. This can be applied when it is needed to cover a large spectral range.

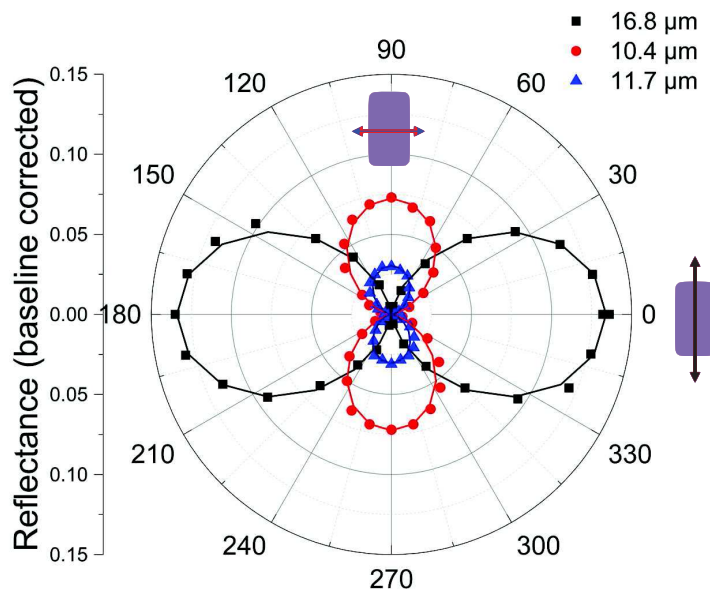


Figure 7.11.: Polar plot of the reflectance intensity at  $10.4 \mu\text{m}$ ,  $11.7 \mu\text{m}$  and  $16.8 \mu\text{m}$ , corresponding to the LSPR wavelengths in  $x$  and  $y$  polarizations, against polarization angle  $\psi$ , defined as the angle between the electric field vector and the long axis of the rectangular resonators. Solid lines are functions of the form  $R_{\text{max}} \cos^2(\alpha)$ , with  $R_{\text{max}}$  fitted to the measurement.



Interestingly, both LSPR lie in the IR spectral range and can thus be exploited for resonant SEIRA for broadband identification. In comparison, typical gold nanorod antenna with resonances in the IR display transverse resonances in another spectral range [DBT<sup>+</sup>13] due to their high aspect ratio, or the transverse resonance is below noise level [NKL<sup>+</sup>06], so that only the longitudinal resonance can effectively be used for resonant SEIRA. In chapter 8, SEIRA of vanillin molecules exploiting both the longitudinal and the transverse resonances of the rectangular InAsSb nanoantennas will be demonstrated.

### 7.3.3. Interaction range in 2D periodic nanoantenna arrays - Influence of the array periodicity

Besides the dimensions of the nanoantennas, another set of accessible parameters in the 2D periodic arrays are the grating periodicities in  $x$  and  $y$ -directions. The influence of the array arrangement on the optical response of the nanoantennas will be investigated next. For this purpose, several nanoantenna arrays with different periods in  $x$  and  $y$ -direction were fabricated. Figure 7.12A displays reflectance spectra of nanoantennas with dimensions  $w_x = 450 \pm 30$  nm,  $w_y = 830 \pm 30$  nm and varying periods in  $x$ -direction. The periodicity in  $y$ -direction is kept constant at  $2 \mu\text{m}$ . A decrease of the reflectance maxima in either polarization direction is observed due to the lower density of nanoantennas on the surface. However, the spectral positions of the resonances are not influenced by the periodicity. The slight fluctuations are likely attributed to the uncertainty on the nanoantenna dimensions. Similar observations are obtained for variation of the period in  $y$ -direction (Figure 7.12C). In this case, the resonator dimensions are  $w_x = 430 \pm 30$  nm,  $w_y = 760 \pm 30$  nm and the constant periodicity in  $x$ -direction is  $1.4 \mu\text{m}$ .

Our experimental measurements are supported by 3D FDTD calculations. The obtained reflectance spectra are shown in Figures 7.12B and D. The model presented in chapter 5 was used for the periodic arrays, but with some modifications for a better match to the experimental conditions, notably the material parameters of the substrate. As the GaSb substrate is slightly doped and becomes transparent at around  $40 \mu\text{m}$ , it is modeled by a Drude dielectric function with the following parameters:  $\epsilon_\infty = 14.2$  corresponding to the square of the typically used constant refractive index  $n = 3.77$  for GaSb,  $\omega_p = \frac{1.745 \times 10^{14}}{\sqrt{\epsilon_\infty}}$  rad/s according to the approximate cross over wavelength (where the dielectric function passes from positive to negative), and  $\gamma = 5 \times 10^{12}$  rad/s, used as fit parameter. The highly doped InAsSb is modeled as usual by a Drude dielectric function, see equation 0.8, with the parameters  $\epsilon_\infty = 10.4$ ,  $\omega_p = \frac{1.157 \times 10^{15}}{\sqrt{\epsilon_\infty}}$  rad/s, and  $\gamma = 1 \times 10^{13}$  rad/s.

The nanoantenna sizes were adapted from SEM images, corresponding to the mean values given above (model for the variation of the transverse period:  $w_x = 450$  nm,  $w_y = 830$  nm; variation of longitudinal period  $w_x = 430$  nm,  $w_y = 760$  nm). We used slightly rounded corners for the resonator geometry with a curvature radius of 20 nm to exclude effects from sharp tips in the electromagnetic field profiles. This curvature radius does however not have a significant impact on the reflectance and transmittance spectra.



## 7. Optical Characterization of Plasmonic Resonator Structures

Figure 7.12B (D) confirms by simulations the decrease in intensity of both longitudinal and transverse LSPR when the periodicity increases in  $x$ - ( $y$ -)direction. We do not evidence spectral shifting of the LSPR depending on the period in the investigated range of array periodicities, in the simulation under the condition of identical dimensions for the resonators. We deduce that the electromagnetic coupling between nanoantennas is negligible. The nanoantennas act as independent objects for the investigated range of periodicities. The reason for this is linked to the contribution of scattering and absorption to the extinction of the nanoantennas and will be discussed in detail below.

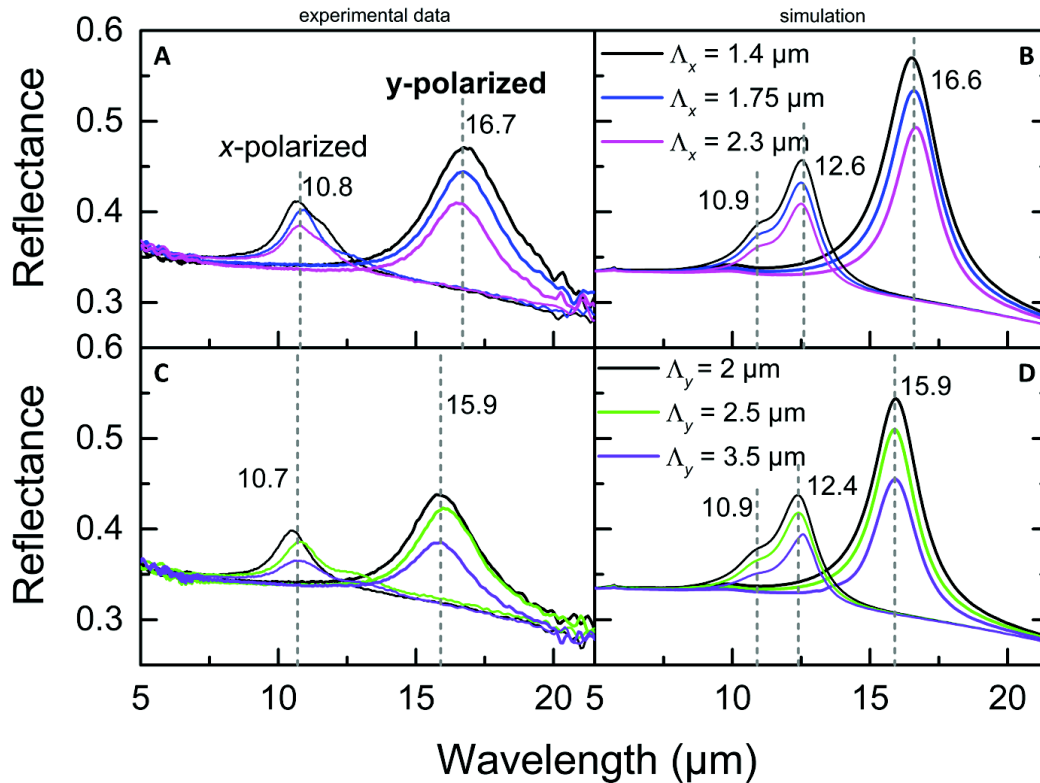


Figure 7.12.: Experimental (A, C) and simulated (B, D) reflectance spectra of rectangular nanoantennas. A and B: Variation of the periodicity in  $x$ -direction. The periodicity in  $y$ -direction is fixed ( $2 \mu\text{m}$ ). Measured nanoantenna dimensions are  $w_x = 450 \pm 30 \text{ nm}$ ,  $w_y = 830 \pm 30 \text{ nm}$ , in simulations  $w_x = 450 \text{ nm}$ ,  $w_y = 830 \text{ nm}$  were used. C and D: Variation of the periodicity in  $y$ -direction. The periodicity in  $x$ -direction is fixed ( $1.4 \mu\text{m}$ ). Measured nanoantenna dimensions are  $w_x = 430 \pm 30 \text{ nm}$ ,  $w_y = 760 \pm 30 \text{ nm}$ , in simulations  $w_x = 430 \text{ nm}$ ,  $w_y = 760 \text{ nm}$ .

### 7.3.4. Propagating modes on the grating

In the following, we will investigate if the array geometry allows interaction between the nanoantennas. Different interaction regimes in nanoparticle arrays have been identified in the literature, based mainly on examples of metallic, often Au and Ag nanoparticles [MW85, LSL<sup>+</sup>00, HMZ<sup>+</sup>03, NOP<sup>+</sup>04, BBI<sup>+</sup>05, CLC16]. Near field interactions arise for gaps between antennas in the range of several tenth of nanometers. This spacing being small compared to optical and IR wavelengths, the interaction is often treated in an electrostatic framework of coupled dipoles [HMZ<sup>+</sup>03], or alternatively by the plasmon hybridization model [NOP<sup>+</sup>04]. Near field interactions have been evidenced by FDTD simulations in chapter 4 for small array periodicities with high filling factors. They can be excluded for the here presented HDSC nanoantenna arrays as the spacing between antennas is the micrometric range.

Long range far field interactions occur due to the scattered field of each antenna in the array, leading eventually to constructive and destructive interference. The fields scattered by all the other antennas in the array impacts the field at the position of the investigated antenna if it has not decayed until reaching this position. To further investigate the origin of the insensitivity to long range interaction in the HDSC antenna arrays, we calculated the scattering and absorption cross sections for a single InAsSb nanoantenna on GaSb substrate (see Figure 7.13), exemplary with the lateral dimensions as in Figures 7.12A and B. The main contribution to the extinction comes from absorption (black solid lines in Figure 7.13), while scattering (blue dashed lines) contributes clearly less. Consequently, the radiated power of the antennas is small, which reduces the antenna interaction [AWP<sup>+</sup>14]. This allows to densify the nanoantennas in arrays while maintaining the resonance quality.

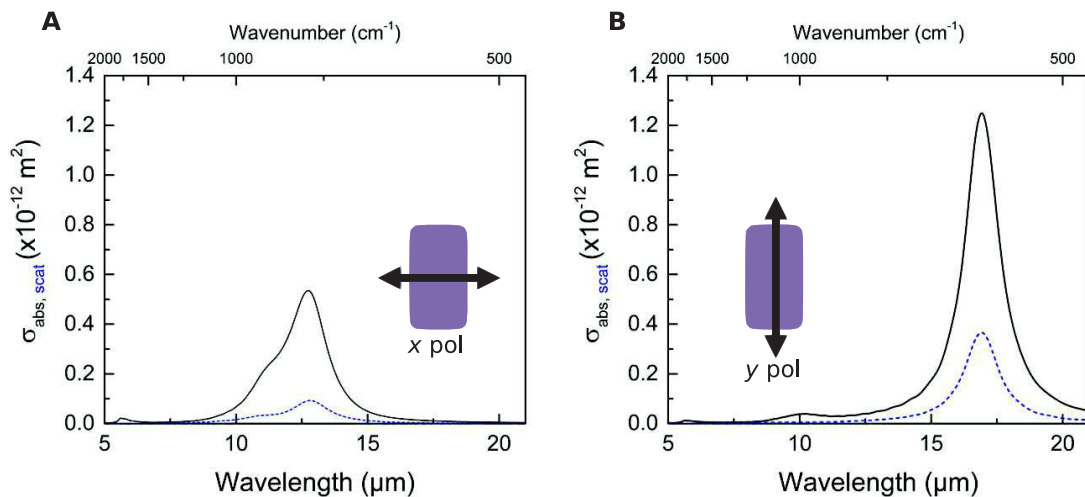


Figure 7.13.: Calculated absorption (black line) and scattering (blue dashed line) cross sections for a single nanoantenna with dimensions  $w_x = 450 \text{ nm}$ ,  $w_y = 830 \text{ nm}$ . A. Transverse resonance. B. Longitudinal resonance. Absorption is the dominant contribution to the extinction.

## 7. Optical Characterization of Plasmonic Resonator Structures

We now investigate under which conditions long range, far field interaction can become apparent in the optical response from the nanoantenna arrays. The approach is to align a grating order (Rayleigh anomaly) spectrally with the LSPR sustained by the nanoantennas to increase its spectral signature. For this purpose, the array period has to be chosen accordingly, see equation 1.36.

Due to the radiative nature of the grating orders, they are damped when they propagate through the substrate [AYA<sup>+</sup>09, NHW<sup>+</sup>17]. Higher orders than the zeroth grating order, that is, the ray which is not deviated, can only become radiative when  $\Lambda \geq \lambda_{\text{eff}}$  [MW85, LSL<sup>+</sup>00, CLC16], otherwise they are evanescent. The effect from these diffractive modes which become radiative might be weak in the HDSC nanoantenna arrays, as the scattering is reduced compared to the nonradiative decay channel as shown above. When tuning diffractive modes to be in resonance with the LSPR, they become nevertheless apparent, as evidenced in simulations. In Figure 7.14, the arrays with diffractive modes spectrally tuned to the transverse (A) or longitudinal (B) resonance are compared to arrays where diffractive modes are not in resonance with the LSPR and where, consequently, these weak features are not or scarcely visible. An estimation for the investigated resonances with  $n_{\text{substrate}} = \sqrt{\epsilon_{\infty}} = 3.77$  yields  $\Lambda_x = 2.9 \mu\text{m}$  and  $3.3 \mu\text{m}$  to have diffractive modes spectrally tuned to the transverse resonances or  $\Lambda_y = 4.2 \mu\text{m}$  to have a diffractive mode tuned to the longitudinal resonance at  $15.9 \mu\text{m}$ .

Combining individual LSPR with array resonances has been proven to be beneficial to enhance the sensitivity in gold nanoantenna arrays [AYA<sup>+</sup>09]. Periods just below the critical one resulted in a deformation of the plasmonic peak becoming narrow and strong in amplitude. Similarly, we demonstrate here the spectral superposition of LSPR and array resonances in HDSC arrays for rather large array periodicities. However, the size relation between the nanoantenna dimensions and the necessary array periodicity is different, as the resonators can be much smaller yet sustaining resonances at long wavelengths due to the low plasma frequency compared to noble metals. As shown in Figure 7.12, densifying the nanoantennas on arrays with smaller periodicities leads to stronger reflectance intensity. This densification is possibly beneficial compared to the large array periodicities necessary for the diffractive orders to become radiative, in this particular case of relatively small sized nanoantennas with long wavelength resonances. Especially, a high densification with unaltered resonance quality should be possible due to the weak contribution of scattering to the extinction [AWP<sup>+</sup>14].

To clarify the nature of the modes that mediate the far field interaction, we underline here that in the case of nanoantennas on a dielectric substrate, the antennas couple via dipolar fields propagating along the substrate [NHW<sup>+</sup>17]. Huck et al. demonstrated that the far field coupling is stronger for inverse structures, particularly in the case of nanoslits compared to linear nanoantenna, as the slits couple via SPPs propagating on the metal-substrate interface [HTN<sup>+</sup>15].

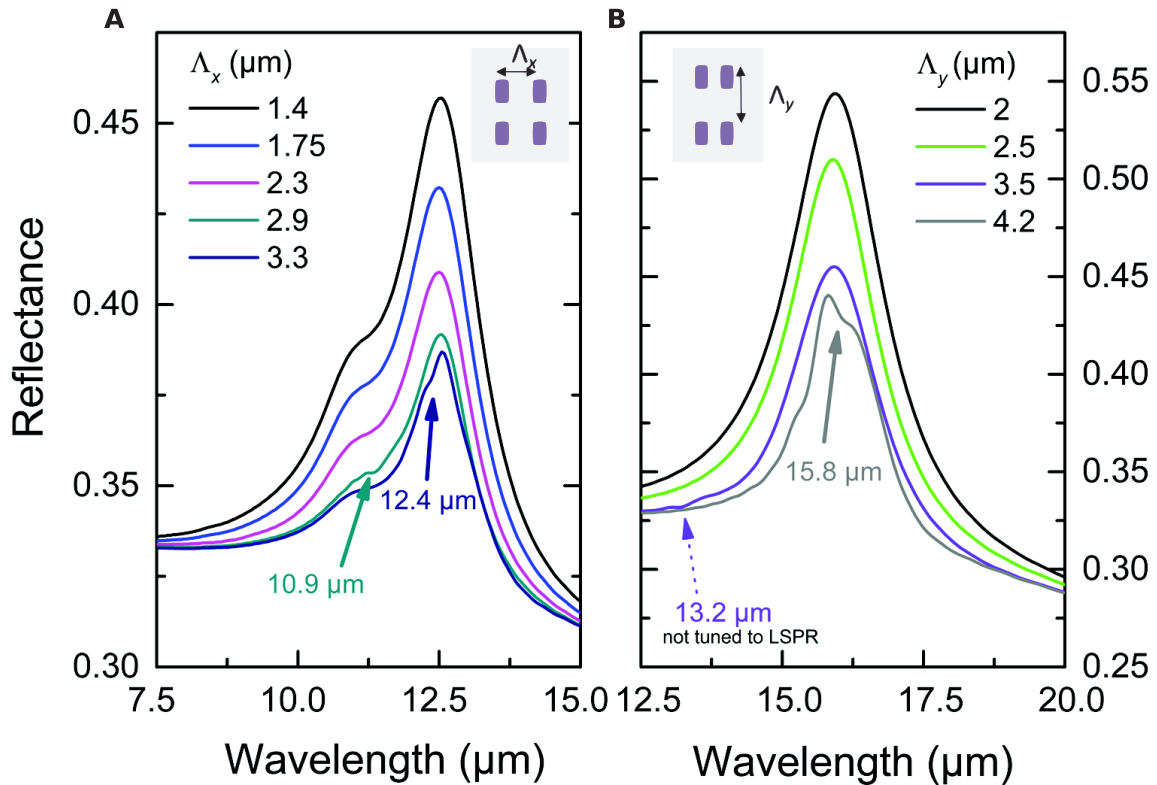


Figure 7.14.: Simulated reflectance spectra of rectangular nanoantenna arrays with large periodicity with a diffractive grating mode spectrally tuned to the LSPR peak. For comparison, the spectra from Figures 7.12B and D are shown where the diffractive modes are not tuned to the LSPR. A: Variation of the transverse periodicity  $\Lambda_x$ . The transverse LSPR is shown only. Values of the periodicity are chosen so that diffractive modes at the array-substrate interface propagating in  $x$ -direction are spectrally tuned to the transverse ( $x$  polarized) resonances. Arrows indicate the wavelengths where the diffractive modes can be observed. B: Variation of the longitudinal periodicity  $\Lambda_y$ . The periodicity was chosen to obtain the diffractive mode propagating in  $y$ -direction in resonance with the longitudinal ( $y$  polarized) resonance. Note that a feature appears for the grating with a periodicity of  $3.5 \mu\text{m}$  at  $13.2 \mu\text{m}$ , indicated by the dashed arrow, which is weakly visible compared to the diffractive feature in resonance with the LSPR for the periodicity  $4.2 \mu\text{m}$ .

## 7.4. Summary

In this chapter, the experimental results concerning the optical properties of different plasmonic nanostructures, specifically 1D periodic gratings and 2D periodic rectangular nanoantenna arrays, were presented. Firstly, the experimental technique FTIR spectroscopy was addressed and the available experimental setup at the Nanomir group of University of Montpellier was presented.

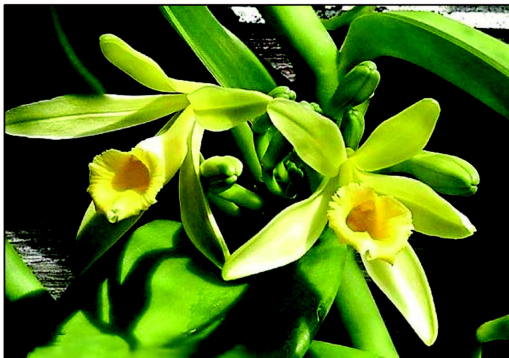
The simplest design approach for the plasmonic transducer for the biosensing devices is the 1D periodic grating. We experimentally verified that it supports LSPR which can be excited when the electric vector has a component perpendicular to the grating's ridges. By the means of oblique incidence reflectance measurements and associated simulations, we investigated the high energy LSPR confined on the surface of the grating's ribbons. Furthermore, the tunability of the LSPR using different ribbon widths or different doping levels yielding different plasma frequencies, was experimentally demonstrated. As a second design proposition, we investigated 2D periodic rectangular nanoantenna arrays. Here we found polarization selective longitudinal and transverse resonances in the mid-IR. The switching between the spectral bands or the excitation of all modes simultaneously can be realized by the change of the optical polarization with respect to the nanoantennas' axes. Subsequently, the influence of the array periodicity was studied. For array periodicities in the micrometer range, the nanoantennas act as isolated scatters. Strongest reflectance intensity is achieved for the smallest investigated array periodicities, hence it is beneficial to densify the nanoantennas on the substrate to get highest signals. Tuning grating orders (Rayleigh anomalies) to the spectral position of the LSPR modifies slightly the line shape, as shown in simulations for large array periodicities, but is nevertheless a weak effect due to dominantly absorbing nanoantennas.



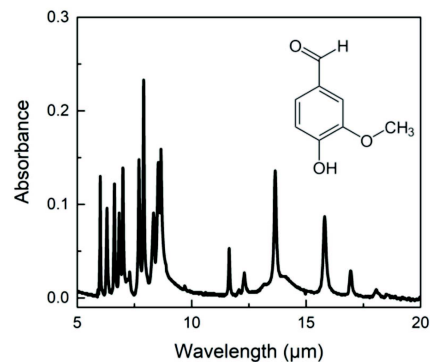


## Part III

# Sensing with all-semiconductor plasmonic nanostructures



Our exemplary analyte vanillin is the primary component of the extract of the vanilla bean but is also chemically synthesized.



Molecular identification, for example of vanillin, is possible by its characteristic vibrational spectrum.





## 8. Sensing with HDSC Plasmonic Nanostructures

This chapter focuses on the demonstration of SEIRA and SPR sensing with the Si-doped InAsSb plasmonic nanoantennas. Both types of structures, 1D periodic gratings and 2D periodic nanoantenna arrays, were studied. They were evaluated in sensing experiments using different polymers and, in the case of the 2D periodic arrays with resonances at high wavelength, the aromatic compound vanillin. In the following, experimental and numerical results concerning the sensing performance are presented.

### 8.1. SEIRA and SPR sensing using a 1D periodic plasmonic grating

A proof of principle experiment was performed using a 1D periodic nanoantenna grating supporting a LSPR at  $10.1 \mu\text{m}$ . The grating is  $100 \text{ nm}$  thick and its periodicity is  $\Lambda = 500 \text{ nm}$ . The ribbon width is  $360 \text{ nm}$  with a slightly trapezoidal ribbon shape.

Reflectance measurements were acquired of the uncoated grating as reference, using the micro-FTIR setup with a sampling zone of  $100 \times 100 \mu\text{m}^2$ , a resolution of  $1 \text{ cm}^{-1}$  and averaging 5 spectra of 500 scans each for the  $x$  polarized measurement where the LSPR is excited. Under  $y$  polarization, one spectrum of 500 scans was acquired. The measured signals are normalized to the signal obtained from a gold mirror serving as reference.

Subsequently, an approximately  $200 \text{ nm}$  thick layer of polymethylmethacrylat (PMMA) was spincoated onto the grating. PMMA is a polymer which features relatively weak absorption lines at  $10.1 \mu\text{m}$  ( $990 \text{ cm}^{-1}$ ) and  $10.35 \mu\text{m}$  ( $966 \text{ cm}^{-1}$ ), spectrally overlapping with the LSPR of the studied sample, besides several stronger lines at  $5.75 \mu\text{m}$  ( $1739 \text{ cm}^{-1}$ ),  $7.87 \mu\text{m}$  ( $1271 \text{ cm}^{-1}$ ),  $8.02 \mu\text{m}$  ( $1247 \text{ cm}^{-1}$ ),  $8.36 \mu\text{m}$  ( $1196 \text{ cm}^{-1}$ ), and  $8.67 \mu\text{m}$  ( $1153 \text{ cm}^{-1}$ ). The spectral positions of the vibrational lines were extracted from the reflectance-absorbance spectrum shown in Figure 8.1A, where they are indicated by the vertical, dashed lines. The spectrum was acquired using a GIR objective measuring the signal from a  $200 \text{ nm}$  thick PMMA layer on a smooth gold surface.

The spectra of the uncoated and the coated sample from the same sampling zone and under identical experimental conditions are shown in Figure 8.1B. Based on the displayed measurements, the SPR shift as well as the signal enhancement of the vibrational line are evaluated. Due to the PMMA deposition, the LSPR initially at  $\lambda_0 = 9.76 \pm 0.02 \mu\text{m}$  shifted to  $\lambda_1 = 10.23 \pm 0.02 \mu\text{m}$ , yielding  $\Delta\lambda = 470 \pm 40 \text{ nm}$ . The refractive index of PMMA is approximately  $n = 1.49$ .

## 8. Sensing with HDSC Plasmonic Nanostructures

The thickness dependent sensitivity is then evaluated to  $S_{200nm}^* = 960 \pm 80 \text{ nm/RIU}$ . This is in coherence with the order of magnitude found in simulations. Indeed, the mean value is even higher than what was found in simulations. This can be explained by the larger ribbon width of the experimentally used grating, as larger nanostructures tend to produce higher field enhancement [NHW<sup>+</sup>17].

To extract the signal strength of the vibrational signals, a method detailed in reference [HNV<sup>+</sup>14] is employed. The experimental spectrum is fitted using the Euler's least square smoothing algorithm, excluding the spectral bands around vibrational lines. The spectrum with the vibrational signals is then normalized to the «plasmonic background» obtained from the Euler's fit. Thus, the amplitude (peak-to-peak distance) of the vibrational signal can be obtained. We proceed analogously with the reflectance spectra obtained with light polarized along the grating's ridges, where no LSPR are excited in the considered spectral range. Figure 8.1C shows the extracted vibrational signals. Strong vibrational features spectrally far from the plasmonic resonance appear in both extracted signals. The main difference is seen close to  $10 \mu\text{m}$ . The weak vibrational features of the polymer appear as dips in the  $x$  polarized measurement where the LSPR is excited, with a signal strength of 1.9% at  $10.1 \mu\text{m}$  and approximately 0.6% at  $10.35 \mu\text{m}$ . The dip indicates a Fano-type interaction with the absorption feature on top of the plasmonic spectrum, other than for the non-enhanced absorption features which appear as peaks. In the  $y$  polarized spectrum, the weak features around  $10 \mu\text{m}$  can in contrary not be observed. As the vibrational feature in  $y$  polarization is below the noise level<sup>1</sup>, its value might be used to estimate the minimal signal increase due to the surface-enhancement effect. It is reasonable to indicate a noise level of 1%. As the vibrational line is not visible, its spectral signature is inferior to this. The factor of signal increase  $I_{\text{SEIRA}}/I_0$  is hence at least 1.9.

To calculate the enhancement factor according to equation 2.10, we estimate the ratio between the unit cell width and the active surface per unit cell width as in the simulations in chapter 4 as  $\frac{A_0}{A_{\text{SEIRA}}} = 25$ . This yields an enhancement factor of 47.5 which is drastically lower than the values obtained in the simulations due to the low signal increase factor  $I_{\text{SEIRA}}/I_0$ . Besides, the active surface is indeed relatively large due to the translational invariance of the grating structure compared to antennas with sharp tips where the active volume is much more limited. While the enhancement factor is not impressive, the grating structure is nevertheless an interesting approach for its large, homogeneous areas of field enhancement. The evaluation suffers indeed from the definition of the enhancement factor which considers that the smallest hotspots are ideal, which might be completely reasonable and justifiable with the aim of single molecule detection.

---

1. The noise level is unfortunately not the same for the measurements due to the different averaging. For future measurements, it has to be considered that it is important to have same noise levels for ideal comparability and quantification.

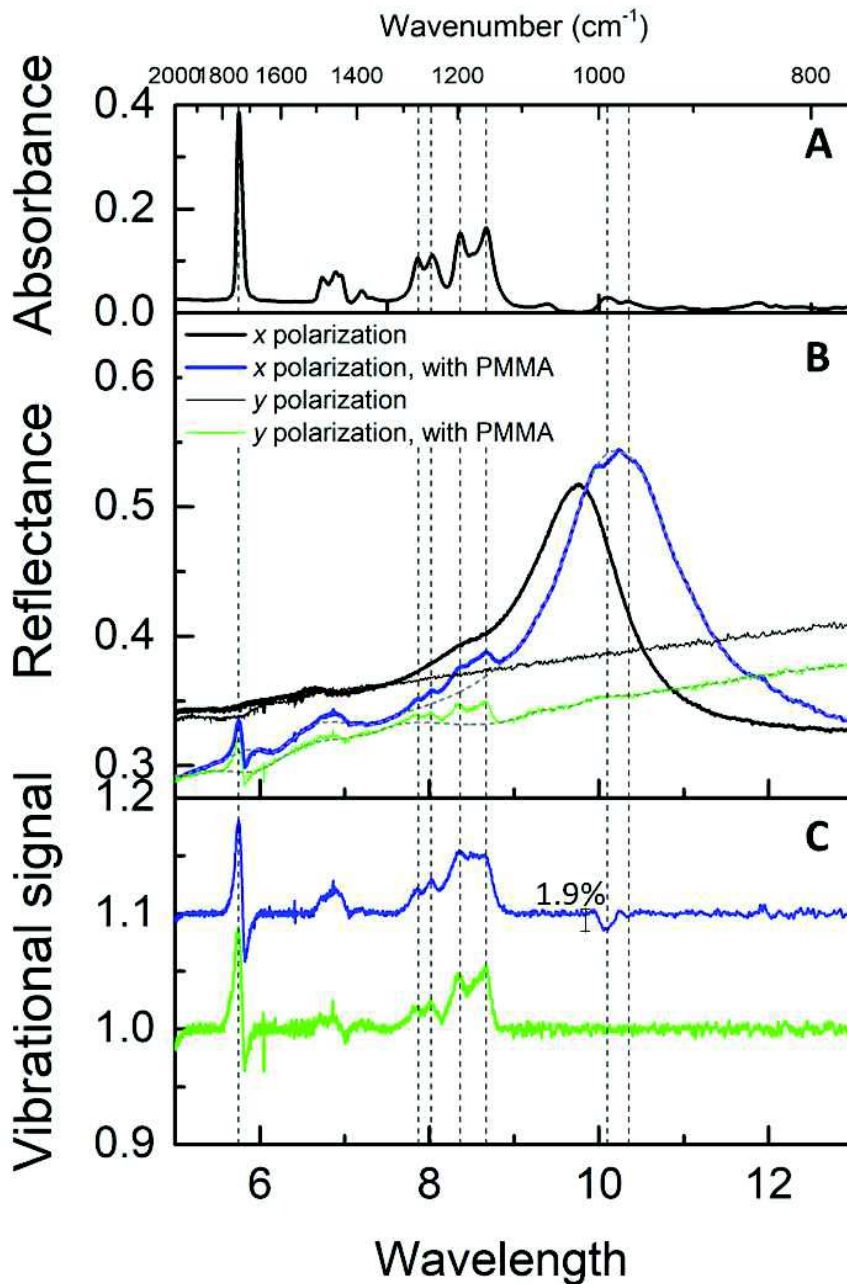


Figure 8.1.: A. Reflectance-absorbance spectrum of PMMA. Principal vibrational lines and the two weak vibrational features close to  $10\ \mu\text{m}$  are indicated by thin dashed lines. B. Experimental reflectance spectra of an uncoated grating (black lines) and the grating covered with 200 nm PMMA in  $x$  (blue) and  $y$  (green) polarization. The gray dashed lines correspond to Euler's fits of the spectra. C. Vibrational signal extracted using the ratio of the measured signal to the Euler's fit.

## 8.2. Comparison of the 1D periodic nanoantenna grating to a gold grating

In the framework of the comparison of InAsSb to the state of the art-material gold in terms of the mid-IR properties (see also section 3.5) and the performance as sensor, we investigated in simulations and experimentally sensing with a gold grating of an equivalent geometry to the InAsSb gratings.

The dimensions found in chapter 3 for the gold grating ribbons ( $w = 1600$  nm) are used, yielding an antenna resonance with a scattering maximum at  $10 \mu\text{m}$  in simulations. Because of the larger ribbon width, a mid-IR sensor based on gold gratings is at least four times larger in scale compared to the semiconductor grating ( $w = 260$  nm) for the same number of resonators, hence for the same number of active zones where the field enhancement is strong. Moreover, for the gold grating, the grating periodicity is in the order of magnitude of the wavelength of light. For this reason, diffraction effects become important. Indeed, in simulations of the periodic gold grating with  $1600$  nm large ribbons, we stated that the spectrum is essentially dominated by diffraction. Simulations for different periodicities and  $w = 1600$  nm are shown in Figure 8.2. The peaks and dips in the calculated spectra can be assigned to Rayleigh anomalies, which are emerging scattering orders into the interface plane (see Figure 1.17), at the upper and lower surface of the grating, as labeled in Figure 8.2. It is found that a grating with  $2.8 \mu\text{m}$  periodicity displays the first grating order at the interface between grating and substrate at  $10.1 \mu\text{m}$  (considering in the simulations the refractive index of the substrate  $n_{\text{GaSb}} = 3.6$ ). Such a grating benefits from a superposition of the calculated scattering maximum and the first grating order.

Before investigating experimentally the gold grating compared to the InAsSb grating, we first continue with further simulations of isolated resonators, to better compare how the scattering maximum is affected by a thin material layer covering the resonator. Figures 8.3A and B show the spectral dependence of the scattering cross section of an InAsSb ribbon and a gold ribbon, with and without a  $2$  nm thin layer modeled with a constant refractive index. While the scattering maximum of InAsSb shifts  $34$  nm, corresponding to a sensitivity  $S_{2\text{nm}}^* = 60$  nm/RIU, no variation can be found in the scattering spectrum of the gold ribbon. This can be accounted for by the different field enhancement factors and the field profiles, shown in chapter 3, Figure 3.8, where it was illustrated that the electric field is less enhanced and confined in the case of gold. Instead of probing the immediate environment, the gold nanostructure experiences another effective refractive index than the InAsSb structure, due to the lower confinement and hence the larger outreach of the electric field distribution for the gold ribbon. The sensitivity is consequently not sufficient to detect the  $2$  nm thin layer. Similar observations are made with regard to the absorption cross section (Figures 8.3C and D). Here, the wavelength shift of the absorption maximum is  $25$  nm for the InAsSb nanostructure, thus slightly less than the shift in the scattering

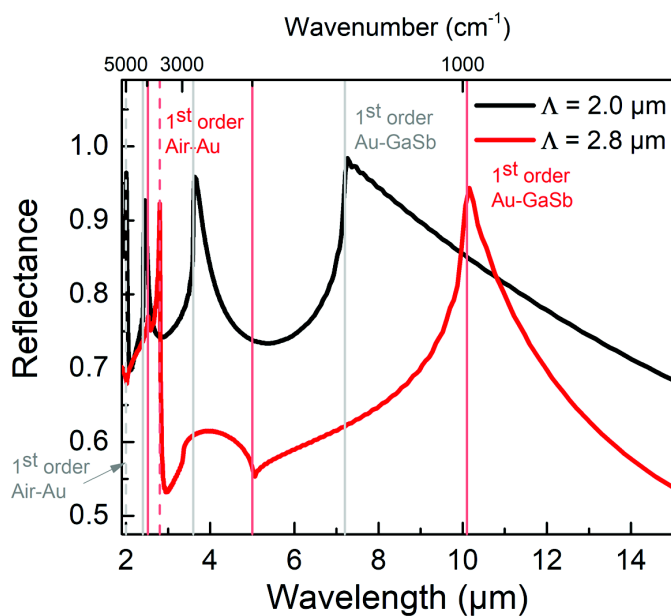


Figure 8.2.: Reflectance spectra of a 100 nm thick grating with periodicities  $2\ \mu\text{m}$  and  $2.8\ \mu\text{m}$  made of  $1.6\ \mu\text{m}$  wide gold ribbons. The spectral position and the assignment of the Rayleigh anomalies is indicated. Solid lines mark the grating orders at the gold-GaSb interface, dashed lines the diffraction orders at the air-gold interface, beginning with the first order at highest wavelength.

cross section. Again, for the gold ribbon, no difference is found between the simulations with and without the thin material layer. Note also the different  $y$ -axis scales in the graphs.

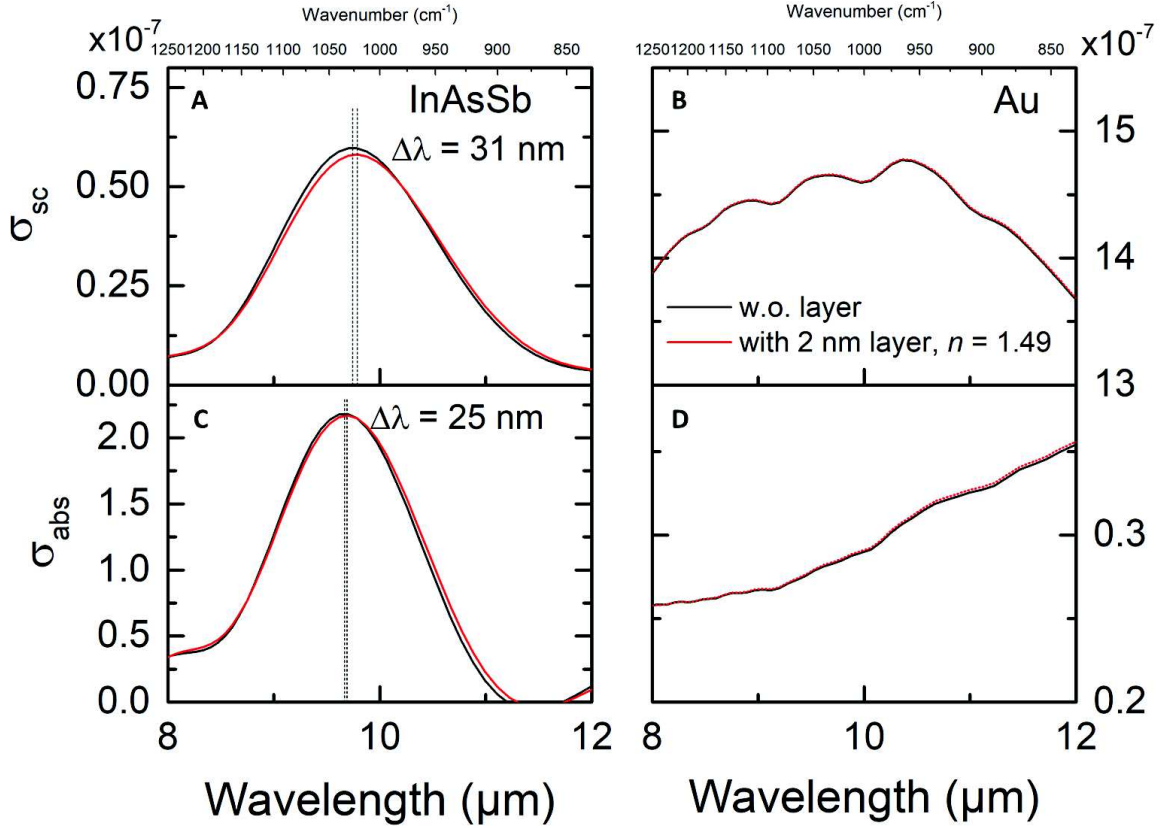


Figure 8.3.: A. and C. Simulated scattering (A.) and absorption (C.) spectra of a bare InAsSb ribbon ( $w = 260$  nm) on a GaSb substrate (black line) and the ribbon coated with 2 nm of a dispersionless material ( $n = 1.49$ , red line). The shift of 34 nm (25 nm) is indicated. B. and D. Same spectra in the case of a gold ribbon ( $w = 1600$  nm). No shift is observed. In the simulations, the meshsize in the region of the refined mesh is 0.25 nm.

To compare the scattering and absorption contributions of the two materials directly, Figure 8.4 shows the extinction, absorption and scattering cross sections for the InAsSb and gold nanostructures, without adlayer, in a same graph. Scattering and extinction cross section of the gold ribbon belong to the right  $y$ -axis which is scaled with a factor one order of magnitude higher than the left  $y$ -axis, to which belong all quantities of the InAsSb ribbon as well as the absorption of the gold ribbon (see arrows). A sharp resonance is found in the optical response of the InAsSb structure, which is mainly dominated by absorption. Scattering contributes less to the extinction, but the scattering spectrum features nevertheless a relatively sharp feature near  $10 \mu\text{m}$ . The optical response of gold is in contrast dominated by a large scattering distribution with its maximum close to  $10 \mu\text{m}$ . The absorption over the whole investigated spectral range is one to

two orders of magnitude smaller than the scattering, so that there is only a slight offset between scattering and extinction cross sections. Absorption resonances of gold can rather be found in the visible spectral range. The large negative real part of the dielectric function in the mid-IR reduces the penetration depth into the gold so that absorption is weak in the noble metal. Similar to what has been found in chapter 7 for the optical properties of the rectangular nanoantennas, we verify that also for the ribbon nanostructures, InAsSb is mainly absorbing, while scattering is less important, so that the antennas are under-coupled (scattering rate < rate of internal losses). The gold ribbons are in contrast over-coupled (rate of internal losses < scattering rate). The typical gold nanoantennas, as for example the linear ones, are often under-coupled or critically coupled which has been found to be the ideal case for SEIRA [NHV<sup>+</sup>15]. This is achieved by the reduced quantity of material and the high aspect ratio, other than in the relatively massive gold ribbons.

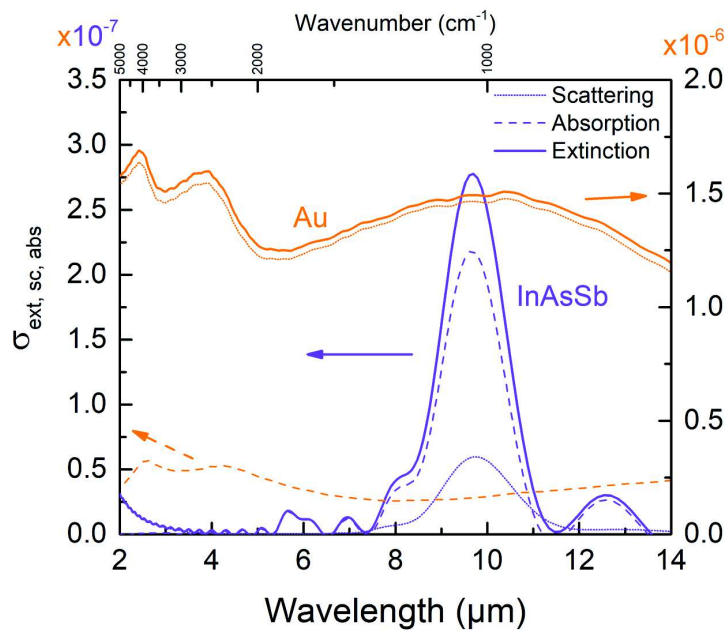


Figure 8.4.: Scattering, absorption and extinction cross sections for an isolated InAsSb ribbon ( $w = 260$  nm) on a GaSb substrate (purple lines, left  $y$  axis) and for an isolated gold ribbon ( $w = 1600$  nm) on a GaSb substrate (orange lines), scattering and extinction belong to the right  $y$  axis, the absorption is shown on the left  $y$  axis due to its smaller magnitude.

After this excursion about the contributions to the optical response from scattering and absorption we now proceed to the experimental comparison, which is performed with the gratings because single structures would not provide sufficient signals when using a standard FTIR setup. For the experimental investigation, a 100 nm thick gold grating with a periodicity of  $2.6 \mu\text{m}$  and a ribbon width of  $1.88 \mu\text{m}$  was fabricated. The periodicity was chosen to be close to the ideal  $2.8 \mu\text{m}$  using the available photomask while providing the necessary ribbon width close to  $1.6 \mu\text{m}$ .



## 8. Sensing with HDSC Plasmonic Nanostructures

What is more, as the model considered a slightly too low refractive index of the substrate, this might be compensated by choosing a smaller periodicity.

The gold grating was fabricated by standard photolithography using a bilayer photoresist (LOR A5 and AZ MIR 701), electron beam evaporation of 3 nm Ti adhesion layer and 100 nm gold, and lift-off in an acetone bath. A SEM image of the sample is shown in Figure 8.5.

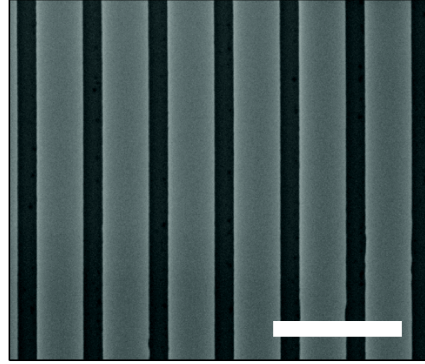


Figure 8.5.: SEM image of the fabricated gold grating. Scale bar is 5  $\mu\text{m}$ .

Reflectance measurements were performed analogously to the ones in section 8.1, see Figure 8.6A. In the spectrum of the uncoated gold grating under  $x$  polarization (perpendicular to the grating's ridges), a major peak at 10.2  $\mu\text{m}$  is observed in the considered wavelength range between 6 and 14  $\mu\text{m}$ , which is attributed to the first grating order propagating on the gold-substrate interface. In  $y$  polarization (parallel to the grating's ridges), high reflectivity near unity is found as the electric field vector points along the homogeneous, strongly reflecting gold ribbons. The electric field probes consequently a uniform material. After the deposition of 200 nm PMMA under equal conditions to what has been described above for the InAsSb grating, the first grating order shifted less than 12 nm in the  $x$  polarized spectrum. This is in the range of the error on the reflectance maximum readout.

We furthermore observe a variation in the reflectance intensity on the long wavelength side of the grating order peak probably related to the modified interface. The  $y$  polarized spectrum is not modified except for the presence of the strong absorption features of PMMA around 7.87 - 8.67  $\mu\text{m}$ , which are visible due to the highly reflecting support facilitating their observation. The strongest vibrational line at 5.75  $\mu\text{m}$  is observable in both spectra. We achieve a qualitatively good agreement of the experimental findings with the simulations shown in Figure 8.6B, where the adlayer was modeled by a constant refractive index, so that the vibrational features are excluded from the evaluation. The geometrical parameters were set according to the fabricated structure ( $w = 1880$  nm,  $\Lambda = 2600$  nm,  $n_{\text{GaSb}} = 3.77$ ). The spectral features under  $x$  polarization are sharper and more intense, because of the ideal interfaces used in simulations. In experiment however, the surface quality of the deposited gold introduces damping pathways which accounts for the broadened and less intense features. Imperfections might also be at the origin of the shoulder in the peak close to 9  $\mu\text{m}$ . In conclusion, neither in experiment nor in simulation, a

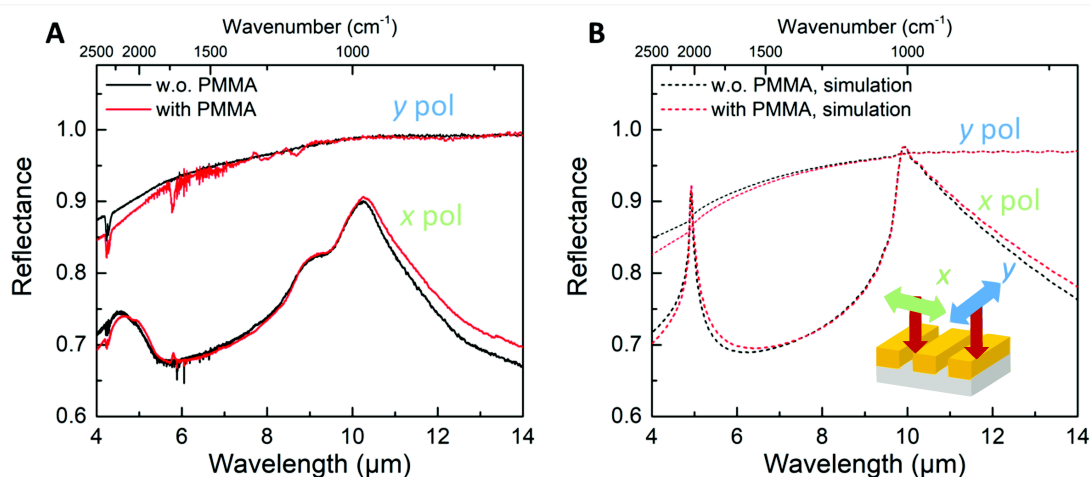


Figure 8.6.: A. Experimental reflectance spectra of an uncoated gold grating (black lines) and the grating covered with 200 nm PMMA (red lines). B. Simulated reflectance spectra of an uncoated gold grating (black lines) and the grating covered with a homogeneous 200 nm thick layer of constant refractive index  $n = 1.49$  (red lines). The inset illustrates the polarization directions.

significant spectral shift due to the PMMA coating could be observed, only a modification of the intensity in some spectral regions. This is in contrast to the results presented in section 8.1 concerning the InAsSb grating, where an SPR shift and SEIRA signals could be evidenced.

### 8.3. Study on the thickness dependence of LSPR sensing

In the simulations shown in section 4.4, we assessed that the LSPR shift depends on the layer thickness of an analyte, indicating the spatial outreach of the electric field which experiences an effective refractive index. A trendline following an exponential saturation process was found and saturation was reached at around  $1 \mu\text{m}$ . The dependency of the LSPR shift on the layer thickness was also investigated experimentally, as detailed in the following. The experiments were performed with 2D periodic nanoantenna arrays. This restricts the comparison to the earlier simulations of the 1D periodic grating to a qualitative one only.

Diluted AZ MIR 701 photoresist was spincoated onto a nanoantenna array and onto a reference silicon substrate to measure the deposited thickness by profilometry. The reflectance of the coated nanoantenna array was measured by micro-FTIR in a  $150 \times 150 \mu\text{m}^2$  sampling zone. Subsequently, the sample was then cleaned and another layer of different thickness was deposited. AZ MIR 701 displays no important absorption features in the spectral range of the plasmonic resonances of the array, so that only the wavelength shift unperturbed by absorption is found. In Figures 8.7A and C, the reflectance spectra of the nanoantenna array with different layer thicknesses of AZMIR 701 are shown in both polarizations. The refractive index of AZ MIR

701 in the IR spectral range is approximately  $n = 1.61$ . The LSPR peak shift for all discernible resonances was extracted from the reflectance curves and is shown in Figures 8.7B and D for the longitudinal and transverse resonances, respectively.

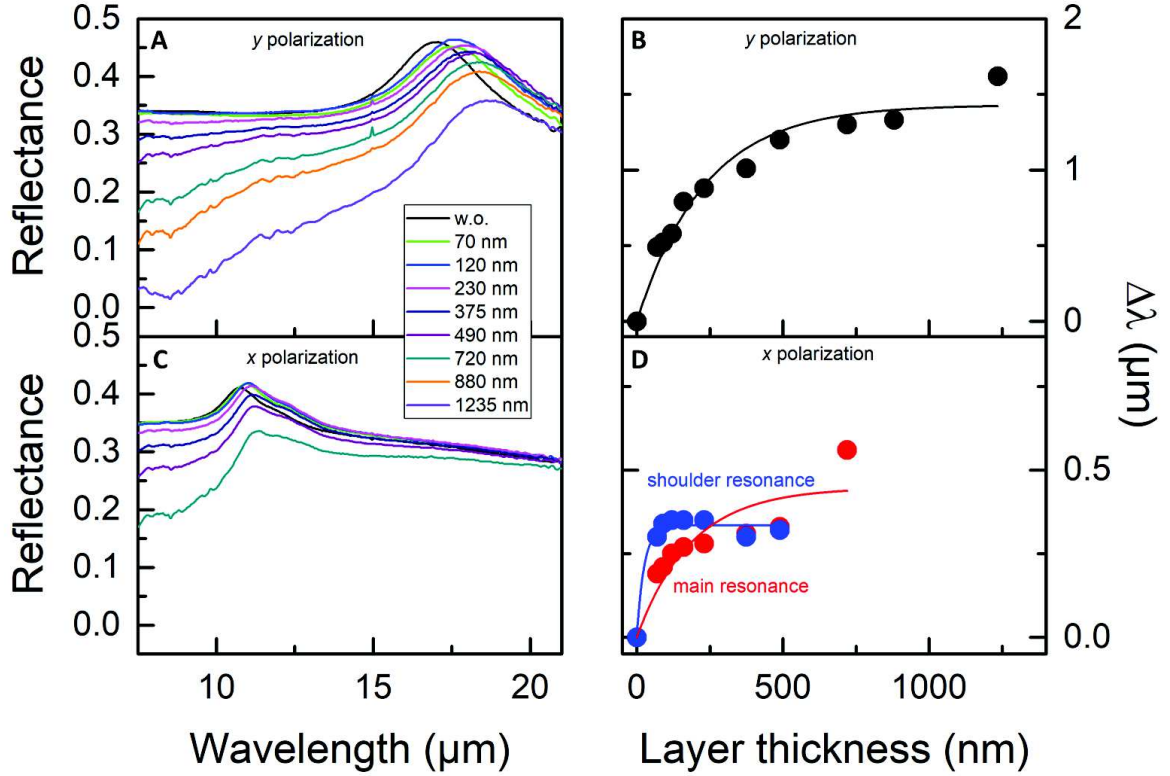


Figure 8.7.: A. (C.) Reflectance spectra of a nanoantenna array with dimensions  $w_x = 450 \pm 30$  nm,  $w_y = 830 \pm 30$  nm,  $\Lambda_x = 1.4 \mu\text{m}$ ,  $\Lambda_y = 2.0 \mu\text{m}$  with differently thick polymer layers in  $y$  ( $x$ ) polarization. B. Extracted LSPR peak shift for the longitudinal resonance. D. Extracted LSPR peak shifts for the main and secondary transverse resonance. Here, the main resonance designates the stronger one at shorter wavelength, as an inversion of the intensity is observed between the transverse resonance at short and longer wavelength.

The data was fitted using equation 2.5 to extract the bulk sensitivity and the decay length. Following values have been found:

- longitudinal resonance:  $S = 2340 \pm 110$  nm,  $l_d = 470 \pm 60$  nm
- transverse «main»resonance:  $S = 730 \pm 100$  nm,  $l_d = 370 \pm 130$  nm
- transverse «shoulder»resonance:  $S = 550 \pm 20$  nm,  $l_d = 50 \pm 20$  nm.

The transverse «shoulder»resonance yields a lower sensitivity than the «main»resonance and the field decays faster. This hints that the electric field profiles are different. Besides, for the highest polymer layer thicknesses, the spectral position cannot be identified clearly. For this reason, these points have been excluded from the evaluation. As known from literature [DBT<sup>+</sup>13, BGN14],

higher order modes are typically associated to lower sensitivities and hence less interesting for sensing. What is unusual here is that the resonance with lower sensitivity in transverse polarization is indeed at higher wavelength. Coming back to the issue addressed in chapter 5, it would be interesting to understand better the nature of the «shoulder» resonance in order to clarify these results.

The sensitivity associated to the longitudinal resonance is significantly higher than for the transverse resonances which is due to the higher dipole moment of the oscillation along the long resonator axis.

Qualitatively, a similar behavior of the saturation curve as shown in the simulations in chapter 4 is found, with a linear regime for small layer thicknesses and an exponential saturation for thick layers. The higher sensitivity for the longitudinal resonance, compared to the values obtained for the 1D periodic gratings, can either be linked to the large dimensions of the rectangular nanoantenna or to a higher field enhancement, with additionally a lightning rod effect on the corners of the rectangular nanoantennas. The sensitivity of the transverse resonances is in the range of what was found for the grating structure. To make a fair comparison, it would be of interest to compare same size nanoribbons and nanoantennas.

## 8.4. Sensing of vanillin using a 2D periodic nanoantenna array

The fabricated 2D periodic arrays of rectangular nanoantennas whose optical properties were assessed in section 7.3 sustain LSPR at high mid-IR wavelengths above  $10\ \mu\text{m}$ . They are particularly interesting to enhance the IR absorption lines situated in this spectral range, which are characteristic for aromatic molecules. For the experiment, we targeted the detection of the vanillin (4-hydroxy-3-methoxybenzaldehyde) molecule. Vanillin is the major compound of the vanilla bean [VFC07] and can be chemically synthesized for mass production. It finds applications in food, pharmaceuticals and perfumery [FSA<sup>+</sup>99]. Other aromatic molecules are for example polycyclic aromatic hydrocarbons (PAHs) that can be toxic [ASM16] and need to be detected for environmental safety. Several drug compounds have also aromatic molecular structures, which underlines the importance of being capable of enhancing the characteristic vibrations in the spectral range below  $1000\ \text{cm}^{-1}$ .

For the nanoantenna arrays, we exploit that a large part of the mid-IR spectral range can be covered due to the longitudinal and transverse LSPR. The condition of the resonant tuning between the large plasmonic resonance and the narrow IR absorption features of molecules is fulfilled around the two center wavelengths. Several absorption features close to the longitudinal and transverse resonance wavelengths are covered, especially on the long wavelength side of the resonance maximum [VHN<sup>+</sup>14].

The transmittance spectrum of vanillin, shown in Figure 8.8A, features several strong IR active vibrational lines of the functional groups present in the molecule as well as the characteristic vibrations of the substituted benzene nucleus in the fingerprint region from  $1500 - 500\ \text{cm}^{-1}$  [CG02],

## 8. Sensing with HDSC Plasmonic Nanostructures

which is to be detected using the nanoantenna arrays. The reference transmittance spectrum was obtained from a high concentrated vanillin solution (50 mg/ml) in ethanol deposited on a transparent KBr platelet. The spectrum was normalized to the one of a clean KBr platelet.

For the experimental demonstration, a nanoantenna array with dimensions  $w_x = 540 \pm 30$  nm and  $w_y = 600 \pm 40$  nm on a square array of  $1.4 \mu\text{m} \times 1.4 \mu\text{m}$  was chosen. The transverse and longitudinal modes display a partial spectral overlap for this nanoantenna geometry. The spectral range of the fingerprint vibrations is covered by the plasmonic resonances, while the vibrations at shorter wavelength can be used as reference for the strength of the vibrations, because the second polarization direction cannot be used as reference, as done in the case of the plasmonic grating structures.

Vanillin was dissolved in ethanol with a concentration of 2 mg/ml. Then, a droplet of few  $\mu\text{l}$  was deposited on the sample surface and the solvent was evaporated. Around 10 nmol are thus deposited on the sample, the molecular mass of vanillin being 152.1 g/mol. Assuming a homogeneous distribution of the vanillin molecules on the sample surface of approximately  $1 \text{ cm}^2$ , 0.5 ng of vanillin is located within the zone of  $150 \times 150 \mu\text{m}^2$  from which the reflectance signal is measured. This yields 12 femtogram per antenna, if we consider the antenna surface area, thus  $5 \times 10^7$  molecules per antenna. The number of molecules is three orders of magnitude higher than the best reported value for the detection of octadecanethiol (ODT) self-assembled monolayers with gold nanorod antenna, where the signal originated from approximately 7 attograms of chemically bound ODT in the nanoantenna hotspots [NHW<sup>+</sup>17].

Reflectance measurements were performed on the same sample position on the bare sample and subsequently on the sample covered with vanillin. Figure 8.8B displays the reflectance curves for the orthogonal polarization directions allowing the excitation of either the longitudinal or the transverse LSPR. For both polarizations, several vibrational lines lie within the spectral band covered and thus interact with the large plasmonic resonance. This can be seen from the Fano line shape of the vibrational lines in this spectral range [GFA<sup>+</sup>11].

In order to evaluate the signal enhancement, the measured reflectance curves were fitted using the smoothing algorithm proposed by Eilers [Eil03] (dashed lines in Figure 8.8B), excluding the vibrational signals, and processed analogously to what was described in section 8.1. Thus, a mainly flat line except for the vibrational signals is obtained (Figures 8.8C and D), allowing to compare the signal strengths in spectral ranges where plasmonic enhancement occurs to not impacted wavelengths.

To assess the increase of the vibrational signal strength, we first obtained the relative intensities from the reference transmittance spectrum of vanillin for the vibrational features at  $13.65 \mu\text{m}$ ,  $15.81 \mu\text{m}$  and  $16.95 \mu\text{m}$ . Intensities are given as percent of the strongest vibrational feature at  $7.9 \mu\text{m}$ , attributed to the C-O stretching vibration of the vanillin molecule. Then, we proceeded analogously for the vibrational signals obtained on the nanoantenna array. The percentage values are indicated in Figures 8.8C and D for the lines where a significant enhancement of more than

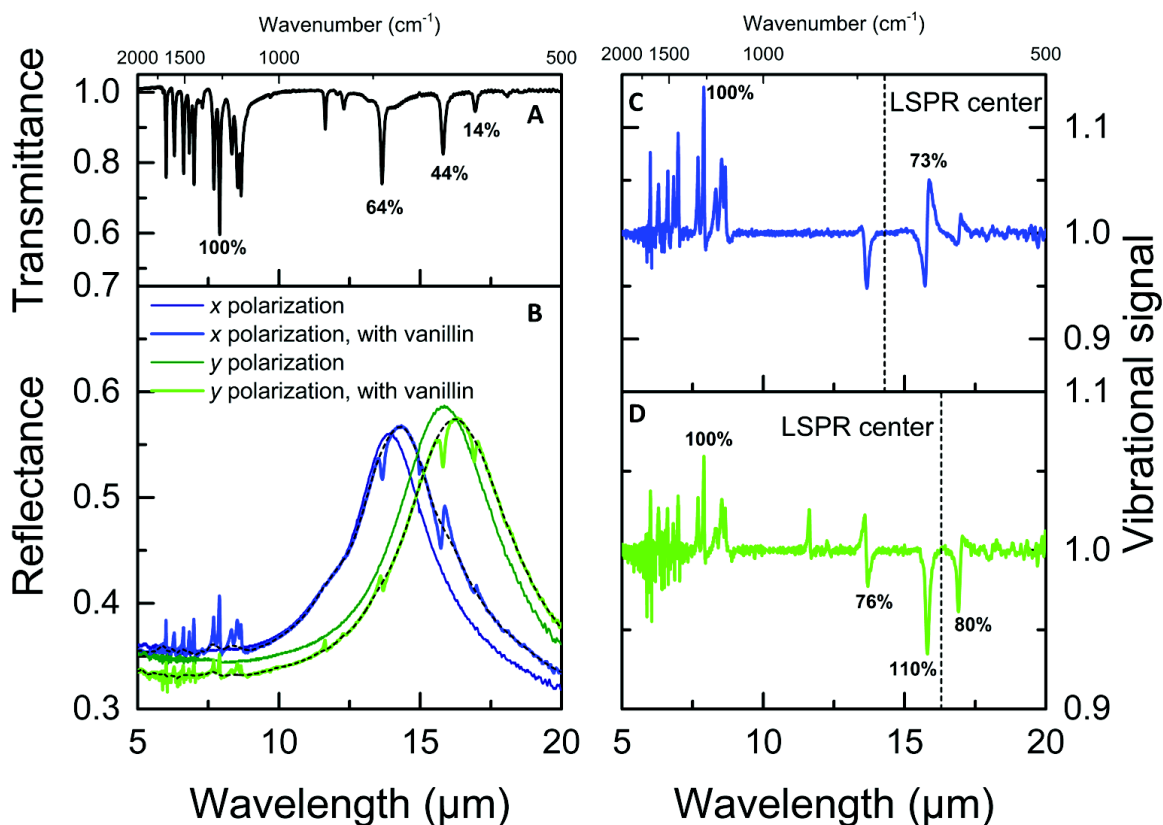


Figure 8.8.: A. Transmittance spectrum of vanillin, shown as reference. B. Reflectance spectra of the nanoantenna array covered with vanillin (thick lines). Thin lines are spectra before vanillin deposition on the same sample position. The black, dashed lines are fits using the Euler's smoothing algorithm, excluding the vibrational features. The Fano line shape of the vibrational features spectrally covered by the large LSPR evidences the coupling between the LSPR and the narrow vibrational lines. Sample size area was  $150 \times 150 \mu\text{m}^2$ . In this area, around 11500 antennas are located. C. Measured data in  $x$  polarization normalized to the Euler's fit. Percentage values indicate the signal strength with respect to the reference line at  $7.9 \mu\text{m}$  to which an intensity of 100% was assigned. The LSPR center wavelength is indicated (black dashed line). D. Measured data in  $y$  polarization normalized to the Euler's fit. Percentage values are indicated for lines with significant enhancement compared to the reference spectrum (more than 10 percentage points increase compared to the relative intensities in the reference spectrum).



## 8. Sensing with HDSC Plasmonic Nanostructures

Wavelength / $\mu\text{m}$ (Wavenum- ber / $\text{cm}^{-1}$ )	Intensity in ref- erence trans- mittance spectrum as % of strongest line	Vibrational signal strength ( $x$ po- larized) as % of reference line	Signal increase compared to ref- erence trans- mittance spectrum ( $I_{\text{SEIRA}}/I_0$ )	Enhancement factor	Vibrational signal strength ( $y$ po- larized) as % of reference line	Signal increase compared to ref- erence trans- mittance spectrum ( $I_{\text{SEIRA}}/I_0$ )	Enhancement factor
7.9 (1266)	100 %	100 %	normalized		100 %	normalized	
13.6 (733)	64 %				76 %	1.2	2900
15.8 (633)	44 %	73 %	1.7	4200	110 %	2.5	6100
16.9 (590)	14 %				80 %	5.7	14000

Table 8.1.: Summary of the signal increase compared to the reference transmittance spectrum of vanillin and the enhancement factors accounting for the active zone. The reference line is the C-O stretching vibration at  $7.9 \mu\text{m}$ .

10 percentage points compared to the reference spectrum is obtained. The comparison to the non-enhanced lines at lower wavelength sets the reference level in each measurement.

Chemical effects and effects due to molecular orientation on the different surfaces [CG02], namely the KBr platelet for the reference transmission measurements or the nanoantenna array, were not assessed, so that we considered only the significantly enhanced lines in the evaluation. Moreover, some line intensities might be reduced, due to the direct absorption of the vanillin. While direct absorption produces peaks in the reflectance spectra, the Fano-type interaction with the plasmonic nanoantenna is here at the origin of an electromagnetic induced transparency, seen as dip in the reflectance spectra. An enhancement can be observed when the electromagnetic effect outbalances the direct absorption.

For further comparison between the reference spectrum and the measurements on the nanoantenna arrays, the relative signal intensity increase was calculated by taking the ratio of the enhanced signals to the reference signal at the investigated wavelengths. Values range from 1.2 to 5.7 and are indicated in table 8.1 associated to each vibrational line.

The enhanced signals originate mainly from the zone of maximum field enhancement close to the nanoantennas. Considering this, we may estimate the enhancement factor defined in equation 2.10.

From the electric field profiles shown in Figure 8.9, it can be found that the electric field is strongest near the nanoantenna corners. The sectional view (Figure 8.9B) indicates that the field is especially enhanced on the substrate-antenna interface and in its immediate proximity. For simplicity, we consider the field distribution particularly in the plane shown in Figure 8.9A,

even if it is weaker in some other planes further away from the interface. We estimate the active surface  $A_{\text{SEIRA}}$  per unit cell area  $A_0$  corresponding to a square of 20 nm side length at each corner. Approximately half of the surface of the squares is accessible to the analyte, the other part being situated inside the nanoantenna. This active surface corresponds to 0.4‰ of the unit cell area. Enhancement factors from 2900 to 14000 are obtained, as indicated in table 8.1.

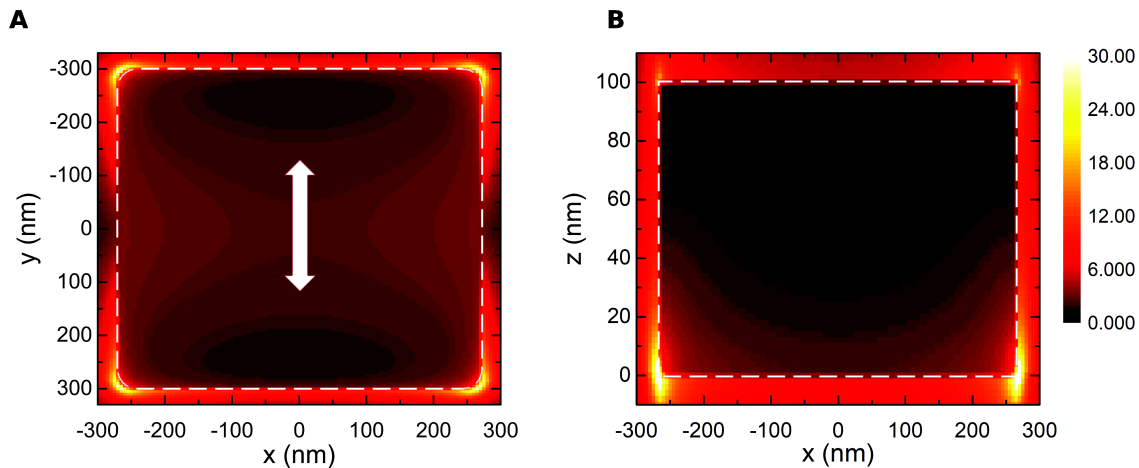


Figure 8.9.: Electric field profile of the longitudinal resonance for the nanoantenna array used for the vanillin detection, with dimensions  $w_x = 560$  nm,  $w_y = 600$  nm and  $\Lambda_x = \Lambda_y = 1.4 \mu\text{m}$ , calculated by FDTD simulations. White dashed lines indicate the edges of the nanoantenna. A. Top view of the electric field in a plane 5 nm above the substrate-nanoantenna interface. The direction of polarization is indicated by the white arrow. B. Sectional view through the long side of the resonator, 10 nm from the edge.

This is one to two orders of magnitude higher than what has been reported for Ge nanoantennas, exploiting additionally a hotspot in a gap between nanoantennas [BSF<sup>+</sup>15]. It is in the range of enhancement factors for noble metal nanoantennas found in other studies which range from 1000 to 100000 depending on antenna shape, material and arrangement [NHW<sup>+</sup>17]. The proposed semiconductor nanoantenna array in the investigated geometrical configuration does not exploit confinement in gaps or the lightning rod effect which is stronger at high aspect ratio nanoantennas, so that there is potential to reach even higher enhancement factors when these more sophisticated geometries are employed.

As discussed in section 2.5.1, the actual value of the enhancement factor depends critically on the considered hotspot area/volume. Geometries with small hotspots tend to reach consequently higher enhancement factors while the overall signal strength is less than for a structure with a large hotspot area. The increase in signal strength might often be more insightful than the enhancement factor itself, which is nevertheless widely applied to benchmark the performance of a SEIRA substrate.



To give an outlook on the SEIRA spectroscopy of vanillin, or other similar molecules, it would be of interest to better control the deposition conditions of the molecular layers. The main issue is the instability of the layers after deposition, as the vanillin layer has tendency to form bulky crystals on the semiconductor surface. While this process is slow enough to perform the spectroscopic measurements, it does not allow to perform additional studies of the layer morphology. An approach could be to deposit the vanillin layer in a vacuum environment to evaporate the solvent faster, or in an environment with controlled temperature for same reasons. The ideal case would be a surface chemical treatment controlling the polar or unpolar properties of the semiconductor surface or a surface functionalization film to chemically bind the molecules. A well controlled deposition of the molecular films would allow to work with different concentrations to study the detection limits. A quantitative comparison between different nanoantenna structures would also be of interest.

### 8.5. Comparison of 1D and 2D periodic nanoantenna arrays

In the sections above, different sensing experiments have been described using HDSC nanostructures that can be fabricated by simple and large-area applicable technological methods. In the following, the two types of structures are compared based on the reported results of the previous and this chapter. With regard to the general optical properties, polarization sensitive LSPR were found for both types of structures. Indeed, the strongest polarization anisotropy is obtained for the 1D periodic grating, where the LSPR is switched «on» for a polarization vector perpendicular to the grating's ridges and «off» for the orthogonal polarization. A second set of resonances in the investigated mid-IR spectral range can be excited in the rectangular nanoantenna arrays for the orthogonal polarization directions. The presented examples displayed an anisotropic response with longitudinal and transverse resonances for polarization along the differently long nanoantenna axes. We highlighted the interest on this for broadband IR spectroscopy using several vibrational lines for identification of a substance. Structures with high symmetry, for example square nanoantennas, can be fashioned to be completely polarization insensitive which is advantageous because of the possibility to work with unpolarized light [BZK<sup>+</sup>13], hence improving the signal-to-noise ratio in measurements thanks to the higher incident light intensity.

With respect to the amplitude of the plasmonic resonances, the gratings provide typically higher signals due to a higher content of metal-like material per unit cell of the structure. Densification of either type of nanostructures is of interest to increase the spectral signature of the plasmonic resonances. Based on FDTD simulations, it was shown that the extinction of both types of investigated InAsSb structures is dominated by absorption because the operation frequency is close to the plasma frequency  $\omega_p$ . The ratio of scattering to absorption can be varied within a range by choosing the size of the nanoantenna. All structures that were included in the study were nevertheless in the under-coupled regime (scattering < absorption). Making structures larger increased the scattering cross section, as expected.

The 2D periodic nanoantenna arrays have more similarities with the nanoantenna substrates that are typically used for SEIRA [MP17]. This implies a better exploitation of the off-resonant enhancement effects such as the lightning rod effect. What is more, the 2D array arrangement is not limited to rectangular nanoantennas, and more complex shapes exploiting various advantages as presented in the state of the art in section 2.5.2 can be imagined.

Refractive index sensing was demonstrated with both types of geometries. For different analyte layer thicknesses, both types of structures showed the exponential saturation dependency with increasing layer thickness.

Furthermore, the SEIRA effect was experimentally proven with a plasmonic grating as well as with a rectangular nanoantenna array. A signal increase factor  $\frac{I}{I_0}$  of 1.9 compared to the unenhanced signal measured in the polarization where no LSPRs are excited was reached with the plasmonic grating. The highest signal increase  $\frac{I}{I_0}$  for the nanoantenna array was 5.7.

Given the different dimensions of the grating and the nanoantenna array, a fair quantitative comparison between the structures is hardly possible. Ideally, a complete quantitative comparison of the two structure types should include an assessment using the same analyte molecule of controlled thickness, with nanoantenna geometries selected to match the specific vibrational feature of interest. This would allow to compare more objectively the LSPR shift, the vibrational signal increase  $\frac{I}{I_0}$  and eventually the enhancement factor EF. The latter however should be considered with care, because of its strong dependence on the chosen hotspot size. Turning this into an advantage, the EF could help to assess the available hotspot size for the structures, when it is given in combination with the ratio of the enhanced signal intensity to the reference signal compared to an adapted reference signal.

## 8.6. Summary

In this chapter, several proof-of-principle experiments were presented to evaluate the performance of the proposed structure designs for refractive index sensing and SEIRA. Experimentally, LSPR sensing and SEIRA could be evidenced with both types of structures. With the plasmonic grating, a 200 nm thick PMMA adlayer was detected. The thickness dependent sensitivity was evaluated to be around  $S_{200\text{nm}}^* = 960 \pm 80 \text{ nm}$  and a signal increase factor  $\frac{I}{I_0}$  of a vibrational line of PMMA of approximately 1.9 was obtained.

In a parenthesis, the performance of a gold grating equivalent to the investigated HDSC grating for sensing was studied. In simulations it could be evidenced that while a LSPR shift can be observed for InAsSb for monolayer detection, the gold grating does not respond to the small modification of the refractive index. Also in experiment, where a thicker polymer layer (200 nm PMMA) was studied, the observed modification in the spectrum of the gold grating was weak and the peak shift was in the range of the spectral resolution.

For the nanoantenna array, LSPR sensing and SEIRA experiments were conducted separately. A polymer without any significant vibrational features in the spectral range of the plasmonic

## 8. Sensing with HDSC Plasmonic Nanostructures

resonances, namely AZ MIR 701 photoresist, was deposited in different thicknesses on a nanoantenna array to study the thickness dependence. Qualitatively, a good coherence with theory, and also with the simulations shown in chapter 4 was found. Using the fit function for the spectral shift as a function of the effective refractive index, expressed by an averaging over the field intensity distribution with an exponential decay, the sensitivity and the decay length of the electromagnetic field were evaluated. A bulk sensitivity of  $2340 \pm 110$  nm/RIU was obtained for the longitudinal resonance, and  $730 \pm 1000$  nm/RIU ( $550 \pm 20$  nm/RIU) for the transverse resonances, due to their lower oscillator strength. Sensitivity values in the range of  $10^2$  to  $10^3$  are typically found in the recent literature for sensing with plasmonic nanoantennas (see section 2.4.2), and are one magnitude lower than the best reported value so far [SAE<sup>+</sup>16] which was obtained using a different type of plasmonic excitation, precisely a bulk plasmon-polariton, in a stacked metamaterial.

The decay length is in the range of  $10^2$  nm for the principal resonances in each polarization direction, also in the simulations in chapter 4, which signifies a fairly good confinement when considering the operation wavelengths in the mid-IR. For the «shoulder» resonance, the decay length is even shorter. Indeed, for propagating SPPs the typical decay lengths are in the range of 25-50% of the wavelength [JCC<sup>+</sup>98] while better confinement is achieved for LSPs. Besides this, the material properties of the HDSC compared to noble metals for which these values are indicated, might reduce the decay length.

A SEIRA effect could be observed using the 2D periodic nanoantenna arrays, enhancing vibrational lines of vanillin as analyte molecule. For the evaluation of the increase of the vibrational signal, a comparison with strong, non-enhanced vibrational features far from the plasmonic resonances was applied. The signal strength increased up to a factor of 5.7. When assuming that this signal originates mainly from electric field hot spots at the nanoantennas' corners, the enhancement factor could be evaluated to be in the range of  $10^3$  to  $10^4$ .

To conclude this chapter, both types of plasmonic nanostructures were compared. While the 1D grating might have advantages concerning simplicity, strong plasmonic resonances, ease of evaluation by an inherent reference measurement in the polarization without excitation of LSPRs, the 2D nanoantenna arrays offer more possibilities to control the optical response, can cover two spectral bands for large band identification or be completely polarization insensitive, and have tendency to provide higher values for the LSPR shift and the signal enhancement of vibrational lines. This last statement should however be carefully investigated with structures of comparable size to exclude the influence of too many factors. The arrays offer furthermore the possibility to replace the simple rectangular shaped nanoantennas by more complex antenna geometries, benefiting from additional enhancement effects such as the lightning rod effect and confinement of the field in small gaps.

# Conclusion

The objective of the research project of this thesis was the fabrication as well as the experimental and numerical study of plasmonic resonator structures made of highly doped InAsSb grown lattice matched on GaSb substrates. Notably, we proposed and investigated 1D periodic grating structures and 2D periodic arrays with rectangular nanoantennas. Other nanostructures such as disk or hole arrays were briefly addressed in this manuscript and are under study. The development and study of different types of plasmonic nanostructures was carried out in the framework of the national research agency project Supreme-B, which aims at developing a biosensing device based on HDSC plasmonics. It is the second PhD project on semiconductor plasmonics in the Nanomir group at the University of Montpellier, where this thesis was conducted.

Starting from material property considerations, it has been shown in quasi-static calculations and FDTD simulations that InAsSb provides as good plasmonic properties in the IR spectral range as silver in the visible, and that it is beneficial in terms of electric field enhancement in the mid-IR compared to gold, due to lower absolute values of both the real and imaginary part of the dielectric function. This is a decisive result for the Supreme-B project wherein it was requested to demonstrate this higher near field enhancement, underlining the potential of highly doped InAsSb for mid-IR plasmonics.

Numerical studies on the geometric parameters of the plasmonic nanostructures allowed to determine how the resonance wavelength of our plasmonic nanostructures can be controlled. The main effects are the following: For the plasmonic grating structure, larger ribbons display their principal LSPR red-shifted, as expected. An effect of the grating's thickness can be evidenced for sufficiently thin gratings where the resonance also red-shifts due to interactions between the LSPR on the interface with the substrate and the LSPR on the upper interface. For small lattice parameters, near field interactions also provide a red-shift of the principal resonance. The thickness and the periodicity effects saturate for sufficiently thick gratings or high lattice parameters but still impact the reflectance intensity. Using FDTD simulations, the response of the plasmonic grating to the presence of an analyte was evaluated, indicating an observable LSPR shift induced by monolayers and enhanced vibrational signals, contrary to what could be observed for an equivalent gold grating. The dependence of the LSPR shift on the layer thickness was also evaluated and found to increase strongly for thin layers while it saturates for thick layers, in accordance with theory.

A study on the geometric parameters has also been conducted in the case of the rectangular nanoantenna arrays, and isolated nanoantennas. The lineshape including additional resonances

## *Conclusion*

apart from the strongest LSPR has been addressed. For a more profound understanding and better matching to the experimental results, additional modeling should be performed. It might however be beneficial to apply lighter simulation methods than the FDTD method or possibly analytical models that provide better insight without need for demanding computational resources.

An interesting point is moreover the investigation of the scattering and absorption cross sections and their ratios allowing us to evaluate the coupling regime of the nanoantennas. The impact of scattering and absorption on the SEIRA signal contrast has been mentioned several times and remains an issue to be studied more deeply for further optimization. Notably, it would be of interest to determine if there are intrinsic limits to the scattering to absorption ratio due to the operation in a spectral range close to the plasma frequency, yielding always under-coupled antenna as in our investigated examples, or if it is possible to obtain also critical- or over-coupled nanoantennas by modification of the shape and the geometrical parameters.

We have fabricated nanoantenna arrays by large scale surface patterning methods such as photolithography or interferential lithography in combination with either chemical etching or reactive ion etching (RIE). A description of the main fabrication steps is given in the manuscript. The main challenge was the fabrication of structures with small lattice parameters where the interferential lithography proved to be beneficial. Chemical etching provides an excellent selectivity between the InAsSb layer and the GaSb substrate but on the other hand leads to a reduction of the size of the nanoantennas due to lateral etching, which can be avoided using RIE. Diverse technological processes had to be redeveloped after a relocation of the clean room facilities, and notably the standard ICP-RIE recipe was adapted for the etching of thin layers. ICP-RIE has given rise to several initial promising results and its optimization should be continued in future work. It avoids notably the different etching kinetics as a function of the crystalline direction, and is applicable also to etch narrow but deep apertures.

Experimentally, an optical characterization by FTIR spectroscopy was performed to investigate the LSPR sustained by the different types of structures. The tunability of the resonance wavelength by the geometric parameters as well as by the doping level was experimentally verified. The rectangular nanoantenna arrays provide LSPR at different wavelengths which can be selected by the optical polarization, a longitudinal LSPR for polarization along the long axis and a transverse LSPR for polarization along the short axis of the nanoantennas. This is beneficial to enlarge the accessible spectral range for resonant SEIRA spectroscopy without losing the advantages of the narrow resonances which signify a high quality factor due to low losses in the material. The interaction range of the nanoantennas organized in arrays was furthermore investigated and found to be relatively short due to the dominantly absorbing material of the nanoantennas.

Going finally towards the objective of chemical or biological sensing, several proof of concept experiments have been performed. It has successfully been demonstrated that the plasmonic nanoantenna substrates respond to the analyte layers. Precisely, different polymers which can be

deposited in controlled thicknesses by spincoating, and the aromatic compound vanillin with absorption features at high mid-IR wavelengths were detected. Bulk sensitivities in the range of  $10^2$  to  $10^3$  nm/RIU were reached in LSPR sensing. Indeed, the value depends possibly strongly on the size of the nanoantennas. The highest value was found for the longitudinal resonance of a rectangular nanoantenna where the dipole moment is higher than for the transverse resonances.

Enhanced vibrational signals of PMMA and vanillin have been detected. The vibrational signals increased of factors ranging between approximately 1.2-5.7 compared to unenhanced signals, and the SEIRA enhancement factor has been estimated to be in the range of  $10^3$  to  $10^4$  for the rectangular nanoantenna arrays, where we have used electric field profiles calculated by the FDTD method to determine the electric field hotspots. Compared to the literature where most demonstrations of SEIRA are performed with gold nanostructures, this is in the range of the usually reported enhancement factors between  $10^3$  and  $10^5$  [NHW<sup>+</sup>17]. Best enhancement factors with gold nanoantennas are typically reached exploiting additionally non-resonant enhancement as the lightning rod effect and confinement in gaps. Besides, considerations on the material quality have become more important, for example the use of monocrystalline gold flakes to avoid additional losses due to material defects [NHW<sup>+</sup>17]. Epitaxially grown III-V materials might be beneficial with respect to this point, as the material quality is good, especially for the lattice matched growth.

More recent SEIRA studies are also concerned with the ratio of external and internal damping and not only with the electric field enhancement, because this provides an additional means to optimize the signal contrast. Calculations of the scattering and absorption cross sections of the InAsSb antennas showed that absorption is always the dominant loss channel for the investigated range of geometries, so that the antennas are in an under-coupled regime. Indeed, the low contribution of scattering reduces the interaction between antennas in an array arrangement. While this limits the possibilities to benefit from collective effects it enables however the densification of the antennas without having to deal with collective interactions that might considerably alter the optical response. Consequently, the proposed nanoantenna arrays are optimal to fabricate dense arrays with strong optical resonances.

Concluding on the achieved results, the adapted material properties of InAsSb for mid-IR plasmonics have been highlighted and we have gone one step further to building plasmonic devices such as sensor platforms based exclusively on highly doped semiconductors. Future objectives in the framework of the Supreme-B project are the integration of the plasmonic nanostructures in a biosensing device, including microfluidics and surface functionalization.

While a performance at the state of the art for semiconductor plasmonic devices has been shown, noble metals with precisely tailored properties reach yet higher sensitivities. To fully exploit the potential of HDSC materials, more sophisticated antenna designs for specific applications are imaginable. Fabrication methods such as electron beam lithography to obtain smaller antennas with more complex shape, potentially benefiting from the lightning rod effect or in combination with gaps, especially for single hotspot devices, could be thought of.

## *Conclusion*

Using the epitaxial growth, a multilayer system of lattice matched materials is relatively uncomplicated to fabricate. As explored in early simulation tests performed during this thesis, MIM structures could be of interest, using either an insulator thickness adapted to match the impedance of the structure to the free space to obtain negligible reflectance and hence perfect absorption or a very thin insulator thickness to excite gap plasmons. As discussed in the state of the art on SEIRA substrates, perfect absorbers are also interesting for sensing.

Furthermore, many recent examples can be found of plasmonic nanoantenna arrays being applied for flat optics, for beam steering and shaping [Gen17, Kuz17]. The technological knowledge acquired during this thesis concerning the fabrication of the InAsSb nanoantenna arrays opens the way to many other applications using similar types of structures, transferring these applications to the mid-IR spectral range.

# Appendix





## A. Derivation of the dispersion relation at a plane interface

In the following, the steps between equations 1.11 and 1.12 are detailed.  
The continuity of the in plane wave vector implies:

$$\beta_1^2 = \beta_2^2 = \beta^2$$

$$\kappa_1^2 + \epsilon_1 \frac{\omega^2}{c^2} = \kappa_2^2 + \epsilon_2 \frac{\omega^2}{c^2}.$$

Replacing  $\kappa_1^2 = \kappa_2^2 \frac{\epsilon_1^2}{\epsilon_2^2}$ :

$$\kappa_2^2 \left( \frac{\epsilon_1^2}{\epsilon_2^2} - 1 \right) = \frac{\omega^2}{c^2} (\epsilon_2 - \epsilon_1),$$

and then  $\kappa_2^2 = \beta^2 - \epsilon_2 \frac{\omega^2}{c^2}$ :

$$\beta^2 \left( \frac{\epsilon_1^2}{\epsilon_2^2} - 1 \right) = \frac{\omega^2}{c^2} \left( \frac{\epsilon_1^2}{\epsilon_2} - \epsilon_1 \right)$$

$$\beta^2 \frac{\epsilon_1^2 - \epsilon_2^2}{\epsilon_2^2} = \frac{\omega^2}{c^2} \epsilon_1 \frac{\epsilon_1 - \epsilon_2}{\epsilon_2}$$

$$\beta^2 = \frac{\omega^2}{c^2} \frac{\epsilon_1 \epsilon_2 (\epsilon_1 - \epsilon_2)}{(\epsilon_1 - \epsilon_2)(\epsilon_1 + \epsilon_2)}$$

$$\beta^2 = \frac{\omega^2}{c^2} \frac{\epsilon_1 \epsilon_2}{\epsilon_1 + \epsilon_2}.$$



## B. The finite-difference time-domain (FDTD) method

The FDTD method can be used to solve Maxwell's equations in complex physical structures, defined by their spatial extension and their dielectric function. It is based on an algorithm proposed by Kane Yee in 1966 [Yee66]. As indicated in the name of the method, spatial and temporal derivatives in Maxwell's equations, notably in Ampère's law (equation 0.1) and Faraday's law (equation 0.2), are replaced by finite differences

$$\left. \frac{df(x)}{dx} \right|_{x=x_0} = \frac{f(x_0 + \frac{\delta}{2}) - f(x_0 - \frac{\delta}{2})}{\delta} + \mathcal{O}(\delta^2). \quad (\text{B.1})$$

This constitutes an approximation of the degree of the neglected higher order term. For example, the original formulation from Yee employs second order central differences.

The equations are solved on a discrete temporal and spatial grid, the so called mesh. The solution is calculated in the time space. From Ampère's and Faraday's laws, the spatial derivative of the magnetic field is expressed by the temporal derivative of the electric field and vice versa. So, to calculate the magnetic field at the time  $t + 1$ , the electric field at all points of space at time  $t$  is needed. The initial field distribution is introduced by a light pulse from a source. The nodes of the mesh of the electric and magnetic fields are shifted of half a cell, as indicated in Figure B.1. The Yee algorithm consists of the following steps [Sch]:

1. Spatial and temporal derivatives in Ampère's and Faraday's law are replaced by finite differences. Time and space are discretized so that the electromagnetic fields  $\mathbf{E}$  and  $\mathbf{H}$  are staggered in time and space.
2. Solving the finite difference equations allows to find «update equations» expressing the unknown future fields in terms of known past fields.
3. Evaluate the magnetic field one time-step into the future using the known electric field at  $t$ . It becomes a past field.
4. Evaluate the electric field one time-step into the future using the known magnetic field at  $t$ . It becomes a past field.
5. Repeat steps 3 and 4 until the complete duration of the simulation is reached.

From the solution in the time-domain, diverse quantities can be obtained by Fourier transformation. The method is especially useful for wide frequency range solutions as the frequencies are contained in the time domain information.

B. The finite-difference time-domain (FDTD) method

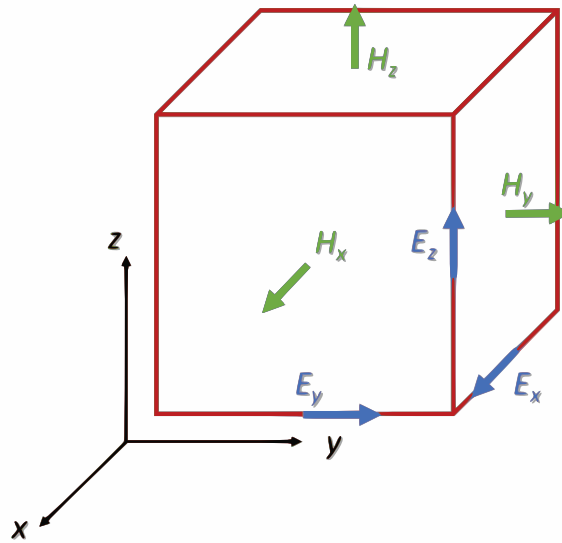


Figure B.1.: Schematic illustration of the Yee cell indicating the positions of the field components. The  $E$  components are in the middle of the edges and the  $H$  components in the center of the faces.

The FDTD method belongs to the resonance region techniques, where the characteristic dimensions of the simulated objects are approximately of the size of the wavelength. If this is not the case, other methods may be more adapted, for example quasi-static approaches when the objects are much smaller than the wavelength, or geometrical ray methods when the objects are much bigger than it. As other numerical methods, the FDTD method can suffer from artifacts due to the implementation and has a limited accuracy depending on the implementation and the numerical errors. The method can require a high amount of memory and time, depending on the number of Yee nodes which can be large for accurate calculations.

## C. List of the plasmonic grating structures with a resonance at $10\ \mu\text{m}$

The following list summarizes the geometrical parameters, the resonance wavelength and the FWHM of the resonance peak of the structures that were investigated in detail for the optimization study for sensing at  $10\ \mu\text{m}$ .

Ribbon thickness $t$ (nm)	Ribbon width $w$ (nm)	LSPR wavelength ( $\mu\text{m}$ )	FWHM ( $\mu\text{m}$ )
50	160	$9.965 \pm 0.001$	$0.973 \pm 0.009$
55	180	$10.061 \pm 0.002$	$1.069 \pm 0.012$
60	190	$10.027 \pm 0.002$	$1.148 \pm 0.014$
65	200	$10.008 \pm 0.002$	$1.145 \pm 0.016$
70	210	$9.999 \pm 0.002$	$1.193 \pm 0.018$
75	220	$9.999 \pm 0.002$	$1.224 \pm 0.019$
80	230	$10.007 \pm 0.002$	$1.246 \pm 0.020$
85	240	$10.023 \pm 0.002$	$1.278 \pm 0.021$
90	250	$10.045 \pm 0.002$	$1.281 \pm 0.020$
100	260	$9.998 \pm 0.002$	$1.406 \pm 0.026$
110	170	$9.976 \pm 0.002$	$1.494 \pm 0.029$
120	280	$9.974 \pm 0.002$	$1.544 \pm 0.032$
130	290	$9.987 \pm 0.002$	$1.602 \pm 0.032$
140	300	$10.013 \pm 0.002$	$1.580 \pm 0.033$
150	300	$9.955 \pm 0.002$	$1.698 \pm 0.034$
200	320	$9.967 \pm 0.001$	$1.766 \pm 0.032$
250	320	$9.907 \pm 0.001$	$1.789 \pm 0.020$
300	320	$9.893 \pm 0.001$	$1.750 \pm 0.015$

Table C.1.: List of the grating geometries sustaining a LSPR at  $10\ \mu\text{m}$ . The periodicity  $\Lambda$  is  $500\ \text{nm}$ .



## D. RCWA calculation of a 2D periodic rectangular nanoantenna array

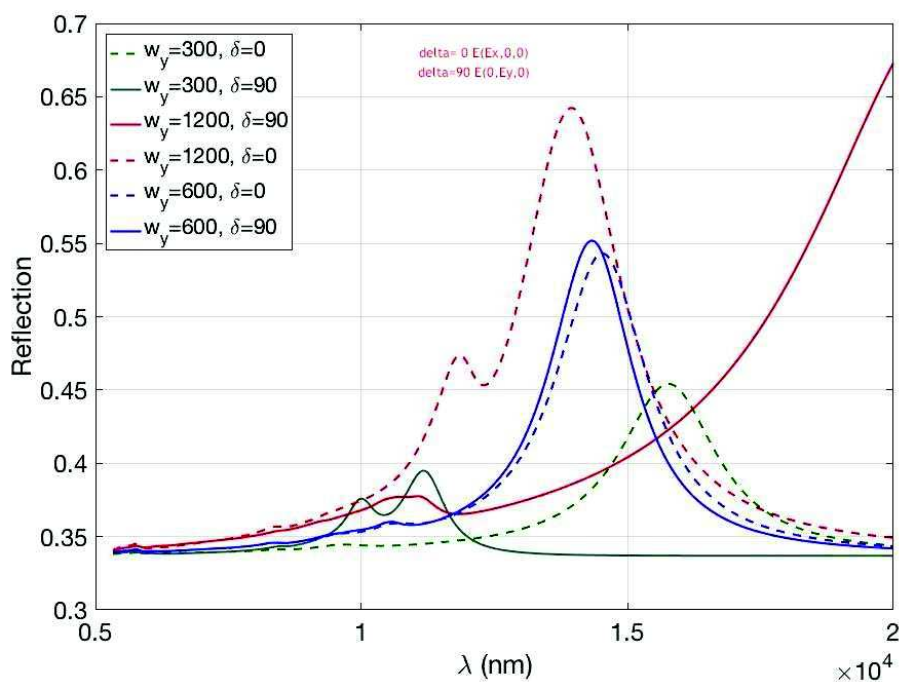


Figure D.1.: RCWA calculation of a 2D periodic nanoantenna array with dimensions  $w_x = 600$  nm,  $w_y$  as indicated in the figure,  $\Lambda_x = 1.4 \mu\text{m}$  and  $\Lambda_y = 2.0 \mu\text{m}$ .  $\delta = 0^\circ$  corresponds to  $x$  polarization, and  $\delta = 90^\circ$  to  $y$  polarization. The calculations were performed by E. Centeno's group at the University Clermont Auvergne.





# E. Overview of the available beam splitters and detectors for the FTIR spectrometer

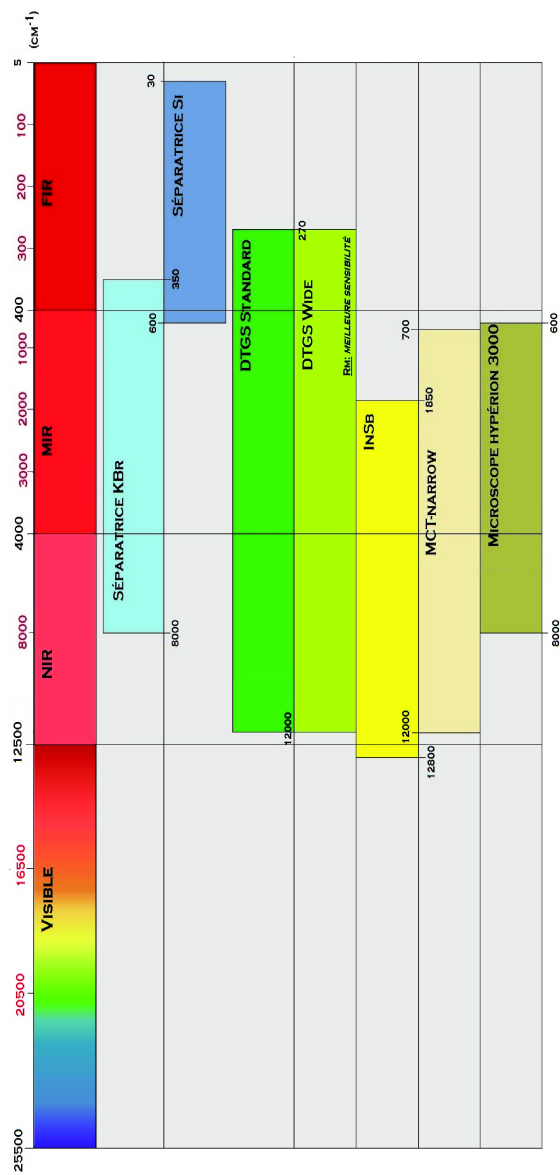


Figure E.1.: Overview of the available beam splitters and detectors for the FTIR spectrometer to cover different spectral ranges. Figure from [Des14].



## Bibliography

- [AAA15] Ronen Adato, Serap Aksu, and Hatice Altug. Engineering mid-infrared nanoantennas for surface enhanced infrared absorption spectroscopy. *Materials Today*, 18(8):436–446, 2015.
- [AAEA13] Ronen Adato, Alp Artar, Shyamsunder Erramilli, and Hatice Altug. Engineered absorption enhancement and induced transparency in coupled molecular and plasmonic resonator systems. *Nano Letters*, 13(6):2584–2591, 2013.
- [Ada89] Sadao Adachi. Optical dispersion relations for GaP, GaAs, GaSb, InP, InAs, InSb,  $\text{Al}_x\text{Ga}_{1-x}\text{As}$ , and  $\text{In}_{1-x}\text{Ga}_x\text{As}_y\text{P}_{1-y}$ . *Journal of Applied Physics*, 66(12):6030, 1989.
- [AHL<sup>+</sup>08] Jeffrey N Anker, W Paige Hall, Olga Lyandres, Nilam C Shah, Jing Zhao, and Richard P Van Duyne. Biosensing with plasmonic nanosensors. *Nat. Mater.*, 7:8–10, 2008.
- [Ani14] Ülkü Anik. Biosensors Nanotechnology. In Ashutosh Tiwari and Anthony P. F. Turner, editors, *Biosensors Nanotechnology*, chapter 3. Scrivener Publishing Wiley, 2014.
- [AOS<sup>+</sup>14] Srdjan S. Acimovic, Maria A. Ortega, Vanesa Sanz, Johann Berthelot, Jose L. Garcia-Cordero, Jan Renger, Sebastian J. Maerkl, Mark P. Kreuzer, and Romain Quidant. LSPR chip for parallel, rapid, and sensitive detection of cancer markers in serum. *Nano Letters*, 14(5):2636–2641, 2014. PMID: 24730454.
- [Aro06] Ricardo Aroca. *Surface-Enhanced Vibrational Spectroscopy*. Wiley, 2006.
- [ARS<sup>+</sup>13] Heykel Aouani, Mohsen Rahmani, Hana Sipova, Victor Torres, Katerina Hegnerova, Miguel Beruete, Jiri Homola, Minghui Hong, Miguel Navarro-Cia, and Stefan A. Maier. Plasmonic nanoantennas for multispectral surface-enhanced spectroscopies. *The Journal of Physical Chemistry C*, 117(36):18620–18626, 2013.
- [AS11] Paul M Amirtharaj and David G Seiler. Optical Properties of Semiconductors. In *Handbook of Optics Volume II Devices Measurements and Properties Second Edition*, volume 54. McGraw-Hill, 2011.
- [ASM16] Hussein I. Abdel-Shafy and Mona S. M. Mansour. A review on polycyclic aromatic hydrocarbons: Source, environmental impact, effect on human health and remediation. *Egyptian Journal of Petroleum*, 25:107–123, 2016.

- [ASR<sup>+</sup>13] Heykel Aouani, Hana Sipova, Mohsen Rahmani, Miguel Navarro-Cia, Katerina Hegnerova, Jiri Homola, Minghui Hong, and Stefan A. Maier. Ultrasensitive broadband probing of molecular vibrational modes with multifrequency optical antennas. *ACS Nano*, 7(1):669–675, 2013. PMID: 23199257.
- [Atw07] Harry A. Atwater. The Promise of Plasmonics. *Scientific American*, 296(4):56–62, 2007.
- [AWP<sup>+</sup>14] Martina Abb, Yudong Wang, Nikitas Papasimakis, C. H. de Groot, and Otto L. Muskens. Surface-enhanced infrared spectroscopy using metal oxide plasmonic antenna arrays. *Nano Letters*, 14(1):346–352, 2014. PMID: 24341902.
- [AYA<sup>+</sup>09] Ronen Adato, Ahmet A Yanik, Jason J Amsden, David L Kaplan, Fiorenzo G Omenetto, Mi K Hong, Shyamsunder Erramilli, and Hatice Altug. Ultra-sensitive vibrational spectroscopy of protein monolayers with plasmonic nanoantenna arrays. *Proc. Natl. Acad. Sci. U.S.A.*, 106(46):19227–19232, 2009.
- [AYA11] Ronen Adato, Ahmet A. Yanik, and Hatice Altug. On chip plasmonic monopole nano-antennas and circuits. *Nano Letters*, 11(12):5219–5226, 2011.
- [BA11] A. Boltasseva and H. A. Atwater. Low-loss plasmonic metamaterials. *Science*, 331(6015):290–291, 2011.
- [BBI<sup>+</sup>05] Alexandre Bouhelier, Renaud Bachelot, Jin Seo Im, Gary P Wiederrecht, Gilles Lerondel, Sergei Kostcheev, and Pascal Royer. Electromagnetic interactions in plasmonic nanoparticle arrays. *J. Phys. Chem. B*, 109:3195–3198, 2005.
- [BCF16] Dmitriy S. Boyuk, Li-Wei Chou, and Michael A. Filler. Strong near-field coupling of plasmonic resonators embedded in Si nanowires. *ACS Photonics*, 3(2):184–189, 2016.
- [BCKT12] B. J. Battersby, A. Chen, D. Kozak, and M. Trau. Woodhead Publishing Series in Biomaterials: Number 45. In Seamus Higson, editor, *Biosensors for medical applications*, chapter 7. Woodhead Publishing, Oxford, Cambridge, Philadelphia, New Delhi, 2012.
- [BDN09] P. Bharadwaj, B. Deutsch, and L. Novotny. Optical antennas. *Adv. Opt. Photon.*, 1:438, 2009.
- [BFV14] Martin D. Baaske, Matthew R. Foreman, and Frank Vollmer. Single-molecule nucleic acid interactions monitored on a label-free microcavity biosensor platform. *Nature Nanotechnology*, 9:933–939, 2014.
- [BGN14] Shahin Bagheri, Harald Giessen, and Frank Neubrech. Large-area antenna-assisted SEIRA substrates by laser interference lithography. *Adv. Optical Mater.*, 2:1050–1056, 2014.
- [BH07] Craig F. Bohren and Donald R. Huffman. *Absorption and Scattering of Light by Small Particles*. John Wiley and Sons, 2007.

- [BHM<sup>+</sup>12] Uwe Bog, Klaus Huska, Frieder Maerkle, Alexander Nesterov-Mueller, Uli Lemmer, and Timo Mappes. Design of plasmonic grating structures towards optimum signal discrimination for biosensing applications. *Optics Express*, 20(10):11357–69, 2012.
- [Bia] Biacore. <https://proteins.gelifesciences.com/products-for-proteins/spr-systems/>. Accessed: 2017-sept.
- [BKS<sup>+</sup>13] Tomas Bertok, Ludmila Klukova, Alena Sediva, Peter Kasak, Vladislav Semak, Matej Micusik, Maria Omastova, Lucia Chovanova, Miroslav Vlcek, Richard Imrich, Alica Vikartovska, and Jan Tkac. Ultrasensitive impedimetric lectin biosensors with efficient antifouling properties applied in glycoprofiling of human serum samples. *Analytical Chemistry*, 85(15):7324–7332, 2013. PMID: 23808876.
- [BLZ<sup>+</sup>17] Abdoullatif Baraket, Michael Lee, Nadia Zine, Monique Sigaud, Joan Bausells, and Abdelhamid Errachid. A fully integrated electrochemical biosensor platform fabrication process for cytokines detection. *Biosensors and Bioelectronics*, 93:170–175, 2017.
- [BM14] Jérémy Butet and Olivier J F Martin. Refractive index sensing with Fano resonant plasmonic nanostructures: a symmetry based nonlinear approach. *Nanoscale*, 6(24):15262–70, 2014.
- [Bro12] Alexandre G. Brolo. Plasmonics for future biosensors. *Nature Photonics*, 6(11):709–713, 2012.
- [Bru] Bruker. Tutorial: Introduction to FTIR spectroscopy.
- [BSF<sup>+</sup>15] Leonetta Baldassarre, Emilie Sakat, Jacopo Frigerio, Antonio Samarelli, Kevin Gallacher, Eugenio Calandrini, Giovanni Isella, Douglas J Paul, Michele Ortolani, and Paolo Biagioni. Midinfrared plasmon-enhanced spectroscopy with germanium antennas on silicon substrates. *Nano Letters*, 15:7225–7231, 2015.
- [BSGO09] Barry Byrne, Edwina Stack, Niamh Gilmartin, and Richard O’Kennedy. Antibody-based sensors: Principles, problems and potential for detection of pathogens and associated toxins. *Sensors*, 9(6):4407–4445, 2009.
- [BT04] Ursula Bilitewski and Anthony P. F. Turner. *Biosensors for Environmental Monitoring*. Taylor & Francis Routledge, 2004.
- [BW02] Max Born and Emil Wolf. *Principles of Optics*. Cambridge University Press, 7 edition, 2002.
- [BWG<sup>+</sup>15] Shahin Bagheri, Ksenia Weber, Timo Gissibl, Thomas Weiss, Frank Neubrech, and Harald Giessen. Fabrication of square-centimeter plasmonic nanoantenna arrays by femtosecond direct laser writing lithography: Effects of collective excitations on SEIRA enhancement. *ACS Photonics*, 2(6):779–786, 2015.

- [BYZ<sup>+</sup>15] Lisa V Brown, Xiao Yang, Ke Zhao, Bob Y Zheng, Peter Nordlander, and Naomi J Halas. Fan-shaped gold nanoantennas above reflective substrates for surface-enhanced infrared absorption (SEIRA). *Nano Letters*, 15(2):1272–80, 2015.
- [BZK<sup>+</sup>13] Lisa V Brown, Ke Zhao, Nicholas Sun King, Heidar Sobhani, Peter Nordlander, and Naomi J Halas. Surface-Enhanced Infrared Absorption using individual cross antennas tailored to chemical moieties Surface-Enhanced Infrared Absorption using individual cross antennas tailored to chemical moieties. *Journal American Chemical Society*, 135:3688–3695, 2013.
- [CA12] Arif E Cetin and Hatice Altug. Fano resonant ring/disk plasmonic nanocavities on conducting substrates for advanced biosensing. *ACS nano*, 6(11):9989–95, 2012.
- [CAA12] Kai Chen, Ronen Adato, and Hatice Altug. Dual-band perfect absorber for infrared spectroscopy. *ACS nano*, 6(9):7998–8006, 2012.
- [Car14] L Pires Carneiro. *Development of an Electrochemical Biosensor Platform and a Suitable Low-Impedance Surface Modification Strategy*. PhD thesis, Karlsruhe Institut für Technologie, 2014.
- [CBF15] Li-Wei Chou, Dmitriy S. Boyuk, and Michael A. Filler. Optically abrupt localized surface plasmon resonances in Si nanowires by mitigation of carrier density gradients. *ACS Nano*, 9(2):1250–1256, 2015. PMID: 25612192.
- [CCSO15] Xiaoshu Chen, Cristian Ciraci, David R. Smith, and Sang-Hyun Oh. Nanogap-enhanced infrared spectroscopy with template-stripped wafer-scale arrays of buried plasmonic cavities. *Nano Letters*, 15(1):107–113, 2015. PMID: 25423481.
- [CDI<sup>+</sup>15] Kai Chen, Thang Duy Dao, Satoshi Ishii, Masakazu Aono, and Tadaaki Nagao. Infrared aluminum metamaterial perfect absorbers for plasmon-enhanced infrared spectroscopy. *Advanced Functional Materials*, 25(42):6637–6643, 2015.
- [CEA14] Arif E. Cetin, Dordaneh Etezadi, and Hatice Altug. Accessible nearfields by nanoantennas on nanop pedestals for ultrasensitive vibrational spectroscopy. *Advanced Optical Materials*, 2(9):866–872, 2014.
- [CG02] J. M. Chalmers and P. R. Griffiths. *Handbook of Vibrational Spectroscopy*. John Wiley and Sons, Ltd., Chichester, 2002.
- [Che09] Yu-Bin Chen. Development of mid-infrared surface plasmon resonance-based sensors with highly-doped silicon for biomedical and chemical applications. *Optics Express*, 17(5):3130–3140, 2009.
- [CKF<sup>+</sup>17] Jonathan Cramer, Stefan G. Krimmer, Veronica Fridh, Tobias Wulsdorf, Robert Karlsson, Andreas Heine, and Gerhard Klebe. Elucidating the origin of long residence time binding for inhibitors of the metalloprotease thermolysin. *ACS Chem. Biol.*, 12:225–233, 2017.

- [CKLH11] Claire E. Chivers, Apurba L. Koner, Edward D. Lowe, and Mark Howarth. How the biotin-streptavidin interaction was made even stronger: investigation via crystallography and a chimaeric tetramer. *Biochemical Journal*, 435(1):55–63, 2011.
- [CLC16] Jungseok Chae, Basudev Lahiri, and Andrea Centrone. Engineering near-field SEIRA enhancements in plasmonic resonators. *ACS Photonics*, 3(1):87–95, 2016.
- [CMO12] C. Crean, C. McGeough, and R. OKennedy. Woodhead Publishing Series in Biomaterials: Number 45. In Seamus Higson, editor, *Biosensors for medical applications*, chapter 11. Woodhead Publishing, Oxford, Cambridge, Philadelphia, New Delhi, 2012.
- [CMS<sup>+</sup>12] Justin W. Cleary, Gautam Medhi, Monas Shahzad, Imen Rezadad, Doug Maukonen, Robert E. Peale, Glenn D. Boreman, Sandy Wentzell, and Walter R. Buchwald. Infrared surface polaritons on antimony. *Optics Express*, 20(3):2693–2705, 2012.
- [CPN<sup>+</sup>14] Susana Campuzano, Maria Pedrero, Gerogia-Paraskevi Nikoleli, José M Pingarron, Dimitrios P. Nikoleis, Nikolaos Tzamtzis, and Vasilios N. Psychoyios. Biosensors Nanotechnology. In Ashutosh Tiwari and Anthony P. F. Turner, editors, *Biosensors Nanotechnology*, chapter 1. Scrivener Publishing Wiley, 2014.
- [CSR<sup>+</sup>12] J. C. Claussen, J. Shi, C. S. Rout, M. S. Artiles, M. M. Roushar, M. C. Stensberg, D. Marshall Porterfield, and T. S. Fisher. Woodhead Publishing Series in Biomaterials: Number 45. In Seamus Higson, editor, *Biosensors for medical applications*, chapter 3. Woodhead Publishing, Oxford, Cambridge, Philadelphia, New Delhi, 2012.
- [CYG15] Fei Cheng, Xiaodong Yang, and Jie Gao. Ultrasensitive detection and characterization of molecules with infrared plasmonic metamaterials. *Scientific reports*, 5:14327, 2015.
- [CYNH16] Benjamin Cerjan, Xiao Yang, Peter Nordlander, and Naomi J. Halas. Asymmetric aluminum antennas for self-calibrating surface-enhanced infrared absorption spectroscopy. *ACS Photonics*, 3(3):354–360, 2016.
- [CZN<sup>+</sup>12] Stefano Cataldo, Jun Zhao, Frank Neubrech, Bettina Frank, Chunjie Zhang, Paul V Braun, and Harald Giessen. Hole-mask colloidal nanolithography for large-area low-cost metamaterials and antenna-assisted surface-enhanced infrared absorption substrates. *ACS nano*, 6(1):979–85, 2012.
- [CZP<sup>+</sup>09] Ertogrul Cubukcu, Shuang Zhang, Yong-Shik Park, Guy Bartal, and Xiang Zhang. Split ring resonator sensors for infrared detection of single molecular monolayers. *Appl. Phys. Lett.*, 95:04113, 2009.
- [DBT<sup>+</sup>13] Cristiano D’Andrea, Jorg Bochterle, Andrea Toma, Christian Huck, Frank Neubrech, Elena Messina, Barbara Fabrizio, Onofrio M Marago, Enzo Di Fabrizio,



- Marc Lamy De La Chapelle, Pietro G Gucciardi, and Annemarie Pucci. Optical nanoantennas for multiband spectroscopy. *ACS Nano*, 7(4):3522–3531, 2013.
- [Des14] Rudy Desgarceaux. Rapport de stage. Université de Montpellier, 2014.
- [DH06] Jakub Dostalek and Jiri Homola. SPR Biosensors for Environmental Monitoring. In Jiri Homola, editor, *Surface Plasmon Resonance Based Sensors*, chapter 8, pages 191–206. Springer, Berlin, Heidelberg, 2006.
- [DH12a] F. Davis and S. P. J. Higson. Woodhead Publishing Series in Biomaterials: Number 45. In Seamus Higson, editor, *Biosensors for medical applications*, chapter 5. Woodhead Publishing, Oxford, Cambridge, Philadelphia, New Delhi, 2012.
- [DH12b] F. Davis and S. P. J. Higson. Woodhead Publishing Series in Biomaterials: Number 45. In Seamus Higson, editor, *Biosensors for medical applications*, chapter 6. Woodhead Publishing, Oxford, Cambridge, Philadelphia, New Delhi, 2012.
- [DKB94] Gregory C Desalvo, Ron Kaspi, and Christopher A Bozada. Citric acid etching of GaAs<sub>x</sub>Sb<sub>x</sub>, Al<sub>0.5</sub>Ga<sub>0.5</sub>Sb, and InAs for heterostructure device fabrication. *Electrochemical Society*, 141(12):12, 1994.
- [DLGA04] Oliver Dier, Chun Lin, Markus Grau, and Markus-Christian Amann. Selective and non-selective wet-chemical etchants for GaSb-based materials. *Semiconductor Science and Technology*, 19(11):1250–1253, 2004.
- [DLJH06] Jakub Dostalek, Jon Ladd, Shaoyi Jiang, and Jiri Homola. SPR Biosensors for Detection of Biological and Chemical Analytes. In Jiri Homola, editor, *Surface Plasmon Resonance Based Sensors*, chapter 7, pages 177–190. Springer, Berlin, Heidelberg, 2006.
- [DLP10] William DiPippo, Bong Jae Lee, and Keunhan Park. Design analysis of doped-silicon surface plasmon resonance immunosensors in mid-infrared range. *Optics Express*, 18(18):19396–19406, 2010.
- [DLTSP16] Francesco De Leonardis, Benedetto Troia, Richard A. Soref, and Vittorio M. N. Passaro. Investigation of mid-infrared second harmonic generation in strained germanium waveguides. *Optics Express*, 24(10):11126–11144, 2016.
- [DLYE04] A. Degiron, H. J. Lezec, N. Yamamoto, and T. W. Ebbesen. Optical transmission properties of a single subwavelength aperture in a real metal. *Optics Communications*, 239(1-3):61–66, 2004.
- [DMB<sup>+</sup>09] Lorenzo Dominici, Francesco Michelotti, Thomas M. Brown, Andrea Reale, and Aldo Di Carlo. Plasmon polaritons in the near infrared on fluorine doped tin oxide films. *Optics Express*, 17(12):10155–10167, 2009.

- [DND<sup>+</sup>12] Daniel Dregely, Frank Neubrech, Huigao Duan, Ralf Vogelgesang, and Harald Giessen. Vibrational near-field mapping of planar and buried three-dimensional plasmonic nanostructures. *Nat. Comm.*, 4:2237, 2012.
- [Dur02] James R. Durig. Utility of Isotopic Data. In J. M. Chalmers and P. R. Griffiths, editors, *Handbook of Vibrational Spectroscopy*. Wiley, Chichester, 2002.
- [dVB14] Manel del Valle and Alessandra Bonanni. Biosensors Nanotechnology. In Ashutosh Tiwari and Anthony P. F. Turner, editors, *Biosensors Nanotechnology*, chapter 4. Scrivener Publishing Wiley, 2014.
- [DVK16] P. Damborsky, J. Vitel, and J. Katrik. Optical biosensors. *Essays In Biochemistry*, 60(1):91–100, 2016.
- [Edi15] Editorial. Commercializing plasmonics. *Nat. Photonics*, 9:477, 2015.
- [Eil03] Paul H C Eilers. A perfect smoother. *Analytical Chemistry*, 75(14):3631–3636, 2003.
- [ELG<sup>+</sup>98] T. W. Ebbesen, H. J. Lezec, H. F. Ghaemi, T. Thio, and P. A. Wolff. Extraordinary optical transmission through sub-wavelength hole arrays. *Nature*, 391:667–669, 1998.
- [Fan61] U. Fano. Effects of configuration interaction on intensities and phase shifts. *Physical Review*, 124(6):1866–1878, 1961.
- [Fel49] P. B. Fellgett. Theory of infra-red sensitivities and its application to investigations of stellar radiation in the near infra-red. *Journal of the Optical Society of America*, 39(11):970, 1949.
- [FHM74] M. Fleischmann, P.J. Hendra, and A.J. McQuillan. Raman spectra of pyridine adsorbed at a silver electrode. *Chemical Physics Letters*, 26(2):163 – 166, 1974.
- [FRG<sup>+</sup>17] Marco Patrick Fischer, Aaron Riede, Alexander Grupp, Kevin Gallacher, Jacopo Frigerio, Giovanni Pellegrini, Michele Ortolani, Douglas J. Paul, Giovanni Isella, Alfred Leitenstorfer, Paolo Biagioni, and Daniele Brida. Mid-infrared third-harmonic emission from heavily-doped germanium plasmonic nanoantennas. In *Conference on Lasers and Electro-Optics*, page FF1G.2. Optical Society of America, 2017.
- [FSA<sup>+</sup>99] Don Farthing, Domenic Sica, Cheryl Abernathy, Itaf Fakhry, John D Roberts, Donald J Abraham, and Paul Swerdlow. High-performance liquid chromatographic method for determination of vanillin and vanillic acid in human plasma, red blood cells and urine. *Journal of Chromatography B*, 726:303–307, 1999.
- [Gai14] Quentin Gaimard. *Diodes lasers DFB à couplage par l'indice émettant entre 2  $\mu\text{m}$  et 3,3  $\mu\text{m}$  sur substrat GaSb*. PhD thesis, University of Montpellier, 2014.
- [GBS14] Urcan Guler, Alexandra Boltasseva, and Vladimir M. Shalaev. Refractory plasmonics. *Science*, 344(6181):263–264, 2014.

- [GBS<sup>+</sup>16] Lili Gui, Shahin Bagheri, Nikolai Strohfeldt, Mario Hentschel, Christine M Zgrabik, Bernd Metzger, Heiko Linnenbank, Evelyn L Hu, and Harald Giessen. Nonlinear refractory plasmonics with titanium nitride nanoantennas. *Nano Letters*, 16:5708–5713, 2016.
- [Gen17] Patrice Genevet. Engineering light propagation with planar or conformable optical metasurfaces. Barcelone, 2017. NANOP 2017, Nanophotonics and Micro/Nano-Optics Conference.
- [GFA<sup>+</sup>11] Vincenzo Giannini, Yan Francescato, Hemmel Amrania, Chris C Phillips, and Stefan A Maier. Fano resonances in nanoscale plasmonic systems : A parameter-free modeling approach. *Nano Letters*, 11(ii):2835–2840, 2011.
- [GJSD11] James C. Ginn, Robert L. Jarecki, Eric A. Shaner, and Paul S. Davids. Infrared plasmons on heavily-doped silicon. *Journal of Applied Physics*, 110(4), 2011.
- [GKBS15] Urcan Guler, Alexander V. Kildishev, Alexandra Boltasseva, and Vladimir M. Shalaev. Plasmonics on the slope of enlightenment: the role of transition metal nitrides. *Faraday Discuss.*, 178:71–86, 2015.
- [GNN<sup>+</sup>13] Urcan Guler, Justus C. Ndukaife, Gururaj V. Naik, A. G. Agwu Nnanna, Alexander V. Kildishev, Vladimir M. Shalaev, and Alexandra Boltasseva. Local heating with lithographically fabricated plasmonic titanium nitride nanoparticles. *Nano Letters*, 13(12):6078–6083, 2013.
- [GRSHBK03] J. Gómez Rivas, C. Schotsch, P. Haring Bolivar, and H. Kurz. Enhanced transmission of thz radiation through subwavelength holes. *Phys. Rev. B*, 68:201306, 2003.
- [GSB15] Urcan Guler, Vladimir M. Shalaev, and Alexandra Boltasseva. Nanoparticle plasmonics: going practical with transition metal nitrides. *Materials Today*, 18(4):227 – 237, 2015.
- [GVMM EK10] F. J. Garcia-Vidal, L. Martin-Moreno, T. W. Ebbesen, and L. Kuipers. Light passing through subwavelength apertures. *Rev. Mod. Phys.*, 82:729–787, 2010.
- [GWDM15] Simon A. Gregory, Yudong Wang, C. H. De Groot, and Otto L. Muskens. Extreme subwavelength metal oxide direct and complementary metamaterials. *ACS Photonics*, 2(5):606–614, 2015.
- [GXZ<sup>+</sup>13] Yongkang Gao, Zheming Xin, Beibei Zeng, Qiaoqiang Gan, Xuanhong Cheng, and Filbert J. Bartoli. Plasmonic interferometric sensor arrays for highperformance label-free biomolecular detection. *Lab Chip*, 13:4755–4764, 2013.
- [HCKVD05] Amanda J. Haes, Lei Chang, William L. Klein, and Richard P. Van Duyne. Detection of a biomarker for alzheimer’s disease from synthetic and clinical samples using a nanoscale optical biosensor. *J. Am. Chem. Soc.*, 127(7):2264–2271, 2005.

- [HFE<sup>+</sup>16] J. L. Hammond, N. Formisano, P. Estrela, S. Carrara, and J. Tkac. Electrochemical biosensors and nanobiosensors. *Essays In Biochemistry*, 60(1):69–80, 2016.
- [HJCT14] Jón Mattis Hoffmann, Hendrik Janssen, Dmitry N Chigrin, and Thomas Taubner. Enhanced infrared spectroscopy using small-gap antennas prepared with two-step evaporation nanosphere lithography. *Optics Express*, 22(12):2231–2236, 2014.
- [HKS<sup>+</sup>15] Anton Hasenkampf, Niels Kröger, Arthur Schönhals, Wolfgang Petrich, and Annemarie Pucci. Surface-enhanced mid-infrared spectroscopy using a quantum cascade laser. *Optics Express*, 23(5):5670–80, 2015.
- [HKT80] A. Hartstein, J. R. Kirtley, and J. C. Tsang. Enhancement of the infrared absorption from molecular monolayers with thin metal overlayers. *Physical Review Letters*, 45(3):201–204, 1980.
- [HMSB16] Alastair D. Humphrey, Nina Meinzer, Timothy A. Starkey, and William L. Barnes. Surface lattice resonances in plasmonic arrays of asymmetric disc dimers. *ACS Photonics*, 3(4):634–639, 2016.
- [HMZ<sup>+</sup>03] Christy L Haynes, Adam D Mcfarland, Linlin Zhao, Richard P Van Duyne, George C Schatz, Linda Gunnarsson, Juris Prikulis, Bengt Kasemo, and Mikael Ka. Nanoparticle optics : The importance of radiative dipole coupling in two-dimensional nanoparticle arrays. *J. Phys. Chem. B*, 107:7337–7342, 2003.
- [HNV<sup>+</sup>14] Christian Huck, Frank Neubrech, Jochen Vogt, Andrea Toma, David Gerbert, Julia Katzmann, Thomas Härtling, and Annemarie Pucci. Surface-enhanced infrared spectroscopy using nanometer-sized gaps. *ACS nano*, 8(5):4908–14, 2014.
- [Hom06a] Jiri Homola. Electromagnetic Theory of Surface Plasmons. In Jiri Homola, editor, *Surface Plasmon Resonance Based Sensors*, chapter 1. Springer, Berlin, Heidelberg, 2006.
- [Hom06b] Jiri Homola. *Surface Plasmon Resonance Based Sensors*, volume 5. Springer, 2006.
- [Hom08] Jiri Homola. Surface plasmon resonance sensors for detection of chemical and biological species. *Chemical Reviews*, 108(2):462–493, 2008. PMID: 18229953.
- [HP06] Jiri Homola and Marek Piliarik. Surface Plasmon Resonance (SPR) Sensors. In Jiri Homola, editor, *Surface Plasmon Resonance Based Sensors*, chapter 2. Springer, Berlin, Heidelberg, 2006.
- [HSB<sup>+</sup>09] Anthony J. Hoffman, Aishwarya Sridhar, Philip X. Braun, Leonid Alekseyev, Scott S. Howard, Kale J. Franz, Liwei Chen, Fow-Sen Choa, Deborah L. Sivco, Viktor A. Podolsky, Evgenii E. Narimanov, and Claire Gmachl. Midinfrared semiconductor optical metamaterials. *Journal of Applied Physics*, 105:122411, 2009.

- [HTN<sup>+</sup>15] Christian Huck, Andrea Toma, Frank Neubrech, Manohar Chirumamilla, Jochen Vogt, Francesco De Angelis, and Annemarie Pucci. Gold nanoantennas on a pedestal for plasmonic enhancement in the infrared. *ACS Photonics*, 2(4):497–505, 2015.
- [HV02] Amanda J. Haes and Richard P. Van Duyne. A nanoscale optical biosensor: Sensitivity and selectivity of an approach based on the localized surface plasmon resonance spectroscopy of triangular silver nanoparticles. *Journal American Chemical Society*, 124(7):10596–10604, 2002.
- [HvHB<sup>+</sup>17] Alexei Halpin, Niels van Hoof, Arkabrata Bhattacharya, Christiaan Mennes, and Jaime Gomez Rivas. Terahertz diffraction enhanced transparency probed in the near field. *Physical Review B*, 96(8):085110, 2017.
- [HWBG13] Mario Hentschel, Thomas Weiss, Shahin Bagheri, and Harald Giessen. Babinet to the half: Coupling of solid and inverse plasmonic structures. *Nano Letters*, 13(9):4428–4433, 2013.
- [HYR<sup>+</sup>13] Jon Mattis Hoffmann, Xinghui Yin, Jens Richter, Andrea Hartung, Tobias W. W Mass, and Thomas Taubner. Low-cost infrared resonant structures for surface-enhanced infrared absorption spectroscopy in the fingerprint region from 3 to 13  $\mu\text{m}$ . *The Journal of Physical Chemistry C*, 117:11311–11316, 2013.
- [HYZ<sup>+</sup>16] Hai Hu, Xiaoxia Yang, Feng Zhai, Debo Hu, Ruina Liu, Kaihui Liu, Zhipei Sun, and Qing Dai. Far-field nanoscale infrared spectroscopy of vibrational fingerprints of molecules with graphene plasmons. *Nature Communications*, 7:1–8, 2016.
- [IJC<sup>+</sup>09] A. Isoyan, F. Jiang, Y. C. Cheng, F. Cerrinab, P. Wachulak, L. Urbanski, J. Rocca, C. Menoni, and M Marconi. Talbot lithography: Self-imaging of complex structures. *J. Vac. Sci. Technol. B*, 27(6):2931–2937, 2009.
- [Ins] Oxford Instruments. <https://www.oxford-instruments.com/products/etching-deposition-and-growth/plasma-etch-deposition/icp-etch>. Accessed: 2017-sept.
- [JC72] P. B. Johnson and R. W. Christy. Optical constants of the noble metals. *Phys. Rev. B*, 6:4370–4379, Dec 1972.
- [JCC<sup>+</sup>98] Linda S Jung, Charles T Campbell, Timothy M Chinowsky, Mimi N Mar, and Sinclair S Yee. Quantitative interpretation of the response of surface plasmon resonance sensors to adsorbed films. *Langmuir*, 14(17):5636–5648, 1998.
- [KB12] Jacob B. Khurgin and Alexandra Boltasseva. Reflecting upon the losses in plasmonics and metamaterials. *MRS Bulletin*, 37(08):768–779, 2012.
- [KCB<sup>+</sup>16] Stefan G. Krimmer, Jonathan Cramer, Michael Betz, Veronica Fridh, Robert Karlsson, Andreas Heine, and Gerhard Klebe. Rational design of thermodynamic

- and kinetic binding profiles by optimizing surface water networks coating protein-bound ligands. *Journal of Medicinal Chemistry*, 59(23):10530–10548, 2016. PMID: 27933956.
- [KFN<sup>+</sup>14] N. Kinsey, M. Ferrera, G. V. Naik, V. E. Babicheva, V. M. Shalaev, and A. Boltas-seva. Experimental demonstration of titanium nitride plasmonic interconnects. *Opt. Express*, 22(10):12238–12247, 2014.
- [Khu15] Jacob B. Khurgin. How to deal with the loss in plasmonics and metamaterials. *Nature Nanotechnology*, 10(1):2–6, 2015.
- [KR68] E. Kretschmann and H. Raether. Radiative decay of non-radiative surface plasmons excited by light. *Z. Naturforsch.*, 23:2135–2136, 1968.
- [KS10] J. B. Khurgin and G. Sun. In search of the elusive lossless metal. *Applied Physics Letters*, 96(18):181102, 2010.
- [KS12] Jacob B. Khurgin and Greg Sun. Practicality of compensating the loss in the plasmonic waveguides using semiconductor gain medium. *Applied Physics Letters*, 100(1):011105, 2012.
- [KSJ<sup>+</sup>16] Alexander S Kuznetsov, Peter Schäfer, Vilfred John, Deepak Prasai, Sergey Sadofev, and Sascha Kalusniak. Enabling novel functionality in heavily doped ZnO:Ga by nanostructuring: an efficient plasmonic refractive index sensor. *Nanotechnology*, 27:02LT02 (5pp), 2016.
- [KT14] Emiko Kazuma and Tetsu Tatsuma. Localized surface plasmon resonance sensors based on wavelength-tunable spectral dips. *Nanoscale*, 6:2397–2405, 2014.
- [Kuz17] Arseniy Kuznetsov. Dielectric and semiconductor nanoantennas. Barcelone, 2017. NANOP 2017, Nanophotonics and Micro/Nano-Optics Conference.
- [KV95] Uwe Kreibig and Michael Vollmer. *Optical Properties of Metal Clusters*. Springer, 1995.
- [KZ70] Uwe Kreibig and Peter Zacharias. Surface plasma resonances in small spherical silver and gold particles. *Z. Physik*, 231:128–143, 1970.
- [LA14] Tony Low and Phaedon Avouris. Graphene plasmonics for terahertz to mid-infrared applications. *ACS Nano*, 8(2):1086–1101, 2014. PMID: 24484181.
- [LA16] Zizhuo Liu and Koray Aydin. Localized surface plasmons in nanostructured monolayer black phosphorus. *Nano Letters*, 16(6):3457–3462, 2016.
- [Lam] LambdaGen. <http://lamdagen.com/>. Accessed: 2017-sept.
- [LATW12] S Law, D C Adams, A M Taylor, and D Wasserman. Mid-infrared designer metals. *Optics Express*, 20(11):12155–12165, 2012.
- [Lav] Philip Laven. Mieplot v4.6. <http://www.philiplaven.com/mieplot.htm>.
- [LE09] Eric Le Ru and Pablo Etchegoin. *Principles of Surface Enhanced Raman Spectroscopy*. Elsevier, 2009.



- [LEW<sup>+</sup>16] Odeta Limaj, Dordaneh Etezadi, Nathan J. Wittenberg, Daniel Rodrigo, Daehan Yoo, Sang Hyun Oh, and Hatice Altug. Infrared plasmonic biosensor for real-time and label-free monitoring of lipid membranes. *Nano Letters*, 16(2):1502–1508, 2016.
- [LLW14] Stephanie Law, Runyu Liu, and Daniel Wasserman. Doped semiconductors with band-edge plasma frequencies. *Journal of Vacuum Science & Technology B, Nanotechnology and Microelectronics: Materials, Processing, Measurement, and Phenomena*, 32(2014):052601, 2014.
- [LM06] Stefan Löfas and Alan McWhirter. The Art of Immobilization for SPR Sensors. In Jiri Homola, editor, *Surface Plasmon Resonance Based Sensors*, chapter 5. Springer, Berlin, Heidelberg, 2006.
- [LMH<sup>+</sup>16] Christina Lambertz, Ariadna Martos, Andreas Henkel, Andreas Neiser, Torben Tobias Kliesch, Andreas Janshoff, Petra Schwille, and Carsten Sönnichsen. Single particle plasmon sensors as label-free technique to monitor minde protein wave propagation on membranes. *Nano Letters*, 16(6):3540–3544, 2016.
- [LN11] Debin Li and C Z Ning. All-semiconductor active plasmonic system in mid-infrared wavelengths. *Optics Express*, 19(15):14594–603, 2011.
- [LPW13] Stephanie Law, Viktor Podolskiy, and Daniel Wasserman. Towards nano-scale photonics with micro-scale photons: The opportunities and challenges of mid-infrared plasmonics. *Nanophotonics*, 2(2):103–130, 2013.
- [LSL<sup>+</sup>00] B Lamprecht, G Schider, R T Lechner, H Ditlbacher, J R Krenn, A Leitner, and F R Aussenegg. Metal nanoparticle gratings : Influence of dipolar particle interaction on the plasmon resonance. *Physical Review Letters*, 84(20):4721–4724, 2000.
- [LSS<sup>+</sup>13] Yongqian Li, Lei Su, Chen Shou, Chunmeng Yu, Jinjun Deng, and Yu Fang. Surface-enhanced molecular spectroscopy (SEMS) based on perfect-absorber metamaterials in the mid-infrared. *Scientific Reports*, 3:2865, 2013.
- [LT10] J. Leon and T. Taliercio. Large tunable photonic band gaps in nanostructured doped semiconductors. *Phys. Rev. B*, 82:195301, 2010.
- [LTJ06] Jon Ladd, Allen Taylor, and Shaoyi Jiang. SPR Biosensors for Food Safety. In Jiri Homola, editor, *Surface Plasmon Resonance Based Sensors*, chapter 9, pages 207–227. Springer, Berlin, Heidelberg, 2006.
- [LVV<sup>+</sup>16] Jiaqi Li, Niels Verellen, Dries Vercruyssen, Twan Bearda, Liesbet Lagae, and Pol Van Dorpe. All-dielectric antenna wavelength router with bidirectional scattering of visible light. *Nano Letters*, 16(7):4396–4403, 2016.
- [LWC<sup>+</sup>12] Lei Liu, Bin Wang, Xuwei Cao, Xiaoxuan Xu, and Yufang Wang. Comparison investigation of near- and far-field properties for plasmon resonance of

- silver nanosphere dimers. *Photonics and Nanostructures - Fundamentals and Applications*, 10(1):16 – 24, 2012.
- [LYF<sup>+</sup>14] Yilei Li, Hugen Yan, Damon B Farmer, Xiang Meng, Richard M Osgood, Tony F Heinz, and Phaedon Avouris. Graphene plasmon enhanced vibrational sensing of surface- adsorbed layers. *Nano Letters*, 14(3):1573–1577, 2014.
- [LYRW13] Stephanie Law, Lan Yu, Aaron Rosenberg, and Daniel Wasserman. All-semiconductor plasmonic nanoantennas for infrared sensing. *Nano letters*, 13(9):4569–74, 2013.
- [LYW13] Stephanie Law, Lan Yu, and Daniel Wasserman. Epitaxial growth of engineered metals for mid-infrared plasmonics. *Journal of Vacuum Science & Technology B: Microelectronics and Nanometer Structures*, 31(3):03C121, 2013.
- [Mai07] Stefan A. Maier. *Plasmonics: Fundamentals and Applications*. Springer, 2007.
- [Mar16] Vadim A. Markel. Introduction to the Maxwell Garnett approximation: tutorial. *Journal of the Optical Society of America A*, 33(7):1244, 2016.
- [MBGP<sup>+</sup>16] M J Milla, F Barho, F González-Posada, L Cerutti, M Bomers, J-B Rodriguez, E Tournié, and T Taliercio. Localized surface plasmon resonance frequency tuning in highly doped InAsSb/GaSb one-dimensional nanostructures. *Nanotechnology*, 27(42):425201, 2016.
- [MBGP<sup>+</sup>17] M. J. Milla, F. Barho, F. Gonzales-Posada, L. Cerutti, B. Charlot, M. Bomers, F. Neubrech, E. Tournié, and T. Taliercio. Surface-enhanced infrared absorption with Si-doped InAsSb/GaSb nano-antennas. *Optics Express*, in press, 2017.
- [MCCS12] P. A. Millner, R. L. Caygill, D. J. R. Conroy, and M. A. Shahidan. Woodhead Publishing Series in Biomaterials: Number 45. In Seamus Higson, editor, *Biosensors for medical applications*, chapter 4. Woodhead Publishing, Oxford, Cambridge, Philadelphia, New Delhi, 2012.
- [MH11] Kathryn M. Mayer and Jason H. Hafner. Localized surface plasmon resonance sensors. *Chemical Reviews*, 111(6):3828–3857, 2011.
- [Mie08] Gustav Mie. Beiträge zur Optik trüber Medien, speziell kolloidaler Metallösungen. *Annalen der Physik*, 330(3):377–445, 1908.
- [Mir82] D. N Mirlin. Surface Phonon Polaritons in Dielectrics and Semiconductors. In V. M. Agranovich and D. L. Mills, editors, *Surface Polaritons*, chapter 1. North-Holland Publishing Company, 1982.
- [MMHG16] Martin Mesch, Bernd Metzger, Mario Hentschel, and Harald Giessen. Nonlinear Plasmonic Sensing. *Nano Letters*, 16(5):3155–3159, 2016.
- [MMP12] L. Micheli, D. Moscone, and G. Palleschi. Woodhead Publishing Series in Biomaterials: Number 45. In Seamus Higson, editor, *Biosensors for medical*



- applications*, chapter 10. Woodhead Publishing, Oxford, Cambridge, Philadelphia, New Delhi, 2012.
- [MP17] Thomas G. Mayerhöfer and Jürgen Popp. Periodic array-based substrates for surface-enhanced infrared spectroscopy. *Nanophotonics*, 0(0), 2017.
- [MSdG<sup>+</sup>17] O. Muskens, K. Sun, C. de Groot, L. Bergamini, N. Zabala, J. Aizpurua, M. Simeoni, A. Urbani, and S. Mengali. Metal oxide metasurfaces for active control and space technology. In *EH-2: New materials for plasmonics and metamaterials*, Munich, 7 2017. CLEO/Europe-EQEC 2017.
- [MW85] M Meier and A Wokaun. Enhanced fields on rough surfaces : dipolar interactions among particles of sizes exceeding the Rayleigh limit. *J. Opt. Soc. Am. B*, 2(6):931–949, 1985.
- [MWA<sup>+</sup>14] Otto Muskens, Yudong Wang, Martina Abb, Stuart Boden, Javier Aizpurua, and Cornelis Hendrik De Groot. Helium ion beam milling for plasmonic nanoantennas. *SPIE Newsroom*, pages 3–5, 2014.
- [MZY<sup>+</sup>09] Tian Ming, Lei Zhao, Zhi Yang, Huanjun Chen, Lingdong Sun, Jianfang Wang, and Chunhua Yan. Strong polarization dependence of plasmon-enhanced fluorescence on single gold nanorods. *Nano Letters*, 9(11):3896–3903, 2009.
- [NBG<sup>+</sup>14] Frank Neubrech, Sebastian Beck, Tobias Glaser, Mario Hentschel, Harald Giessen, and Annemarie Pucci. Spatial extent of plasmonic enhancement of vibrational signals in the infrared. *ACS nano*, 8(6):6250–8, 2014.
- [NCR<sup>+</sup>12] V. N'Tsame Guilengui, L. Cerutti, J.-B. Rodriguez, E. Tournié, and T. Taliercio. Localized surface plasmon resonances in highly doped semiconductors nanostructures. *Applied Physics Letters*, 101(16):161113, 2012.
- [NFK<sup>+</sup>09] Z H Nie, D Fava, E Kumacheva, H E Ruda, and A Shik. Plasmon spectra in two-dimensional nanorod arrays. *Nanotechnology*, 20:295203/1–295203/9, 2009.
- [NG13] Vilianne NTsame Guilengui. *Technologie et étude de résonateurs plasmoniques à base d'InAsSb : vers une plasmonique tout semi-conducteur*. PhD thesis, University of Montpellier, 2013.
- [NHS<sup>+</sup>14] Yoshiaki Nishijima, Yoshikazu Hashimoto, Gediminas Seniutinas, Lorenzo Rosa, and Saulius Juodkazis. Engineering gold alloys for plasmonics. *Appl. Phys. A*, 117:641–645, 2014.
- [NHV<sup>+</sup>15] Tomáš Neuman, Christian Huck, Jochen Vogt, Frank Neubrech, Rainer Hillenbrand, Javier Aizpurua, and Annemarie Pucci. Importance of plasmonic scattering for an optimal enhancement of vibrational absorption in seira with linear metallic antennas. *Journal of Physical Chemistry C*, 119(47):26652–26662, 2015.

- [NHW<sup>+</sup>17] Frank Neubrech, Christian Huck, Ksenia Weber, Annemarie Pucci, and Harald Giessen. Surface-enhanced infrared spectroscopy using resonant nanoantennas. *Chemical Reviews*, 117:5110–5145, 2017.
- [NKL<sup>+</sup>06] F. Neubrech, T. Kolb, R. Lovrincic, G. Fahsold, A. Pucci, J. Aizpurua, T. W. Cornelius, M. E. Toimil-Molares, R. Neumann, and S. Karim. Resonances of individual metal nanowires in the infrared. *Applied Physics Letters*, 89(25):253104, 2006.
- [NLK<sup>+</sup>12] G. V. Naik, J. Liu, A. V. Kildishev, V. M. Shalaev, and A. Boltasseva. Demonstration of Al:ZnO as a plasmonic component for near-infrared metamaterials. *Proceedings of the National Academy of Sciences*, 109(23):8834–8838, 2012.
- [NOP<sup>+</sup>04] Peter Nordlander, C. Oubre, E. Prodan, K. Li, and M. I. Stockman. Plasmon hybridization in nanoparticle dimers plasmon hybridization in nanoparticle. *Nano Letters*, 4(5):899–903, 2004.
- [Nov09] Lukas Novotny. Optical antennas. *Frontiers of Engineering*, 39(4):14–20, 2009.
- [NP13] F. Neubrech and A. Pucci. Plasmonic enhancement of vibrational excitations in the infrared. *IEEE Journal of Selected Topics in Quantum Electronics*, 19(3):4600809–4600809, 2013.
- [NPC<sup>+</sup>08] Frank Neubrech, Annemarie Pucci, Thomas Walter Cornelius, Shafqat Karim, Aitzol García-Etxarri, and Javier Aizpurua. Resonant plasmonic and vibrational coupling in a tailored nanoantenna for infrared detection. *Physical Review Letters*, 101(15):157403, 2008.
- [NSB13] Gururaj V Naik, Vladimir M Shalaev, and Alexandra Boltasseva. Alternative plasmonic materials: beyond gold and silver. *Advanced materials*, 25(24):3264–94, 2013.
- [NWK<sup>+</sup>12] Frank Neubrech, Daniel Weber, Julia Katzmann, Christian Huck, Andrea Toma, Enzo Di Fabrizio, Annemarie Pucci, and Thomas Ha. Infrared optical properties of nanoantenna dimers with photochemically narrowed gaps in the 5 nm regime. *ACS nano*, 6(8):7326–7332, 2012.
- [Osa01] Masatoshi Osawa. Surface-enhanced infrared absorption. *Topics Appl. Phys.*, 81:163–187, 2001.
- [Ott68] Andreas Otto. Excitation of nonradiative surface plasma waves in silver by the method of frustrated total reflection. *Zeitschrift für Physik*, 216:398–410, 1968.
- [Pal02] Edward D. Palik, editor. *Handbook of Optical Constants of Solids volume I - III*. Academic Press, Burlington, 2002.
- [PH06] Marek Piliarik and Jiri Homola. Spr sensor instrumentation. In Jiri Homola, editor, *Surface Plasmon Resonance Based Sensors*, chapter 4. Springer, Berlin, Heidelberg, 2006.

- [Pin56] David Pines. Collective energy losses in solids. *Reviews of Modern Physics*, 28(3):184–198, 1956.
- [PKA<sup>+</sup>11] Imogen M Pryce, Yousif A Kelaita, Koray Aydin, Harry A Atwater, and Pryce E T Al. Compliant metamaterials for resonantly enhanced infrared absorption spectroscopy and refractive index sensing. *ACSNano*, 5(10):8167–8174, 2011.
- [PKE12] C. Parsajoo, J-M. Kauffmann, and M. Elkaoutit. Woodhead Publishing Series in Biomaterials: Number 45. In Seamus Higson, editor, *Biosensors for medical applications*, chapter 9. Woodhead Publishing, Oxford, Cambridge, Philadelphia, New Delhi, 2012.
- [PM08] Ilaria Palchetti and Marco Mascini. Electroanalytical biosensors and their potential for food pathogen and toxin detection. *Analytical and Bioanalytical Chemistry*, 391(2):455–471, 2008.
- [PMS<sup>+</sup>14] A. K. Pradhan, R. M. Mundle, Kevin Santiago, Skuza. J. R., Bo Xiao, K. D. Song, M. Bahoura, Ramez Cheaito, and Patrick E. Hopkins. Extreme tunability in aluminum doped zinc oxide plasmonic materials for near-infrared applications. *Scientific Reports*, 4(6415), 2014.
- [PNW<sup>+</sup>10] A. Pucci, F. Neubrech, D. Weber, S. Hong, T. Toury, and M. Lamy de la Chapelle. Surface enhanced infrared spectroscopy using gold nanoantennas. *Physica Status Solidi (B)*, 247(8):2071–2074, 2010.
- [Poh17] Miroslav Pohanka. The piezoelectric biosensors: Principles and applications, a review. *International Journal of Electrochemical Science*, 12(1):496–506, 2017.
- [Pro08] Liviu Prodan. *Mid-infrared characterization of two-dimensional photonic crystal slabs fabricated in silicon with laser interference lithography*. PhD thesis, University of Twente, 2008.
- [PSCE07] J. M. Pitarke, V. M. Silkin, E. V. Chulkov, and P. M. Echenique. Theory of surface plasmons and surface-plasmon polaritons. *Rep. Prog. Phys.*, 70:1–87, 2007.
- [PSV75] R. B. Pettit, J. Silcox, and R. Vincent. Measurement of surface-plasmon dispersion in oxidized aluminum films. *Physical Review B*, 11(8):3116–3123, 1975.
- [PZT<sup>+</sup>13] Xiaomei Pei, Bing Zhang, Juan Tang, Bingqian Liu, Wenqiang Lai, and Dianping Tang. Sandwich-type immunosensors and immunoassays exploiting nanostructure labels: A review. *Analytica Chimica Acta*, 758:1 – 18, 2013.
- [Rae80] Heinz Raether. *Excitation of Plasmons and Interband Transitions by Electrons*. Springer Verlag, 1980.
- [Rae82] Heinz Raether. Surface Plasmons and Roughness. In V. M. Agranovich and D. L. Mills, editors, *Surface Polaritons*, chapter 9. North-Holland Publishing Company, 1982.

- [Rae86] Heinz Raether. *Surface Plasmons on Smooth and Rough Surfaces and on Gratings*. Springer, 1986.
- [RBL<sup>+</sup>15] S. Roux, P. Barritault, O. Lartigue, L. Cerutti, E. Tournié, B. Gérard, and A. Grisard. Mid-infrared characterization of refractive indices and propagation losses in GaSb/AlXGa1-XAsSb waveguides. *Applied Physics Letters*, 107(17):1–7, 2015.
- [RCE<sup>+</sup>08] C. Rhodes, M. Cerruti, A. Efremenko, M. Losego, D. E. Aspnes, J.-P. Maria, and S. Franzen. Dependence of plasmon polaritons on the thickness of indium tin oxide thin films. *Journal of Applied Physics*, 103(9):093108, 2008.
- [RHL<sup>+</sup>03] W. Rechberger, A. Hohenau, A. Leitner, J.R. Krenn, B. Lamprecht, and F.R. Aussenegg. Optical properties of two interacting gold nanoparticles. *Optics Communications*, 220(1):137 – 141, 2003.
- [Rit57] Rufus H. Ritchie. Plasma losses by fast electrons in thin films. *Physical Review*, 106(5):874–881, 1957.
- [RJBK05] J. Gómez Rivas, Christof Janke, Peter Haring Bolivar, and Heinrich Kurz. Transmission of THz radiation through InSb gratings of subwavelength apertures. *Optics Express*, 13(3):847–859, 2005.
- [RKB<sup>+</sup>04] J. Gómez Rivas, M. Kuttge, P. Haring Bolivar, H. Kurz, and J. A. Sánchez-Gil. Propagation of surface plasmon polaritons on semiconductor gratings. *Phys. Rev. Lett.*, 93:256804, 2004.
- [RLJ<sup>+</sup>15] Daniel Rodrigo, Odeta Limaj, Davide Janner, Dordaneh Etezadi, F Javier García De Abajo, Valerio Pruneri, and Hatice Altug. Mid-infrared plasmonic biosensing with graphene. *Science*, 349(6244), 2015.
- [RPAB14] Alexander S Roberts, Anders Pors, Ole Albrektsen, and Sergey I Bozhevolnyi. Subwavelength plasmonic color printing protected for ambient use. *Nano Letters*, 14:783–787, 2014.
- [RSL<sup>+</sup>14] Aaron Rosenberg, Joshua Surya, Runyu Liu, William Streyer, Stephanie Law, L Suzanne Leslie, Rohit Bhargava, and Daniel Wasserman. Flat mid-infrared composite plasmonic materials using lateral doping-patterned semiconductors. *Journal of Optics*, 16(9):094012, 2014.
- [Rum] Raymond Rumpf. Computational electrodynamics. <http://emlab.utep.edu/ee5390cem.htm>. Lecture notes.
- [SAE<sup>+</sup>16] Kandammathe Valiyaveedu Sreekanth, Yunus Alapan, Mohamed Elkabbash, Efe Ilker, Michael Hinczewski, Umut A Gurkan, Antonio De Luca, and Giuseppe Strangi. Extreme sensitivity biosensing platform based on hyperbolic metamaterials. *Nature materials*, 15:621–627, 2016.
- [Sch] John B. Schneider. Understanding the FDTD method. <http://www.eecs.wsu.edu/~schneidj/ufdtd/>.

- [SDC<sup>+</sup>15] S. Scarano, E. Dausse, F. Crispo, J.-J. Toulmé, and M. Minunni. Design of a dual aptamer-based recognition strategy for human matrix metalloproteinase 9 protein by piezoelectric biosensors. *Analytica Chimica Acta*, 897:1 – 9, 2015.
- [SHC12] Richard Soref, Joshua Hendrickson, and Justin W Cleary. Mid- to long-wavelength infrared plasmonic-photonics using heavily doped n-Ge/Ge and n-GeSn/GeSn heterostructures. *Optics Express*, 20(4):3814–24, 2012.
- [SLG<sup>+</sup>13] Edward Sachet, Mark D. Losego, Joshua Guske, Stefan Franzen, and Jon-Paul Maria. Mid-infrared surface plasmon resonance in zinc oxide semiconductor thin films. *Applied Physics Letters*, 102(5):051111, 2013.
- [SMP<sup>+</sup>11] Monas Shahzad, Gautam Medhi, Robert E. Peale, Walter R. Buchwald, Justin W. Cleary, Richard Soref, Glenn D. Boreman, and Oliver Edwards. Infrared surface plasmons on heavily doped silicon. *Journal of Applied Physics*, 110(12):123105, 2011.
- [Sor10] Richard Soref. Mid-infrared photonics in silicon and germanium. *Nature Photonics*, 4:495–497, 2010.
- [SPK<sup>+</sup>14] Jung-Hun Seo, Jung Ho Park, Seong-Il Kim, Bang Ju Park, Zhenqiang Ma, Jinnil Choi, and Byeong-Kwon Ju. Nanopatterning by laser interference lithography: Applications to optical devices. *Journal of Nanoscience and Nanotechnology*, 14(2):1521–1532, 2014.
- [SSW<sup>+</sup>15] Florian Sterl, Nikolai Strohfeldt, Ramon Walter, Ronald Griessen, Andreas Tittl, and Harald Giessen. Magnesium as novel material for active plasmonics in the visible wavelength range. *Nano Letters*, 15(12):7949–7955, 2015.
- [SSZ<sup>+</sup>16] Wei Chuan Shih, Gregg M. Santos, Fusheng Zhao, Oussama Zenasni, and Md Masud Parvez Arnob. Simultaneous chemical and refractive index sensing in the 1-2.5  $\mu\text{m}$  near-infrared wavelength range on nanoporous gold disks. *Nano Letters*, 16(7):4641–4647, 2016.
- [Sto12] Mark I. Stockmann, editor. *Experimental Demonstration of Plasmonic-Grating-Assisted Optical Biosensor*, volume 8457 of *Plasmonics: Metallic Nanostructures and Their Optical Properties X*. Proc. of SPIE, 2012.
- [STS<sup>+</sup>14] Nikolai Strohfeldt, Andreas Tittl, Martin Schäferling, Frank Neubrech, Uwe Kreibig, Ronald Griessen, and Harald Giessen. Yttrium hydride nanoantennas for active plasmonics. *Nano Letters*, 14:1140–1147, 2014.
- [SWZ<sup>+</sup>03] K.-H. Su, Q.-H. Wei, X. Zhang, J. J. Mock, D. R. Smith, and S. Schultz. Interparticle coupling effects on plasmon resonances of nanogold particles. *Nano Letters*, 3(8):1087–1090, 2003.
- [TGC<sup>+</sup>14] Thierry Taliercio, Vilianne Ntsame Guilengui, Laurent Cerutti, Eric Tournié, and Jean-Jacques Greffet. Brewster "mode" in highly doped semiconductor

- layers: an all-optical technique to monitor doping concentration. *Optics Express*, 22(20):24294–303, 2014.
- [Tok90] Eisuke Tokumitsu. Correlation between fermi level stabilization positions and maximum free carrier concentrations in iii-v compound semiconductors. *Japanese Journal of Applied Physics*, 29(Part 2, No. 5):L698–L701, 1990.
- [Tom12] S. Tombelli. Woodhead Publishing Series in Biomaterials: Number 45. In Seamus Higson, editor, *Biosensors for medical applications*, chapter 2. Woodhead Publishing, Oxford, Cambridge, Philadelphia, New Delhi, 2012.
- [TT14] Ashutosh Tiwari and Anthony P. F. Turner. Biosensors Nanotechnology. In Ashutosh Tiwari and Anthony P. F. Turner, editors, *Biosensors Nanotechnology*, chapter Preface. Scrivener Publishing Wiley, 2014.
- [TZZ<sup>+</sup>14] Shawn J Tan, Lei Zhang, Di Zhu, Xiao Ming Goh, Ying Min Wang, Karthik Kumar, Cheng-Wei Qiu, and Joel K W Yang. Plasmonic color palettes for photorealistic printing with aluminum nanostructures. *Nano letters*, 14(7):4023–9, 2014.
- [VCK12] A. J. Veloso, X. R. Cheng, and K. Kerman. Woodhead Publishing Series in Biomaterials: Number 45. In Seamus Higson, editor, *Biosensors for medical applications*, chapter 1. Woodhead Publishing, Oxford, Cambridge, Philadelphia, New Delhi, 2012.
- [VDLG10] Tuan Vo-Dinh, Robert A. Lieberman, and Günter Gauglitz, editors. *Infrared surface plasmon resonance biosensor*, volume 7673 of *Advanced Environmental, Chemical, and Biological Sensing Technologies VII*. Proc. of SPIE, apr 2010.
- [VFC07] Claudia Valdez-Flores and M P Can. Food chemistry on-line dilution and detection of vainillin in vanilla extracts obtained by ultrasound. *Food Chemistry*, 105:1201–1208, 2007.
- [VH06] Hana Vaisocherova and Jiri Homola. SPR Biosensors for Medical Diagnostics. In Jiri Homola, editor, *Surface Plasmon Resonance Based Sensors*, chapter 9, pages 229–247. Springer, Berlin, Heidelberg, 2006.
- [VHN<sup>+</sup>14] Jochen Vogt, Christian Huck, Frank Neubrech, Andrea Toma, David Gerbert, and Annemarie Pucci. Impact of the plasmonic near- and far-field resonance-energy shift on the enhancement of infrared vibrational signals. *Physical chemistry chemical physics : PCCP*, 17(33):21169–75, 2014.
- [WAAG<sup>+</sup>11] Daniel Weber, Pablo Albella, Pablo Alonso-González, Frank Neubrech, Han Gui, Tadaaki Nagao, Rainer Hillenbrand, Javier Aizpurua, and Annemarie Pucci. Longitudinal and transverse coupling in infrared gold nanoantenna arrays: long range versus short range interaction regimes. *Optics Express*, 19(16):15047–61, 2011.



- [WAvW11] H Wolferen, Leon Abelmann, and Henk van Wolferen. Laser interference lithography. *Lithography: Principles, Processes and Materials*, pages 133–148, 2011.
- [WIN<sup>+</sup>10] Paul R. West, Satoshi Ishii, Gururaj V. Naik, Naresh K. Emani, Vladimir M. Shalaev, and Alexandra Boltasseva. Searching for better plasmonic materials. *Laser and Photonics Reviews*, 4(6):795–808, 2010.
- [WKA<sup>+</sup>12] Chihhui Wu, Alexander B. Khanikaev, Ronen Adato, Nihal Arju, Ahmet Ali Yanik, Hatice Altug, and Gennady Shvets. Fano-resonant asymmetric metamaterials for ultrasensitive spectroscopy and identification of molecular monolayers. *Nature Materials*, 11:69–75, 2012.
- [WMM<sup>+</sup>14] Martin Wagner, Alexander S. McLeod, Scott J. Maddox, Zhe Fei, Mengkun Liu, Richard D. Averitt, Michael M. Fogler, Seth R. Bank, Fritz Keilmann, and D. N. Basov. Ultrafast dynamics of surface plasmons in InAs by time-resolved infrared nanospectroscopy. *Nano Letters*, 14(8):4529–4534, 2014. PMID: 25046340.
- [WMS<sup>+</sup>16] T. Weiss, M. Mesch, M. Schäferling, H. Giessen, W. Langbein, and E. A. Muljarov. From dark to bright: First-order perturbation theory with analytical mode normalization for plasmonic nanoantenna arrays applied to refractive index sensing. *Phys. Rev. Lett.*, 116:237401, 2016.
- [WV07] Katherine A Willets and Richard P Van Duyne. Localized surface plasmon resonance spectroscopy and sensing. *Annual review of physical chemistry*, 58:267–97, 2007.
- [Yee66] Kane S. Yee. Numerical solution of initial boundary value problems involving maxwell’s equations in isotropic media. *IEEE Transactions of Antennas and Propagation*, May:302–307, 1966.
- [YGL15] Jianji Yang, Harald Giessen, and Philippe Lalanne. Simple analytical expression for the peak-frequency shifts of plasmonic resonances for sensing. *Nano letters*, 15(5):3439–44, 2015.
- [YLG<sup>+</sup>12] Nimet Yildirim, Feng Long, Ce Gao, Miao He, Han-Chang Shi, and April Z. Gu. Aptamer-based optical biosensor for rapid and sensitive detection of 17 $\beta$ -estradiol in water samples. *Environmental Science & Technology*, 46(6):3288–3294, 2012. PMID: 22296460.
- [YW05] Nan Yao and Zhong Lin Wang. *Handbook of microscopy for nanotechnology*. Kluwer Academic Publishers, Boston, Dordrecht, New York, London, 2005.
- [ZMHW15] Yujun Zhong, Shyamala Devi Malagari, Travis Hamilton, and Daniel Wasserman. Review of mid-infrared plasmonic materials. *Journal of Nanophotonics*, 9:093791, 2015.
- [ZN11] Jorge Zuloaga and Peter Nordlander. On the energy shift between near-field and far-field peak intensities in localized plasmon systems. *Nanolett.*, 11:1280–1283, 2011.

- [ZSM05] Anatoly V. Zayats, Igor I. Smolyaninov, and Alexei A. Maradudin. Nano-optics of surface plasmon polaritons. *Physics Reports*, 408(3-4):131–314, 2005.
- [ZZBG12] Jun Zhao, Chunjie Zhang, Paul V. Braun, and Harald Giessen. Large-area low-cost plasmonic nanostructures in the NIR for Fano resonant sensing. *Adv. Mater.*, 24:OP247–OP252, 2012.



## *Bibliography*

# Listes des publications et communications effectuées sur le sujet

## Articles dans des revues internationales à comité de lecture

*Highly doped semiconductor plasmonic nanoantenna arrays for polarization selective broadband surface-enhanced infrared absorption spectroscopy of vanillin*

**F. B. Barho**, F. Gonzalez-Posada, M.-J. Milla-Rodrigo, M. Bomers, L. Cerutti, T. Taliercio  
Nanophotonics 2017, in press.

*All-semiconductor plasmonic gratings for biosensing applications in the mid-infrared spectral range*

**F. B. Barho**, F. Gonzalez-Posada, M.-J. Milla-Rodrigo, M. Bomers, L. Cerutti, T. Taliercio  
Optics Express 2016, 24 (14), 16175-16190.

*Surface-Enhanced Infrared Absorption with Si-doped InAsSb/GaSb nano-antennas*

M.-J. Milla-Rodrigo, **F. Barho**, F. Gonzalez-Posada, M. Bomers, L. Cerutti, T. Taliercio  
Optics Express 2017, in press.

*Localized surface plasmon resonance frequency tuning in highly doped InAsSb/GaSb one-dimensional nanostructures*

M.-J. Milla, **F. Barho**, F. Gonzalez-Posada, L. Cerutti, M. Bomers, J-B. Rodriguez, E. Tournié, T. Taliercio  
Nanotechnology 2016, 27, 425201.

*Fano-like resonances sustained by Si doped InAsSb plasmonic resonators integrated in GaSb matrix*

T. Taliercio, V. NTsame Guilengui, L. Cerutti, J-B. Rodriguez, **F. Barho**, M-J. Milla Rodrigo, F. Gonzalez-Posada, E. Tournié, M. Niehle, A. Trampert  
Optics Express 2015, 23 (23), 29423.

## Conférences internationales à comité de lecture

as presenting author

*Highly doped semiconductor plasmonic resonators for surface enhanced infrared absorption spectroscopy* (oral)

**F. Barho**, F. Gonzalez-Posada Flores, M. Bomers, M.-J. Milla Rodrigo, L. Cerutti, E. Tournié, T. Taliercio

Nanop 2016 Nanophotonics and Micro/Nano optics, Dec 7-9, 2016, Paris (France).

*Optimization of plasmonic grating resonators based on highly doped semiconductors for sensing applications using 2D finite-difference time-domain simulations* (oral)

**F. B. Barho**, M.-J. Milla Rodrigo, F. Gonzalez-Posada Florès, T. Taliercio

SPIE Opto 2016, Photonics West, Feb 13-18, 2016, San Francisco (USA).

*From 1-dimensional to 2-dimensional Periodic Semiconductor Plasmonic Resonators: Designing the Optical Response for Sensing Applications* (poster)

**F. B. Barho**, F. Gonzalez-Posada, M. Bomers, M.-J. Milla, L. Cerutti, E. Tournié and T. Taliercio

CLEO/Europe-ECEQ 2017, Conference on Lasers and Electro-optics - European Quantum Electronics Conference, June 25-29, 2017, Munich (Germany).

as coauthor

*Surface enhanced infrared absorption with highly doped InAsSb plasmonic nano-antenna arrays* (oral)

**F. Barho**, M. J. Milla, M. Bomers, F. Gonzalez-Posada Flores, L. Cerutti, E. Tournié, T. Taliercio

Nanop 2017 Nanophotonics and Micro/Nano optics, Sept 13-15, 2017, Barcelona (Spain).

*GaSb oxidation for plasmonic enhanced mid-IR molecular spectroscopy* (oral)

M. Bomers, **F. Barho**, A. Mezy, M. J. Milla, L. Cerutti, F. Gonzalez-Posada Flores, E. Tournié, T. Taliercio

Nanop 2017 Nanophotonics and Micro/Nano optics, Sept 13-15, 2017, Barcelona (Spain).

*Plasmonic bio-sensing based on highly doped semiconductors* (oral)

**F. Barho**, M.J. Milla, F. Gonzalez-Posada, L. Cerutti, M. Bomers, E. Tournié, T. Taliercio

SPIE Optics and Photonics 2017, Aug 6-10, 2017, San Diego (USA).

*Enhanced molecular sensing by all semiconductor plasmonic devices functionalized with phospho-*

*nates* (poster)

M. Bomers, A Mezy, **F. Barho**, M.J. Milla, L. Cerutti, F. González-Posada, E. Tournié, T. Taliercio

SPP8, The 8th International Conference of Surface Plasmon Photonics, May 22-26, 2017, Taipeh (Taiwan).

*Impact of GaSb oxidation on the mid-IR properties of InAsSb:Si / GaSb based plasmonic biosensors* (poster)

M. Bomers, M. J. Milla, D. M. Di Paola, **F. Barho**, L. Cerutti, F. González-Posada, A. Patané, E. Tournié, and T. Taliercio

SPP8, The 8th International Conference of Surface Plasmon Photonics, May 22-26, 2017, Taipeh (Taiwan).

*Surface enhanced infrared absorption monitoring in 1-dimensional Si-doped InAsSb nano-antennas* (poster)

M.J. Milla, F. González-Posada, **F. Barho**, M. Bomers, L. Cerutti, E. Tournié and T. Taliercio

SPP8, The 8th International Conference of Surface Plasmon Photonics, May 22-26, 2017, Taipeh (Taiwan).

*Highly doped InAsSb plasmonic arrays for mid-infrared biosensing* (oral)

**Franziska Barho**, Fernando Gonzalez-Posada, Maria-Jose Milla Rodrigo, Mario Bomers, Laurent Cerutti, Thierry Taliercio

NMDC 2016, 11th IEEE Nanotechnology Materials and Devices Conference, Oct 9-12, 2016, Toulouse (France).

*Tuning of the localized surface plasmon wavelength in highly doped InAsSb/GaSb nanostructures* (oral)

Maria-Jose Milla Rodrigo, **Franziska B. Barho**, Fernando Gonzales-Posada Florès, Laurent Cerutti, Jean-Baptiste Rodriguez, Eric Tournié, Thierry Taliercio

SPIE Opto 2016, Photonics West, Feb 13-18, 2016, San Francisco (USA).

*Brewster mode: optical monitoring of the semiconductor doping level* (oral)

Maria-Jose Milla Rodrigo, Thierry Taliercio, Laurent Cerutti, Fernando Gonzales-Posada Florès, **Franziska B. Barho**, Jean-Baptiste Rodriguez, Eric Tournié, Jean-Jaques Greffet

SPIE Opto 2016, Photonics West, Feb 13-18, 2016, San Francisco (USA).

## **Conférences nationales**

*A plasmonic biosensor for the mid-infrared* (poster)

**F. B. Barho**, M. Bomers, M-J. Milla-Rodrigo, F. Gonzalez-Posada, L. Cerutti, T. Taliercio  
Doctiss 2016, Journée des doctorants de l'école doctorale Information, Structures et Systèmes  
(Conférence de vulgarisation), 30 juin, 2016, Montpellier (France).

## Abstract

The detection and identification of biological and chemical substances can be performed with biosensors. Biosensors are required to be simple and rapid to use, small, and sensitive in order to detect minute amounts of analyte molecules. Plasmonic devices have proven their utility as biosensing transducers. Surface plasmon-polaritons (SPP), collective oscillations of the electron cloud in metallic media coupled to an electromagnetic wave, are sensitive to the refractive index of their environment, providing thus an efficient way to probe the presence of molecules by the refractive index modification. This technique is called surface plasmon resonance (SPR) sensing. Moreover, SPP confine the incident electric field to sub-wavelength dimensions and enhance the field strength. Molecules located in these so-called field hotspots interact more efficiently with incident light due to a coupling mechanism mediated by the SPP, so that their infrared (IR) absorption cross section is increased. While IR spectroscopy is a standard tool for molecular identification, it does not provide sufficient sensitivity for the detection of smallest quantities. Exploiting the surface enhanced IR absorption (SEIRA) due to the plasmonic enhancement enables the detection of small amounts of analyte.

While surface plasmons were mainly discovered using noble metals such as gold and silver, nowadays other material systems are also considered which display complementary or improved properties compared to the standard materials in plasmonics, especially to enlarge the spectral range where plasmonic effects can be observed and exploited. Material science enables to tailor the dielectric function of a material and consequently to control the plasmonic properties. Highly doped III-V semiconductors constitute an alternative to gold and silver for mid-IR plasmonics, due to their dielectric function which resembles the one of the noble metals, but shifted to the mid-IR spectral range. Indeed, InAsSb in the IR is even less lossy than gold in the visible. SEIRA using plasmonic resonances spectrally tuned to molecular absorption lines, or resonant SEIRA, requires nanoantenna substrates displaying their resonances in the IR. Highly doped InAsSb grown lattice matched on GaSb substrates is an interesting material system for this task. InAsSb is plasmonic for wavelengths above approximately  $5\ \mu\text{m}$ .

In this work, we propose InAsSb:Si/GaSb nanostructures as SEIRA and SPR substrates for an application in biosensing devices. InAsSb nanoantennas on GaSb substrates have been prepared using photolithography and wet chemical etching by a citric acid: hydrogen peroxyde solution or alternatively, by interferential lithography and reactive ion etching, especially to reduce the lattice parameter. An optical characterization of the structures was performed by FTIR spectroscopy, supported by numerical finite-difference time-domain (FDTD) calculations which were also applied to study the impact of geometrical parameters on the optical response. Notably, two types of structure designs were proposed: one-dimensional periodic gratings and two-dimensional arrays of rectangular shaped nanoantennas which provide localized surface plasmon resonances (LSPR) in both polarization directions contrary to the gratings and enable hence a dual band optical response. SPR sensing and SEIRA have successfully been demonstrated using both types of structures, with proof-of-concept analytes such as different polymers and the aromatic compound vanillin with absorption features at high IR wavelengths. A bulk sensitivity in the range of  $10^2$  to  $10^3\ \text{nm}/\text{RIU}$  was reached. The vibrational signals increased of factors ranging between approximately 1.2-5.7, and the SEIRA enhancement was estimated to be in the range of  $10^3$  to  $10^4$  for the rectangular nanoantenna arrays.

## Résumé

La détection et l'identification des substances biologiques ou chimiques peuvent être accomplies par des biocapteurs. On exige des biocapteurs d'être simple et rapide à utiliser, d'avoir une taille réduite, et d'être suffisamment sensible afin de pouvoir détecter des molécules en petite quantité. Des dispositifs plasmoniques se sont révélés adaptés pour l'usage en tant qu'élément transducteur des biocapteurs. Les plasmon-polaritons de surface (SPP) sont des oscillations collectives du nuage électronique des métaux, couplées à des ondes électromagnétiques. Leur fréquence de résonance dépend de l'indice de réfraction de leur environnement diélectrique. Ceci permet de sonder de manière efficace la présence des molécules par la modification de l'indice de réfraction engendrée par celles-ci. La technique reposant sur ce principe s'appelle la détection par résonance des plasmons de surface (SPR sensing en anglais). De plus, les SPP confinent le champ électrique incident à des volumes sub-longueurs d'onde et l'exaltent ainsi. Les molécules qui se situent dans ces zones de forte exaltation du champ électrique interagissent plus efficacement avec la lumière incidente par l'intermédiaire du SPP, tel que leur section efficace de l'absorption infrarouge (IR) augmente. La spectroscopie IR est une technique standard d'identification de molécules en quantités suffisantes. Pour améliorer la sensibilité, la spectroscopie vibrationnelle d'absorption exaltée par la surface (SEIRA pour surface enhanced infrared absorption en anglais) est particulièrement bien adaptée.

Alors que la plasmonique s'est principalement développée dans le visible via les métaux nobles, les semi-conducteurs III-V fortement dopés présentent une alternative intéressante pour la plasmonique dans le moyen IR. Leur fonction diélectrique ressemble à celle des métaux nobles dans le visible, mais décalée dans le moyen IR. Leur densité de charges moindre que celle de l'or permet de réduire considérablement leurs pertes. La spectroscopie SEIRA utilise des nanoantennes plasmoniques dont les résonances se situent dans l'IR pour couvrir la gamme spectrale des modes vibrationnels moléculaires. L'InAsSb fortement dopé accordé en maille sur un substrat en GaSb présente des propriétés plasmoniques au-delà de  $5\ \mu\text{m}$  de longueurs d'onde.

Dans ce manuscrit, nous proposons des nanostructures en InAsSb :Si/GaSb pour développer un biocapteur utilisant les techniques de SEIRA et de SPR «sensing». Les nanostructures ont été réalisées soit par photolithographie et gravure chimique humide soit par lithographie interférentielle et gravure par plasma réactif. Les caractérisations optiques ont été effectuées par spectroscopie IR à transformée de Fourier. Des calculs numériques par la méthode des différences finies dans le domaine temporel (FDTD) ont permis d'étudier l'effet des paramètres géométriques sur la réponse optique des structures. Deux types de structure ont été proposés : des réseaux unidimensionnels ainsi que des réseaux bidimensionnels de nanoantennes rectangulaires supportant des résonances de plasmon de surface localisé (LSPR) dans les deux directions de polarisation de la lumière par rapport aux axes de la structure. Ce type de structures permet ainsi une réponse optique ayant des résonances dans deux bandes spectrales différentes. Les techniques de SPR «sensing» et de SEIRA ont été démontrées pour l'ensemble des structures uni- et bidimensionnelles. Différents types d'analytes comme les polymères et le benzaldéhyde vanilline ont servi de systèmes de tests pour les structures plasmoniques. Les sensibilités se situent entre  $10^2$  et  $10^3$  nm/RIU. Les facteurs d'augmentation des signaux vibrationnels obtenus sont compris dans une gamme de 1,2 à 5,7 et les facteurs d'exaltation ont été évalués autour de  $10^3$  à  $10^4$  pour les réseaux bidimensionnels de nanoantennes plasmoniques.